STUK-A223 / NOVEMBER 2007

A

Thermomechanics of swelling unsaturated porous media

Compacted bentonite clay in spent fuel disposal

Petri Jussila

Säteilyturvakeskus
Strålsäkerhetscentralen
Radiation and Nuclear Safety Authority
STUK

STUK-A223 / NOVEMBER 2007

Thermomechanics of swelling unsaturated porous media

Compacted bentonite clay in spent fuel disposal

Petri Jussila

ACADEMIC DISSERTATION

Dissertation for the degree of Doctor of Science in Technology to be presented with due permission of the Department of Engineering Physics and Mathematics, for public examination and debate in Auditorium E at Helsinki University of Technology (Espoo, Finland) on the 13th of November, 2007, at 12 noon.

Radiation and Nuclear Safety Authority, STUK

Helsinki University of Technology
Department of Engineering Physics and Mathematics
Institute of Mathematics

STUK • SÄTEILYTURVAKESKUS
STRÅLSÄKERHETSCENTRALEN
RADIATION AND NUCLEAR SAFETY AUTHORITY

Osoite/Address • Laippatie 4, 00880 Helsinki
Postiosoite / Postal address • PL / P.O.Box 14, FIN-00881 Helsinki, FINLAND
Puh./Tel. +358 9 759 881 • Fax +358 9 759 88 500 • www.stuk.fi

Supervised by:
Professor Rolf Stenberg
Department of Engineering Physics and Mathematics
Helsinki University of Technology, Finland

Professor Emeritus Martti Mikkola
Department of Engineering Physics and Mathematics
Helsinki University of Technology, Finland

Reviewed by:
Professor Markku Kataja
University of Jyväskylä, Finland

Dr Reijo Kouhia
Helsinki University of Technology, Finland

Opponent:
Dr Jonny Rutqvist
Lawrence Berkeley National Laboratory, CA, USA

Helsinki 2007

The conclusions in the STUK report series are those of the authors and do not necessarily represent the official position of STUK.

ISBN 978-952-478-265-4 (print)
ISBN 978-952-478-266-1 (pdf)
ISSN 0781-1705

Yliopistopaino, Helsinki 2007

Sold by:
STUK – Radiation and Nuclear Safety Authority
P.O. Box 14, FIN-00881 Helsinki, Finland
Tel. +358-9-759881
Fax +358-9-75988500

JUSSILA Petri. Thermomechanics of swelling unsaturated porous media. Compacted bentonite clay in spent fuel disposal. STUK-A223. Helsinki 2007, 198 pp.

Keywords: engineered barrier, nuclear waste, coupled behavior, swelling, suction, adsorption, phase change, mixture theory, constitutive equations, mathematical modeling

Abstract

A barrier of compacted bentonite clay is planned to be used in geological disposal of spent nuclear fuel. In addition to providing mechanical stability to the waste containers the barrier is supposed to prevent or delay the movement of groundwater and the consequential transport of radionuclides from the repository. Fluid flow, phase changes, mechanical behavior of the buffer, rock, and the containers, and the heat produced by the radioactive waste constitute a coupled thermo–hydro–mechanical (THM) system.

The objective of the thesis is to model the coupled THM behaviour of the bentonite buffer. For this purpose a general thermomechanical and mixture theoretical model is derived and applied to the fully coupled THM description of swelling compacted bentonite. The particular form of the free energy of the system is chosen to take into account interactions of the mixture components, namely, mixing of the gaseous components (water vapor and air) and adsorption and swelling interactions between the liquid water and the solid skeleton. The mechanical part of the model is limited to reversible behavior within the limit of small strains. Numerical implementation is done with the multi-purpose finite element method software ELMER.

The model is applied to various coupled experiments: two kinds of laboratory scale tests for Febex bentonite, larger scale mock-up and in-situ tests for Febex bentonite, and to three kinds of laboratory scale experiments for MX-80 bentonite. In addition, a brief consideration of the difference of the large scale Febex experiments and the real disposal situation is done by incorporating more realistic temperature evolutions of the containers.

The inclusion of the mixing interaction yields Clausius-Clapeyron equations which are valid both for the total pressure (i.e. the boiling pressure) and for the partial pressure of saturated vapor. Additionally, together with an appropriate dissipation function the mixing interaction yields a common form of the Fick law. The adsorption interaction together with the mixing interaction

yields a modified Clausius-Clapeyron equation for the vapor-liquid equilibrium inside the porous medium with suction as the macroscopic result. The swelling interaction yields the macroscopic swelling deformation and swelling pressure in confined condition. Together with the adsorption interaction function and the appropriate dissipation function a modified form of the Darcy law is obtained.

The model is validated by the simulated experiments to reproduce the main coupled features of unsaturated swelling porous medium satisfactorily.

The main results are related to the important questions of the evolution of resaturation and the final hydration stage.

- The observations for the Febex in-situ and, especially, Febex mock-up experiment exhibit an unexpected transient behaviour that the continuum model does not reproduce. This phenomenon is the fast initial wetting of the internal points of the buffer. This phenomenon is attributed here to the prewetting and, especially, to the anisotropic brick-wall like structure of the Febex buffer. Validation of this claim is based on the facts that the phenomenon is not encountered in the continuum mechanical simulations found in the literature, or in other experiments having a more homogeneous structure. Furthermore, by neglecting the initial transient by assuming a higher initial water content the simulation results are consistent with the observations after the transient.
- The simulations of the THM experiments predict a steady unsaturated state. Despite the artificial wetting a Febex type bentonite buffer will not fully saturate if a high temperature gradient prevails as in the experimental setups considered.
- In realistic disposal conditions the simulations do predict a fully saturated state. However, the predicted time to achieve the full saturation is longer than commonly expected for a Febex type buffer.

The difference between the results for the experiments and for the realistic disposal conditions is due to the different heating powers and, consequently, different temperature profiles involved.

JUSSILA Petri. Paisuvan huokoisen aineen termomekaniikka. Puristettu bentoniittisavi ydinjätteen loppusijoituksessa. STUK-A223. Helsinki 2007, 198 s.

Avainsanat: tekninen este, käytetty ydinpolttoaine, loppusijoitus, kytketty käyttäytyminen, paisuminen, imu, imupaine, adsorptio, faasimuutos, seosteoria, konstitutiiviset yhtälöt, matemaattinen mallintaminen

Tiivistelmä

Puristetusta bentoniittisavesta valmistetun puskurin käyttäminen kuuluu käytetyn ydinpolttoaineen geologisen loppusijoituksen suunnitelmiin. Puskurin tärkeimpiä tehtäviä jätekapselien mekaanisen tukemisen ohella ovat pohjaveden virtauksen estäminen ja radionuklidien kulkeutumisen hidastaminen loppusijoituskapselista kallioon. Nesteen ja kaasun virtaus, faasimuutokset, puskurin, kallion ja kapseleiden mekaaninen käyttäytyminen sekä radioaktiivisen jätteen tuottama lämpö muodostavat kytketyn termo–hydro–mekaanisen (THM) järjestelmän.

Väitöskirjan tarkoituksena on mallintaa bentoniittipuskurin kytkettyä THM-käyttäytymistä. Tätä tarkoitusta varten johdettiin yleinen termomekaniikkaan ja seosteoriaan perustuva malli, jota sovellettiin paisuvan huokoisen aineen täysin kytketyn THM-käyttäytymisen kuvaamiseen. Järjestelmää kuvaamaan valittu vapaan energian lauseke ottaa huomioon seoskomponenttien vuorovaikutukset: kaasumaisten komponenttien eli vesihöyryn ja ilman sekoittumisen sekä nestemäisen veden ja kiinteän rungon väliset adsorptio- ja paisuntavuorovaikutukset. Mallin mekaaninen osuus rajoittuu palautuvaan käyttäytymiseen ja pieniin muodonmuutoksiin. Numeerinen laskenta toteutettiin ELMER-nimisellä elementtimenetelmäohjelmistolla.

Mallilla simuloitiin useita kytkettyjä kokeita: kahdentyyppiset laboratoriomittakaavan kokeet Febex-bentoniitille, suuremman mittakaavan mock-up- ja in-situ-kokeet Febex-bentoniitille sekä kolmentyyppiset laboratoriomittakaavan kokeet MX-80-bentoniitille. Tämän lisäksi arvioitiin erikseen suuren mittakaavan Febex-kokeen ja todellisen loppusijoituksen olosuhteiden eroja simuloimalla realistisempia jätekapselin lämpötilakehityskulkuja.

Sekoittumisvuorovaikutuksen ottaminen huomioon tuottaa Clausiuksen-Clapeyronin yhtälöt, jotka pätevät sekä kokonaispaineelle (eli kiehumispaineelle) että kylläisen höyryn osapaineelle. Tämän lisäksi sekoittumisvuorovaikutus yhdessä valitun dissipaatiofunktion kanssa tuottaa yleisesti tunnetun muodon Fickin laista. Adsorptiovuorovaikutus yhdessä sekoittumisvuorovaikutuksen

kanssa tuottaa modifioidun Clausiuksen-Clapeyronin yhtälön, joka pätee höyryn ja nesteen tasapainolle huokoisen aineen sisäpuolella ja jonka makroskooppinen ilmenemismuoto on huokoisen aineen imupaine. Paisuntavuorovaikutus tuottaa makroskooppisen paisuntamuodonmuutoksen sekä paisuntapaineen tilavuudeltaan rajoitetuissa olosuhteissa. Adsorptiovuorovaikutusfunktio yhdessä valitun dissipaatiofunktion kanssa tuottaa modifioidun muodon Darcyn laista. Malli validoitiin simuloinneilla, joilla saatiin tyydyttävällä tavalla tuotettua keskeisimmät kokeellisesti havaitut paisuvan huokoisen aineen kytketyt ominaisuudet.

Tärkeimmät tulokset koskevat puskurin kastumista ja sen lopullista kosteustilaa.

- Febex in-situ- ja etenkin mock-up-kokeessa on havaittu odottamaton alkutransientti, jota jatkuvan aineen malli ei toteuta. Tämä ilmiö on puskurin sisäosan mittapisteiden nopea kastuminen kokeen alkuvaiheessa. Ilmiön selitetään väitöskirjassa johtuvan sekä puskurin esikastelemisesta että etenkin Febex-bentoniittipuskurin anisotrooppisesta tiilimuuria muistuttavasta rakenteesta. Väite perustellaan seuraavilla tosiasioilla: ilmiötä ei ole havaittu jatkuvaan aineeseen perustuvissa simulaatioissa eikä sellaisissa kokeissa, joissa puskuri on mittauksen kannalta isotrooppisempi. Lisäksi tässä työssä simuloitu tulos vastaa havaintoa alkutransientin jälkeen, kun simulaatiossa oletetaan korkeampi alkutransientin jälkeistä tilaa vastaava alkukosteus.
- THM-kokeiden simuloinnit ennustavat alisaturoituneen tasapainotilan. Keinotekoisesta kastelusta huolimatta Febex-tyyppinen puskuri ei kastu täysin, mikäli kokeissa käytetty suuri lämpötilagradientti säilyy.
- Todellisia loppusijoitusolosuhteita vastaavat simuloinnit ennustavat puskurin täyden kastumisen. Ennustettu täyteen kastumiseen tarvittava aika on pidempi kuin yleisesti on otaksuttu Febex-tyyppiselle puskurille.

Koetulosten ja realistisen loppusijoitustilanteen ero johtuu puskurin erilaisesta lämpötilaprofiilista, joka puolestaan johtuu todellisen jätekapselin ja sitä koetilanteessa simuloivan lämmittimen erilaisesta lämpötehosta.

Acknowledgements

Majority of this dissertation was conducted at the Department of Engineering Physics and Mathematics of the Helsinki University of Technology. It was started at the Laboratory of Mechanics and continued at the Institute of Mathematics. Finally, it was finished at the Nuclear Waste Office, Nuclear Waste and Material Regulation, at STUK. I wish to express my gratitude to Esko Ruokola, Principal Adviser, Risto Paltemaa, Head of the Nuclear Waste Office, and Tero Varjoranta, Director of Nuclear Waste and Material Regulation, for their positive attitude towards the finishing of my dissertion project.

I wish to express my gratitude to my supervisors, Professor Rolf Stenberg and Professor Emeritus Martti Mikkola for their guidance. I am grateful to Professor Markku Kataja and Dr Reijo Kouhia for reviewing the thesis with constructive criticism. A special thanks is given to Mr Juha Hartikainen for his efforts to teach me the thermomechanical theory involved and the application of it to the modelling of porous medium. This thesis would look totally different without him. Also, the application would not have been possible without the numerical implementation and the tireless effort and co-operation of Mr Juha Ruokolainen, who, as his colleagues at the Finnish IT centre for science (CSC), deserves my most sincere gratitude and humble respect. I thank Mr Antti Lempinen for his guidance to the coupled behaviour of bentonite. Mr Jordi Alcoverro deserves my gratitude because of his sincere interest in and criticism against the current theoretical approach, for providing me with data and literature, and for being a good friend even at a distance. I want to thank Mr Juha Häikiö for technical help and for his assistance in the final processing of the thesis. I would also like to thank Dr Esko Eloranta for guiding me to the whole area of disposal modelling from the very beginning, and for being always available for a mathematical discussion.

The financial support from the National Graduate School in Engineering Mechanics and from Radiation and Nuclear Safety Authority (STUK) during 2000–2003, and from the Finnish Research Programme on Nuclear Waste Management (KYT) during 2004–2005 is gratefully acknowledged.

Kiitän lämpimästi vanhempiani Arvoa ja Sannaa luottamuksesta ja mahdollisuuksien tarjoamisesta. Lopuksi haluan kiittää vaimoani Tarjaa ja lapsiani Eveliinaa ja Eetua rakkaudesta ja kärsivällisyydestä.

Helsinki, October 2007
Petri Jussila

Contents

Nomenclature

Latin symbols

a	constant material parameters in adsorption and swelling interactions [-]
b	constant mechanical parameter [-]
$\hat{A}$	subgradient belonging to the subdifferential of the indicator function J [$m^5/(s^2kg)$]
$\hat{B}$	subgradient component belonging to subdifferential of indicator function I; equals to intrinsic gaseous pressure [Pa]
c	specific heat [J/(kgK)]
C	feasible set of the molar volume fractions
dx	constant parameter in the experimental thermal conductivity
D	diffusivity [m^2/s]
$\mathbf{D}$	rate of deformation [1/s]
e	specific internal energy [J/kg]
E	Young's modulus [Pa]
f	adsorption function [-]
f_Π	swelling function [-]
F	right hand side vector in numerical time integration scheme
$\mathbf{g}$	gravitational acceleration vector [m/s^2]
G	shear modulus [Pa]
h	specific enthalpy [J/kg]
H	heat transfer coefficient [$J/(Km^2)$]
I	indicator function for the molar volume fraction restrictions
$\mathbf{I}$	identity tensor
J	indicator function for the constant density constituents
k	permeability [m^2]
K	bulk modulus [Pa]
K	matrix containing spatial derivative and reaction terms
l	latent heat of vaporization [J/kg]
L	abbreviation, $L = l_0 - (c_v^p - c_l^p)T_0$ [J/kg]
m	mass [kg]
$\mathbf{m}$	rate of production of linear momentum [N/m^3]
M	molar mass [kg/mol]
M	time derivative coefficient matrix
n	mole number [mol]
$\mathbf{n}$	normal vector [m]
p	pressure, spherical part of Cauchy's stress [Pa]
$\mathbf{q}$	heat flux density [W/m^2]

r	radial coordinate [m]
R	universal gas constant [J/(molK)]
RH	relative humidity [-]
s	specific entropy [J/(kgK)]
t	time [s]
T	temperature [K]
$\mathbf{u}$	displacement [m]
$\mathbf{U}$	absolute velocity [m/s]
v	volume [m^3]
$\tilde{v}$	specific volume [m^3/kg]
w	gravimetric water content [-]
$\mathbf{V}$	relative velocity [m/s]
x	molar fraction [-]
X	numerical solution vector
z	height coordinate [m]
$\mathbf{X}$	generalized irreversible force

Greek symbols

α	constant parameter in the experimental diffusivity [-]
β	volume fraction [-]
γ	rate of production of entropy [W/(Km^3)]
Δt	time step size [s]
ϵ	numerical convergence tolerance
$\boldsymbol{\epsilon}$	strain [-]
ε	void ratio [-]
ζ	vapor fraction [-]
η	porosity [-]
θ	rate of production of mass [kg/(m^{3}s)]
ι	rate of production of energy [W/m^3]
λ	thermal conductivity [W/(Km)]
μ	dynamic viscosity [kg/(sm)]
ν'	Lagrangian multiplier [-]
ν	abbreviation, $\nu = \nu'/(1+\nu')$ [-]
ξ	molar volume fraction [-]
π	pore pressure [Pa]
Π	swelling pressure [Pa]
ρ	apparent density [kg/m^3]
$\tilde{\rho}$	intrinsic density [kg/m^3]

$\boldsymbol{\sigma}$	Cauchy's stress [Pa]
υ	Poisson's ratio [-]
ϕ	dissipation function [W/m^3]
χ	liquid saturation [-]
χ'	specific value of liquid saturation in the experimental thermal conductivity
ψ	specific constituent free energy [J/kg]
$\tilde{\psi}$	specific constituent free energy without the contribution of molar volume fraction restrictions [J/kg]
Ψ	total free energy [J/m^3]
$\partial\Omega$	boundary

Superscripts

D	deviatoric
p	constant pressure
T	transpose
v	constant volume
ξ	interaction of the mixture constituents
0	outside the porous medium, a mixture of gas and liquid

Subscripts

*	reference (velocity)
0	reference state
a	air
c	capillary, suction
dry	value at dry state
eff	effective
g	gas
init	initial value
i, j, k	general mixture constituents
IRR	irreversible
l	liquid
max	maximum
ref	reference state of the experimental diffusivity
rel	relative
rev	representative elementary volume
REV	reversible

s	solid
sat	value at saturated state
v	vapor
V	vertical
vg	relative velocity of vapor and gas

Abbreviations

HLW	High Level Waste (i.e. spent nuclear fuel)
HM	Hydro-Mechanical
THM	Thermo-Hydro-Mechanical
THMC	Thermo-Hydro-Mechano-Chemical

Author's contribution to the thesis

Petri Jussila has derived the presented model, performed the presented analyses, and written the manuscript. DI Juha Ruokolainen from CSC has implemented the model to the numerical ELMER software and written together with Jussila the corresponding Chapter 5.

Chapter 1

Introduction

1.1 Background

Nuclear power plants produce various kinds of radioactive wastes the most hazardous ones of which have to be isolated from the biosphere. In Finland, as in many other countries, the natural option is the final disposal of high level waste (HLW), i.e., the spent fuel, in deep geological formations. HLW from the Finnish power plants will, in accordance with the Nuclear Energy Act, be disposed of in domestic bedrock. The Finnish Government has made and the Parliament has ratified a decision in principle on the disposal facility to be located at Olkiluoto in Eurajoki municipality.

The bedrock constitutes the natural barrier against the escape of the radionuclides. However, during long periods of time groundwater can degrade the waste containers and transport radioactive material from the repository. Mainly for this reason the present HLW disposal plans involve a use of engineered barriers to confirm the isolation of the waste. A buffer of compacted bentonite clay is supposed to suck groundwater, swell and to constitute a stable isolating barrier around the containers. Groundwater flow, water vapor and air flows, phase changes, mechanical behavior of the buffer, rock, and the containers, and the heat produced by the radioactive waste constitute a complicated coupled thermo-hydro-mechanical (THM) system.

Because of the obvious risks involved and the huge financial investments it is crucial to assess performance and safety of HLW disposal in advance. Important information is obtained empirically by experiments ranging from small size laboratory scale to in-situ scale. However, because of the large size of the repository and the surrounding bedrock and the large times scales involved, the performance has to be investigated by means of theoretical and

numerical modelling.

1.2 State of the art

A rough division of the approaches in THM modelling of (swelling) porous media in the literature can be done based on the theoretical framework and the primary purpose of the studies. The first category includes incorporation of well known practical constitutive laws enhanced with some ad hoc addition of swelling. The second category includes more theoretical approaches for the thermomechanical characterization of the complicated coupled behaviour of swelling porous media.

Practical approaches

Most success in macroscopic thermo-hydro-mechanical modeling of swelling porous medium has been obtained by practical engineering approaches as in the international Decovalex projects [99], [100], [2], [29]. Rutqvist *et al* [99], [100] present the general governing equations and a thorough comparison of four computational approaches to model coupled thermo-hydro-mechanical behavior of porous medium in relation to the spent fuel disposal. Typical for these practical or phenomenological approaches is to directly incorporate well-known empirical constitutive relations. E.g. the thermo-hydraulic behavior is described by Fourier's law for heat conduction, Darcy's law for fluid flow, Fick's law for diffusion, Dalton's law for gaseous pressures along with the ideal gas state equations, Henry's law for gas solubility in liquid, and by Kelvin's law for suction. The dependence of the model parameters, e.g. thermal and fluid conductivities and diffusion coefficients, on the primary variables and on the medium properties are experimentally determined. The basis for such thermohydraulic approaches is set by Philip and DeVries [92] and DeVries [32] and adopted by numerous authors, e.g. [58], [90], [118], [64], [108], [3], [86], [14], [39], [40], [87], [91], and [20]. The hydromechanical behaviour is typically enhanced with a swelling description by correction terms [13], [99] or by a state-surface approach [108], [42], [43], [99], [87], [56], [2], [88]. In general, the macroscopic behavior is complicated due to the couplings between different structural levels of swelling material [41]. Consequently, the capability of the practical approaches of utilizing microscopical information obtained by experimental techniques (e.g., [105], [16], [77], [78], [106]) or by molecular simulations (e.g., [31], [18], [12], [65], [57], [54], [107]) is limited. For quantitative modeling purposes, more suitable information on the mechanical behavior of swelling materials is obtained by

macroscopical experimental techniques (e.g., [67], [68], [30], [112], [113], [93], [24], [72], [96], [98], [117], [66], [111]).

Thermomechanical approaches

Following Ziegler [119] we define *thermomechanics* as a combination of *thermodynamics* and *continuum mechanics*. In contrast to the aforementioned practical approaches, the aim of thermomechanics (e.g. [119], [53], [44], [120], [21], [22], [38], [27], [25], [26], [76], [51], [102], [103], [11], [60], [61], [70], and *the current thesis*) is to develop constitutive equations systematically by exploiting the entropy inequality. The choice of the independent variables and the dependence of the specific energy on them is carefully analyzed. The results for such thermomechanical approaches can usually be regarded as generalizations of well-known empirical models. E.g., extensions to the conventional Darcy law presented e.g. by Gray and Hassanizadeh [45], [46], Murad and Cushman [84], [85], Bennethum and Cushman [8], Schrefler [102], [103], and de Boer and Didwania [26] suggest extra terms depending on the gradients of temperature and volume fractions. Common to these approaches is the incorporation of the physico-chemical interaction between solid and liquid yielding the volume fraction gradients as additional driving forces for the liquid flow.

A rigorous thermomechanical theory for swelling clay is proposed by Murad and Cushman [85] who treat clay as a three-scale (micro-, meso-, and macro-scale) system whose macroscopic equations are derived by upscaling the microstructure. At the microscale the model consists of clay platelets and adsorbed water, at the meso scale (the homogenized microscale) of clay particles (adsorbed water plus clay platelets) and bulk water. At the macroscale the medium is treated as a homogenized mixture of clay particles and bulk-phase water. The framework originates from the work of Hassanizadeh and Gray [52], [53] of volume averaging the microscopic balance equations and of using the method of Coleman and Noll [19] to achieve macroscopic constitutive relations which incorporate interfacial effects. This method of combining volume averaging and mixture theory called hybrid mixture theory was used by Achanta [1] to model two-scale isothermal swelling systems such as compacted clays. The framework was extended to three-scale isothermal swelling systems by Murad *et al* [82], Bennethum and Cushman [6], [7], and Murad and Cushman [83], [84], to two-scale non-isothermal non-swelling systems by Murad [80], to three-scale non-isothermal swelling systems by Murad [81], Bennethum and Cushman [8], and Murad and Cushman [85], and to macroscopic swelling systems with

electroquasistatics by Bennethum and Cushman [9], [10].

The current trend of the theoretical modelling of swelling porous media is towards a coupled combination of thermo-hydro-mechano-chemistry (THMC) with electrical phenomena [9], [10], [48], [33], [55], [75], [63], [79]. All these phemonema are relevant in the description of swelling biological tissues and bio-polymers. This seemingly ambitious goal aims at the simultaneous coupled solution of continuum mechanical conservation equations and Maxwell's equations and, hence, constitutes a very interesting and educational synthesis of the basic laws of nature. Although impressive theoretical results have been obtained the inevitable outcome for this approach is the ever complicated and obscure theory which seems to deviate from its applicability to the practical problems.

1.3 Methods

The THM modelling approach of the current thesis is purely macroscopic – microscopic features and phase interfaces are not considered. The general part of the study is based on the work of Mikkola and Hartikainen [50], [76], [51] to model ground freezing by means of thermomechanics and the mixture theory. The entropy inequality is taken into account in the manner introduced by Ziegler [119], [120]. A key feature is that the system behavior is described by particular chosen expressions for the free energy and the dissipation function. The free energy of the system is chosen to take into account the individual nondissipative behaviors of the constituents and their mutual interactions. The considered interactions have a physico-chemical origin. All soils and rocks exhibit molecular adsorption interaction with the polar water molecules yielding macroscopic capillarity and suction. The thermodynamical properties of liquid are affected by the presence of the solid phase [73], [104], [114]. Additionally, for a swelling soil the skeleton structure is affected by the presence of water. In bentonite the key mineral is montmorillonite that has a layered structure that swells upon wetting. If the volume change is restricted swelling pressure develops. The considered interactions in the free energy expressions are

- mixing of the gaseous constituents,
- adsorption of the liquid on the solid, and
- swelling and shrinking due to changes in the water content.

The choice is based on the equilibrium conditions for the water species in different combinations of the constituents. Dissipation function yields the

laws for heat conduction, fluid flow, and relative movement of the gaseous constituents, which complete the constitution. The result is a thermodynamically consistent model describing the macroscopic behavior of the mixture.

The approach to cover vaporization and the behavior of gaseous constituents is a modified extension to that of Frémond and Nicolas [38]. The choice for the free energyexpression yields the relative humidity of the gaseous phase inside the porous medium and, consequently, the capillary pressure directly as functions of the moisture content [60]. This is in contrast to the common approach of expressing the liquid pressure as the difference between the gaseous pressure and the experimentally determined capillary pressure (see e.g. [32], [90], [39], [40], [91], [99]).

The mechanical part of the model is limited to reversible behavior within the limit of small strains. The new feature is the inclusion of a swelling function [61] taking into account the influence of the presence of the liquid phase on the solid free energy. The theory is applied to the thermo-hydro-mechanical modeling of a mixture of compacted bentonite, liquid water, vapor, and air. The resulting model is a system of coupled nonlinear partial differential equations that have to be solved numerically. The numerical implementation is done by means of finite element software ELMER [23].

1.4 Objective and scope

The obvious drawbacks of the modelling approaches found in the literature are, roughly, that the practical approaches lack a profound theory and the thermomechanical approaches are not applicable enough to the fully coupled THM real world problems considered here.

The current thesis is an attempt to combine the two worlds, with the aim to include the most relevant phenomena and, most importantly, to obtain rational results for the real world problem. The electrical phenomena are considered negligible. The mechanical part of the model is limited to reversible behavior within the limit of small strains.

The objective of the thesis is to

- derive a macroscopic thermodynamically consistent thermo-hydro-mechanical model for an arbitrary mixture to describe a general porous medium,
- apply it to modelling of swelling compacted clay, and
- obtain qualitative and quantitative information on the evolution of the THM behaviour of the resaturation phase of the bentonite buffer in a HLW repository.

The model is applied to the simulations of various coupled experiments for compacted bentonite, namely,

- four small scale HM laboratory experiments for Febex bentonite [93],
- a small scale THM experiment for Febex bentonite [110],
- a large scale THM mock-up experiment for Febex bentonite [47], [34], [74],
- a large scale THM in-situ experiment for Febex bentonite [47], [34], [74], [116],
- a small scale HM experiment for MX-80 bentonite [13], [17],
- a small scale THM experiment for MX-80 bentonite [13], [17], and
- a small scale THM mock-up experiment for MX-80 bentonite [17].

In addition, a brief consideration of the difference of the large scale Febex experiments and the real HLW disposal situation is done by incorporating more realistic temperature evolutions of the containers.

One of the fundamental questions is to study the evolution and duration of the full resaturation that are known to involve major uncertainties. A relatively quick achievement of a complete saturation is favorable to ensure the planned safety functions of the buffer, e.g., to seal the construction gaps and to isolate the waste, to achieve a sufficient swelling pressure to mechanically support the waste container and to decrease the microbial behavior in the buffer, to increase the heat conductivity of the buffer to dissipate the heat generated by the waste, and to achieve stable chemical conditions. The emphasis of the study, however, is on the verification and validation of the model performance. This can be done by comparative simulations only, i.e., by comparing to relevant measurements.

1.5 Structure of the thesis

This doctoral thesis consists of the following chapters: Introduction, Theory, Analysis, Discussion, Conclusions, and Appendix.

As the work is interdisciplinary including both the theory and the application, and because there are several application targets, various separate discussion or review sections are included after the corresponding sections. For example, the theoretical part is reviewed in section 2.3 and the results of

individual application targets are reviewed in sections following immediately after the corresponding result sections.

The theoretical *Part I* consists of the derivation of a general model for porous media, its application to the swelling unsaturated porous medium and the review of the model with comparison to the literature.

The analytical *Part II* consists of a brief description of the numerical finite element implementation, application of the model to two kinds of small scale laboratory tests and two large scale tests for Febex bentonite, and the application of the model to two kinds of laboratory tests for MX-80 bentonite.

1.6 Relation to the published work

This thesis bases on the work published in two articles in Transport in Porous Media [60, 61]. The basic theory, especially, the general constitution (2.38–2.44) is presented in [60]. In [61] the fully coupled THM application with the free energies (3.3–3.5), dissipation function (3.6), and the final THM model (3.62–3.78) was published and a preliminary calibration of the model to HM and THM small scale laboratory experiments for Febex bentonite was presented.

In relation to the already published work the current thesis includes at least the following additions and extensions.

- An extended presentation and discussion of the theory with comparison to literature is included.
- More sophisticated parameter values and their variations are applied and discussed.
- In addition, for the simulation of the HM laboratory experiment for Febex bentonite the applied vertical loads and the time stepping are more detailed than in [61],
- In addition, for the simulation of the THM laboratory experiment the applied mechanical boundary condition of the bottom of the domain and the thermal boundary conditions are different and the time stepping is more detailed than in [61].
- Total of 10 individual experiments are simulated including the extra material of MX-80 bentonite.

Part I

Theory

Chapter 2

General model

2.1 Basic concepts

Constituents

In the current study the microscopical details and chemistry are neglected. The objective is the characterization of the macroscopic behaviour of compacted clay. Essentially this is done by appropriate choice for the macroscopically sensible state variables. In a simplified continuum mechanical and mixture theoretical framework the structure of porous medium is illustrated by a representative elementary volume (rev) (Figure 2.1.). The rev includes all of the constituents of the porous medium occupying it with their physical proportions, i.e., their volume fractions.

The multiconstituent system consists of solid skeleton (s), liquid water (l), water vapor (v), and air (a). Vapor and air occupy the same gaseous (g) volume fraction. The molar volume fraction

$$\xi_{\mathrm{k}} = \begin{cases} \beta_{\mathrm{k}}, & \text{for } \mathrm{k} \in \{\mathrm{s}, \mathrm{l}\}, \\ x_{\mathrm{k}}\beta_{\mathrm{g}}, & \text{for } \mathrm{k} \in \{\mathrm{v}, \mathrm{a}\}, \end{cases} \tag{2.1}$$

of constituent k is defined by means of the volume fraction

$$\beta_{\mathrm{j}} = \frac{v_{\mathrm{j}}}{v_{\mathrm{rev}}} \tag{2.2}$$

of the phase j $\in$ {s, l, g}, where

$$v_{\mathrm{rev}} = \sum_{\mathrm{j}} v_{\mathrm{j}} \tag{2.3}$$

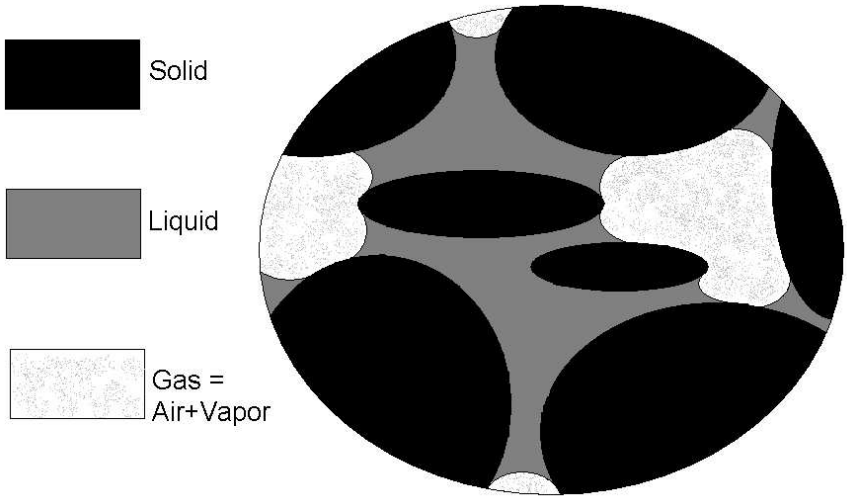

Figure 2.1: The representative elementary volume (rev) of unsaturated porous medium.

is the representative elementary volume, and the molar fraction

$$x_{\mathrm{k}} = \frac{n_{\mathrm{k}}}{n_{\mathrm{a}} + n_{\mathrm{v}}} \tag{2.4}$$

for k $\in$ {a, v}, where n_{k} is the mole number. The molar volume fractions are restricted by the following obvious relations

$$\sum_{\mathrm{k}} \xi_{\mathrm{k}} = 1, \quad \xi_{\mathrm{k}} \geq 0, \ \forall \ \mathrm{k}. \tag{2.5}$$

A constituent with mass m_{k} has the apparent density $\rho_{\mathrm{k}} = m_{\mathrm{k}}/v_{\mathrm{rev}}$, which is related to the intrinsic density $\tilde{\rho}_{\mathrm{k}}$ by the equation

$$\rho_{\mathrm{k}} = \xi_{\mathrm{k}} \tilde{\rho}_{\mathrm{k}}. \tag{2.6}$$

In the general framework the proportions of the constituents are expressed by the molar volume fractions. As alternative variables porosity, void fraction, liquid saturation, and vapor fraction are defined as

$$\eta = 1 - \xi_{\mathrm{s}}, \quad \varepsilon = \frac{1 - \xi_{\mathrm{s}}}{\xi_{\mathrm{s}}}, \quad \chi = \frac{\xi_{\mathrm{l}}}{1 - \xi_{\mathrm{s}}}, \quad \zeta = \frac{\xi_{\mathrm{v}}}{\xi_{\mathrm{a}} + \xi_{\mathrm{v}}}, \tag{2.7}$$

respectively. As density related alternative variables specific volume and gravimetric water content are defined as

$$\tilde{v}_{\mathrm{k}} = \frac{1}{\tilde{\rho}_{\mathrm{k}}}, \quad w = \frac{m_{\mathrm{l}}}{m_{\mathrm{s}}} = \frac{\rho_{\mathrm{l}}}{\rho_{\mathrm{s}}}, \tag{2.8}$$

respectively.

Kinematics

The absolute velocity of constituent k is denoted by $\mathbf{U}_\mathrm{k}$ and a relative velocity by $\mathbf{V}_\mathrm{k} = \mathbf{U}_\mathrm{k} - \mathbf{U}_*$, where $\mathbf{U}_*$ is a reference velocity. The material time derivative is $d^\mathrm{k}/dt = \partial/\partial t + \mathbf{U}_\mathrm{k} \cdot \nabla$. Tensors can be divided into deviatoric and spherical parts, e.g. the Cauchy stress is

$$\boldsymbol{\sigma}_\mathrm{k} = \boldsymbol{\sigma}_\mathrm{k}^\mathrm{D} + \mathrm{tr}(\boldsymbol{\sigma}_\mathrm{k}/3)\mathbf{I} = \boldsymbol{\sigma}_\mathrm{k}^\mathrm{D} - p_\mathrm{k}\mathbf{I}, \tag{2.9}$$

where p_k is the pressure. Strain and rate of deformation are defined by

$$\boldsymbol{\epsilon}_\mathrm{k} = \frac{1}{2}(\nabla \mathbf{u}_\mathrm{k} + (\nabla \mathbf{u}_\mathrm{k})^\mathrm{T}), \tag{2.10}$$

$$\mathbf{D}_\mathrm{k} = \frac{1}{2}(\nabla \mathbf{U}_\mathrm{k} + (\nabla \mathbf{U}_\mathrm{k})^\mathrm{T}), \tag{2.11}$$

respectively, where $\mathbf{u}_\mathrm{k}$ is the displacement.

As a simplifying assumption, the solid grains are considered incompressible, i.e., the intrinsic density of the solid $\tilde{\rho}_\mathrm{s}$ is assumed to be constant. The volume changes of the skeleton are associated with changes in the apparent density of the solid (i.e. dry density), or alternatively, with changes in the solid (molar) volume fraction, porosity, or in the void fraction. The relative change of volume $\mathrm{tr}\boldsymbol{\epsilon}_\mathrm{s} = (v_\mathrm{rev} - v_\mathrm{rev,init})/v_\mathrm{rev,init}$ can be expressed by means of proportions of the mixture in the following alternative ways

$$\mathrm{tr}\boldsymbol{\epsilon}_\mathrm{s} = \frac{\xi_\mathrm{s,init}}{\xi_\mathrm{s}} - 1 = \frac{\eta - \eta_\mathrm{init}}{1 - \eta} = \frac{\varepsilon - \varepsilon_\mathrm{init}}{1 + \varepsilon_\mathrm{init}}. \tag{2.12}$$

Variables of state and dissipation

The reversible behavior of the system is described by the specific free energies ψ_k, which are functions of the state variables. In the general model the state is defined by state variables including molar volume fractions, intrinsic densities, and strains of the constituents, and the common temperature T, i.e., by

$$\xi_\mathrm{k},\ \tilde{\rho}_\mathrm{k},\ \boldsymbol{\epsilon}_\mathrm{k},\ T, \tag{2.13}$$

respectively.

Dissipative behavior of the system is described by the dissipative variables, which in the general work are chosen to be the rates of deformation,

the relative velocities, the heat flux densities, and the rates of mass production, i.e., by

$$\mathbf{D}_{\mathrm{k}},\ \mathbf{V}_{\mathrm{k}},\ \mathbf{q}_{\mathrm{k}},\ \theta_{\mathrm{k}}. \tag{2.14}$$

respectively.

The dissipation function ϕ is a function of the state variables and the dissipative variables, i.e.,

$$\phi = \phi(\xi_{\mathrm{k}},\ \tilde{\rho}_{\mathrm{k}},\ \boldsymbol{\epsilon}_{\mathrm{k}},\ T,\ \mathbf{D}_{\mathrm{k}},\ \mathbf{V}_{\mathrm{k}},\ \mathbf{q}_{\mathrm{k}},\ \theta_{\mathrm{k}}). \tag{2.15}$$

2.2 Fundamental laws for a mixture

The fundamental laws for an arbitrary mixture, i.e., conservations of mass, momentum and energy and the second law of thermodynamics are stated here in the form suggested by Mikkola and Hartikainen [76]. With a different notation they can be found e.g. in [5]. The mixture theoretical conservation laws are presented by means of the respective rates of production of mass, linear momentum and energy

$$\theta_{\mathrm{k}} = \frac{\partial \rho_{\mathrm{k}}}{\partial t} + \nabla \cdot (\rho_{\mathrm{k}} \mathbf{U}_{\mathrm{k}}), \tag{2.16}$$

$$\mathbf{m}_{\mathrm{k}} = \rho_{\mathrm{k}} \frac{d^{\mathrm{k}} \mathbf{U}_{\mathrm{k}}}{dt} + \theta_{\mathrm{k}} \mathbf{U}_{\mathrm{k}} - \nabla \cdot \boldsymbol{\sigma}_{\mathrm{k}} - \rho_{\mathrm{k}} \mathbf{g}, \tag{2.17}$$

$$\begin{aligned} \iota_{\mathrm{k}} &= \rho_{\mathrm{k}} \frac{d^{\mathrm{k}} e_{\mathrm{k}}}{dt} + \Big(e_{\mathrm{k}} - \frac{1}{2} \mathbf{U}_{\mathrm{k}} \cdot \mathbf{U}_{\mathrm{k}}\Big) \theta_{\mathrm{k}} - \boldsymbol{\sigma}_{\mathrm{k}} : \mathbf{D}_{\mathrm{k}} + \mathbf{m}_{\mathrm{k}} \cdot \mathbf{U}_{\mathrm{k}} + \\ &+ \nabla \cdot \mathbf{q}_{\mathrm{k}} - Q_{\mathrm{k}}, \end{aligned} \tag{2.18}$$

where $\mathbf{g}$ is the gravitational acceleration vector, e_{k} is the specific internal energy and Q_{k} is the energy source. The respective conservations laws of mass, linear momentum and energy are

$$\sum_k \theta_{\mathrm{k}} = 0, \tag{2.19}$$

$$\sum_k \mathbf{m}_{\mathrm{k}} = 0, \tag{2.20}$$

$$\sum_k \iota_{\mathrm{k}} = 0, \tag{2.21}$$

The second law of thermodynamics is expressed by means of the rate of production of entropy γ_{k} defined as

$$\gamma_{\mathrm{k}} = \rho_{\mathrm{k}} \frac{d^{\mathrm{k}} s_{\mathrm{k}}}{dt} + s_{\mathrm{k}} \theta_{\mathrm{k}} + \nabla \cdot \Big(\frac{\mathbf{q}_{\mathrm{k}}}{T}\Big) - \frac{Q_{\mathrm{k}}}{T}, \tag{2.22}$$

for which we have

$$\begin{aligned} T\gamma_{\mathrm{k}} &= \boldsymbol{\sigma}_{\mathrm{k}} : \mathbf{D}_{\mathrm{k}} - \rho_{\mathrm{k}} \Big(\frac{d^{\mathrm{k}} \psi_{\mathrm{k}}}{dt} + s_{\mathrm{k}} \frac{d^{\mathrm{k}} T}{dt}\Big) - \Big(\psi_{\mathrm{k}} - \frac{1}{2} \mathbf{U}_{\mathrm{k}} \cdot \mathbf{U}_{\mathrm{k}}\Big) \theta_{\mathrm{k}} - \\ &- \mathbf{m}_{\mathrm{k}} \cdot \mathbf{U}_{\mathrm{k}} - \frac{\nabla T}{T} \cdot \mathbf{q}_{\mathrm{k}} + \iota_{\mathrm{k}}, \end{aligned} \tag{2.23}$$

where s_{k} is the specific entropy. The mixture entropy inequality

$$\sum_{\mathrm{k}} \gamma_{\mathrm{k}} \geqslant 0 \tag{2.24}$$

yields by means of (2.21, 2.23) the Clausius-Duhem inequality as

$$\begin{aligned}\sum_{\mathrm{k}} T\gamma_{\mathrm{k}} &= \sum_{\mathrm{k}} \Big[\boldsymbol{\sigma}_{\mathrm{k}} : \mathbf{D}_{\mathrm{k}} - \rho_{\mathrm{k}}\Big(\frac{d^{\mathrm{k}}\psi_{\mathrm{k}}}{dt} + s_{\mathrm{k}}\frac{d^{\mathrm{k}}T}{dt}\Big) - \\ &- \Big(\psi_{\mathrm{k}} - \frac{1}{2}\mathbf{U}_{\mathrm{k}}\cdot\mathbf{U}_{\mathrm{k}}\Big)\theta_{\mathrm{k}} - \mathbf{m}_{\mathrm{k}}\cdot\mathbf{V}_{\mathrm{k}} - \frac{\nabla T}{T}\cdot\mathbf{q}_{\mathrm{k}}\Big] \geqslant 0, \quad (2.25)\end{aligned}$$

where the result of (2.20) for $\sum_{\mathrm{k}} \mathbf{m}_{\mathrm{k}}\cdot\mathbf{U}_{\mathrm{k}} = \sum_{\mathrm{k}} \mathbf{m}_{\mathrm{k}}\cdot(\mathbf{U}_{*}+\mathbf{V}_{\mathrm{k}}) = \sum_{\mathrm{k}} \mathbf{m}_{\mathrm{k}}\cdot\mathbf{V}_{\mathrm{k}}$ is used.

2.3 General constitutive equations

The procedure introduced by Hartikainen and Mikkola [50] of using the principle of maximal rate of entropy production [119], [120] is followed to ensure that the entropy inequality (2.25) is not violated. According to the principle the evolution of a system at a given state is made to occur in the direction of the largest dissipation or entropy production. The dissipation function is defined as

$$\phi = \sum_{\mathrm{k}} T\gamma_{\mathrm{k}}. \tag{2.26}$$

The dissipation function can be expressed by means of j generalized and mutually independent irreversible forces $\mathbf{X}_{\mathrm{k,j}}$ and fluxes $\mathbf{J}_{\mathrm{k,j}}$ of constituent k as

$$\phi = \sum_{\mathrm{k,j}} \mathbf{X}_{\mathrm{k,j}} : \mathbf{J}_{\mathrm{k,j}}. \tag{2.27}$$

The evolution of the system, i.e. the set of fluxes $\mathbf{J} \ni \mathbf{J}_{\mathrm{k,j}}$ at a given state, is characterized by the solution to the following extremum problem

$$\max \sum_{\mathrm{k,j}} \mathbf{X}_{\mathrm{k,j}} : \mathbf{J}_{\mathrm{k,j}} \quad \text{subject to} \tag{2.28}$$

$$\phi(\mathbf{J}) - \sum_{\mathrm{k,j}} \mathbf{X}_{\mathrm{k,j}} : \mathbf{J}_{\mathrm{k,j}} = 0. \tag{2.29}$$

The first-order solution for the forces is

$$\mathbf{X}_{\mathrm{k,j}} = \frac{\nu'}{1+\nu'} \frac{\partial \phi}{\partial \mathbf{J}_{\mathrm{k,j}}} \tag{2.30}$$

and for the dissipation function

$$\phi(\mathbf{J}) = \frac{\nu'}{1+\nu'} \sum_{\mathrm{k,j}} \frac{\partial \phi}{\partial \mathbf{J}_{\mathrm{k,j}}} : \mathbf{J}_{\mathrm{k,j}}, \tag{2.31}$$

where ν' [–] is the Lagrangian multiplier associated with the restriction (2.29) of the extremum problem. With the choice of the constituent fluxes, i.e. the dissipative variables $\{\mathbf{D}_{\mathrm{k}}, \mathbf{q}_{\mathrm{k}}, \mathbf{V}_{\mathrm{k}}, \theta_{\mathrm{k}}\}$ the dependence of the dissipation function on the dissipative variables is of the form

$$\phi = \nu \sum_{\mathrm{k}} \left[\frac{\partial \phi}{\partial \mathbf{D}_{\mathrm{k}}^{\mathrm{D}}} : \mathbf{D}_{\mathrm{k}}^{\mathrm{D}} + \frac{\partial \phi}{\partial \mathrm{tr}\mathbf{D}_{\mathrm{k}}} \mathrm{tr}\mathbf{D}_{\mathrm{k}} + \frac{\partial \phi}{\partial \mathbf{q}_{\mathrm{k}}} \cdot \mathbf{q}_{\mathrm{k}} + \frac{\partial \phi}{\partial \mathbf{V}_{\mathrm{k}}} \cdot \mathbf{V}_{\mathrm{k}} + \frac{\partial \phi}{\partial \theta_{\mathrm{k}}} \theta_{\mathrm{k}} \right], \tag{2.32}$$

where

$$\begin{aligned}\nu = & \quad \tfrac{\nu'}{1+\nu'} \\ = & \quad \phi\Big[\textstyle\sum_{\mathrm{k}}\Big\{ \quad \dfrac{\partial\phi}{\partial\mathbf{D}_{\mathrm{k}}^{\mathrm{D}}} : \mathbf{D}_{\mathrm{k}}^{\mathrm{D}} + \dfrac{\partial\phi}{\partial(\mathrm{tr}\mathbf{D}_{\mathrm{k}})}\mathrm{tr}\mathbf{D}_{\mathrm{k}} + \\ & \qquad + \dfrac{\partial\phi}{\partial\mathbf{q}_{\mathrm{k}}}\cdot\mathbf{q}_{\mathrm{k}} + \dfrac{\partial\phi}{\partial\mathbf{V}_{\mathrm{k}}}\cdot\mathbf{V}_{\mathrm{k}} + \dfrac{\partial\phi}{\partial\theta_{\mathrm{k}}}\theta_{\mathrm{k}}\Big\}\Big]^{-1}. \end{aligned} \tag{2.33}$$

The sum of material time derivatives of the free energies in the Clausius-Duhem inequality (2.25) can be expanded in the following way

$$\begin{aligned}\sum_{\mathrm{k}}\rho_{\mathrm{k}}\frac{d^{\mathrm{k}}\psi_{\mathrm{k}}}{dt} \quad &= \sum_{\mathrm{k}} \quad \rho_{\mathrm{k}}\frac{d^{\mathrm{k}}\psi_{\mathrm{k}}(\boldsymbol{\epsilon}_{\mathrm{k}}^{\mathrm{D}}, \mathrm{tr}\boldsymbol{\epsilon}_{\mathrm{k}}, \xi_{\mathrm{j}}, T, \tilde{\rho}_{\mathrm{k}})}{dt} \\ &= \sum_{\mathrm{k}} \quad \rho_{\mathrm{k}}\Bigg[\frac{\partial\psi_{\mathrm{k}}}{\partial\boldsymbol{\epsilon}_{\mathrm{k}}^{\mathrm{D}}} : \mathbf{D}_{\mathrm{k}}^{\mathrm{D}} + \frac{\partial\psi_{\mathrm{k}}}{\partial(\mathrm{tr}\boldsymbol{\epsilon}_{\mathrm{k}})}\mathrm{tr}\mathbf{D}_{\mathrm{k}} + \frac{\partial\psi_{\mathrm{k}}}{\partial T}\frac{d^{\mathrm{k}}T}{dt} + \\ &\qquad + \sum_{\mathrm{j}}\left(\frac{\partial\psi_{\mathrm{k}}}{\partial\xi_{\mathrm{j}}}\frac{d^{\mathrm{k}}\xi_{\mathrm{j}}}{dt}\right) + \frac{\partial\psi_{\mathrm{k}}}{\partial\tilde{\rho}_{\mathrm{k}}}\frac{d^{\mathrm{k}}\tilde{\rho}_{\mathrm{k}}}{dt}\Bigg] \\ &= \sum_{\mathrm{k}}\Bigg[\quad \rho_{\mathrm{k}}\frac{\partial\psi_{\mathrm{k}}}{\partial\boldsymbol{\epsilon}_{\mathrm{k}}^{\mathrm{D}}} : \mathbf{D}_{\mathrm{k}}^{\mathrm{D}} + \left(\rho_{\mathrm{k}}\frac{\partial\psi_{\mathrm{k}}}{\partial(\mathrm{tr}\boldsymbol{\epsilon}_{\mathrm{k}})} - \xi_{\mathrm{k}}\sum_{\mathrm{j}}\rho_{\mathrm{j}}\frac{\partial\psi_{\mathrm{j}}}{\partial\xi_{\mathrm{k}}}\right)\mathrm{tr}\mathbf{D}_{\mathrm{k}} + \\ &\qquad + \rho_{\mathrm{k}}\frac{\partial\psi_{\mathrm{k}}}{\partial T}\frac{d^{\mathrm{k}}T}{dt} + \sum_{\mathrm{j}}\left(\rho_{\mathrm{k}}\frac{\partial\psi_{\mathrm{k}}}{\partial\xi_{\mathrm{j}}}\nabla\xi_{\mathrm{j}} - \rho_{\mathrm{j}}\frac{\partial\psi_{\mathrm{j}}}{\partial\xi_{\mathrm{k}}}\nabla\xi_{\mathrm{k}}\right)\cdot\mathbf{V}_{\mathrm{k}} + \\ &\qquad + \left(\rho_{\mathrm{k}}\frac{\partial\psi_{\mathrm{k}}}{\partial\tilde{\rho}_{\mathrm{k}}} - \frac{\xi_{\mathrm{k}}}{\tilde{\rho}_{\mathrm{k}}}\sum_{\mathrm{j}}\rho_{\mathrm{j}}\frac{\partial\psi_{\mathrm{j}}}{\partial\xi_{\mathrm{k}}}\right)\frac{d^{\mathrm{k}}\tilde{\rho}_{\mathrm{k}}}{dt} + \sum_{\mathrm{j}}\rho_{\mathrm{j}}\frac{\partial\psi_{\mathrm{j}}}{\partial\xi_{\mathrm{k}}}\frac{\theta_{\mathrm{k}}}{\tilde{\rho}_{\mathrm{k}}}\Bigg] \end{aligned} \tag{2.34}$$

In (2.34), strain and rate of deformation are separated into deviatoric and spherical parts, the small strain approximation $d^{\mathrm{k}}\boldsymbol{\epsilon}_{\mathrm{k}}/dt \approx \mathbf{D}_{\mathrm{k}}$ is used, and the material derivative of molar volume fraction has been expressed by means of the rate of mass production (2.16) in the form

$$\frac{d^{\mathrm{k}}\xi_{\mathrm{j}}}{dt} = \frac{d^{\mathrm{k}}(\rho_{\mathrm{j}}/\tilde{\rho}_{\mathrm{j}})}{dt} = \frac{\theta_{\mathrm{j}}}{\tilde{\rho}_{\mathrm{j}}} - \xi_{\mathrm{j}}\mathrm{tr}\mathbf{D}_{\mathrm{j}} + (\mathbf{V}_{\mathrm{k}} - \mathbf{V}_{\mathrm{j}})\cdot\nabla\xi_{\mathrm{j}} - \frac{\xi_{\mathrm{j}}}{\tilde{\rho}_{\mathrm{j}}}\frac{d^{\mathrm{j}}\tilde{\rho}_{\mathrm{j}}}{dt}. \tag{2.35}$$

From (2.25, 2.26, 2.32, 2.34) we get

$$\sum_{\mathrm{k}}\Bigg[\qquad \left(\boldsymbol{\sigma}_{\mathrm{k}}^{\mathrm{D}} - \rho_{\mathrm{k}}\frac{\partial\psi_{\mathrm{k}}}{\partial\boldsymbol{\epsilon}_{\mathrm{k}}^{\mathrm{D}}} - \nu\frac{\partial\phi}{\partial\mathbf{D}_{\mathrm{k}}^{\mathrm{D}}}\right) : \mathbf{D}_{\mathrm{k}}^{\mathrm{D}} +$$

$$
\begin{aligned}
&+ \Big(- p_{\rm k} - \rho_{\rm k}\frac{\partial \psi_{\rm k}}{\partial({\rm tr}\boldsymbol{\epsilon}_{\rm k})} + \xi_{\rm k}\sum_{\rm j}\rho_{\rm j}\frac{\partial \psi_{\rm j}}{\partial \xi_{\rm k}} - \nu\frac{\partial \phi}{\partial({\rm tr}\mathbf{D}_{\rm k})}\Big){\rm tr}\mathbf{D}_{\rm k} + \\
&+ \Big(- \rho_{\rm k}s_{\rm k} - \rho_{\rm k}\frac{\partial \psi_{\rm k}}{\partial T}\Big)\frac{d^{\rm k}T}{dt} + \\
&+ \Big(- \rho_{\rm k}\frac{\partial \psi_{\rm k}}{\partial \tilde{\rho}_{\rm k}} + \frac{\xi_{\rm k}}{\tilde{\rho}_{\rm k}}\sum_{\rm j}\rho_{\rm j}\frac{\partial \psi_{\rm j}}{\partial \xi_{\rm k}}\Big)\frac{d^{\rm k}\tilde{\rho}_{\rm k}}{dt} + \\
&+ \Big(- \frac{\nabla T}{T} - \nu\frac{\partial \phi}{\partial \mathbf{q}_{\rm k}}\Big)\cdot\mathbf{q}_{\rm k} + \\
&+ \Big(- \mathbf{m}_{\rm k} - \sum_{\rm j}\rho_{\rm k}\frac{\partial \psi_{\rm k}}{\partial \xi_{\rm j}}\nabla\xi_{\rm j} + \sum_{\rm j}\rho_{\rm j}\frac{\partial \psi_{\rm j}}{\partial \xi_{\rm k}}\nabla\xi_{\rm k} - \nu\frac{\partial \phi}{\partial \mathbf{V}_{\rm k}}\Big)\cdot\mathbf{V}_{\rm k} + \\
&+ \Big(- \psi_{\rm k} + \frac{1}{2}\mathbf{U}_{\rm k}\cdot\mathbf{U}_{\rm k} - \frac{\xi_{\rm k}}{\rho_{\rm k}}\sum_{\rm j}\rho_{\rm j}\frac{\partial \psi_{\rm j}}{\partial \xi_{\rm k}} - \nu\frac{\partial \phi}{\partial \theta_{\rm k}}\Big)\theta_{\rm k} \quad \Bigg] = 0. \quad (2.36)
\end{aligned}
$$

For any independent velocities

$$
\mathbf{D}^{\rm D}_{\rm k}, \quad {\rm tr}\mathbf{D}_{\rm k}, \quad \frac{d^{\rm k}T}{dt}, \quad \frac{d^{\rm k}\tilde{\rho}_{\rm k}}{dt}, \quad \mathbf{q}_{\rm k}, \quad \mathbf{V}_{\rm k}, \quad \theta_{\rm k} \tag{2.37}
$$

equation (2.36) yields the following general constitutive relations

$$
\boldsymbol{\sigma}^{\rm D}_{\rm k} = \rho_{\rm k}\frac{\partial \psi_{\rm k}}{\partial \boldsymbol{\epsilon}^{\rm D}_{\rm k}} + \nu\frac{\partial \phi}{\partial \mathbf{D}^{\rm D}_{\rm k}}, \tag{2.38}
$$

$$
p_{\rm k} = -\rho_{\rm k}\frac{\partial \psi_{\rm k}}{\partial({\rm tr}\boldsymbol{\epsilon}_{\rm k})} - \nu\frac{\partial \phi}{\partial({\rm tr}\mathbf{D}_{\rm k})} + p^{\xi}_{\rm k}, \tag{2.39}
$$

$$
s_{\rm k} = -\frac{\partial \psi_{\rm k}}{\partial T}, \tag{2.40}
$$

$$
p^{\xi}_{\rm k} = \xi_{\rm k}\tilde{\rho}^2_{\rm k}\frac{\partial \psi_{\rm k}}{\partial \tilde{\rho}_{\rm k}}, \tag{2.41}
$$

$$
-\frac{\nabla T}{T} = \nu\frac{\partial \phi}{\partial \mathbf{q}_{\rm k}}, \tag{2.42}
$$

$$
-\mathbf{m}_{\rm k} - \sum_{\rm j}\rho_{\rm k}\frac{\partial \psi_{\rm k}}{\partial \xi_{\rm j}}\nabla\xi_{\rm j} + \sum_{\rm j}\rho_{\rm j}\frac{\partial \psi_{\rm j}}{\partial \xi_{\rm k}}\nabla\xi_{\rm k} = \nu\frac{\partial \phi}{\partial \mathbf{V}_{\rm k}}, \tag{2.43}
$$

$$
\psi_{\rm i} - \frac{1}{2}\mathbf{U}_{\rm i}\cdot\mathbf{U}_{\rm i} + \frac{p^{\xi}_{\rm i}}{\rho_{\rm i}} - \Big(\psi_{\rm j} - \frac{1}{2}\mathbf{U}_{\rm j}\cdot\mathbf{U}_{\rm j} + \frac{p^{\xi}_{\rm j}}{\rho_{\rm j}}\Big) = 2\nu\frac{\partial \phi}{\partial \theta_{\rm j}}, \tag{2.44}
$$

where

$$p_{\mathrm{k}}^{\xi} \equiv \xi_{\mathrm{k}} \sum_{\mathrm{j}} \rho_{\mathrm{j}} \frac{\partial \psi_{\mathrm{j}}}{\partial \xi_{\mathrm{k}}} \left(= \xi_{\mathrm{k}} \tilde{\rho}_{\mathrm{k}}^{2} \frac{\partial \psi_{\mathrm{k}}}{\partial \tilde{\rho}_{\mathrm{k}}} \right) \tag{2.45}$$

is the constituent interaction pressure representing how the constituent pressure p_{k} is affected by the changes in the free energy due to the interaction of the constituents.

In the above, (2.38–2.41) are state equations and (2.42–2.44) are generalized equations of heat conduction, diffusion, and phase change, respectively. Because the mass production rates θ_{k} are mutually dependent through the mass conservation (2.19), the phase change equation (2.44) is not general. Instead, it is expressed by means of two arbitrary constituents (i and j) among which a phase change is assumed to occur corresponding to the situation $\theta_{\mathrm{i}} + \theta_{\mathrm{j}} = 0$, and $\theta_{\mathrm{k}} = 0 \ \forall \mathrm{k} \neq \{\mathrm{i}, \mathrm{j}\}$.

The general constitutive relations (2.38-2.45) have been published by Jussila [60]. They are essentially the same as presented by Hartikainen and Mikkola [50] and Mikkola and Hartikainen [76] except for the extra state equation (2.41) due to the inclusion of intrinsic densities $\tilde{\rho}_{\mathrm{k}}$ as state variables and for the use of molar volume fractions ξ_{k} instead of volume fractions β_{k} as state variables.

2.4 Non-smoothness of free energy

By molar volume fractions

The constituents are asumed to occupy the whole rev with the proportions of their molar volume fractions. The interpenetration of the molar volume fractions is restricted via the equations (2.5). Such an internal constraint can be handled by using indicator functions [38], [37]. The indicator function taking care of the restriction for the molar volume fractions is

$$I(\xi_{\mathrm{s}}, \xi_{\mathrm{l}}, \xi_{\mathrm{v}}, \xi_{\mathrm{a}}) = \begin{cases} 0, & (\xi_{\mathrm{s}}, \xi_{\mathrm{l}}, \xi_{\mathrm{v}}, \xi_{\mathrm{a}}) \in C, \\ +\infty, & \text{otherwise}, \end{cases} \tag{2.46}$$

where the feasible set is

$$C = \Big\{ (\xi_{\mathrm{s}}, \xi_{\mathrm{l}}, \xi_{\mathrm{v}}, \xi_{\mathrm{a}}) \in \mathbb{R}^4 \mid \sum_{\mathrm{k}} \xi_{\mathrm{k}} = 1, \xi_{\mathrm{k}} \geq 0, \mathrm{k} \in \{\mathrm{s}, \mathrm{l}, \mathrm{v}, \mathrm{a}\} \Big\}. \tag{2.47}$$

The total free energy of the system is

$$\Psi = \sum_{\mathrm{k}} \rho_{\mathrm{k}} \psi_{\mathrm{k}} = \sum_{\mathrm{k}} \rho_{\mathrm{k}} \Big(\tilde{\psi}_{\mathrm{k}} + \frac{T}{\tilde{\rho}_{\mathrm{k}}} I \Big) = \sum_{\mathrm{k}} \rho_{\mathrm{k}} \tilde{\psi}_{\mathrm{k}} + TI, \tag{2.48}$$

where $\tilde{\psi}_{\mathrm{k}}$ is the specific free energy of constituent k without the restrictions (2.5). For the non-smooth free energy (2.48) the generalized diffusion law (2.43) and the interaction pressure (2.45) get the forms

$$\begin{aligned} -\mathbf{m}_{\mathrm{k}} &- \sum_{\mathrm{j}} \Big(\rho_{\mathrm{k}} \frac{\partial \tilde{\psi}_{\mathrm{k}}}{\partial \xi_{\mathrm{j}}} + \xi_{\mathrm{k}} \hat{B}_{\mathrm{j}} \Big) \nabla \xi_{\mathrm{j}} + \sum_{\mathrm{j}} \Big(\rho_{\mathrm{j}} \frac{\partial \tilde{\psi}_{\mathrm{j}}}{\partial \xi_{\mathrm{k}}} + \xi_{\mathrm{j}} \hat{B}_{\mathrm{k}} \Big) \nabla \xi_{\mathrm{k}} \\ &= \nu \frac{\partial \phi}{\partial \mathbf{V}_{\mathrm{k}}}, \end{aligned} \tag{2.49}$$

$$p_{\mathrm{k}}^{\xi} = \xi_{\mathrm{k}} \Big(\hat{B}_{\mathrm{k}} + \sum_{\mathrm{j}} \rho_{\mathrm{j}} \frac{\partial \tilde{\psi}_{\mathrm{j}}}{\partial \xi_{\mathrm{k}}} \Big), \tag{2.50}$$

respectively, where $\hat{B}_{\mathrm{k}}$ is a component of subgradient belonging to subdifferential of the indicator function (2.46), i.e.

$$(\hat{B}_{\mathrm{s}}, \hat{B}_{\mathrm{l}}, \hat{B}_{\mathrm{v}}, \hat{B}_{\mathrm{a}}) \in T\partial I(\xi_{\mathrm{s}}, \xi_{\mathrm{l}}, \xi_{\mathrm{v}}, \xi_{\mathrm{a}}). \tag{2.51}$$

By constant density

Another source of non-smoothness is the density dependence of the interaction pressure (2.41). Another indicator function

$$J(\tilde{\rho}_{\mathrm{k}}) = \begin{cases} 0, & \tilde{\rho}_{\mathrm{k}} = \tilde{\rho}_{\mathrm{k},0}, \\ +\infty, & \text{otherwise}, \end{cases} \tag{2.52}$$

is introduced in the free energy of any constituent k whose density is a constant $\tilde{\rho}_{\mathrm{k},0}$ in the form $\tilde{\psi}_{\mathrm{k}}(\tilde{\rho}_{\mathrm{k}}) = TJ(\tilde{\rho}_{\mathrm{k}})$. Consequently, the interaction pressure (2.41) for an incompressible constituent is

$$p_{\mathrm{k}}^{\xi} = \xi_{\mathrm{k}}\tilde{\rho}_{\mathrm{k}}^{2}\hat{A}_{\mathrm{k}} - \xi_{\mathrm{k}}TI, \tag{2.53}$$

where $\hat{A}_{\mathrm{k}}$ belongs to the subdifferential of the indicator function (2.52), i.e.

$$\hat{A}_{\mathrm{k}} \in T\partial J(\tilde{\rho}_{\mathrm{k}}). \tag{2.54}$$

As for any other constituent the interaction pressure of an incompressible constituent is obtained from the molar volume fraction dependence (2.45) or (2.50). The use of the indicator function (2.52) is a way of ensuring that the interaction pressure for an incompressible constituent (2.53) is not identically zero.

2.5 Interpretations for stresses

Because of the characterization of stresses is an important topic in literature [11] some of the pressure terms involved in the current model are reviewed here in more detail. In addition to dividing the total stress into deviatoric and spherical parts it can also be divided into *reversible, irreversible* and *interaction pressure* parts in the following way

$$
\begin{aligned}
\boldsymbol{\sigma} &= \sum_{\mathrm{k}} \{\boldsymbol{\sigma}_{\mathrm{k}}^{\mathrm{D}} - p_{\mathrm{k}}\mathbf{I}\} \\
&= \sum_{\mathrm{k}} \left[\left(\rho_{\mathrm{k}} \frac{\partial \psi_{\mathrm{k}}}{\partial \boldsymbol{\epsilon}_{\mathrm{k}}^{\mathrm{D}}} + \nu \frac{\partial \phi}{\partial \mathbf{D}_{\mathrm{k}}^{\mathrm{D}}} \right) - \right. \\
&- \left. \left(-\rho_{\mathrm{k}} \frac{\partial \psi_{\mathrm{k}}}{\partial (\mathrm{tr}\boldsymbol{\epsilon}_{\mathrm{k}})} - \nu \frac{\partial \phi}{\partial (\mathrm{tr}\mathbf{D}_{\mathrm{k}})} + \xi_{\mathrm{k}} \sum_{\mathrm{j}} \rho_{\mathrm{j}} \frac{\partial \psi_{\mathrm{j}}}{\partial \xi_{\mathrm{k}}} \right) \mathbf{I} \right] \\
&= \sum_{\mathrm{k}} \left[\left(\rho_{\mathrm{k}} \frac{\partial \psi_{\mathrm{k}}}{\partial \boldsymbol{\epsilon}_{\mathrm{k}}^{\mathrm{D}}} + \rho_{\mathrm{k}} \frac{\partial \psi_{\mathrm{k}}}{\partial (\mathrm{tr}\boldsymbol{\epsilon}_{\mathrm{k}})} \mathbf{I} \right) + \left(\nu \frac{\partial \phi}{\partial \mathbf{D}_{\mathrm{k}}^{\mathrm{D}}} + \nu \frac{\partial \phi}{\partial (\mathrm{tr}\mathbf{D}_{\mathrm{k}})} \mathbf{I} \right) - \right. \\
&- \left. \xi_{\mathrm{k}} \sum_{\mathrm{j}} \rho_{\mathrm{j}} \frac{\partial \psi_{\mathrm{j}}}{\partial \xi_{\mathrm{k}}} \mathbf{I} \right] \\
&= \sum_{\mathrm{k}} \left[\rho_{\mathrm{k}} \frac{\partial \psi_{\mathrm{k}}}{\partial \boldsymbol{\epsilon}_{\mathrm{k}}} + \nu \frac{\partial \phi}{\partial \mathbf{D}_{\mathrm{k}}} - \xi_{\mathrm{k}} \sum_{\mathrm{j}} \rho_{\mathrm{j}} \frac{\partial \psi_{\mathrm{j}}}{\partial \xi_{\mathrm{k}}} \mathbf{I} \right] \\
&\equiv \boldsymbol{\sigma}_{\mathrm{REV}} + \boldsymbol{\sigma}_{\mathrm{IRR}} - p^{\xi}\mathbf{I}. \qquad (2.55)
\end{aligned}
$$

In the following section, where the free energy and the dissipation function are chosen, it follows that the reversible stress in the absense of dissipative irreversible stresses coincides with the effective stress and the interaction pressure coincides with the pore pressure.

In (2.45)

$$
\frac{p_{\mathrm{k}}^{\xi}}{\xi_{\mathrm{k}}} = \sum_{\mathrm{j}} \rho_{\mathrm{j}} \frac{\partial \psi_{\mathrm{j}}}{\partial \xi_{\mathrm{k}}} \qquad (2.56)
$$

is the intrinsic constituent interaction pressure representing how the intrinsic constituent pressure $p_{\mathrm{k}}/\xi_{\mathrm{k}}$ is affected by the changes in the free energy due to the interaction of the constituents. By means of (2.41) the intrinsic interaction pressure (2.56) can be identified as the classical pressure [11]

$$
-\frac{\partial \psi_{\mathrm{k}}}{\partial \tilde{v}_{\mathrm{k}}} = -\frac{\partial \psi_{\mathrm{k}}}{\partial \tilde{\rho}_{\mathrm{k}}} \frac{\partial \tilde{\rho}_{\mathrm{k}}}{\partial \tilde{v}_{\mathrm{k}}} = \tilde{\rho}_{\mathrm{k}}^{2} \frac{\partial \psi_{\mathrm{k}}}{\partial \tilde{\rho}_{\mathrm{k}}} = \frac{p_{\mathrm{k}}^{\xi}}{\xi_{\mathrm{k}}}, \qquad (2.57)
$$

which is the change in free energy with respect to the specific volume $\tilde{v}_{\mathrm{k}} = 1/\tilde{\rho}_{\mathrm{k}}$ while keeping the molar volume fraction fixed.

By means of (2.50) the intrinsic interaction pressure (2.56) (i.e. the classical pressure, (2.57)) is divided into two components.

1. The term $\hat{B}_{\mathrm{k}}$ for which $\hat{B}_{\mathrm{s}} = \hat{B}_{\mathrm{l}} = \hat{B}_{\mathrm{v}} = \hat{B}_{\mathrm{a}} \equiv \hat{B}$ arises from the restrictions (2.5) for the molar volume fractions. It expresses the contact force restricting the interpenetration of the molar volume fractions.

2. The term $\sum_{\mathrm{j}} \rho_{\mathrm{j}}(\partial\tilde{\psi}_{\mathrm{j}}/\partial\xi_{\mathrm{k}})$ expresses the physico-chemical interaction forces which are due to the occurrence of constituent k in the mixture.

Chapter 3

Thermo-hydro-mechanical model for swelling material

3.1 Constitution

3.1.1 The choice for the state variables

The general theory presented in the previous section is applied to thermo-hydro-mechanical modeling of bentonite buffer the strain of which is $\boldsymbol{\epsilon} = \boldsymbol{\epsilon}_{\mathrm{s}}$. The solid phase velocity is taken as the reference velocity, i.e.

$$\mathbf{U}_* = \mathbf{U}_{\mathrm{s}} \approx \frac{\partial \mathbf{u}}{\partial t}. \tag{3.1}$$

The respective sets of state and dissipative variables are reduced to

$$\boldsymbol{\epsilon},\ \xi_{\mathrm{s}},\ \xi_{\mathrm{l}},\ \xi_{\mathrm{v}},\ \xi_{\mathrm{a}},\ \tilde{\rho}_{\mathrm{s}},\ \tilde{\rho}_{\mathrm{l}},\ \tilde{\rho}_{\mathrm{v}},\ \tilde{\rho}_{\mathrm{a}},\ T;$$
$$\mathbf{q}_{\mathrm{s}},\ \mathbf{q}_{\mathrm{l}},\ \mathbf{q}_{\mathrm{v}},\ \mathbf{q}_{\mathrm{a}},\ \mathbf{V}_{\mathrm{l}},\ \mathbf{V}_{\mathrm{v}},\ \mathbf{V}_{\mathrm{a}}.$$

Although $\tilde{\rho}_{\mathrm{s}}$ and $\tilde{\rho}_{\mathrm{l}}$ are assumed to be constants they are included for generality. The subscript $()_0$ denotes the value of the corresponding quantity at a reference state

$$\{\boldsymbol{\epsilon}, \xi_{\mathrm{k}}, \tilde{\rho}_{\mathrm{k}}, T\}_0,\ \mathrm{k} \in \{\mathrm{s}, \mathrm{l}, \mathrm{v}, \mathrm{a}\}. \tag{3.2}$$

The reference state can be set freely and is chosen afterwards.

3.1.2 The choice for the free energy and the dissipation function

The constitution is obtained from the general constitutive relations (2.38-2.45) with appropriate choices of the free energies and the dissipation func-

tion [60].

A simple and sufficient criterion for the dissipation is a dissipation function which is a non-negative quadratic function of the dissipative variables. This choice ensures the fulfilment of the entropy inequality (2.25, 2.26) and yields linear constitutive flow equations. The theoretical requirements for the free energy arise from the characterization of a stable equilibrium state corresponding to the maximum of entropy [15]. A sufficient condition for the free energy is strict concavity with respect to temperature and with respect to density (convexity with respect to volume), and strict convexity with respect to molar volume fractions [49]. In addition to these theoretical requirements that ensure that the fundamental laws are not violated, a necessary practical requirement is the consistency of the predictions of the model with the experimental observations.

The objective is to formulate a model which is valid for any combination of the constituents. The free energies cover the non-dissipative individual behaviors of the constituents and their mutual interactions in any mixture combination. The chosen interactions are

- mixing of the gaseous constituents,
- adsorption between the liquid and solid constituents, and
- swelling between the liquid and solid constituents.

The gas mixing is incorporated by a simple and definite term involving the molar fractions. The adsorption and swelling interactions, instead, are incorporated by arbitrary functions the forms of which are determined by the model fitting to experiments. The chosen expressions for the specific free energies of the constituents are

$$\begin{aligned}
\psi_{\mathrm{s}}(\boldsymbol{\epsilon}, \xi_{\mathrm{j}}, \tilde{\rho}_{\mathrm{s}}, T) &= \psi_{\mathrm{s},0} - s_{\mathrm{s},0}(T - T_0) + c_{\mathrm{s}}^{v}(T - T_0) - c_{\mathrm{s}}^{v} T \ln \frac{T}{T_0} + \\
&\quad + T J(\tilde{\rho}_{\mathrm{s}}) + \frac{1}{\tilde{\rho}_{\mathrm{s}}} G(\xi_{\mathrm{s}}, \xi_{\mathrm{l}}) \boldsymbol{\epsilon}^{\mathrm{D}} : \boldsymbol{\epsilon}^{\mathrm{D}} + \frac{1}{2\tilde{\rho}_{\mathrm{s}}} K(\xi_{\mathrm{s}}, \xi_{\mathrm{l}}) (\mathrm{tr}\boldsymbol{\epsilon})^2 + \\
&\quad + \frac{1}{\tilde{\rho}_{\mathrm{s}}} f_{\Pi}(\xi_{\mathrm{s}}, \xi_{\mathrm{l}}) \hat{B}_0 \mathrm{tr}\boldsymbol{\epsilon} + \frac{T}{\tilde{\rho}_{\mathrm{s}}} I(\xi_{\mathrm{j}}), \qquad (3.3) \\
\psi_{\mathrm{l}}(\xi_{\mathrm{j}}, \tilde{\rho}_{\mathrm{l}}, T) &= \psi_{\mathrm{l},0} - s_{\mathrm{l},0}(T - T_0) + c_{\mathrm{l}}^{v}(T - T_0) - c_{\mathrm{l}}^{v} T \ln \frac{T}{T_0} + \\
&\quad + T J(\tilde{\rho}_{\mathrm{l}}) + \frac{RT}{M_{\mathrm{v}}} f(\xi_{\mathrm{s}}, \xi_{\mathrm{l}}) + \frac{T}{\tilde{\rho}_{\mathrm{l}}} I(\xi_{\mathrm{j}}), \qquad (3.4) \\
\psi_{\mathrm{k}}(\xi_{\mathrm{j}}, \tilde{\rho}_{\mathrm{k}}, T) &= \psi_{\mathrm{k},0} - s_{\mathrm{k},0}(T - T_0) + c_{\mathrm{k}}^{v}(T - T_0) - c_{\mathrm{k}}^{v} T \ln \frac{T}{T_0} +
\end{aligned}$$

$$+\frac{RT}{M_{\mathrm{k}}}\ln\left(\frac{\tilde{\rho}_{\mathrm{k}}}{\tilde{\rho}_{\mathrm{k},0}}\right)+\frac{RT}{M_{\mathrm{k}}}\ln\left(\frac{\xi_{\mathrm{k}}}{\xi_{\mathrm{a}}+\xi_{\mathrm{v}}}\Bigg/\left(\frac{\xi_{\mathrm{k}}}{\xi_{\mathrm{a}}+\xi_{\mathrm{v}}}\right)_0\right)+$$
$$\frac{T}{\tilde{\rho}_{\mathrm{k}}}I(\xi_{\mathrm{j}}),\quad \mathrm{k}\in\{\mathrm{a},\mathrm{v}\},\tag{3.5}$$

where

c_{k}^{v}	is the specific heat at constant volume,
G	is the shear modulus,
K	is the bulk modulus,
M_{k}	is the molar mass,
R	is the universal gas constant,
f	is an adsorption function,
f_{Π}	is a swelling function, and
$\hat{B}_0$	is a reference pressure.

The free energies (3.3–3.5) were introduced by Jussila and Ruokolainen [61]. They were chosen as an extension to the ones given by Jussila [60] with an inclusion of the strain dependent terms and the swelling function in the free energy of the solid constituent.

The chosen dissipation function is

$$\begin{aligned}\phi(\mathbf{q}_{\mathrm{k}},\mathbf{V}_{\mathrm{l}},\mathbf{V}_{\mathrm{v}},\mathbf{V}_{\mathrm{a}}) &= \sum_{\mathrm{k}\in\{\mathrm{s,l,v,a}\}}\frac{1}{\xi_{\mathrm{k}}\lambda_{\mathrm{k}}T}\mathbf{q}_{\mathrm{k}}\cdot\mathbf{q}_{\mathrm{k}}+\\ &+\sum_{\mathrm{k}\in\{\mathrm{l,g}\}}\frac{\mu_{\mathrm{k}}}{k_{\mathrm{k}}}(\beta_{\mathrm{k}}\mathbf{V}_{\mathrm{k}})\cdot(\beta_{\mathrm{k}}\mathbf{V}_{\mathrm{k}})+\\ &+\tilde{\rho}_{\mathrm{v}}\frac{RT}{M_{\mathrm{v}}}\frac{1}{D}\frac{\beta_{\mathrm{g}}}{\zeta(1-\zeta)}(\zeta\mathbf{V}_{\mathrm{vg}})\cdot(\zeta\mathbf{V}_{\mathrm{vg}}),\end{aligned}\tag{3.6}$$

where

λ_{k}	is the thermal conductivity,
μ_{k}	is the dynamic viscosity,
k_{k}	is the permeability,
D	is the diffusivity,
$\mathbf{V}_{\mathrm{g}}=\zeta\mathbf{V}_{\mathrm{v}}+(1-\zeta)\mathbf{V}_{\mathrm{a}}$	is the molar weighted relative velocity of gas, and
$\mathbf{V}_{\mathrm{vg}}=\mathbf{V}_{\mathrm{v}}-\mathbf{V}_{\mathrm{g}}$.	

As in ([60], [61]) this quadratic form of the dissipation function yields $\nu = 1/2$.

3.1.3 State equations

Stress

With the chosen free energies (3.3–3.5) and the dissipation function (3.6) the constituent stresses by (2.38, 2.39, 2.41, 2.50) get the forms

$$\boldsymbol{\sigma}_{\mathrm{s}}^{\mathrm{D}} = 2\xi_{\mathrm{s}} G \boldsymbol{\epsilon}^{\mathrm{D}}, \tag{3.7}$$

$$\begin{aligned} p_{\mathrm{s}} &= \xi_{\mathrm{s}}\Bigg(\hat{B} + \rho_{\mathrm{l}}\frac{RT}{M_{\mathrm{v}}}\frac{\partial f}{\partial \xi_{\mathrm{s}}} + \xi_{\mathrm{s}}\frac{\partial G}{\partial \xi_{\mathrm{s}}}\boldsymbol{\epsilon}^{\mathrm{D}} : \boldsymbol{\epsilon}^{\mathrm{D}} + \frac{1}{2}\xi_{\mathrm{s}}\frac{\partial K}{\partial \xi_{\mathrm{s}}}(\mathrm{tr}\boldsymbol{\epsilon})^2 + \\ &\quad + \xi_{\mathrm{s}}\frac{\partial f_{\Pi}}{\partial \xi_{\mathrm{s}}}\hat{B}_0 \mathrm{tr}\boldsymbol{\epsilon} - f_{\Pi}\hat{B}_0 - K\mathrm{tr}\boldsymbol{\epsilon}\Bigg), \end{aligned} \tag{3.8}$$

$$\begin{aligned} p_{\mathrm{l}} &= \xi_{\mathrm{l}}\Bigg(\hat{B} + \rho_{\mathrm{l}}\frac{RT}{M_{\mathrm{v}}}\frac{\partial f}{\partial \xi_{\mathrm{l}}} + \xi_{\mathrm{s}}\frac{\partial G}{\partial \xi_{\mathrm{l}}}\boldsymbol{\epsilon}^{\mathrm{D}} : \boldsymbol{\epsilon}^{\mathrm{D}} + \frac{1}{2}\xi_{\mathrm{s}}\frac{\partial K}{\partial \xi_{\mathrm{l}}}(\mathrm{tr}\boldsymbol{\epsilon})^2 + \\ &\quad + \xi_{\mathrm{s}}\frac{\partial f_{\Pi}}{\partial \xi_{\mathrm{l}}}\hat{B}_0 \mathrm{tr}\boldsymbol{\epsilon}\Bigg), \end{aligned} \tag{3.9}$$

$$p_{\mathrm{k}} = \xi_{\mathrm{k}}\hat{B} = \rho_{\mathrm{k}}\frac{RT}{M_{\mathrm{k}}} - \xi_{\mathrm{k}} T I, \ \mathrm{k} \in \{\mathrm{v}, \mathrm{a}\}. \tag{3.10}$$

By choosing the respective forms of adsorption function, swelling function, bulk modulus, and shear modulus such that

$$f = f(\xi_{\mathrm{s}}/\xi_{\mathrm{l}}), \quad f_{\Pi} = f_{\Pi}(\xi_{\mathrm{s}}/\xi_{\mathrm{l}}), \quad K = K(\xi_{\mathrm{s}}/\xi_{\mathrm{l}}), \quad G = G(\xi_{\mathrm{s}}/\xi_{\mathrm{l}}) \tag{3.11}$$

the total stress of the mixture gets the form

$$\boldsymbol{\sigma} = \boldsymbol{\sigma}_{\mathrm{s}}^{\mathrm{D}} - \sum_{\mathrm{k}} p_{\mathrm{k}}\mathbf{I} \tag{3.12}$$

$$= \Big(2\xi_{\mathrm{s}} G \boldsymbol{\epsilon}^{\mathrm{D}} + (\xi_{\mathrm{s}} K \mathrm{tr}\boldsymbol{\epsilon} + \xi_{\mathrm{s}} f_{\Pi}\hat{B}_0)\mathbf{I}\Big) - \hat{B}\mathbf{I} \tag{3.13}$$

$$\equiv \boldsymbol{\sigma}_{\mathrm{eff}} - \pi\mathbf{I}. \tag{3.14}$$

By (3.10) and by (3.14) the pressure term $\hat{B}$ equals to

1. the intrinsic pressures of the gaseous constituents,
2. pore pressure π, and to
3. the total mixture pressure at an undeformed state with vanishing swelling interaction.

Entropy

The constituent entropies by (2.40, 3.3–3.5) get the forms

$$s_{\mathrm{s}} = s_{\mathrm{s},0} + c_{\mathrm{s}}^{v} \ln \frac{T}{T_0} - J(\tilde{\rho}_{\mathrm{s}}) - \frac{I(\xi_{\mathrm{j}})}{\tilde{\rho}_{\mathrm{s}}}, \tag{3.15}$$

$$s_{\mathrm{l}} = s_{\mathrm{l},0} + c_{\mathrm{l}}^{v} \ln \frac{T}{T_0} - J(\tilde{\rho}_{\mathrm{l}}) - \frac{R}{M_{\mathrm{v}}} f - \frac{I(\xi_{\mathrm{j}})}{\tilde{\rho}_{\mathrm{l}}}, \tag{3.16}$$

$$\begin{aligned} s_{\mathrm{k}} = {} & s_{\mathrm{k},0} + c_{\mathrm{k}}^{v} \ln \frac{T}{T_0} - \frac{R}{M_{\mathrm{k}}} \ln \left(\frac{\tilde{\rho}_{\mathrm{k}}}{\tilde{\rho}_{\mathrm{k},0}} \right) - \\ & - \frac{R}{M_{\mathrm{k}}} \ln \left(\frac{\xi_{\mathrm{k}}}{\xi_{\mathrm{a}} + \xi_{\mathrm{v}}} \Bigg/ \left(\frac{\xi_{\mathrm{k}}}{\xi_{\mathrm{a}} + \xi_{\mathrm{v}}} \right)_0 \right) - \frac{I(\xi_{\mathrm{j}})}{\tilde{\rho}_{\mathrm{k}}}, \quad \mathrm{k} \in \{\mathrm{v}, \mathrm{a}\}. \end{aligned} \tag{3.17}$$

3.1.4 Thermodynamic potentials and phase change

Internal energy

The specific internal energies

$$e_{\mathrm{k}} = \psi_{\mathrm{k}} + T s_{\mathrm{k}} \tag{3.18}$$

by (3.3–3.5, 3.15–3.17) get the forms

$$\begin{aligned} e_{\mathrm{s}} = {} & e_{\mathrm{s},0} + c_{\mathrm{s}}^{v}(T - T_0) + \\ & + \tilde{v}_{\mathrm{s}} \Big(G \boldsymbol{\epsilon}^{\mathrm{D}} : \boldsymbol{\epsilon}^{\mathrm{D}} + \frac{K}{2} (\mathrm{tr}\boldsymbol{\epsilon})^2 + f_{\Pi} \hat{B}_0 \mathrm{tr}\boldsymbol{\epsilon} \Big), \end{aligned} \tag{3.19}$$

$$e_{\mathrm{k}} = e_{\mathrm{k},0} + c_{\mathrm{k}}^{v}(T - T_0), \qquad \mathrm{k} \in \{\mathrm{l}, \mathrm{v}, \mathrm{a}\}. \tag{3.20}$$

where

$$e_{\mathrm{k},0} = \psi_{\mathrm{k},0} + T_0 s_{\mathrm{k},0} \tag{3.21}$$

is the specific internal energy at the reference state.

Enthalpy and latent heat

The specific enthalpies

$$h_{\mathrm{k}} = e_{\mathrm{k}} + \frac{p_{\mathrm{k}}}{\rho_{\mathrm{k}}} \tag{3.22}$$

by (3.8–3.10) get the forms

$$\begin{aligned} h_{\mathrm{s}} = {} & h_{\mathrm{s},0} + c_{\mathrm{s}}^{v}(T - T_0) + \hat{B}\tilde{v}_{\mathrm{s}} - (\hat{B}\tilde{v}_{\mathrm{s}})_0 + \\ & + \frac{\tilde{\rho}_{\mathrm{l}}}{\tilde{\rho}_{\mathrm{s}}} \frac{RT}{M_{\mathrm{v}}} \xi_{\mathrm{l}} \frac{\partial f}{\partial \xi_{\mathrm{s}}} + \end{aligned}$$

$$
\begin{aligned}
&+\tilde{v}_{\mathrm{s}}\Big[-f_{\Pi}\hat{B}_0 - K\mathrm{tr}\boldsymbol{\epsilon} + \frac{\partial(\xi_{\mathrm{s}} f_{\Pi})}{\partial \xi_{\mathrm{s}}}\hat{B}_0\mathrm{tr}\boldsymbol{\epsilon} + \\
&\quad + \frac{1}{2}\frac{\partial(\xi_{\mathrm{s}} K)}{\partial \xi_{\mathrm{s}}}(\mathrm{tr}\boldsymbol{\epsilon})^2 + \frac{\partial(\xi_{\mathrm{s}} G)}{\partial \xi_{\mathrm{s}}}\boldsymbol{\epsilon}^{\mathrm{D}} : \boldsymbol{\epsilon}^{\mathrm{D}}\Big], \qquad (3.23)
\end{aligned}
$$

$$
\begin{aligned}
h_{\mathrm{l}} &= h_{\mathrm{l},0} + c_{\mathrm{l}}^{v}(T - T_0) + \hat{B}\tilde{v}_{\mathrm{l}} - (\hat{B}\tilde{v}_{\mathrm{l}})_0 + \\
&\quad + \frac{RT}{M_{\mathrm{v}}}\xi_{\mathrm{l}}\frac{\partial f}{\partial \xi_{\mathrm{l}}} + \\
&\quad + \tilde{v}_{\mathrm{l}}\Big[\xi_{\mathrm{s}}\frac{\partial f_{\Pi}}{\partial \xi_{\mathrm{l}}}\hat{B}_0\mathrm{tr}\boldsymbol{\epsilon} + \frac{1}{2}\xi_{\mathrm{s}}\frac{\partial K}{\partial \xi_{\mathrm{l}}}(\mathrm{tr}\boldsymbol{\epsilon})^2 + \xi_{\mathrm{s}}\frac{\partial G}{\partial \xi_{\mathrm{l}}}\boldsymbol{\epsilon}^{\mathrm{D}} : \boldsymbol{\epsilon}^{\mathrm{D}}\Big], \qquad (3.24) \\
h_{\mathrm{k}} &= h_{\mathrm{k},0} + c_{\mathrm{k}}^{v}(T - T_0) + \hat{B}\tilde{v}_{\mathrm{k}} - (\hat{B}\tilde{v}_{\mathrm{k}})_0, \qquad \mathrm{k} \in \{\mathrm{v}, \mathrm{a}\}, \qquad (3.25)
\end{aligned}
$$

where

$$
h_{\mathrm{k},0} = e_{\mathrm{k},0} + \hat{B}_0\tilde{v}_{\mathrm{k},0} \qquad (3.26)
$$

is the specific enthalpy at the reference state. The latent heat of vaporization l is the enthalpy difference of vapor and liquid

$$
\begin{aligned}
l &= h_{\mathrm{v}} - h_{\mathrm{l}} \qquad (3.27) \\
&= l_0 + (c_{\mathrm{v}}^{v} - c_{\mathrm{l}}^{v})(T - T_0) + \hat{B}(\tilde{v}_{\mathrm{v}} - \tilde{v}_{\mathrm{l}}) - \hat{B}_0(\tilde{v}_{\mathrm{v}} - \tilde{v}_{\mathrm{l}})_0 - \\
&\quad - \frac{RT}{M_{\mathrm{v}}}\xi_{\mathrm{l}}\frac{\partial f}{\partial \xi_{\mathrm{l}}} - \\
&\quad - \tilde{v}_{\mathrm{l}}\left[\xi_{\mathrm{s}}\frac{\partial f_{\Pi}}{\partial \xi_{\mathrm{l}}}\hat{B}_0\mathrm{tr}\boldsymbol{\epsilon} + \frac{1}{2}\xi_{\mathrm{s}}\frac{\partial K}{\partial \xi_{\mathrm{l}}}(\mathrm{tr}\boldsymbol{\epsilon})^2 + \xi_{\mathrm{s}}\frac{\partial G}{\partial \xi_{\mathrm{l}}}\boldsymbol{\epsilon}^{\mathrm{D}} : \boldsymbol{\epsilon}^{\mathrm{D}}\right], \qquad (3.28)
\end{aligned}
$$

where

$$
\begin{aligned}
l_0 &= (h_{\mathrm{v}} - h_{\mathrm{l}})_0 \qquad (3.29) \\
&= (e_{\mathrm{v}} - e_{\mathrm{l}})_0 + \hat{B}_0(\tilde{v}_{\mathrm{v}} - \tilde{v}_{\mathrm{l}})_0 \qquad (3.30)
\end{aligned}
$$

is the specific latent heat of vaporization at the reference state.

Phase equilibrium of liquid and vapor

Neglecting of kinetic energy and dissipation in (2.44) yields the classical free enthalpy equilibrium which for the water species by (3.15–3.17) in the feasible region ($I = J = 0$) yields

$$
\begin{aligned}
l &= T(s_{\mathrm{v}} - s_{\mathrm{l}}) \\
&= T(s_{\mathrm{v}} - s_{\mathrm{l}})_0 + (c_{\mathrm{v}}^{v} - c_{\mathrm{l}}^{v})T\ln\frac{T}{T_0} - \frac{RT}{M_{\mathrm{v}}}\ln\frac{\zeta\tilde{\rho}_{\mathrm{v}}}{(\zeta\tilde{\rho}_{\mathrm{v}})_0} + \frac{RT}{M_{\mathrm{v}}}f. \qquad (3.31)
\end{aligned}
$$

The gaseous phase state equation (3.10) in the feasible region ($I = 0$) along with (3.28, 3.31) yields

$$\begin{aligned}\ln\frac{\zeta\hat{B}}{(\zeta\hat{B})_0} &= \frac{M_\mathrm{v}}{RT}\Big[L\frac{T-T_0}{T_0} + (c_\mathrm{v}^p - c_\mathrm{l}^p)T\ln\frac{T}{T_0} + (\hat{B}-\hat{B}_0)\tilde{v}_\mathrm{l}\Big] + \\ &+\frac{\partial(\xi_\mathrm{l} f)}{\partial\xi_\mathrm{l}} + \\ &+\tilde{v}_\mathrm{l}\frac{M_\mathrm{v}}{RT}\Big[\xi_\mathrm{s}\frac{\partial f_\Pi}{\partial\xi_\mathrm{l}}\hat{B}_0\mathrm{tr}\boldsymbol{\epsilon} + \frac{1}{2}\xi_\mathrm{s}\frac{\partial K}{\partial\xi_\mathrm{l}}(\mathrm{tr}\boldsymbol{\epsilon})^2 + \xi_\mathrm{s}\frac{\partial G}{\partial\xi_\mathrm{l}}\boldsymbol{\epsilon}^\mathrm{D}:\boldsymbol{\epsilon}^\mathrm{D}\Big] \end{aligned} \tag{3.32}$$

where

$$c_\mathrm{l}^p = c_\mathrm{l}^v, \tag{3.33}$$

$$c_\mathrm{v}^p = c_\mathrm{v}^v + R/M_\mathrm{v} \tag{3.34}$$

are the respective specific heats of liquid and vapor at constant pressure, and

$$L = l_0 - (c_\mathrm{v}^p - c_\mathrm{l}^p)T_0 \tag{3.35}$$

is an abbreviation. Equation (3.32) is a generalized Clausius-Clapeyron equation giving the partial pressure of saturated vapor $\zeta\hat{B}$ for the mixture of solid, liquid, vapor, and air as a function of temperature, total pressure, the proportions of the liquid and solid phases, and strain. For the simpler mixture of liquid, vapor, and air the Clausius-Clapeyron equation (3.32) reduces to

$$\ln\frac{(\zeta\hat{B})^0}{(\zeta\hat{B})_0} = \frac{M_\mathrm{v}}{RT}\Big[L\frac{T-T_0}{T_0} + (c_\mathrm{v}^\mathrm{p} - c_\mathrm{l}^\mathrm{p})T\ln\frac{T}{T_0} + (\hat{B}^0-\hat{B}_0)\tilde{v}_\mathrm{l}\Big], \tag{3.36}$$

where the superscript $()^0$ denotes a value "outside the porous medium", i.e. for a mixture without the solid constituent. For the even simpler mixture of liquid and vapor the Clausius-Clapeyron equation (3.36) reduces to

$$\ln\frac{\hat{B}^0}{\hat{B}_0} = \frac{M_\mathrm{v}}{RT}\Big[L\frac{T-T_0}{T_0} + (c_\mathrm{v}^\mathrm{p} - c_\mathrm{l}^\mathrm{p})T\ln\frac{T}{T_0} + (\hat{B}^0-\hat{B}_0)\tilde{v}_\mathrm{l}\Big]. \tag{3.37}$$

The latent heat outside the porous medium by (3.28) and (3.10, 3.33, 3.34) reduces to

$$l^0 = l_0 + (c_\mathrm{v}^p - c_\mathrm{l}^p)(T-T_0) - \frac{\hat{B}^0-\hat{B}_0}{\tilde{\rho}_\mathrm{l}}. \tag{3.38}$$

3.1.5 The reference and initial states

A natural choice for both the reference state and the initial state could be the fully swollen and fully saturated state, in which the system is in equilibrium with its surroundings without any applied external forces and with zero swelling pressure. However, the model is limited to small strains only and the initial state of the application target is compacted clay far below the fully expanded state. For this reason we choose as the reference state the initial compacted state at full saturation. The reference state is

$$\{\boldsymbol{\epsilon},\ \xi_\mathrm{s},\ \xi_\mathrm{l},\ \xi_\mathrm{v},\ \xi_\mathrm{a},\ \tilde{\rho}_\mathrm{s},\ \tilde{\rho}_\mathrm{l},\ \tilde{\rho}_\mathrm{v},\ \tilde{\rho}_\mathrm{a},\ T\}_0 = \\ \Big\{\boldsymbol{\epsilon}_0,\ 1-\eta_0,\ \eta_0\chi_0,\ \eta_0(1-\chi_0)\zeta_0,\ \eta_0(1-\chi_0)(1-\zeta_0), \\ \tilde{\rho}_{\mathrm{s},0},\ \tilde{\rho}_{\mathrm{l},0},\ \hat{B}_0\frac{M_\mathrm{v}}{RT_0},\ \hat{B}_0\frac{M_\mathrm{a}}{RT_0},\ T_0\Big\},$$

in which

$$\begin{aligned}
\boldsymbol{\epsilon}_0 &= \boldsymbol{\epsilon}_\mathrm{init} = \mathbf{0}, \\
\eta_0 &= \eta_\mathrm{init}, \\
\chi_0 &= \chi_\mathrm{max}, \\
\zeta_0 &= (p_\mathrm{v,sat}/\hat{B})_0, \\
\hat{B}_0 &= 1\ \mathrm{ATM}, \\
T_0 &= (20+273.15)\ \mathrm{K}.
\end{aligned}$$

Additional requirements for the reference state to satisfy equations (3.3–3.24) are

$$f_0 = \left(\frac{\partial f}{\partial \xi_\mathrm{s}}\right)_0 = \left(\frac{\partial f}{\partial \xi_\mathrm{l}}\right)_0 = f_{\mathrm{II},0} = 0. \tag{3.39}$$

If the initial and the reference states are different from each other the last requirement of (3.39) makes the total stress (3.14) defined relative to the initial state.

For $\mathrm{k} \in \{\mathrm{s}, \mathrm{l}, \mathrm{a}\}$ it can be set

$$e_{\mathrm{k},0} = s_{\mathrm{k},0} = 0 \Rightarrow \psi_{\mathrm{k},0} = 0. \tag{3.40}$$

The corresponding values for the vapor constituent by (3.30, 3.31), and (3.21) become

$$e_{\mathrm{v},0} = l_0 - \hat{B}_0(1/\tilde{\rho}_\mathrm{v} - 1/\tilde{\rho}_\mathrm{l})_0, \tag{3.41}$$

$$s_{\mathrm{v},0} = l_0/T_0, \tag{3.42}$$

$$\psi_{\mathrm{v},0} = -\hat{B}_0(1/\tilde{\rho}_\mathrm{v} - 1/\tilde{\rho}_\mathrm{l})_0, \tag{3.43}$$

respectively. With these values the chosen free energies (3.3–3.5) are exactly determined.

3.1.6 Suction

Frémond and Nicolas [38] defined the relative humidity RH inside the porous medium as

$$RH = \frac{p_{vs}}{p_{vs}^0} \tag{3.44}$$

where p_{vs} is the saturated vapor pressure inside the porous medium and p_{vs}^0 is the saturated vapor pressure outside the porous medium. In the present paper the partial pressure of vapor $\zeta\hat{B}$ inside the porous medium is the product of the intrinsic pressure of the gaseous phase $\hat{B}$ and the molar fraction of the vapor among the gaseous phase ζ. The total intrinsic gaseous pressure is the sum of the partial pressures of the gaseous components (vapor and air), i.e., apparently

$$\hat{B} = \zeta\hat{B} + (1-\zeta)\hat{B} = \frac{\xi_{\mathrm{v}}}{\xi_{\mathrm{v}}+\xi_{\mathrm{a}}}\hat{B} + \frac{\xi_{\mathrm{a}}}{\xi_{\mathrm{v}}+\xi_{\mathrm{a}}}\hat{B}. \tag{3.45}$$

Traditionally, the relative humidity of *free air* at a given temperature is defined as the ratio of the current vapor pressure and the maximum vapor pressure. The maximum vapor pressure is the pressure of saturated vapor, i.e., it corresponds to the situation in which the vapor is in equilibrium with free liquid water. We denote this maximum vapor pressure as $(\zeta\hat{B})^0$. Consistently, the relative humidity of the gaseous phase inside the porous medium is defined as the ratio

$$RH \equiv \frac{\zeta\hat{B}}{(\zeta\hat{B})^0}. \tag{3.46}$$

The relative humidity inside the porous medium is the maximum when the vapour inside the porous medium is in equilibrium with saturated free vapor pressure (i.e. maximum free vapor pressure). In such situation it is also in equilibrium with free water and the porous medium is fully saturated. By combining (3.32) and (3.36) at the same temperature the relative humidity (3.46) inside the porous medium is obtained as

$$\begin{aligned}\ln RH \;=\;& \tilde{v}_{\mathrm{l}}\frac{M_{\mathrm{v}}}{RT}(\hat{B}-\hat{B}^0) + \frac{\partial(\xi_{\mathrm{l}}f)}{\partial\xi_{\mathrm{l}}} + \\ &+\tilde{v}_{\mathrm{l}}\frac{M_{\mathrm{v}}}{RT}\Big[\xi_{\mathrm{s}}\frac{\partial f_{\Pi}}{\partial\xi_{\mathrm{l}}}\hat{B}_0\mathrm{tr}\boldsymbol{\epsilon} + \frac{1}{2}\xi_{\mathrm{s}}\frac{\partial K}{\partial\xi_{\mathrm{l}}}(\mathrm{tr}\boldsymbol{\epsilon})^2 + \xi_{\mathrm{s}}\frac{\partial G}{\partial\xi_{\mathrm{l}}}\boldsymbol{\epsilon}^{\mathrm{D}}:\boldsymbol{\epsilon}^{\mathrm{D}}\Big],\end{aligned} \tag{3.47}$$

and the Kelvin law

$$p_{\mathrm{c}} = -\tilde{\rho}_{\mathrm{l}} \frac{RT}{M_{\mathrm{v}}} \ln RH \tag{3.48}$$

for the suction pressure p_{c} as

$$\begin{aligned} p_{\mathrm{c}} &= -(\hat{B} - \hat{B}^0) - \tilde{\rho}_{\mathrm{l}} \frac{RT}{M_{\mathrm{v}}} \frac{\partial(\xi_{\mathrm{l}} f)}{\partial \xi_{\mathrm{l}}} - \\ & -\xi_{\mathrm{s}} \frac{\partial f_{\Pi}}{\partial \xi_{\mathrm{l}}} \hat{B}_0 \mathrm{tr}\boldsymbol{\epsilon} - \frac{1}{2} \xi_{\mathrm{s}} \frac{\partial K}{\partial \xi_{\mathrm{l}}} (\mathrm{tr}\boldsymbol{\epsilon})^2 - \xi_{\mathrm{s}} \frac{\partial G}{\partial \xi_{\mathrm{l}}} \boldsymbol{\epsilon}^{\mathrm{D}} : \boldsymbol{\epsilon}^{\mathrm{D}}. \end{aligned} \tag{3.49}$$

Equation (3.49) suggests that the suction pressure depends on the gaseous pressure, the adsorption interaction, swelling interaction, and strain. For a confined experiment with constant gaseous pressure the suction pressure becomes

$$p_{\mathrm{c}}^{v} = -\tilde{\rho}_{\mathrm{l}} \frac{RT}{M_{\mathrm{v}}} \frac{\partial(\xi_{\mathrm{l}} f)}{\partial \xi_{\mathrm{l}}}. \tag{3.50}$$

3.1.7 Swelling

Let us consider an experiment in which a sample is placed in a container allowing at least partial swelling. By applying a uniform wetting of the sample the developing swelling stress can be defined as the difference of the current and initial mixture stresses (3.14). By neglecting the deviatoric components the swelling pressure is

$$\Pi \equiv \hat{B} - \hat{B}_{\mathrm{init}} - \xi_{\mathrm{s}} K \mathrm{tr}\boldsymbol{\epsilon} - [\xi_{\mathrm{s}} f_{\Pi} - (\xi_{\mathrm{s}} f_{\Pi})_{\mathrm{init}}] \hat{B}_0. \tag{3.51}$$

An interesting special case is that of constant volume and constant gaseous pressure for which the swelling pressure (3.51) gets the form

$$\Pi^{v} = -\xi_{\mathrm{s,init}} (f_{\Pi} - f_{\Pi,\mathrm{init}}) \hat{B}_0. \tag{3.52}$$

The maximum confined swelling pressure Π^{v}_{max} occurs at full saturation corresponding to the reference state at which $f_{\Pi,0} = 0$ (3.39). Consequently, the constant initial value for the swelling function is $f_{\Pi,\mathrm{init}} = \Pi^{v}_{\mathrm{max}}/(\xi_{\mathrm{s,init}} \hat{B}_0)$.

3.1.8 Flow equations

When the inertial terms are neglected in the rate of production of linear momentum the flow relations, i.e., the Darcy law for liquid, the Darcy law

for gas, the Fick law for the relative velocity of vapor, and the Fourier heat conduction law [60] are

$$\beta_{\mathrm{l}}\mathbf{V}_{\mathrm{l}} = -\frac{k_{\mathrm{l}}}{\mu_{\mathrm{l}}}\Big[\nabla\Big(\frac{p_{\mathrm{l}}}{\xi_{\mathrm{l}}}\Big) - \tilde{\rho}_{\mathrm{l}}\mathbf{g} + \tilde{\rho}_{\mathrm{l}}\frac{RT}{M_{\mathrm{v}}}\nabla f\Big], \tag{3.53}$$

$$\beta_{\mathrm{g}}\mathbf{V}_{\mathrm{g}} = -\frac{k_{\mathrm{g}}}{\mu_{\mathrm{g}}}\Big[\nabla\hat{B} - \frac{\rho_{\mathrm{a}}+\rho_{\mathrm{v}}}{\beta_{\mathrm{g}}}\mathbf{g}\Big], \tag{3.54}$$

$$\zeta\mathbf{V}_{\mathrm{vg}} = -D\Big[\nabla\zeta - \zeta(1-\zeta)\frac{M_{\mathrm{v}}-M_{\mathrm{a}}}{RT}\mathbf{g}\Big], \tag{3.55}$$

$$\mathbf{q}_{\mathrm{k}} = -\xi_{\mathrm{k}}\lambda_{\mathrm{k}}\nabla T, \tag{3.56}$$

respectively. The liquid pressure gradient in (3.53) can be expanded by means of (3.9) yielding

$$\begin{aligned}\beta_{\mathrm{l}}\mathbf{V}_{\mathrm{l}} = -\frac{k_{\mathrm{l}}}{\mu_{\mathrm{l}}}\Big[&\nabla\hat{B} - \tilde{\rho}_{\mathrm{l}}\mathbf{g} + \tilde{\rho}_{\mathrm{l}}\frac{RT}{M_{\mathrm{v}}}\nabla\Big(\frac{\partial(\xi_{\mathrm{l}}f)}{\partial\xi_{\mathrm{l}}}\Big) + \rho_{\mathrm{l}}\frac{R}{M_{\mathrm{v}}}\frac{\partial f}{\partial\xi_{\mathrm{l}}}\nabla T + \\ &+\boldsymbol{\epsilon}^{\mathrm{D}}:\boldsymbol{\epsilon}^{\mathrm{D}}\nabla\Big(\xi_{\mathrm{s}}\frac{\partial G}{\partial\xi_{\mathrm{l}}}\Big) + \xi_{\mathrm{s}}\frac{\partial G}{\partial\xi_{\mathrm{l}}}\nabla(\boldsymbol{\epsilon}^{\mathrm{D}}:\boldsymbol{\epsilon}^{\mathrm{D}}) + \\ &+\frac{1}{2}(\mathrm{tr}\boldsymbol{\epsilon})^2\nabla\Big(\xi_{\mathrm{s}}\frac{\partial K}{\partial\xi_{\mathrm{l}}}\Big) + \Big(\xi_{\mathrm{s}}\frac{\partial K}{\partial\xi_{\mathrm{l}}}\mathrm{tr}\boldsymbol{\epsilon} + \xi_{\mathrm{s}}\frac{\partial f_{\Pi}}{\partial\xi_{\mathrm{l}}}\hat{B}_0\Big)\nabla(\mathrm{tr}\boldsymbol{\epsilon}) + \\ &+\hat{B}_0\mathrm{tr}\boldsymbol{\epsilon}\nabla\Big(\xi_{\mathrm{s}}\frac{\partial f_{\Pi}}{\partial\xi_{\mathrm{l}}}\Big)\Big].\end{aligned} \tag{3.57}$$

The terms involving G and K are due to the postulated dependence of the elasticity of the skeleton on the proportions of the solid and liquid molar volume fractions. These terms are supposedly of minor importance and neglected. On the other hand, the terms involving the swelling interaction are taken into account in the following.

3.2 The thermo-hydro-mechanical model

3.2.1 The final conservation equations

The final primary variables are porosity, gaseous pressure, saturation, displacement, and temperature, i.e.,

$$\eta, \quad \hat{B}, \quad \chi, \quad \mathbf{u}, \quad T, \tag{3.58}$$

respectively. Inertial and convectional terms are neglected as well as the mechanical contribution to the energy conservation. Hence, the respective rates of change of mass (2.16), momentum (2.17), and energy (2.18) reduce to

$$\theta_{\mathrm{k}} = \frac{\partial \rho_{\mathrm{k}}}{\partial t} + \nabla \cdot (\rho_{\mathrm{k}} \mathbf{U}_{\mathrm{k}}), \tag{3.59}$$

$$\mathbf{m}_{\mathrm{k}} = -\nabla \cdot \boldsymbol{\sigma}_{\mathrm{k}} - \rho_{\mathrm{k}} \mathbf{g}, \tag{3.60}$$

$$\iota_{\mathrm{k}} = \rho_{\mathrm{k}} \frac{\partial e_{\mathrm{k}}}{\partial t} + e_{\mathrm{k}} \theta_{\mathrm{k}} + \nabla \cdot \mathbf{q}_{\mathrm{k}} - Q_{\mathrm{k}}. \tag{3.61}$$

The corresponding conservations of mass (2.19) of solid, air, and water, and the conservations of momentum (2.20) and energy (2.21) become

$$\frac{\partial \rho_{\mathrm{s}}}{\partial t} + \nabla \cdot \left(\rho_{\mathrm{s}} \frac{\partial \mathbf{u}}{\partial t} \right) = 0, \tag{3.62}$$

$$\frac{\partial \rho_{\mathrm{a}}}{\partial t} + \nabla \cdot \left(\rho_{\mathrm{a}} \mathbf{V}_{\mathrm{a}} + \rho_{\mathrm{a}} \frac{\partial \mathbf{u}}{\partial t} \right) = 0, \tag{3.63}$$

$$\frac{\partial (\rho_{\mathrm{l}} + \rho_{\mathrm{v}})}{\partial t} + \nabla \cdot \left(\rho_{\mathrm{l}} \mathbf{V}_{\mathrm{l}} + \rho_{\mathrm{v}} \mathbf{V}_{\mathrm{v}} + (\rho_{\mathrm{l}} + \rho_{\mathrm{v}}) \frac{\partial \mathbf{u}}{\partial t} \right) = 0, \tag{3.64}$$

$$\nabla \cdot \boldsymbol{\sigma} + \rho \mathbf{g} = 0, \tag{3.65}$$

$$(\rho c)_{\mathrm{eff}} \frac{\partial T}{\partial t} - (e_{\mathrm{v}} - e_{\mathrm{l}}) \theta_{\mathrm{l}} + \nabla \cdot \mathbf{q} - Q = 0, \tag{3.66}$$

respectively, where

$$\rho = \sum_{\mathrm{k}} \rho_{\mathrm{k}}, \tag{3.67}$$

$$(\rho c)_{\mathrm{eff}} = \sum_{\mathrm{k}} \rho_{\mathrm{k}} c_{\mathrm{k}}^{v}, \tag{3.68}$$

$$\mathbf{q} = \sum_{\mathrm{k}} \mathbf{q}_{\mathrm{k}}, \tag{3.69}$$

$$Q = \sum_{\mathrm{k}} Q_{\mathrm{k}}. \tag{3.70}$$

3.2.2 The final constitutive equations

The constitutive relations are reduced to the following respective forms of Clausius-Clapeyron equation by (3.32)

$$\begin{aligned}\ln\frac{\zeta\hat{B}}{(\zeta\hat{B})_0} &= \frac{M_\mathrm{v}}{RT}\Big[L\frac{T-T_0}{T_0}+(c_\mathrm{v}^p-c_\mathrm{l}^p)T\ln\frac{T}{T_0}+\frac{\hat{B}-\hat{B}_0}{\tilde{\rho}_\mathrm{l}}\Big]+\\ &\quad+\frac{\partial(\xi_\mathrm{l}f)}{\partial\xi_\mathrm{l}}+\\ &\quad+\frac{1}{\tilde{\rho}_\mathrm{l}}\frac{M_\mathrm{v}}{RT}\Big[\xi_\mathrm{s}\frac{\partial f_\Pi}{\partial\xi_\mathrm{l}}\hat{B}_0\mathrm{tr}\boldsymbol{\epsilon}+\frac{1}{2}\xi_\mathrm{s}\frac{\partial K}{\partial\xi_\mathrm{l}}(\mathrm{tr}\boldsymbol{\epsilon})^2\Big],\end{aligned} \tag{3.71}$$

where the term involving the deviatoric stress is neglected, stress-strain relation by (3.13)

$$\boldsymbol{\sigma}=2\xi_\mathrm{s}G\boldsymbol{\epsilon}^\mathrm{D}-(\hat{B}-\xi_\mathrm{s}K\mathrm{tr}\boldsymbol{\epsilon}-\xi_\mathrm{s}f_\Pi\hat{B}_0)\mathbf{I}, \tag{3.72}$$

gaseous phase state equation (3.10)

$$\hat{B}=\tilde{\rho}_\mathrm{k}\frac{RT}{M_\mathrm{k}},\qquad \mathrm{k}\in\{\mathrm{a},\mathrm{v}\}, \tag{3.73}$$

Darcy's law for liquid by (3.57), the results of Darcy's law for gas (3.54) and Fick's law for vapor (3.55)

$$\begin{aligned}\rho_\mathrm{l}\mathbf{V}_\mathrm{l} &= -\tilde{\rho}_\mathrm{l}\frac{k_\mathrm{l}}{\mu_\mathrm{l}}\Big[\nabla\hat{B}-\tilde{\rho}_\mathrm{l}\mathbf{g}+\tilde{\rho}_\mathrm{l}\frac{RT}{M_\mathrm{v}}\nabla\Big(\frac{\partial(\xi_\mathrm{l}f)}{\partial\xi_\mathrm{l}}\Big)+\rho_\mathrm{l}\frac{R}{M_\mathrm{v}}\frac{\partial f}{\partial\xi_\mathrm{l}}\nabla T+\\ &\quad+\xi_\mathrm{s}\frac{\partial f_\Pi}{\partial\xi_\mathrm{l}}\hat{B}_0\nabla(\mathrm{tr}\boldsymbol{\epsilon})+\hat{B}_0\mathrm{tr}\boldsymbol{\epsilon}\nabla\Big(\xi_\mathrm{s}\frac{\partial f_\Pi}{\partial\xi_\mathrm{l}}\Big)\Big],\end{aligned} \tag{3.74}$$

$$\rho_\mathrm{v}\mathbf{V}_\mathrm{v} = -\tilde{\rho}_\mathrm{v}\beta_\mathrm{g}D\nabla\zeta-\zeta\tilde{\rho}_\mathrm{v}\frac{k_\mathrm{g}}{\mu_\mathrm{g}}\nabla\hat{B}, \tag{3.75}$$

$$\rho_\mathrm{a}\mathbf{V}_\mathrm{a} = \tilde{\rho}_\mathrm{a}\beta_\mathrm{g}D\nabla\zeta-(1-\zeta)\tilde{\rho}_\mathrm{a}\frac{k_\mathrm{g}}{\mu_\mathrm{g}}\nabla\hat{B}, \tag{3.76}$$

where gravitation for gas and the terms involving G and K for liquid are neglected, Fourier's law for heat conduction (3.56),

$$\mathbf{q}=-\sum_\mathrm{k}\xi_\mathrm{k}\lambda_\mathrm{k}\nabla T\equiv-\lambda\nabla T, \tag{3.77}$$

and to the internal energy difference (3.20) of the water species

$$e_\mathrm{v}-e_\mathrm{l}=l_0+(c_\mathrm{v}^p-c_\mathrm{l}^p)(T-T_0)-RT/M_\mathrm{v}. \tag{3.78}$$

Table 3.1: Miscellaneous general rock parameter values.

c [J/(kgK)]	ρ [kg/m^3]	λ [W/(Km)]	k_{sat} [m^2]
$1.0{\cdot}10^3$	2660	3.0	$5.0\ {\cdot}10^{-19}$

3.3 Parameters

The forms of the parameters required by the model are given for compacted bentonite as well as for the host rock. For the model specific parameters, namely, suction, swelling, mechanical and flow parameters, the values are fitted in the subsequent analysis part of the thesis. The values for the more general type parameters that have not required a thorough fitting are tabulated already in the current section. This is especially the case for the host rock the modelling of which is required in the sensitivity analysis of the Febex in-situ test. The needed parameters for rock are density, specific heat, thermal conductivity, permeabilities, and suction parameters. The general rock parameter values are collected in Table 3.1 while the suction parameters are fitted in the analysis part. Other common literature values and the chosen reference values are given in Table 3.2.

3.3.1 Suction and swelling parameters

The interactions in the mixture are chosen to depend on the proportions of the interacting constituents. The considered adsorption and swelling interactions increase upon drying and decrease upon wetting. The adsorption interaction and suction vanish upon full saturation and the swelling interaction vanishes at the fully swollen state. The respective choices for the adsorption and swelling functions are

$$f = f\left(\frac{\xi_{\mathrm{s}}}{\xi_{\mathrm{l}}}\right) = \begin{cases} a_1\left(\frac{\xi_{\mathrm{s}}}{\xi_{\mathrm{l}}} - \left(\frac{\xi_{\mathrm{s}}}{\xi_{\mathrm{l}}}\right)_0\right)^{a_2}, & \text{for } \frac{\xi_{\mathrm{s}}}{\xi_{\mathrm{l}}} \geqslant \left(\frac{\xi_{\mathrm{s}}}{\xi_{\mathrm{l}}}\right)_0, \\ 0, & \text{for } \frac{\xi_{\mathrm{s}}}{\xi_{\mathrm{l}}} < \left(\frac{\xi_{\mathrm{s}}}{\xi_{\mathrm{l}}}\right)_0, \end{cases} \tag{3.79}$$

$$f_{\Pi} = f_{\Pi}\left(\frac{\xi_{\mathrm{s}}}{\xi_{\mathrm{l}}}\right) = a_3\left(\frac{\xi_{\mathrm{s}}}{\xi_{\mathrm{l}}}\right)^2 + a_4\left(\frac{\xi_{\mathrm{s}}}{\xi_{\mathrm{l}}}\right) + a_5, \tag{3.80}$$

where $a_{1\ldots5}$ are non-dimensional parameters that determine how the interactions depend on the proportions of the solid and liquid volume fractions. They depend e.g. on the inner structure of the material, its permanent electrical charge, and specific surface. The swelling function (3.80) is chosen to

be a quadratic function satisfying the following requirements

$$f_\Pi\Big(\Big(\frac{\xi_\mathrm{s}}{\xi_\mathrm{l}}\Big)_\mathrm{init}\Big) = \frac{\Pi^v_\mathrm{max}}{\xi_\mathrm{s,init}\hat{B}_0}, \tag{3.81}$$

$$f_\Pi\Big(\Big(\frac{\xi_\mathrm{s}}{\xi_\mathrm{l}}\Big)_0\Big) = 0, \tag{3.82}$$

$$\frac{\partial f_\Pi}{\partial(\xi_\mathrm{s}/\xi_\mathrm{l})}\Big(\Big(\frac{\xi_\mathrm{s}}{\xi_\mathrm{l}}\Big)_\mathrm{min}\Big) = 0. \tag{3.83}$$

As the initial and reference states are fixed, it suffices to determine the experimental maximum confined swelling pressure Π^v_max and the fully swollen state $(\xi_\mathrm{s}/\xi_\mathrm{l})_\mathrm{min}$ by means of which $a_{3,4,5}$ can be analytically determined.

3.3.2 Mechanical parameters

Equations (3.49, 3.51) can be used in the assessment of the bulk modulus $K(\xi_\mathrm{s}/\xi_\mathrm{l})$ if the shear strain is neglected and the total volume change is associated with a change in porosity. This is equivalent to assuming incompressible solid grains and corresponds to the use of equation (2.12). However, the final values for the elasticity parameters are determined by dynamic simulations of various HM-experiments for Febex bentonite presented in the subsequent analysis part of the thesis. The softening due to wetting is taken into account by choosing the bulk modulus in the following form

$$K = K(\xi_\mathrm{s}/\xi_\mathrm{l}) = K_\mathrm{init}\Big(\frac{\xi_\mathrm{s}/\xi_\mathrm{l}}{(\xi_\mathrm{s}/\xi_\mathrm{l})_\mathrm{init}}\Big)^b, \tag{3.84}$$

with the conventional relations between the elasticity parameters

$$E = 3(1-2\upsilon)K, \tag{3.85}$$

$$G = E/2(1+\upsilon), \tag{3.86}$$

where E is Young's modulus and υ is Poisson's ratio.

3.3.3 Hydraulic parameters

The permeability of fluid phase $\mathrm{j} \in \{\mathrm{l}, \mathrm{g}\}$ inside the porous medium consists of the respective intrinsic and fluid dependent parts in the following usual way

$$k_\mathrm{j} = k_\mathrm{j,rel} k_\mathrm{sat}. \tag{3.87}$$

The intrinsic permeability is calibrated by means of flow experiments. The relative permeabilities of liquid and gas are assumed to have the following respective forms

$$k_{\mathrm{l,rel}} = k_{\mathrm{l,rel}}(\chi) = \chi^n, \tag{3.88}$$

$$k_{\mathrm{g,rel}} = k_{\mathrm{g,rel}}(1-\chi) \approx const. \tag{3.89}$$

For rock the permeability parameters are not adjusted but merely taken as average representative values from the literature (Table 3.1, [2]). The relative permeability of liquid in granite can be expressed [62] as

$$k_{\mathrm{l,rel}} = \chi^{0.5}[1-(1-\chi^{1/0.33})^{0.33}]^2. \tag{3.90}$$

Because the permeability of rock is considerably higher than that of the bentonite buffer, the relative permeability of gas for rock is set to unity.

The respective dynamic viscosities of liquid and gas are assumed to be temperature dependent as given by [43] in the following way

$$\mu_{\mathrm{l}} = 2.1 \cdot 10^{-6}\,\frac{\mathrm{kg}}{\mathrm{sm}} e^{\frac{1808.5\ \mathrm{K}}{T}}, \tag{3.91}$$

$$\mu_{\mathrm{g}} = 1.48 \cdot 10^{-6}\,\frac{\mathrm{kg}}{\mathrm{sm}} \frac{\sqrt{T/(1\ \mathrm{K})}}{(1+(119.4\ \mathrm{K})/\mathrm{T})}. \tag{3.92}$$

For diffusivity of the vapor-air mixture the following simple experimental relation

$$D = D_{\mathrm{ref}}(T/T_{\mathrm{ref}})^{\alpha} \tag{3.93}$$

[109] is used.

3.3.4 Thermal parameters

For Almerian (Febex) bentonite the following respective forms of specific heat of solid and thermal conductivity [34] are used

$$c_{\mathrm{s}}^{v} = c_{\mathrm{s}}^{v}(T) = 1.38\frac{\mathrm{J}}{\mathrm{kgK}^2}(T-273.15\ \mathrm{K}) + 732.5\frac{\mathrm{J}}{\mathrm{kgK}}, \tag{3.94}$$

$$\lambda = \lambda(\chi) = \lambda_{\mathrm{sat}} + (\lambda_{\mathrm{dry}} - \lambda_{\mathrm{sat}})/(1+e^{(\chi-\chi')/dx}), \tag{3.95}$$

where λ_{dry} and λ_{sat} are thermal conductivities for dry and fully saturated medium, respectively, χ' is the saturation for which the thermal conductivity is the average value between the extreme values, and dx is a parameter. The specific heat of the mixture for Almerian bentonite is approximated by $(\rho c)_{\mathrm{eff}} \approx \rho_{\mathrm{l}} c_{\mathrm{l}}^{v} + \rho_{\mathrm{dry}} c_{\mathrm{s}}^{v}$.

Table 3.2: Reference values and common literature parameters.

$\hat{B}_0$	$1.01 \cdot 10^5$ Pa	M_v	0.018 kg/mol	D_ref	$0.216 \cdot 10^{-4}$ m^2/s
T_0	20+273.15 K	M_a	0.029 kg/mol	T_ref	273 K
ζ_0	0.023	c_v^p	$1.87 \cdot 10^3$ J/(kgK)	α	1.8
l_0	$2.45 \cdot 10^6$J/kg	c_l^p	$4.18 \cdot 10^3$ J/(kgK)		
$\tilde{\rho}_\mathrm{l}$	998 kg/m^3	R	8.314 J/(molK)		

The respective relations for MX-80 bentonite [17] are the following

$$c_\mathrm{eff} \approx \frac{\rho_\mathrm{s} c_\mathrm{s} + \rho_\mathrm{l} c_\mathrm{l}}{\rho_\mathrm{s} + \rho_\mathrm{l}} = \frac{c_\mathrm{s} + c_\mathrm{l} w}{1 + w} \approx \frac{800 \frac{\mathrm{J}}{\mathrm{kgK}} + 4200 \frac{\mathrm{J}}{\mathrm{kgK}} w}{1 + w}, \tag{3.96}$$

$$\lambda = \lambda(\chi) = \sum_{i=0}^{6} \lambda_i \chi^i. \tag{3.97}$$

The values of the thermal conductivities of the bentonite materials are given in Table 3.3.

For rock the specific heat c = $1.0 \cdot 10^3$ J/(kgK) and thermal conductivity $\lambda = 3.0$ W/(Km) are taken as constant representative values from the literature [2].

3.3.5 Initial values

From our modelling perspective the composition of the porous medium is determined by the proportions of the solid material, its porosity and the water content. In the literature this information is usually given by means of dry density and gravimetric water content. The needed initial values for our model, i.e., porosity and saturation degree can be obtained when the mineral density is known. The given values are $\tilde{\rho}_s = 2700$ kg/m^3 [34] for Febex bentonite and $\tilde{\rho}_s = 2780$ kg/m^3 [13] for MX-80 bentonite. The dry density and, especially, the water content has varied considerably in the used experiments. The initial values for the considered experiments are collected in Table 3.4.

Table 3.3: Thermal conductivity parameters for the bentonite materials.

Febex	λ_{sat} [W/(Km)]	λ_{dry} [W/(Km)]	χ' [-]	dx [-]
	1.28	0.57	0.65	0.1
MX-80	λ_0 [W/(Km)]	λ_1 [W/(Km)]	λ_2 [W/(Km)]	λ_3 [W/(Km)]
	0.29992	-0.22103	-1.27634	16.40662
	λ_4 [W/(Km)]	λ_5 [W/(Km)]	λ_6 [W/(Km)]	
	-23.14611	8.44418	0.793	

Table 3.4: Initial values in the simulated experiments.

Material	Experiment	ρ_{dry} [kg/m^3]	w [-]	η [-]	χ [-]
Febex	HM	1650	0.133	0.41	0.54
	THM	1660	0.118	0.40	0.49
	In-situ	1600	0.144	0.42	0.54
	Mock-up	1770	0.136	0.36	0.66
MX-80	CEA & SKB	1570	0.170	0.44	0.61
Rock	'In-situ'	2660	-	0.007	0.99

Chapter 4

Review of the theory

4.1 General

In this section some interesting key issues of the presented theoretical approach are reviewed and discussed. In connection with the literature a special emphasis is given to the *State of the art report* by Villar [115]. This is because of the following reasons.

- To the authors knowledge, the Spanish research program represented by Villar from the experimental point of view is the most comprehensive disposal oriented bentonite program available.
- The report [115] gives a very thorough picture of the coupled behaviour of bentonite based on experimental evidence to which any theory should be compared.
- The open questions stated by Villar in [115] are related to the wetting of the bentonite buffer in disposal conditions, and to which this Thesis gives further knowledge.

4.1.1 The key issue: buffer resaturation in repository conditions

The buffer resaturation in realistic disposal conditions is the key issue of the current thesis. In this respect we adopt a direct reference to the following statement given by Villar.

According to Villar [115], it is expected that full saturation of the buffer is reached before the fading out of the thermal gradient. However, for Villar it remained unclear whether the high temperatures around the canister would

hinder the full saturation to the inner part of the barrier or just delay it, but this seems to closely depend on the actual temperatures reached in the barrier and on its thickness. In the 1-year test performed at Äspö for the LOT Project the bentonite barrier 10 cm thick had reached almost full saturation, the temperature during the test being below 90 °C. On the contrary, at the BCE test performed at Lac du Bonnet (Canada), the areas of the buffer (whose thickness was 25 cm) adjacent to the heater had a water content below the initial one after 2.5 years of heating. In the Febex in-situ test the water content of the bentonite close to the heater increased after intense initial drying, but was still below the initial value after five years. In this case the surface temperature of the heater was 100 °C and the thickness of the bentonite barrier was 65 cm.

The effect of a thermal gradient on the kinetics of hydration has been studied in laboratory tests in which a 40 cm long column of compacted Febex bentonite is hydrated under thermal gradient and at isothermal conditions. [115]

4.1.2 Open questions given by Villar [115]

According to Villar [115], with respect to the barrier saturation there are two key questions to understand and model the time to reach full saturation and the evolution in the final stages:

1. The repercussion of the thermal gradient on saturation, especially for high temperatures. Experimental results confirm that saturation is delayed when a thermal gradient exists, especially if the temperatures reached in the barrier are higher than 100 °C. It remains unclear if full saturation would be hindered up to dissipation of the thermal gradient.

2. The possible existence of a hydraulic gradient threshold, which would prevent the movement of water in the final stages of the repository, when suction is very low and the only driving force is the hydraulic pressure.

4.1.3 A response to the open questions

The main purpose of the buffer is to contribute to the isolation of the disposed containers from the groundwater. In this respect it is most important to get information on hydraulic behaviour of the buffer, especially, on the evolution of the resaturation and the final steady state.

According to Villar [115], the water movement in porous medium is governed by the classical Darcy law driving the water by means of a head gradient. The main hydraulic properties are the hydraulic conductivity and the water retention capacity, i.e., suction-water content relation. [115]

The model of the current thesis has a fundamental difference in relation to the hydraulic properties, i.e., Darcy law driven flow and the retention, emphasized by Villar. The approach yields a different kind of retention relation by which the energy state, and consequently the suction, is described straightly as a function of the composition and the deformational state of the system. This also affects the flow equations for which the traditional Darcy law is replaced by a more sophisticated relation (3.74) in which the volumetric flow of water depends also on the gradients of the water content and porosity. These theoretical differences also yield simulation results that differ from the expectations stated by Villar [115]. Especially, the reduction of the wetting rate observed during the large scale Febex mock-up and in-situ tests is a natural consequence of the approaching of an unsaturated steady state predicted by the current model. Instead of this, Villar [115] states that efforts have been put forward on the experimental research of this unexpected behaviour with an assumption that the properties of the material have changed during the experiment. Of course, more detailed experimental knowledge is always welcomed by a theoretical modeller.

What comes to the results of the new experiments described by Villar and given in [115], the hot zone seems not to saturate any more after more than two years of heating.

4.2 On the choices for the thermodynamic potentials

4.2.1 Theoretical and practical requirements

The use of the free energies and the dissipation function constitutes the backbone of the theoretical approach of the current thesis. Obviously, there is no correct set of free energies and dissipation function, but they can be chosen to be *appropriate* in such a way that they meet certain theoretical and practical requirements.

The theoretical validation of the choice is given just prior to the chosen expressions (3.3–3.6). The principle of maximum rate of entropy production is a way of deriving constitutive equations that do not conflict with the entropy inequality. By choosing a non-negative quadratic dissipation function the entropy inequality is not violated. This is a sufficient theoretical requirement for the dissipation function. Sufficient theoretical requirements for the free energy are strict concavity with respect to temperature and density, and strict convexity with respect to molar volume fractions.

A practical requirement is that the results given by the model are satisfactorily consistent with the observations. Specifically, the chosen free energies yield common forms of internal energy (3.19, 3.20) with an inclusion of the swelling interaction, ideal gas state equation (3.10), Clausius-Clapeyron equations for boiling pressure (3.37) and for partial pressure of vapor (3.36), and the latent heat of vaporization (3.38). Furthermore, the chosen free energies yield a form of suction pressure (3.49) which is compatible with the observations (Figure 6.1), and the chosen free energies and the dissipation function yield sensible flow equations (3.53–3.56). The forthcoming analytical part of the thesis shows the apparent consistency of the simulations and the observations.

To conclude, the choices for the free energies and the dissipation function meet the theoretical and practical requirements, i.e. the choices are appropriate.

4.2.2 The interaction functions

The choice for the interaction functions in the free energy expressions is the core of the current modelling approach. The physical background is that the behavior of the liquid and solid constituents in their mixture differs from that of the free constituents because of their mutual interaction. In particular, liquid does not behave as a fluid inside the porous medium when

it is adsorbed on the solid structure. It behaves like a structured solid and more and more external energy is required to take the liquid out of the porous medium either in mechanical form (i.e. suction) or in thermal form (i.e. heating) when the moisture content of the medium decreases. In addition, the solid structure of a swelling kind of medium is affected by the moisture content. In particular, the volume is increased when the moisture content increases and a swelling stress is encountered if the volume of the solid is restricted.

Actually, there is nothing new in the choice for the adsorption interaction function. Similar expressions have been introduced by, e.g., Fremond [37] and Hartikainen and Mikkola [50] for different materials. The swelling interaction, on the other hand, is a new type of interaction analogical to thermal expansion. The current study and the already published article by the author [61] are the first and crude attempts to capture the moisture swelling behaviour by the free energy expression approach in the limit of small strains.

4.3 Thermo-Hydraulics

One of they key application targets of the model is the wetting behaviour of the repository buffer, the simulation results of which are essentially controlled by the thermo-hydraulic model. As the derived phase equilibrium and the modified Darcy law dominate the thermohydraulics of the model, they constitute the core of the current thesis.

4.3.1 Thermal properties

Theoretically, the list of thermal parameters consists of specific heat, thermal conductivity, and thermal expansion coefficient.

The specific heat depends essentially on the properties and composition of the solid and liquid phases. The dependence on temperature has also been measured for Febex bentonite [34]. It is used also in the current analysis (3.94), although the significance is minor. Note, that the use of temperature dependent specific heat violates the chosen thermodynamical theory assuming constant specific heat (3.3). This error could be overcome by taking the temperature dependence of the specific heat of solid into acocunt in the free energy expression and the consequences of this choice in the thermodynamic potentials. However, as the heat capacity of the buffer does in general have a minor importance this refinement of the model would have negligible practical consequences.

According to Villar [115], the thermal conductivity is the most important parameter to explain heat transport in a bentonite barrier. In homogeneous soils uniformly moist, heat flow may be assumed to be conductive and equal to a thermal conductivity times a temperature gradient, where it is implicitly assumed that thermal conductivity includes the thermal vapour flux induced by the temperature gradient. [115]

However, thermal experiments are not isolated, i.e., thermo-hydraulic couplings like vaporization can not be excluded. A thermal gradient causes vaporization and condensation, and the resulting latent heat affects the results of thermal conductivity measurements. The measured value of this effective thermal conductivity fitted to uncoupled thermal model is not consistent with any coupled thermo-hydraulic model in which the phase change is explicitly taken into account. This is also the case in the current approach and will be further discussed in the analysis part of the thesis.

According to Villar [115], results focused on the thermal influence on volume change behaviour of unsaturated soils have been limited. In the modelling approach of the current thesis any direct influence of the tem-

perature on the mechanical behaviour, e.g. thermal expansion, has been tacitly omitted. It is hard to imagine totally isolated thermo-mechanical experiments in which the hydraulic behaviour with vaporization-condensation and consequential hydro-mechanical behaviour, i.e., swelling and shrinking, do not occur at least locally.

4.3.2 Phase change

A conventional equilibrium condition for a liquid and its vapor is the entropy balance resulting in equal intrinsic pressures, temperatures, and chemical potentials of the liquid and the vapor at their plane interface. From these conditions the conventional Clausius-Clapeyron equation can be derived to give the total pressure of ideal saturated vapor, i.e. the boiling pressure as a function of temperature. Customarily this equation is also used for partial pressure of saturated vapor.

It was shown by Jussila [60] that by considering the equilibrium of the water species in different mixtures the conventional Clausius-Clapeyron equation can be reduced from the general phase change equation (2.44) with the free energy and dissipation function choices (3.3–3.6) for both the total (or boiling) pressure and for the partial pressure of saturated vapor. The derived Clausius-Clapeyron equation (3.37) and the latent heat (3.38) coincide with the conventional equilibrium condition for the boiling pressure $\hat{B}^0$ of ideal vapor if the pressure term is neglected. The derived more general Clausius-Clapeyron equation (3.36) expresses the same functional form for the partial pressure of saturated vapor $(\zeta\hat{B})^0$ among the gaseous phase.

4.3.3 Suction

According to Villar [115], the water retention curve is a fundamental relation to estimate the water content evolution of the barrier. The observed retentions depend on the strain state, i.e., whether the experiment is confined or free, on the initial dry density of the material and on the direction of the process that takes place in the experiment. Generally, the observed suction at a given water content is higher for confined samples, for denser materials and for drying paths. [115]

In the current modelling approach the derived suction pressure (3.49) is a function of the intrinsic properties and the deformational state of the porous medium. This is a modified extension to the approach presented by Frémond and Nicolas [38]. It differs from the conventional approach of using directly the suction pressure given by the Kelvin law (3.48), which does not

take into account the interaction of the mixture components and of using an experimental fit to relate the water content of the porous medium to the relative humidity of the atmosphere with which the porous medium is in equilibrium.

4.3.4 The liquid flow model

In the current modelling approach, according to the derived constitutive law (3.57) the liquid flow is driven by, in addition to the conventional pressure gradient and gravitation, by the gradients of molar volume fraction and temperature. The form resembles generalized Darcy's laws presented by a number of authors. The form suggested by Gray and Hassanizadeh (e.g. [45], [46]) and adopted by Schrefler ([102], [103]) includes a *wettability potential* and liquid saturation gradient. The mesoscopic near equilibrium law presented by Murad and Cushman ([84], [85]) includes a *hydration pressure* and liquid volume fraction gradient, and the macroscopic binary law of Bennethum and Cushman [11] includes a *swelling potential* and liquid volume fraction gradient. In the form presented by de Boer and Didwania [26] the liquid flow is driven by the gradients of liquid volume fraction and apparent density of the liquid. In all of these thermomechanical approaches extensions to the conventional Darcy law are obtained by making the free energy in one way or another to depend on the liquid content of the porous medium. Consequently, the physico-chemical interaction of the solid and liquid phases are taken into account and the liquid flow is made to be driven by the gradients of the volume fractions.

4.3.5 Permeability

According to Villar [115], in any soil, water permeability increases with the degree of saturation. Relative permeability is related to the degree of saturation in accordance with a potential law. Gas permeability decreases as water content increases. The intrinsic permeability depends only on soil structure. Ideally, the intrinsic permeability has the same value for gas and liquid flow. The value is obtained either from gas flow tests in the totally dry soil or from water flow test in the saturated soil, and should be the same. However, if fluid-media interactions alter the medium structure, the intrinsic permeability can be greatly altered. This is the case of expansive soils like bentonite, in which water reacts with clay minerals causing the swelling of the clay lattice, thereby reducing the pore space available for flow. The main factors having a significant influence on the permeability

value are the liquid degree of saturation, the void ratio, the temperature and the salinity of the permeant in the case of liquid fluid. [115]

According to Villar [115], the variation of permeability with the saturation can be obtained by gas permeability tests. The gas permeability is mainly related to the accessible void ratio $\varepsilon(1-\chi)$ with which the observed permeability values show a high correlation. The intrinsic permeability results obtained by means of gas flow and by means of water flow exhibit a drastic difference. The observed values have a difference of about eight orders of magnitude. These observations suggest that fundamental difference in the microstructural arrangement of the saturated and the unsaturated sample exists due to the swelling of the clay as it saturates. During the hydration of the clay at constant volume, the volume occupied by micropores increases, while the volume occupied by macropores decreases. The change in the mean pore diameter available for flow explains the big differences between the values of measured intrinsic permeability for dry and saturated swelling clay. In addition, most of the water in a bentonite saturated under constant volume will be in the interlamellar space, and the water molecules constituting this film will be strongly adsorbed to the clay mineral surfaces leaving only narrow, tortuous interparticle channels for water and ion transportation. Unsaturated permeability can be estimated by a back-analysis of the measurements and by using a theoretical model. As a result the total water permeability is expressed by means of intrinsic permeability depending on the dry density, and the relative permeability depending on the saturation degree, and on the temperature dependence of the liquid viscosity. The effect of temperature on water viscosity and the effect of pore volume on intrinsic permeability allow to explain the different infiltration velocities observed in the tests performed under different temperatures and with different dry densities. [115]

In the current modelling approach the experimental temperature dependencies of free fluid viscosities (3.91, 3.92) are applied. For water this is highly questionable because the viscosity of the water inside expansive soil is totally different from that of free water.

In the approach of the current thesis the interaction of the micro and macroporosity have not been taken into account. For this reason there is no sense of assigning any porosity dependence to the intrinsic permeability. Instead, a constant value k_{sat} is used (3.87). Because the Darcy law is an extension of the traditional one that is expected in the coupled experiments, the absolute constant value is not the same and does not necessarily have the same interpretation. For the same reason any artificial tortuosity factors are neglected.

For the relative permeability of liquid $k_{\mathrm{l,rel}}$ (3.88) similar expression as suggested by Villar [115] is used and the exponent is fitted to the experiments.

For the relative permeability of gas $k_{\mathrm{g,rel}}$ there are various relations used in the literature (e.g. [108], [42], [40], [91], [87]). However, according to the performed simulations it seems that the permeability of gas has to be a lot higher than that of liquid in order to avoid build-up of high gaseous pressure that prevents vaporization near a hot heater. Consequently, a simple constant high value of $k_{\mathrm{g,rel}}$ is used in the simulations. According to Villar [115], the intrinsic permeability measured by gaseous flow experiments is about eight orders of magnitude higher than for liquid flow. For this reason the variation of plausible value of $k_{\mathrm{g,rel}}$ among different experiments has to be high. This is one of the most uncertain parameter values in the model and its variation has significant influences on the results. The influence, however, is physically reasonable. In the simulation of the thermal experiments, decreasing of the permeability increases the gaseous pressure and decreases the drying induced by vaporisation.

4.4 Hydro-Mechanics

In the current modelling approach the emphasis has been on the thermo-hydraulic behaviour while the mechanical behaviour and the swelling are incorporated by a crude approach. In particular, a proper description of the mechanical behaviour of expansive clay requires the incorporation of the microstructure. In fact, many details of the coupled behaviour of bentonite originate from the interplay of the micro and macro structural levels of the bentonite [41], [115], [71].

4.4.1 Mechanical properties

According to Villar [115], the main mechanical properties of expansive soil in addition to the compressive and tensile strength which affects the behaviour of blocks during construction, are swelling, compressibility, and elastic shear modulus. The main factors affecting the expansion of a soil may be divided into three groups: 1) intrinsic properties of the particles and the condition of the soil mass: type of clay mineral and its proportions, dry density, water content, the orientation of the particles and the type and quantity of cation adsorbed, 2) composition and properties of saturation water, 3) external factors: soil stress history, temperature and the availability of water. [115]

The swelling capacity of a material may be indicated by two parameters: the swelling pressure developed under confined conditions and the expansion upon saturation. The swelling capacity and the swelling pressure of a bentonite depend greatly on its content of smectite and the type of adsorbed cations. The increase of the dry density rises the swelling deformation of the bentonite exponentially and the swelling pressure, although the increase of the former is not as remarkable. Conversely, the swelling pressure of Febex Ca-bentonite does no seem to be affected by the initial water content of the clay. On the contrary, the swelling deformation for a particular dry density after saturation under a fixed vertical stress decreases with the initial water content of the clay.

On the other hand, the kinetics of the development of the swelling pressure is not well known. According to experiments, the development of the swelling pressure in pellets/powder mixtures shows three phases: a first one with a quick swelling pressure increase, a second one with either a quasi-constant level or even a decrease of the swelling pressure, and the last one with a new increase of the swelling pressure. The interaction between micro and macrostructure accounts for this pattern. At saturation and for equal density, precompacted samples and pellets/powder samples display the same

swelling pressure. [115]

To the authors knowledge, this kind of dynamic swelling behaviour is due to two macroscopic factors:

1. The mechanical properties of the swelling material depend on its composition, e.g., water content and dry density. Because of this the local behaviour of the material changes during the wetting process when the local moisture content and porosity change. In particular, the initially very stiff and dry bentonite becomes considerably softer when wetting and expanding. The explanation for the change of mechanical behaviour during wetting is due to the intrinsic changes of the sample. This has to occur in the way explained by Villar [115], i.e., by the interaction of the two structural levels of the material. In particular, the softening while wetting has to be due to the increasing collapsibility of the macropores.

2. The wetting of the macroscopic sample does not occur simultaneously at every point of the sample. Consequently, the observed swelling pressure development depends on the location of the observation point especially for large samples. More specifically, a typical arrangement is an oedometric experiment in which the wetting is applied from the bottom boundary while the vertical total stress is measured or controlled on the top boundary.

As a consequence of these two macroscopic factors, the authors interpretation for a typical evolution of a confined swelling pressure experiment is the following.

1. The wetted lower portion of the sample starts to swell. To conserve the total volume the upper portion has to shrink. The expanding lower portion becomes softer and the shrinking upper portion becomes stiffer. The rate of increase of vertical total stress at the upper portion is high.

2. The wetting intrudes to the central portion of the sample which starts to swell. Consequently, to conserve the total volume other portions of the sample have to shrink. The already shrunken and stiff upper portion does not shrink any more. Instead, the swollen and softer lower portion has to shrink. The change of vertical total stress at the upper portion decreases, stops or is even reversed.

3. The wetting intrudes to the upper portion of the sample which starts to swell. To conserve the total volume other portions have to shrink. The final deformation profile approaches the initial zero profile. The rate of change of vertical total stress at the upper portion increases again before the approaching of the steady state of maximum stress.

The mechanical interaction of the two structural levels of bentonite yields local plastic behaviour observed at the macroscopical level. This behaviour can not be accounted for by the simple elastic small deformation approach of the current thesis. However, the approach of assuming the bulk modulus to depend on the composition of the material (3.84) does yield simulational results that reproduce the corresponding observations in a satisfactory manner (see e.g. Figure 7.7). It must be emphasized, however, that the model can not be applied to large deformations.

Villar [115] attributes the water content dependence to dependence on suction. In the current approach the system behaviour is described by means of the chosen state variables. Suction is not a state variable but it can be defined by means of the state variables, especially the material composition, i.e., solid and liquid volume fractions, and by means of the deformational state.

According to Villar [115], one of the main external factors affecting the volume change behaviour of the bentonite is the availibility of water, which in turn is related to the suction level. The swelling pressure depends greatly on the suction level and it sharply increases as suction decreases, especially at the beginning of hydration, when suction is high.

This statement of Villar seems to be in contradiction to the previous one stating that the swelling pressure does not depend on the initial water content. Most likely Villar has meant that in a confined experiment for highly compacted clay the maximum swelling pressure at full saturation depends on the dry density and not on the initial saturation. This is expected in highly compacted clay in which the macroporosity has disappeared in fully saturated state. The unsaturated swelling pressure, however, and its development depend greatly on the initial saturation (or initial suction).

4.4.2 On the parameters of elasticity

In the current modelling approach the shear and bulk moduli introduced in the solid component free energy (3.3) are that for the solid component without any consideration to the other mixture components or boundary conditions leading to the stress-strain relation (3.72). Such use of the moduli

is questionable because of the assumption of incompressible grains. When the other components vanish the relation reduces to $\boldsymbol{\sigma} = 2G\boldsymbol{\epsilon}^D + K(\mathrm{tr}\boldsymbol{\epsilon})\mathbf{I}$ suggesting that G and K are the intrinsic moduli of the solid phase. Ideally, if such values could be measured they should be used for the model with the respective effective moduli of the skeleton as $\xi_\mathrm{s}G$ and $\xi_\mathrm{s}K$. In practice, however, the applied situation with porosity $\eta = 1 - \xi_\mathrm{s} \approx 0.4$ is far from the pure solid phase and the actual effective modulus of the skeleton is considerably smaller than the value of $\xi_\mathrm{s}K$ obtained by the bulk modulus of the solid grain K. Consequently, the effective parameters $\xi_\mathrm{s}G$ and $\xi_\mathrm{s}K$ that are actually used in the model have to be merely considered as average characteristics of the solid skeleton in the vicinity of the applied situation.

In soil mechanics it is common to define various elasticity parameters depending, e.g., on the prevailing hydraulic or chemical boundary conditions. In our approach, however, this is not appropriate because the system is described by means of its free energy, which is a function of the state of the system. The state, on the other hand, is a *response* of the system to the external loads and boundary conditions and not a *function* of them. Consequently, the system parameters can not depend on the boundary conditions.

4.4.3 On the swelling model

In the current modelling approach the derived swelling pressure equations (3.51) and (3.52) express the wetting of a small volume element or a theoretical idealized situation in which a small sample is homogeneously wetted at its every material point simultaneously. In practise, a sample is wetted by flooding it at one of its boundaries or by forcing air of controlled moisture content to flow through the sample. This means that, in reality, wetting of a sample always penetrates the sample from a certain direction. Consequently, local swelling at the wetting front and possible local shrinking at the drier portion of the sample occur even if the total volume of the sample would be kept constant. For this reason the equations (3.51, 3.52) do not give the actual total swelling pressure of a macroscopic sample. In our crude approach the only needed swelling parameters are the maximum constant volume swelling pressure Π^v_max and the theoretical maximum void ratio ε_max at a fully swollen state. The maximum swelling pressure is simply taken as the observed average value. The exact value of the maximum porosity is actually not very important because we are limited to small deformation at the close vicinity of the initial volume far from the fully swollen state. In contrast to this rather trivial choice for the swelling parameters the values for the other mechanical parameters, i.e., the elasticity parameters involved

in (3.84–3.86) are chosen by means of the dynamic simulations of hydro-mechanical oedometer tests.

4.5 Salinity

According to Villar [115], the type of water used as a permeating agent, and especially its salinity, may have an impact on the coefficient of permeability of a soil due to various mechanisms. However, the effect of salinity on the hydraulic conductivity of the compacted saturated bentonite is not very important, while the effect on the unsaturated permeability of less expansive granite/bentonite mixtures is more significant. The swelling pressure decreases with the saline content of the solution. However, for montmorillonite compacted at high density the influence of the salinity of the water on the value of the swelling pressure is negligible. Additionally, the type of exchangeable cations in the exchange complex has an influence on the effect of salinity on swelling properties. [115]

The solutes in the saturating water are not taken into account in the modelling approach of the current Thesis. The inclusion of the solutes would be straightforward as has been done by Hartikainen and Mikkola [51] by taking them as new mixture components having the same volume fraction as water. However, the extended model would not take into account the details of the physico-chemical interaction of the solutes and the solid mineral at the microscopic level. Instead, the inclusion of the solutes would lead merely to a modification of the adsorption and swelling parameters of the current model. As the solutes are significant and saline or brackish water is encountered in the real coastal disposal sites, this kind of extension of the current approach would be interesting and useful.

Part II

Analysis

Chapter 5

Numerical implementation with ELMER

In the numerical implementation of the model the author has relied on the expertise of Finnish IT Center for Science (CSC). The model was implemented using the Finite Element Method (FEM) software ELMER [23], which has been developed by CSC. The particular version of the code to solve the model introduced in the previous chapter was written by Juha Ruokolainen at CSC. The following description of the numerical implementation is a moderate extension to the information given by Jussila and Ruokolainen [61].

FEM was used to solve the system of equations (3.62–3.71). The equations for gaseous pressure, saturation, temperature and vapor fraction (3.63, 3.64, 3.66, 3.71) were solved strongly coupled using one matrix equation. The solid mass conservation equation for porosity (3.62) was solved separately, as was the Navier equation for displacement (3.65). In addition, a field variable representing the relative volume change $\mathrm{tr}\boldsymbol{\epsilon}$ was solved separately using the previously obtained displacement field. This variable was used then in the water mass conservation equation (3.64) where $\nabla \cdot (\nabla(\mathrm{tr}\boldsymbol{\epsilon}))$ is needed via (3.74).

For the integration in time the first order method from the Backward Differences Formulaes (BDF) family of methods was used. This method may be written as

$$\left(\frac{1}{\Delta t}\mathsf{M} + \mathsf{K}\right)\left(X^{i+1} - X^{i}\right) = F^{i+1}, \tag{5.1}$$

where Δt is the size of the time step, M is the time derivative coefficient matrix, K contains the spatial derivative terms and the reaction terms, F

is the right hand side vector, and X the solution vector. The superscript indicates the time step. The method is fully implicit and absolutely stable, so that large time steps may be used. The loose coupling of the different systems of equations might restrict the size of the time steps, though.

Each strongly coupled system of nonlinear equations was solved using Newton iteration. The different sets of equations were solved using sequential iteration: within a time step each equation for a set of field variables was solved sequentially, using the newest available values for the other field variables, until convergence of all sets of equations reached the predefined tolerance

$$2|(||X_{i+1} - X_i||)/(||X_{i+1}|| + ||X_i||)| < \epsilon, \tag{5.2}$$

where the subscript indicates the sequential iteration number within the time step.

Galerkin FEM was used to discretize all the equations besides the solid mass conservation (3.62) for which a stabilized formulation was used [36], [35].

All the linearized and discretized matrix equations were solved using the Biconjugate Gradient Stabilized (BiCGStab) method. This is an iterative linear system solving method from the family of Krylov subspace iteration methods [4]. An Incomplete LU decomposition (ILU) was used as a preconditioner for the iterative method.

Chapter 6

General scheme

6.1 The simulated materials

The model is applied to the simulation of two bentonite materials that are under consideration and studied for disposal purposes - Febex type bentonite from Almeria Spain and MX-80 from Wyoming USA. The materials differ from each other at least by their mineral composition, chemistry, retention, and swelling capacity. From our physically simplistic modelling perspective those materials are quite similar. The main practical difference is that a more comprehensive experimental data are available for Febex bentonite. Mainly for this reason, the majority of the analysis of the current model including a complete set of basic parameter calibration is done for Febex bentonite. The MX-80 analysis is included, despite for completeness, for it is the current reference material in the Finnish and the Swedish disposal plans and it provides also important reference when compared to some key findings of the Febex analysis.

In addition, the model is also applied to the thermo-hydraulic modelling of the host rock in a special case based on the Febex in-situ experiment.

6.2 The parameter fitting

The approach to apply the model to simulations of experiments started with a step-by-step fitting of the parameters. The preliminary phase is the collection of material independent or common literature values (Table 3.2). Also, certain material specific parameters may be expected to be model independent enough so that experimental values found in the literature for the same material can be used. This is the case of thermal conductivity and

Table 6.1: Suction and swelling parameters for the considered materials.

	a_1	a_2	$\chi_{\max}$	$\Pi^v_{\max}$	$\varepsilon_{\max}$
Febex	0.2	1.8	0.999	5.0 MPa	0.9
MX-80	0.1	1.6	0.99	8.0 MPa	1.2
Rock	$0.17{\cdot}10^{-4}$	1.3	0.99	0	-

specific heat whose values were given already in the previous chapter.

The parameters for the adsorption function (a_1, a_2, $\chi_{\max}$) and for the swelling function ($\Pi^v_{\max}$, $\varepsilon_{\max}$) can be achieved without any numerical simulation. The adsorption function parameters are adjusted by fitting the theoretical confined suction pressure (3.50) to the corresponding experimental retention curve. Figure 6.1 illustrates the confined suction pressure as a function of saturation (3.50) and the corresponding experimental fit for three different materials considered in this work. The experimental data can be found at [34] for Febex bentonite, at [95] for MX-80 bentonite, and at [2] for Grimsel rock. The swelling function parameters are merely taken as the average confined fully saturated swelling pressure of the given material and the porosity (or void ratio) of a freely expanded sample. The needed values for the suction and swelling interaction parameters for the three materials are given in Table 6.1. The remarkable difference in the suction ability between bentonite and rock can be seen in the value of the parameter a_1 determining the magnitude of the adsorption interaction, which is four orders of magnitude smaller for rock than for bentonite. Although the maximum void ratio is physically a very clear parameter its value for the bentonite materials is not taken as strictly correct. This is because we are dealing with a swelling interaction in the close vicinity of the initial volume which is very far from the maximally swollen state. Accordingly, the absolute value of the parameter is not very meaningful in the model either.

After this preliminary fitting the sequential approach of fitting the rest of the parameters is the following.

1. The mechanical parameters K_{init}, υ, and b are adjusted by means of small scale hydro-mechanical laboratory experiments for Febex bentonite. The four chosen combinations for the parameters are given in Table 7.1. For MX-80 bentonite not any corresponding experiments were found. Consequently, the base case values of the mechanical parameters of Febex bentonite were used for the analysis of the MX-80 bentonite.

2. Hydraulic parameters k_{sat}, $k_{\text{l,rel}}$, and $k_{\text{g,rel}}$ are adjusted by the small

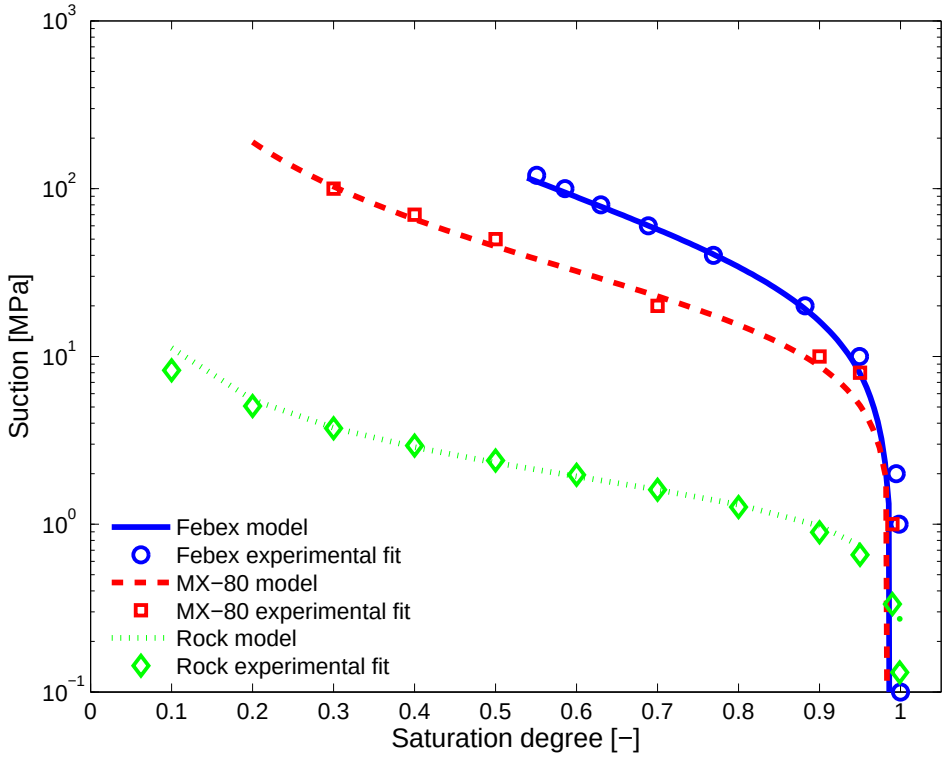

Figure 6.1: The confined suction pressure as a function of saturation (3.50) and the corresponding experimental fit for three different materials considered; Febex bentonite [34], MX-80 bentonite [95], and Grimsel rock [2].

scale thermo-hydro-mechanical laboratory experiment. The three chosen values for each of these parameters for Febex bentonite are given in Table 7.2.

In practice, the sequence has not been linear but rather iterative. Validation of the Febex parameters is done by the large scale mock-up and in-situ experiments.

Chapter 7

Analysis of Febex bentonite

7.1 General

FEBEX is a demonstration and research project, which has been being carried out by an international consortium led by the Spanish agency ENRESA and has simulated components of the engineering barrier system in accordance with the ENRESA's Deep Geological Disposal reference concept. The project has included tests on three scales: an in situ test at full scale in natural conditions (Figure 7.1); a mock up test at almost full scale in controlled conditions (Figure 7.2); and a series of laboratory tests to complement the information from the two large-scale tests. [2], [34], [47], [74].

The Febex project represents the top in the field with a systematic arrangement of versatile and exhaustive experiments at different scales along with a wide co-operation of experts on different experimental and theoretical fields.

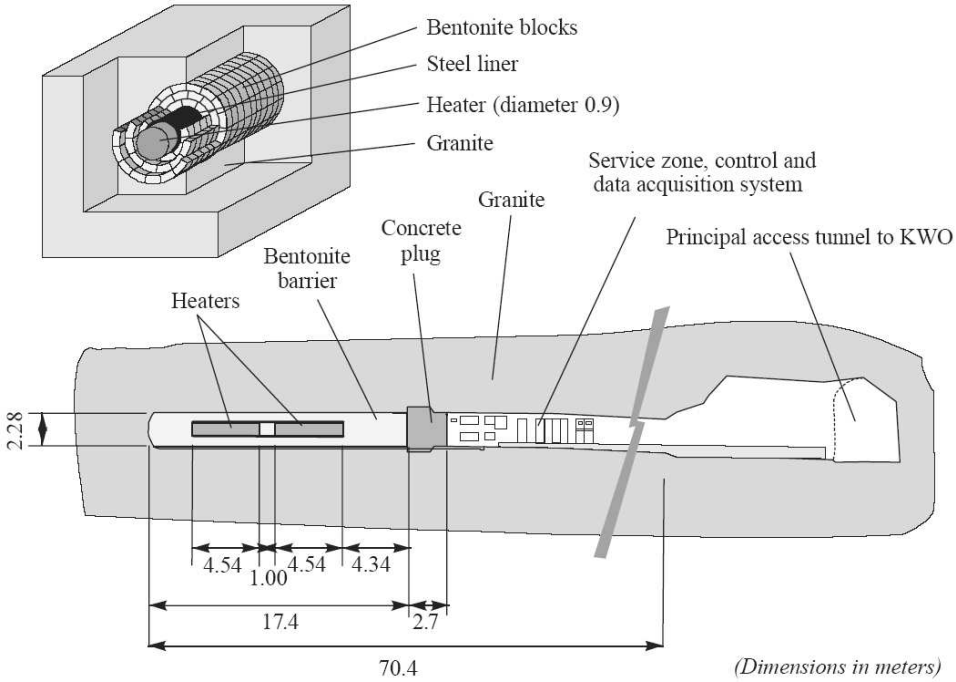

Figure 7.1: Layout of the Febex in-situ experiment [115].

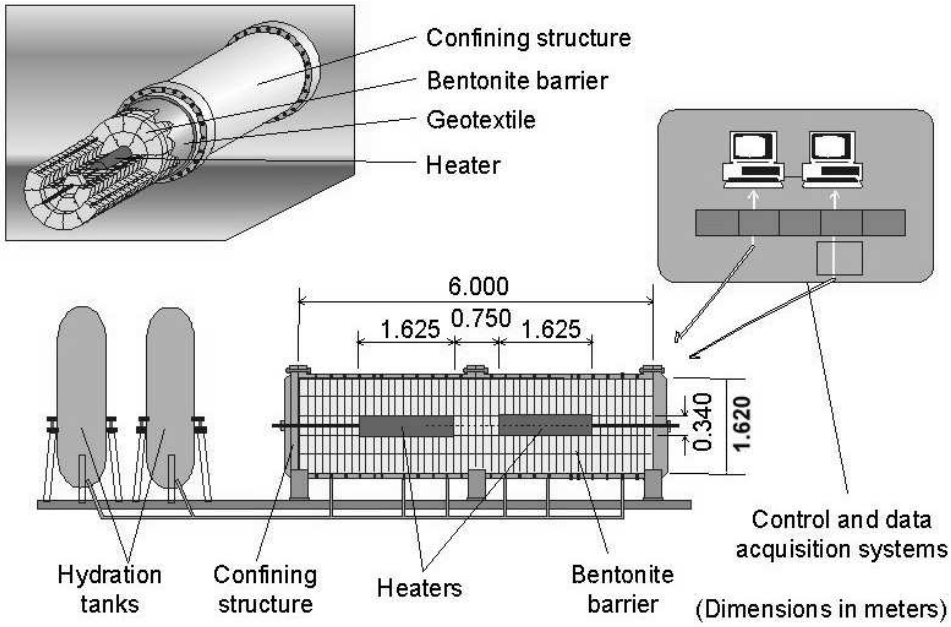

Figure 7.2: Layout of the Febex mock-up experiment [47].

7.2 Hydro-mechanical laboratory experiments

7.2.1 General

A large amount of suction controlled oedometer experiments has been performed for the Almerian (Febex) bentonite [112], [113], [34], [93], [72]. The experimental set-up presented in [93] is illustrated in Figure 7.3. In the experiments volume change of small cylindrical samples has been measured while suction and vertical load have been controlled. The suction has been applied either by controlling relative humidity of the atmosphere in the high

Table 7.1: The elasticity parameters in the simulation of the HM and THM experiments for Febex bentonite.

CASE	b [-]	K_{init} [GPa]	υ [-]	comment
M1	2	0.48	0.25	-
M2	2	0.58	0.35	BASE CASE
M3	2	0.66	0.40	-
M4	1	0.75	0.25	special case

Table 7.2: The hydraulic parameters in the simulation of the HM and THM experiments for Febex bentonite.

CASE	k_{sat} [m^2]	$k_{\mathrm{l,rel}}$ [-]	$k_{\mathrm{g,rel}}$ [-]
lower variant	$1.9{\cdot}10^{-21}$	χ^2	10^3
base case	$2.1{\cdot}10^{-21}$	χ^3	10^5
upper variant	$2.3{\cdot}10^{-21}$	χ^4	10^7

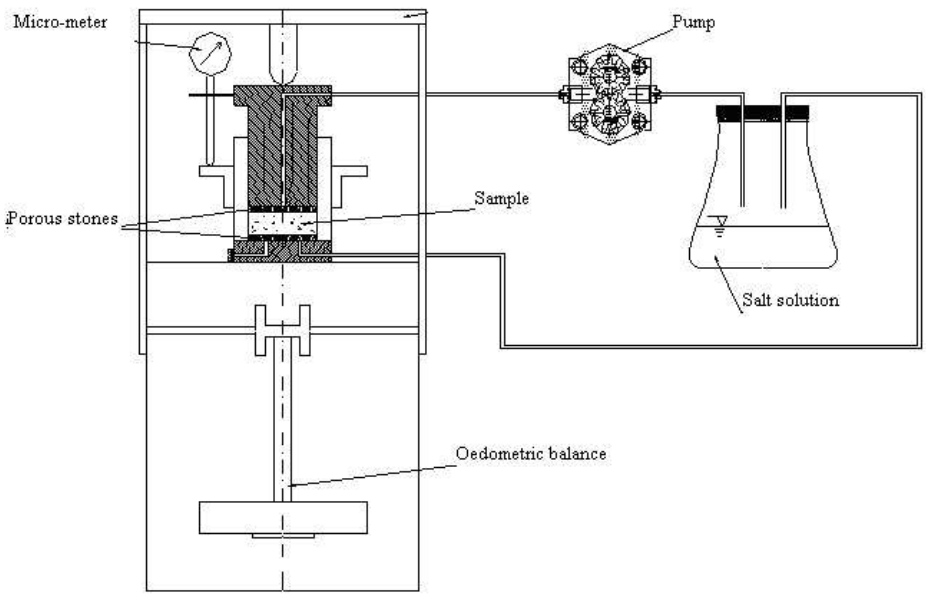

Figure 7.3: The set-up for the HM experiment. Modified after [93].

suction range, by applying an axis-translation technique using nitrogen as the gas fluid in the low suction range, or by flooding the sample to achieve a fully saturated condition. Four of the experiments performed at the Technical University of Catalonia (UPC) corresponding to different paths of evolution of the buffer, and denoted by trajectory 2, 3, 6, and 7 [93], respectively, have been chosen for the calibration of the hydro-mechanical part of the current model. The choice is based on the relatively small strains involved and on the suitable average values of initial dry density (1650 kg/m^3) and expected maximum swelling pressure (5 MPa). All of the trajectories have a hypothetical counterpart in a buffer surrounding a waste container in a geological repository hole as follows.

- Trajectory 2 represents a point of the buffer near the hot container encountering heat induced drying followed by loading by the increasing swelling pressure from the outer regions of the buffer, and subsequent wetting under high constant load.
- Trajectory 3 represents a point near the rock wetting under increasing load.
- Trajectory 6 represents a point in the middle of the buffer encountering compression due to the swelling of the outer buffer followed by wetting under high constant load.
- Trajectory 7 represents an alternative point in the middle encountering drying followed by wetting under increasing load.

The changing of the hydraulic and mechanical loads have been applied in a stepwise manner. The measurements for each phase of constant load and suction have involved several or dozens of days until an achievement of a steady state.

The 2-dimensional axially symmetric domain (Figure 7.4a) with radius of 2.5 cm and height of 1.5 cm was meshed (Figure 7.4b) with 126 nodes and 104 quadrilateral elements. Calculations for each phase of constant load and suction involved from 9 to 16 time steps of variable size. Generally, a time span of 10 to 20 days was found to be enough to achieve a steady state for each individual phase. The constant temperature was $T = T_0$ and the initial values were

$$\{\eta, \chi, \hat{B}, \mathbf{u}\}_{\text{init}} = \{0.41, 0.54, \hat{B}_0, \mathbf{0}\}. \tag{7.1}$$

The applied vertical load $\boldsymbol{\sigma}_{\text{V}}(t)$ at the top and the applied suction $p_{\text{c}}(t)$ at the top and the bottom were known. At the boundaries $\partial\Omega_{2,4}$ (Figure 7.4a)

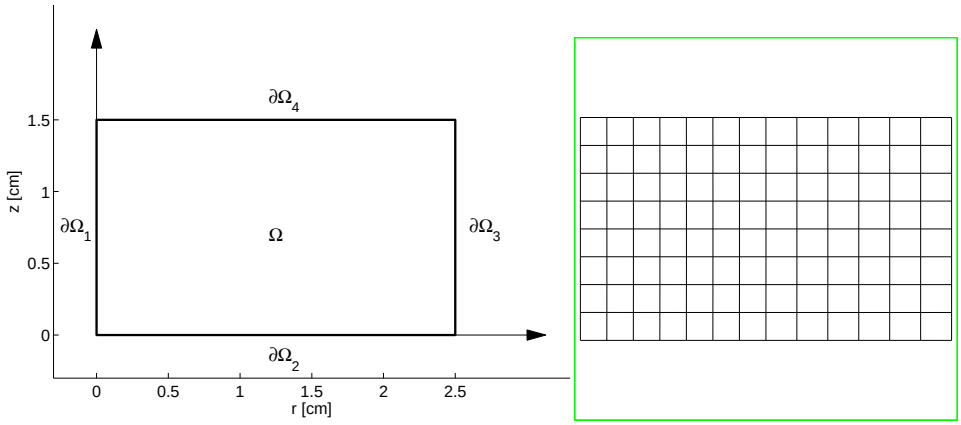

a) HM geometry. b) HM mesh.

Figure 7.4: a) The axially symmetric 2-dimensional domain for the HM simulations along with the boundary notations. b) The corresponding mesh with 126 nodes and 104 quadrilateral elements.

the vapor fraction was set to be compatible with the conventional Kelvin law and the saturation degree was forced to satisfy the Clausius-Clapeyron equation (3.71). The boundary conditions (Figure 7.4a) were the following.

$$\begin{aligned} \mathbf{u}\cdot\mathbf{n} = 0 \quad &\text{on} \quad \partial\Omega_{1,3}, \\ \chi = \chi(\mathrm{tr}\boldsymbol{\epsilon}, \eta, \zeta, t),\ \hat{B} = \hat{B}_0,\ \mathbf{u}\cdot\mathbf{n} = 0,\ \zeta = \zeta(p_c, t) \quad &\text{on} \quad \partial\Omega_2, \\ \chi = \chi(\mathrm{tr}\boldsymbol{\epsilon}, \eta, \zeta, t),\ \hat{B} = \hat{B}_0,\ \boldsymbol{\sigma} = \boldsymbol{\sigma}_\mathrm{V}(t),\ \zeta = \zeta(p_c, t) \quad &\text{on} \quad \partial\Omega_4. \end{aligned}$$

The applied load $\boldsymbol{\sigma}_\mathrm{V}(t)$ for the trajectory 3 is approximated from the figure found in [94] and illustrated in Figure 7.5. For the trajectories 2, 6, and 7 the applied loads were simpler and approximated by a constant value for each phase. These values are presented in the result Figures 7.6–7.9.

7.2.2 Results

The main results are the relative changes of volume against the applied vertical load or applied suction. The values are the final values achieved at the end of each phase. Here the deformation is defined as the relative change of volume with respect to the volume achieved after the initial stabilization phase. The initial phase of all the simulations was a stabilization of the sample with a moderate suction of $p_\mathrm{c} = 122 \ldots 146$ MPa and a nominal vertical load of $\boldsymbol{\sigma}_\mathrm{V} = 0.11 \ldots 0.15$ MPa. The observed results are calculated

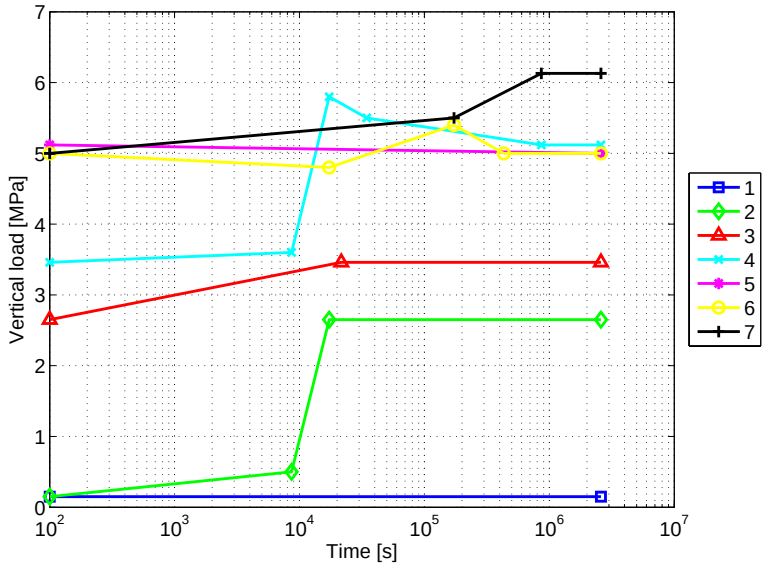

Figure 7.5: Evolution of applied vertical load for trajectory 3. Approximation of the graph given in [94]

by the void ratios given by Pintado [93] by using equation (2.12) assuming incompressible solid grains. This approach is verified by the fact that both the volume changes and the corresponding void ratios of some of these experiments (but not all of them, though) are given and they are compatible with this choice.

The comparisons of observed and simulated trajectories 3, 6, 7, and 2 for the four mechanical parameter cases M1, M2, M3, and M4 (Table 7.1) are illustrated in Figures 7.6, 7.7, 7.8, and 7.9, respectively.

Details of the deformation evolutions during the individual phases of the experiments for the base case M2 (see Figure 7.7) are presented in Figures 7.10–7.13.

Note that the deformations illustrated in the evolution Figures 7.10–7.13 are with respect to the initial state of the sample. Instead, as stated above, the final deformations illustrated in Figures 7.6–7.9 are calculated with respect to the state achieved after the initial stabilization Phase 1.

Details of the approach of setting the mechanical boundary condition for a swelling cylindrical sample and of calculating the volume change are presented in Appendix 1.

7.2.3 Discussion

Comparison of the base case to the observation

The base case results are presented in Figure 7.7. The simulations for the trajectories 3 and 6 are satisfactorily consistent with the observations. In trajectory 3 the sample swells when wetted until the applied load is set to exceed $\Pi^v_{\max} = 5.0$ MPa causing the partially saturated sample to collapse. After that the volume change during wetting is very small. In trajectory 6 the sample is first compressed under constant suction and increasing load. During the subsequent wetting under a high constant load of 8.3 MPa a small collapse of the sample occurs.

The simulated result for trajectory 7 is less consistent. The simulated desiccation is too small and the subsequent expansion due to wetting and the collapse due to the increasing load are too strong. However, the qualitative behavior is satisfactory, even for the swelling following unloading of the fully saturated sample from 8.08 to 4.16 MPa of vertical load. The simulated result for trajectory 2 is the least consistent. The simulated desiccation and compression are too small. During the subsequent wetting under load phase the simulated expansion and the following collapse are smaller than the measured ones.

On the discrepancies

The softening of clay due to wetting is taken into account by choosing the bulk modulus to be a function of the solid-liquid ratio. This resembles the choice of suction dependence in the state surface approaches (e.g., [88]). In this approach Poisson's ratio is taken as a constant although it is evident that it should also depend on the proportions of the mixture. The approach is rather crude and does not cover the complex interplay of different structural levels of bentonite. However, the simple model seems to simulate the small strain behaviour in the vicinity of the initial state in a satisfactory manner.

The mechanical parameter cases M1, M2, and M3 yielded approximately equal overall results (Figure 7.6–7.8). On the other hand, an alternative value for the exponent b as in case M4 makes the overall result worse. Only the fit for the shrinkage due to drying as in the first phases of trajectories 7 (Figure 7.9c) and 2 (Figure 7.9d) are better for this smaller value of b.

The considered material samples were not completely compacted in which case there exists a significant amount of large pores between the mineral aggregates. This is a source of plastic behavior when large strains are allowed by the experimental set-up. In the model, which is designed for small re-

versible strains, this kind of behavior is not taken into account and the large compression observed for trajectory 2 does not occur in the hydro-mechanical simulation.

From the deformation evolutions (Figure 7.10–7.13) it can be seen that for all the trajectories under the nominal load of the initial stabilization Phase 1 the simulated volume of the sample has considerably decreased. This is because the initial relative humidity of the circulating air is lower than the chosen original relative humidity of the sample which makes the sample to dessicate.

On the contrary, the observed deformations of the stabilization phases of the actual samples have varied between shrinking and swelling. This is because, despite the aim of the set-up, the samples have not been identical. Instead, they have exhibited various initial void ratios and water contents. As the initial state of the current model is fixed, the approach was chosen that the compared deformations are with respect to the stabilized state. The fitting would be more reliable if multiple measurements were available for samples initially as identical as possible.

When compared to the actual experimental set-up the roles of load and response are reversed in the simulational approach. For example, in the experimental set-up for trajectory 3 the mechanical load has been controlled in order to keep the volume as constant as possible. In other words, the boundary condition is changed as a response to the behaviour of the sample. On the contrary, in the simulation the experimentally obtained set-up for the mechanical boundary condition is used. In other words, the response of the sample to the boundary condition is controlled by varying the mechanical parameters of the model.

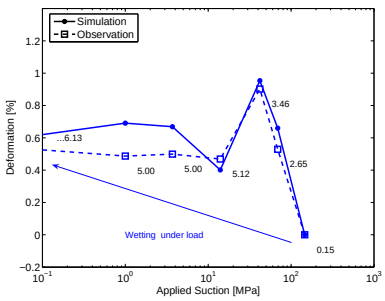

a) Trajectory 3 - 'Near the rock'.

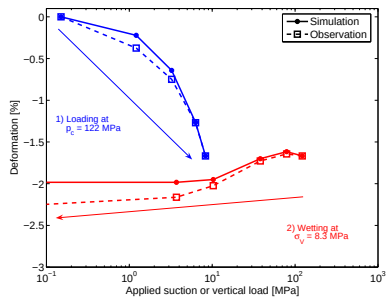

b) Trajectory 6 - 'In the middle'.

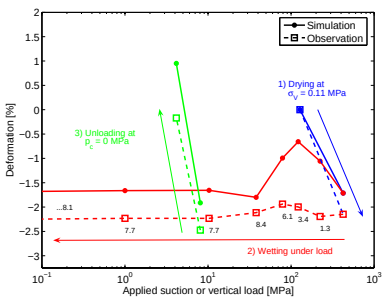

c) Trajectory 7 - 'In the middle'.

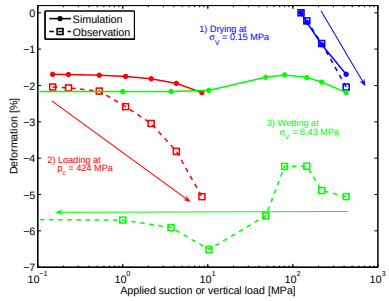

d) Trajectory 2 - 'Near the container'

Figure 7.6: HM experiments 3, 6, 7, and 2. Case M1: $\nu = 0.25$, $K_{\text{init}} = 0.48$ GPa, $b = 2$. The displayed figures beside the wetting under load curves are the applied vertical loads $\boldsymbol{\sigma}_{\text{V}}$ [MPa].

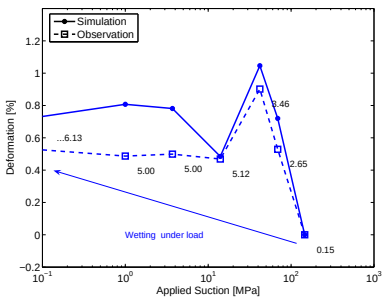

a) Trajectory 3 - 'Near the rock'.

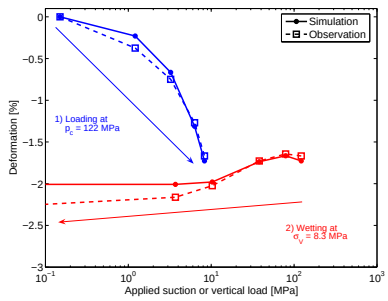

b) Trajectory 6 - 'In the middle'.

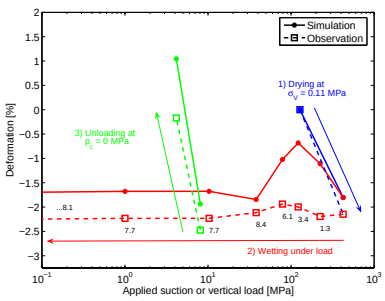

c) Trajectory 7 - 'In the middle'.

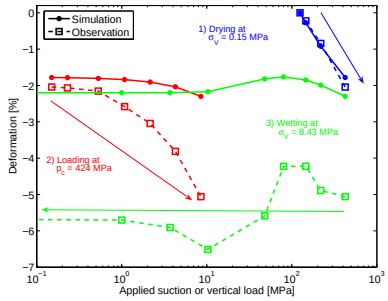

d) Trajectory 2 - 'Near the container'

Figure 7.7: HM experiments 3, 6, 7, and 2. The base case M2: $\nu = 0.35$, $K_{\text{init}} = 0.58$ GPa, $b = 2$. The displayed figures beside the wetting under load curves are the applied vertical loads $\boldsymbol{\sigma}_{\text{V}}$ [MPa].

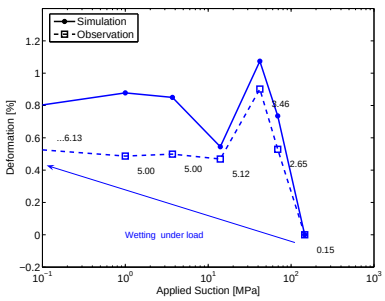

a) Trajectory 3 - 'Near the rock'.

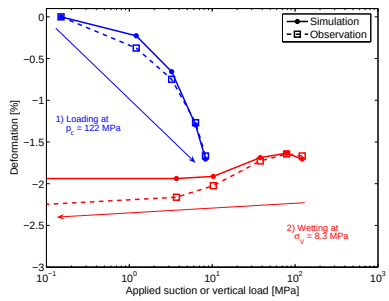

b) Trajectory 6 - 'In the middle'.

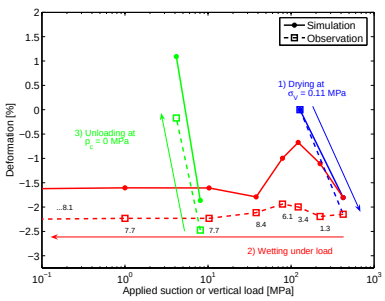

c) Trajectory 7 - 'In the middle'.

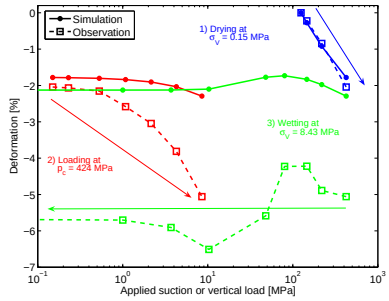

d) Trajectory 2 - 'Near the container'

Figure 7.8: HM experiments 3, 6, 7, and 2. Case M3: $\nu = 0.40$, $K_{\text{init}} = 0.66$ GPa, $b = 2$. The displayed figures beside the wetting under load curves are the applied vertical loads $\boldsymbol{\sigma}_{\text{V}}$ [MPa].

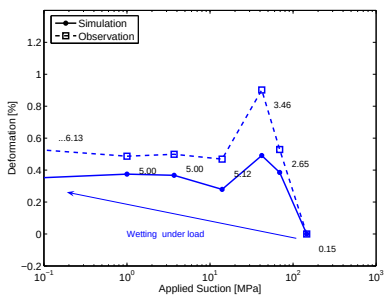

a) Trajectory 3 - 'Near the rock'.

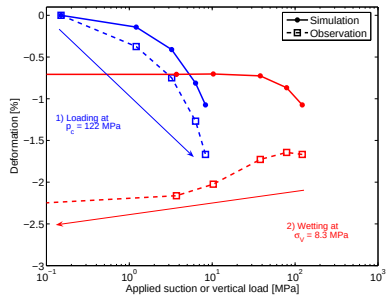

b) Trajectory 6 - 'In the middle'.

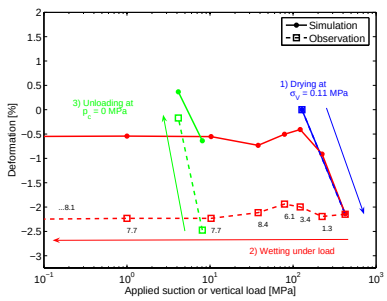

c) Trajectory 7 - 'In the middle'.

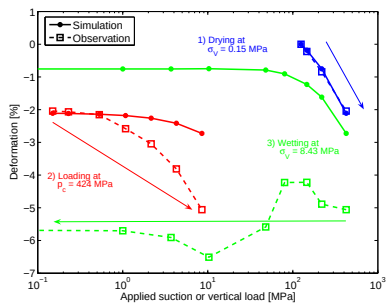

d) Trajectory 2 - 'Near the container'

Figure 7.9: HM experiments 3, 6, 7, and 2. Case M4: $\nu = 0.25$, $K_{\text{init}} = 0.75$ GPa, $b = 1$. The displayed figures beside the wetting under load curves are the applied vertical loads $\boldsymbol{\sigma}_{\text{V}}$ [MPa].

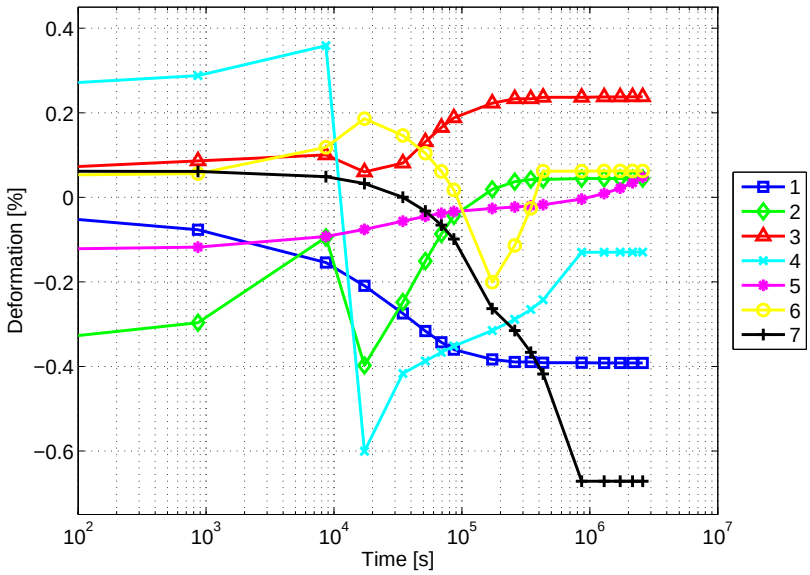

Figure 7.10: HM Base Case M2. Deformation evolutions during the seven phases of trajectory 3.

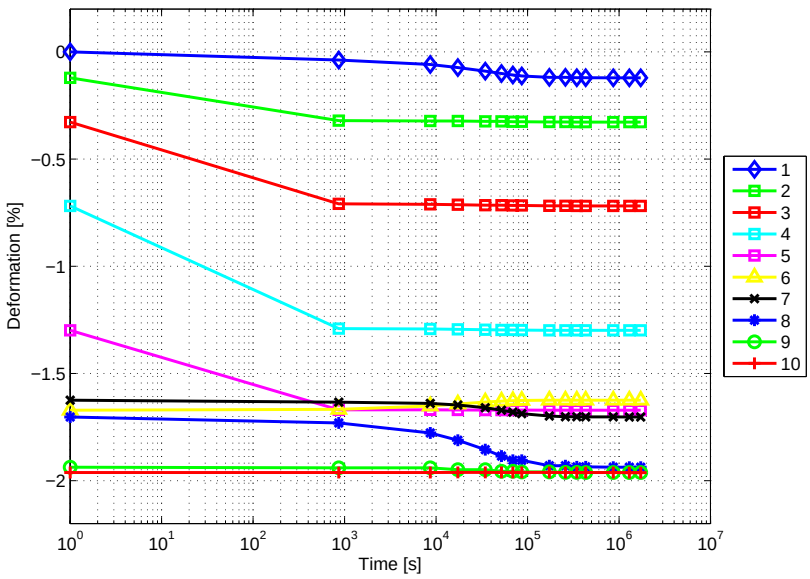

Figure 7.11: HM Base Case M2. Deformation evolutions during the ten phases of trajectory 6.

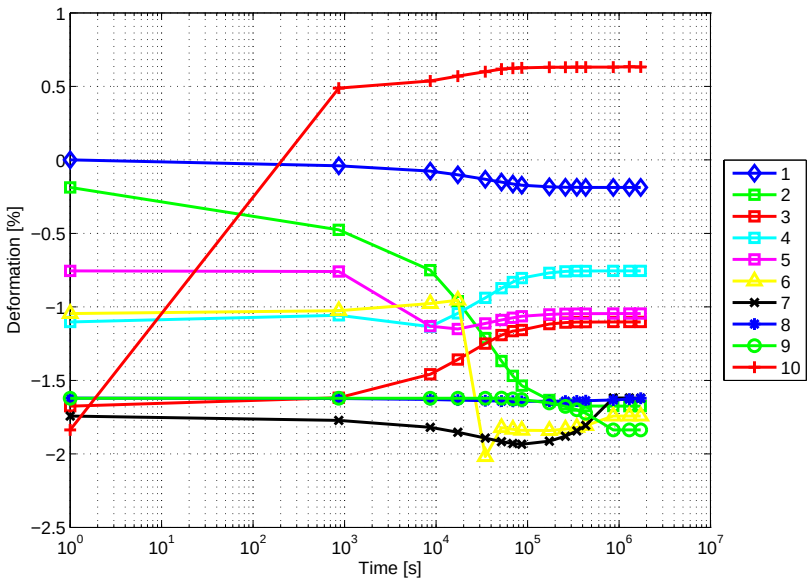

Figure 7.12: HM Base Case M2. Deformation evolutions during the ten phases of trajectory 7.

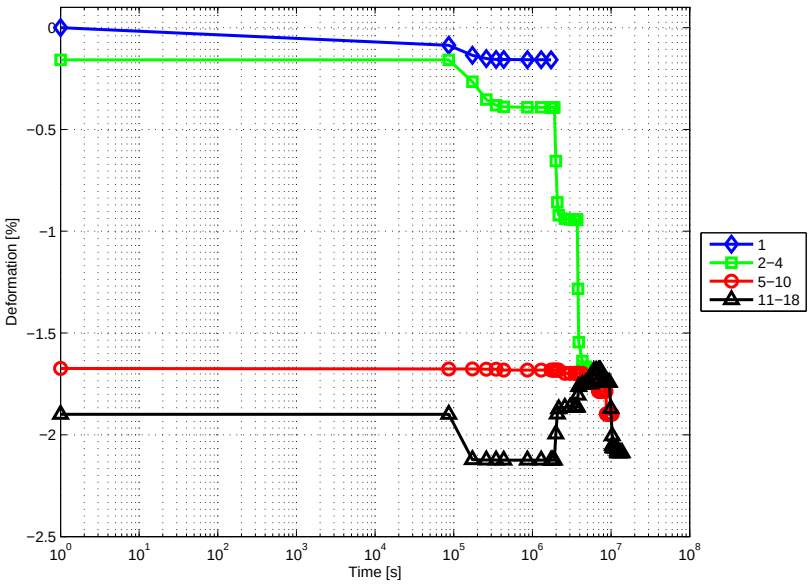

Figure 7.13: HM Base Case M2. Deformation evolutions during the eighteen phases of trajectory 2.

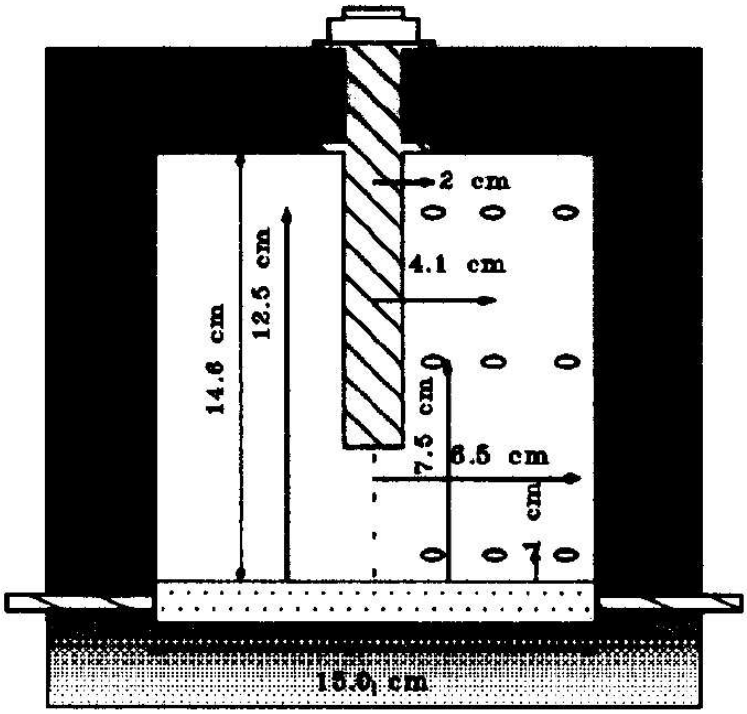

Figure 7.14: Layout of the THM laboratory experiment [110].

7.3 Thermo-hydro-mechanical laboratory experiment

7.3.1 General

The experiment no 8 introduced by Villar et al. [110] has been simulated by [87] and [20] and chosen as the thermo-hydro-mechanical simulation target for the present paper. The experiment involves a cylindrical bentonite sample with a radius of 7.5 cm and a height of 14.6 cm compacted in a steel container to an average dry density of 1660 kg/m^3. A cylindrical heater with a radius of 1 cm and a length of 10 cm is inserted in the upper region of the sample along the axis, see Figure 7.14. The temperature of the heater has been set to 100 ^{o}C at maximum. The sample is hydrated by injecting water at a pressure of 1 MPa through a porous stone under the sample.

The 2-dimensional axially symmetric domain (Figure 7.15a) was meshed (Figure 7.15b) with 134 nodes and 110 quadrilateral elements. Calculation

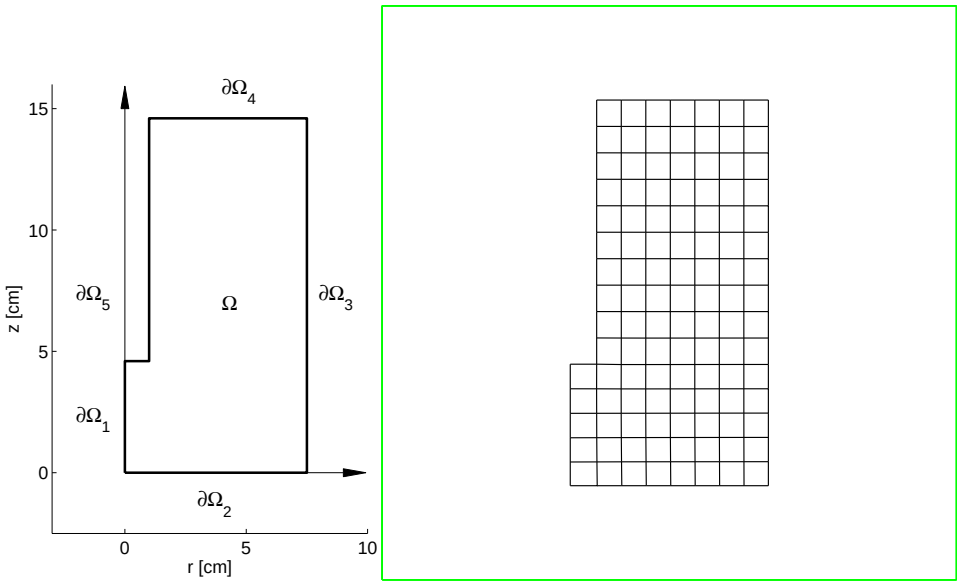

a) THM geometry. b) THM mesh.

Figure 7.15: a) The axially symmetric 2-dimensional domain for the THM simulations along with the boundary notations. b) The corresponding mesh with 134 nodes and 110 quadrilateral elements.

reaching about 100 days (2401.6 hours) involved 28 time steps of variable size. The initial values were

$$\{\eta, \chi, \hat{B}, \mathbf{u}, T\}_{\text{init}} = \{0.40, 0.49, \hat{B}_0, \mathbf{0}, T_0\}. \tag{7.2}$$

The boundary conditions (Figure 7.15a) were the following.

$$\begin{aligned} \mathbf{u}\cdot\mathbf{n} = 0 \quad &\text{on} \quad \partial\Omega_1, \\ \chi = \chi_{\max},\ \hat{B} = \hat{B}_0,\ \mathbf{u}\cdot\mathbf{n} = 0,\ H = 8\ \text{J/(Km}^2) \quad &\text{on} \quad \partial\Omega_2, \\ \mathbf{u}\cdot\mathbf{n} = 0,\ H = 8\ \text{J/(Km}^2) \quad &\text{on} \quad \partial\Omega_3, \\ \mathbf{u}\cdot\mathbf{n} = 0,\ H = 5\ \text{J/(Km}^2) \quad &\text{on} \quad \partial\Omega_4, \\ \mathbf{u}\cdot\mathbf{n} = 0,\ T = T(z) \quad &\text{on} \quad \partial\Omega_5, \end{aligned}$$

where H is a heat transfer coefficient in the Robin condition $\mathbf{q}\cdot\mathbf{n} = H(T - T_0)$ and the steady heater temperature $T(z)$ is assessed from the measured values [87], [20] varying between 65 and 100 $^{\circ}$C.

7.3.2 Results

Basic results are illustrated as a comparison of measured results (if available) and simulated contour plots at the end of the experiment at 2401.6 h.

As global measures of the experiment

- the change of total water volume and
- the radial swelling pressure against the outer boundary at a point 1 cm above the bottom

are illustrated.
The base case contour plots are illustrated as follows

- displacement and saturation in Figure 7.16,
- gas pressure and temperature in Figure 7.17,
- vapor fraction and porosity in Figure 7.18, and
- water content and dry density in Figure 7.19.

The sensitivity cases are set up by variating the corresponding parameter while keeping the other parameters at there base case values. The contour plots are illustrated as follows

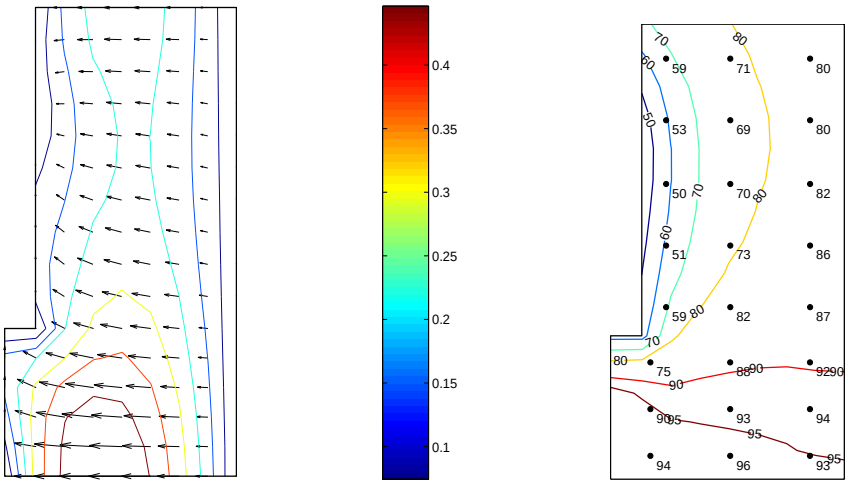

a) Displacement. b) Saturation degree.

Figure 7.16: a) Simulated contours of displacement [mm] and b) saturation degree [-] at the end of the experiment. Base case results.

- saturation for different values of relative permeability of liquid in Figure 7.20,
- gas pressure for different values of relative permeability of gas in Figure 7.21,
- saturation for different values of relative permeability of gas in Figure 7.22,
- dry density for different values of the elasticity parameters in Figure 7.23, and
- water content for different values of the elasticity parameters in Figure 7.24.

In addition, the global measures are the following

- evolution of water volume for different values of the relative permeability of liquid in Figure 7.25 and
- evolution of radial swelling pressure for different values of the elasticity parameters in Figure 7.26.

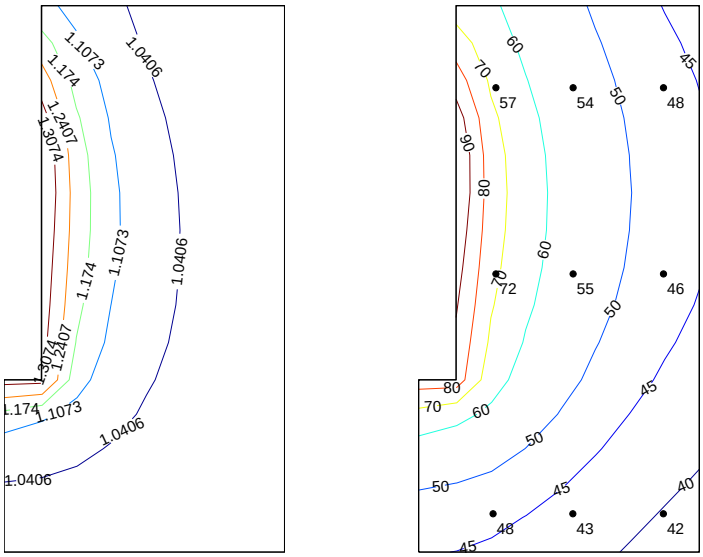

a) Gas pressure. b) Temperature.

Figure 7.17: a) Simulated contours of gaseous pressure [1e5 Pa] and b) temperature [^{o}C] at the end of the experiment. Base case results.

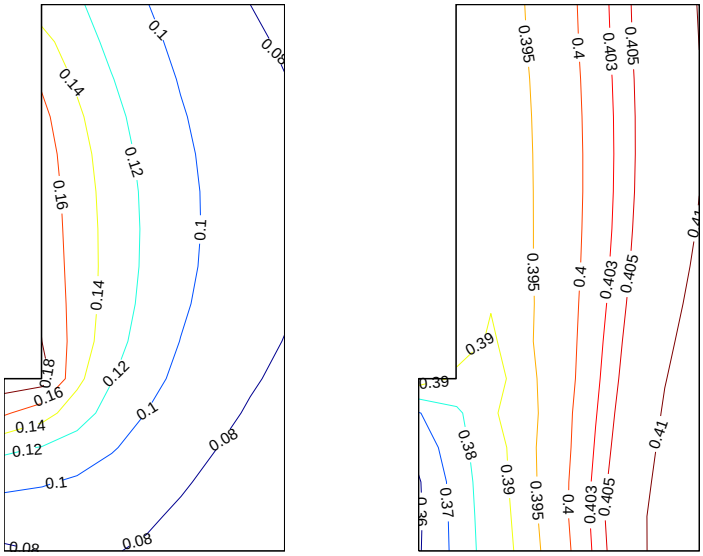

a) Vapor fraction. b) Porosity.

Figure 7.18: a) Simulated contours of vapor fraction [-] and b) porosity [-] at the end of the experiment. Base case results.

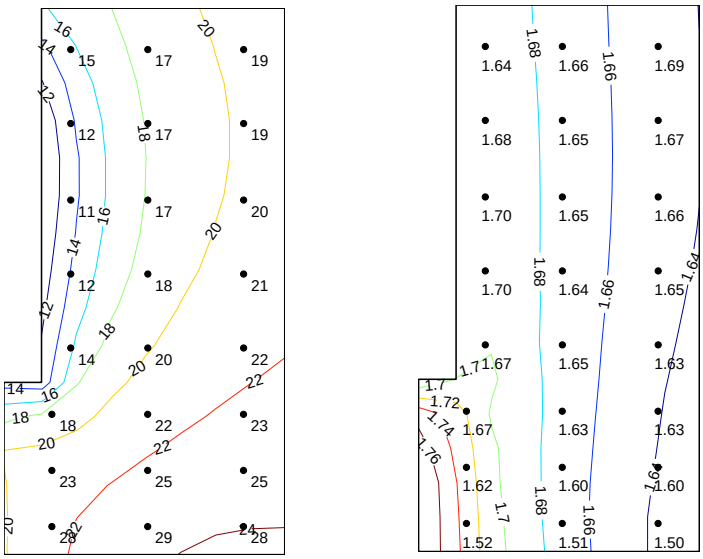

a) Water content. b) Dry density.

Figure 7.19: a) Simulated contours of water content [-] and b) dry density [g/cm^3] at the end of the experiment. Base case results.

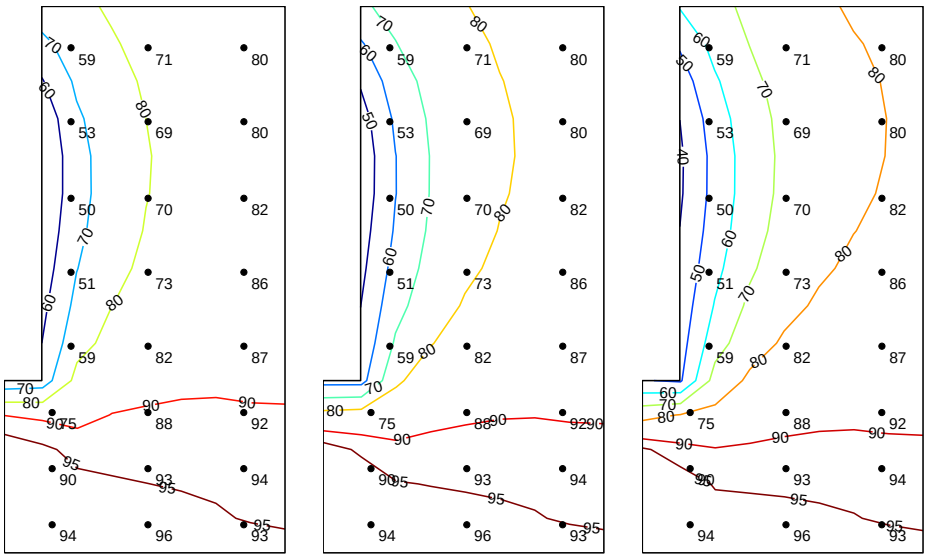

$k_{\mathrm{l,rel}} = \chi^2$ $k_{\mathrm{l,rel}} = \chi^3$ $k_{\mathrm{l,rel}} = \chi^4$

Figure 7.20: Saturation degree contours. Variation of relative permeability of liquid. The figure in the middle corresponds to the Base Case.

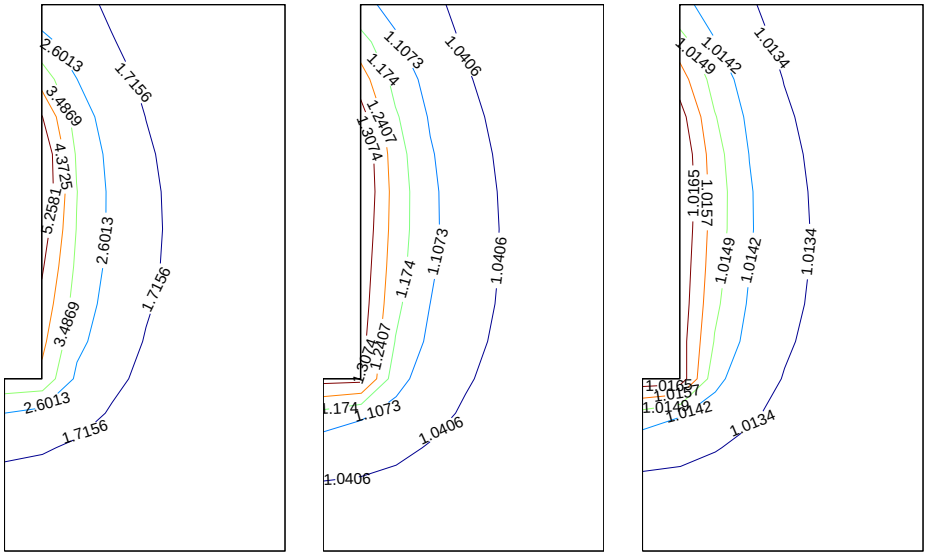

$k_{\mathrm{g,rel}} = 10^3$ $k_{\mathrm{g,rel}} = 10^5$ $k_{\mathrm{g,rel}} = 10^7$.

Figure 7.21: Gaseous pressure contours. The figure in the middle corresponds to the Base Case.

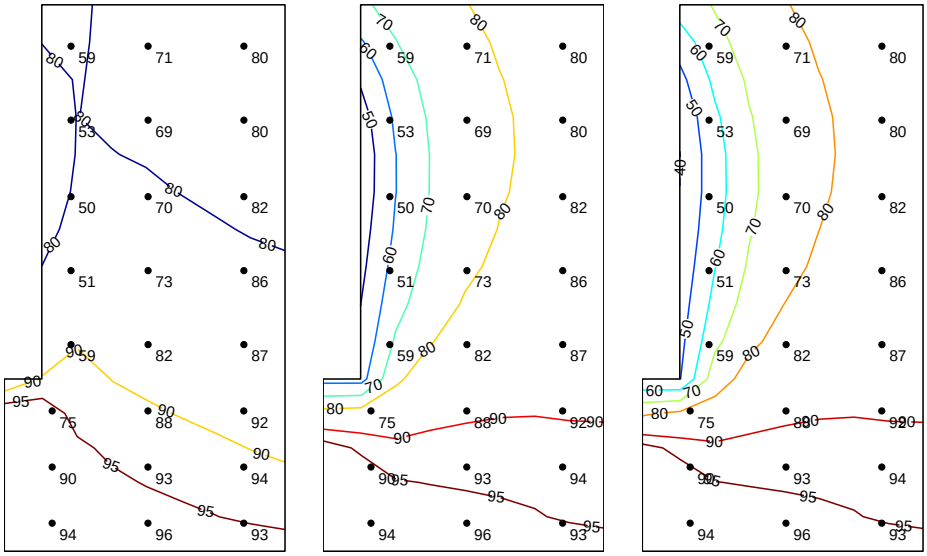

$k_{\mathrm{g,rel}} = 10^3$ $k_{\mathrm{g,rel}} = 10^5$ $k_{\mathrm{g,rel}} = 10^7$.

Figure 7.22: Saturation degree contours. Variation of relative permeability of gas. The figure in the middle corresponds to the Base Case.

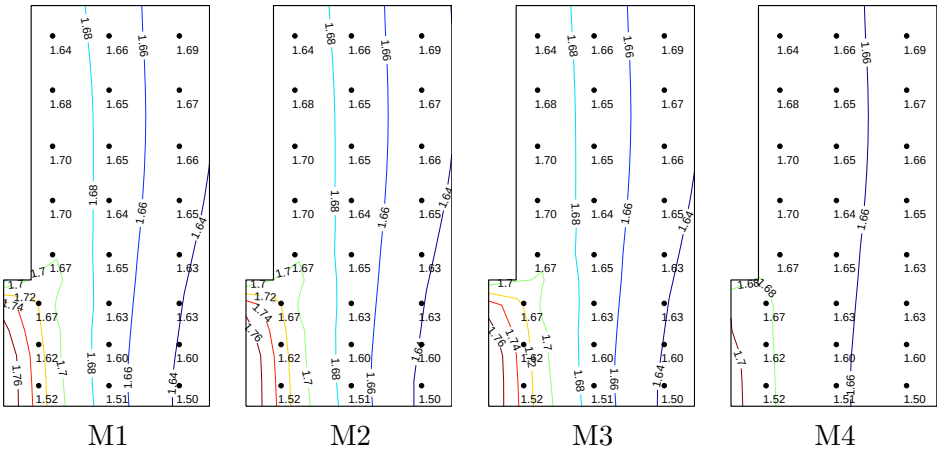

Figure 7.23: Dry density contours. Variation of the elasticity parameters. The second figure from the left (M2) is the Base Case.

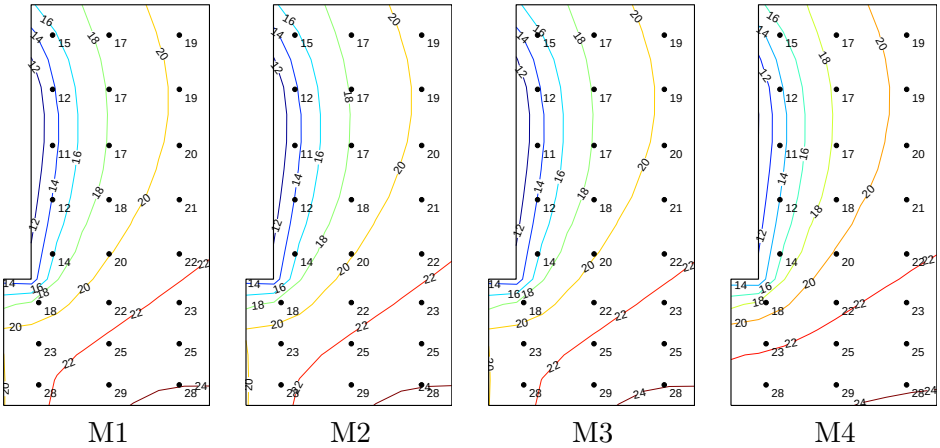

Figure 7.24: Water ratio contours. Variation of the elasticity parameters. The second figure from the left (M2) is the Base Case.

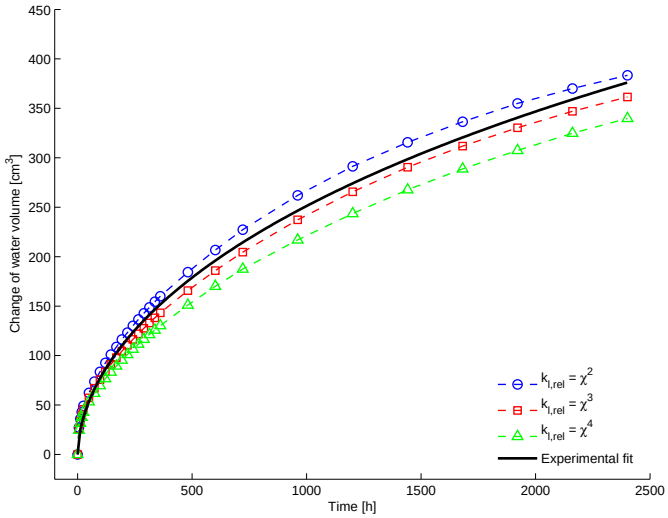

Figure 7.25: Evolution of water volume. The curve in the middle with n = 3 corresponds to the Base Case.

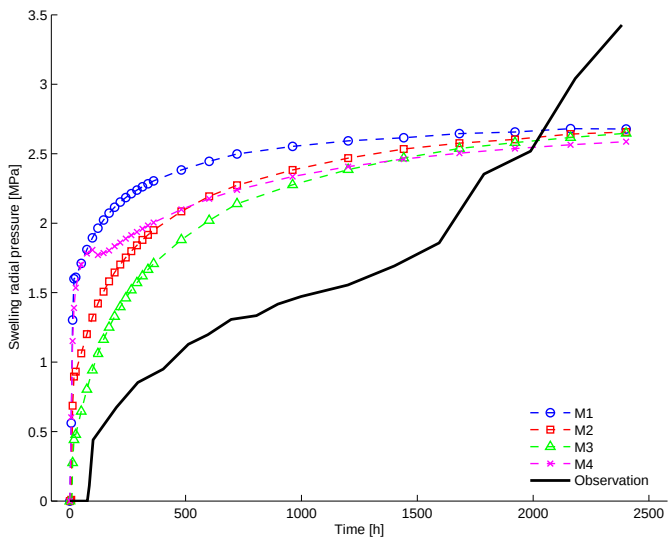

Figure 7.26: Evolution of swelling pressure at the container wall 1 cm above the bottom. M2 corresponds to the Base Case.

7.3.3 Discussion

The basic features and comparison to the observations

The simulated temperature (Figure 7.17b) and saturation degree (Figure 7.16b) are close to the observations. Complete saturation is observed and simulated in the bottom region. A small layer of a few mm around the hottest portion of the heater has dried below the initial saturation degree of 49 % or water content of 11.8 %. As the pore volume around the heater is reduced, the water volume fraction of the same region is reduced significantly.

The steel container has conducted heat away from the heater yielding a more uniform radial temperature in the upper region of the domain than in the simulation. The temperature field was determined by the coupled temperature equation and the simple type of boundary conditions a) applied Dirichlet type of condition at the heater and b) applied Robin type of condition at the outer boundaries with a variable heat transfer coefficient H. In order to be more realistic, the steel container with the known thickness and literature values of thermal properties could have been taken into account.

In principle, the used Robin condition is appropriate, because due to the superior heat conductivity of the steel material temperature in the container does not significantly depend on the distance between the respective outer boundaries of the bentonite sample and the container. In other words, in the perpendicular direction against the outer boundaries the temperature at the interface of bentonite and container is the same as the temperature between container and the surrounding air. Thus the situation is covered with a Robin condition in which the value of H describes the efficiency of heat transfer of each portion of the bentonite boundary, which ultimately depends on the temperature at the respective portion.

The temperature induced vaporization near the heater causes an increase both in gaseous pressure and in vapor fraction. This is physically reasonable although measurements are not available for the validation of the model.

The agreement between the measurements and the simulations for water content (Figure 7.19a) and dry density (Figure 7.19b) is less accurate than for saturation and temperature. The simulated water contents in the upper region drier than $w = 21$ % are fairly accurate. The reason for the discrepancy below this region is related to the discrepancy between the simulated and measured dry density. Because the value of the simulated density is higher the corresponding value of water content is smaller than the observed one. The simulated swelling has occurred almost horizontally which

can be seen either from the displacement (Figure 7.16a), porosity (Figure 7.18b), or from the dry density (Figure 7.19b). The outer region has swollen under wetting and the inner region has compressed under the developed swelling pressure especially around the central axis below the heater.

The simulated and measured water volumes (Figure 7.25) are mutually consistent except that the simulation seems to predict a slightly faster developing steady state. The simulated result for the radial swelling pressure is rational as it develops uniformly approaching a steady value smaller than $\Pi^v_{\max} = 5.0$ MPa. The observed speed of pressure development increases after 1600 hours.

The actual material of the THM-experiment was initially not homogenous because the clay was compacted in the same container in which the measurements were done. Because of this arrangement, the upper region had initially larger and the lower region initially smaller dry density than the average 1660 kg/m^3. Consequently, the simulated and observed dry densities are not consistent. This can be a further explanation for the intermediate increasing of the experimental rate of change of swelling pressure. A larger swelling pressure may have started to develop after full resaturation of the less dense bottom region. However, the shape of the observed swelling pressure curve is as expected as was explained in the review of the theory.

The simulated change of total water volume (Figure 7.25) could be fitted arbitrarily accurately. Several uncertainties are involved, however. Most of the change occurred in the lower region which is both close to the water source and far from the heater. As the material was initially not homogenous with a relatively large pore volume near the bottom a larger water volume could have entered this region than in the simulation.

The modelled driving force restricting the wetting through the temperature gradient may be too strong. A modification in the adsorption function could change the result. Also, the adsorption function was calibrated by means of a retention curve for wetting in constant volume. As some volume change may have occurred in those measurements, the suction expected by the model can be too small. Furthermore, as the drying curves are higher than the wetting curves, the model underestimates the suction in the dried region near the heater.

The high water pressure of 1 MPa was not taken into account in the simulation which has a moderate influence on the result. Finally, the observed water volume change was probably a measure of the inflowing water which does not take into account a portion of the water that possibly evaporates and leaks out of the system.

Sensitivity cases

When varying the relative permeability of liquid (Figure 7.20), increasing of the exponent improves the fit at the top of the geometry near the heater. However, at the same time the fit to the global measure of total water content (Figure 7.25) gets worse. This is because most of the actual water volume change occurs at the lower portion of the geometry where the simulated and the measured results are the least consistent.

The effect of variation of relative permeability of gas can be seen in the Figures 7.21 and 7.22. Decreasing of the permeability results in increasing gaseous pressure at the heater, which in turn prevents the vaporization and decreases the drying.

The effect of variation of the elasticity parameters can be seen in the Figures 7.23, 7.24, and 7.26. It can be seen that the mechanical parameter combinations corresponding to the cases M1, M2, and M3 yield almost identical dry densities and water contents and similar swelling pressure evolutions. In the case M4 the material is stiffer yielding smaller deformation, i.e., smaller change of dry density and schematically a water content field which is more consistent with the observation in the portion below the heater. In addition, the high stiffness in case M4 yields a sharp peak in the deformation and swelling pressure development at the time when the wetting front passes the observation point close to the beginning of the simulation.

Table 7.3: The hydraulic parameters in the simulation of the Febex mock-up experiment.

CASE	k_{sat} [m^2]	$k_{\mathrm{l,rel}}$ [-]	$k_{\mathrm{g,rel}}$ [-]
lower variant	$1.9{\cdot}10^{-21}$	χ^2	10^4
base case	$2.1{\cdot}10^{-21}$	χ^3	10^5
upper variant	$2.3{\cdot}10^{-21}$	χ^4	10^7

7.4 Febex mock-up experiment

7.4.1 General

The components of the mock-up test are similar to those of the in-situ test: two electric heaters, a clay barrier consisting of highly compacted bentonite blocks, instrumentation, automatic control of heaters, and a data acquisition system for the data generated. The heterogeneities of the natural system (granite formation) are avoided, the hydration process is controlled with unlimited amount of water at constant pressure, and the boundary conditions are better defined than in the in-situ test. The operational phase started in February 1997. It was initially planned to last for three years, but it has been decided to extend the operational phase to get as complete saturation of the buffer as possible. In contrast to the in-situ test, full steady state conditions, both thermal and hydraulic, were expected to be reached, as the processes would be accelerated by the injection of pressurised water around the barrier. The mock-up tests surpass the space-scale limitation of the laboratory tests, by adoption of the actual dimensions of the repository, but they do not prevent the time-scale limitation. The short duration of the tests, related to the operative life of the repository, induces uncertainty to extrapolate the future behavior of the clay barrier from the experimental transient state. [74]

The simulation results are illustrated and compared to the observations in five cross-sections defined in Figure 7.27. The locations for temperature and relative humidity measurement points are illustrated in Figure 7.28.

The base case mechanical parameters from the small scale laboratory experiments are used (Table 7.1).

The sensitivity cases are given in Table 7.3. The cases are the same as for the small scale laboratory tests (Table 7.2) except that the lowest variant for the relative permeability of gas is higher.

The same calculation geometry is used as for the THM laboratory simulation. Because now the set-up is horizontal, gravity is neglected to obtain

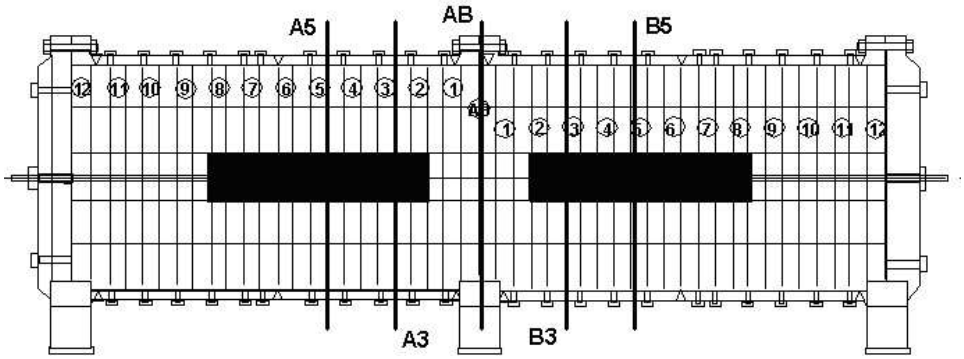

Figure 7.27: Notation for the cross sections involved in the Febex mock-up experiment. Modified after [115].

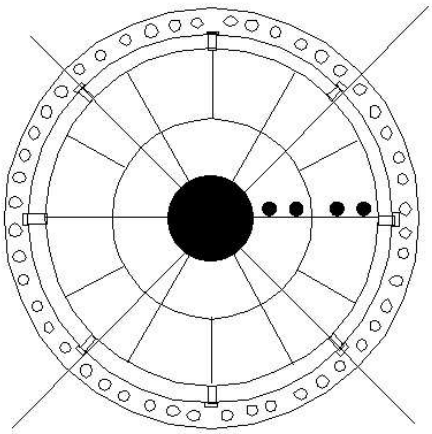

Figure 7.28: Typical cross-section of the Febex mock-up experiment with the approximate locations (black dots) of the material points at which the time dependent simulation results are illustrated: From center: $r = 0.22$–0.23, 0.37, 0.55, and 0.70 m. Modified after [74].

cylindrical symmetry. The 2-dimensional axially symmetric domain (Figure 7.29a) was meshed (Figure 7.29b) with 407 nodes and 818 triangular elements. Calculation reaching 1400 days involved 23 time steps the sizes of which varied between 1 to 200 days. The initial values were

$$\{\eta, \chi, \hat{B}, \mathbf{u}, T\}_{\text{init}} = \{0.3633, 0.6639, \hat{B}_0, \mathbf{0}, T_0\}. \tag{7.3}$$

The boundary conditions (Figure 7.29a) were the following.

$$\begin{aligned} \mathbf{u}\cdot\mathbf{n} = 0 \quad &\text{on} \quad \partial\Omega_{1,2,4}, \\ \chi = \chi_{\max},\ \hat{B} = \hat{B}_0,\ \mathbf{u}\cdot\mathbf{n} = 0,\ H = 10 \quad &\text{on} \quad \partial\Omega_3, \\ \mathbf{u}\cdot\mathbf{n} = 0,\ T = T(t) \quad &\text{on} \quad \partial\Omega_5, \end{aligned}$$

where the heater temperature is set to increase linearly from the initial value of T_0 to the constant maximum value of $T_{\max} = 100$ °C in $t_{\text{crit}} = 15$ days, i.e., $T(t) = T_0 + ((T_{\max} - T_0)/t_{\text{crit}})t$ for $t < t_{\text{crit}}$ and $T = T_{\max}$ for $t > t_{\text{crit}}$.

To compare to the observations the relative humidity is calculated from the simulated result using the equation (3.47) and by neglecting the shear deformation.

In addition to these a special case with a higher initial saturation of 0.73 is applied for reasons discussed further in the following. The initial condition for this special case is

$$\{\eta, \chi, \hat{B}, \mathbf{u}, T\}_{\text{init}} = \{0.3633, 0.73, \hat{B}_0, \mathbf{0}, T_0\}. \tag{7.4}$$

7.4.2 Results

The observed results for the Febex mock-up test are systematic enough to be sensibly illustrated in the same figure with the sensitivity cases. The main results are shown in Figures 7.30–7.37 as follows.

- Comparison of simulated base case evolution of temperature to the observations at four material points of sections A5 and B5 is illustrated in Figure 7.30.
- Comparison of simulated evolution of relative humidity to the observations at four material points of sections A3 and B3 with variation of the permeability parameters is illustrated in the following figures.
  - Variation of intrinsic permeability in Figure 7.31.
  - Variation of relative permeability of liquid in Figure 7.32.

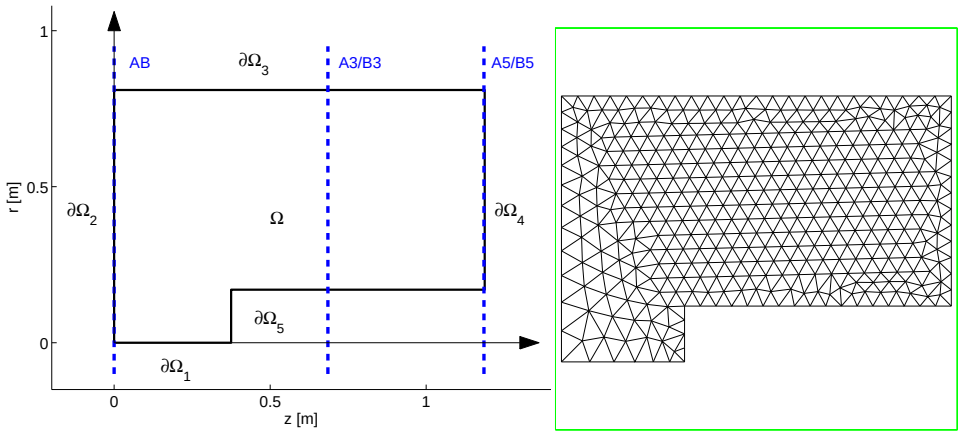

a) Febex mock-up geometry. b) Febex mock-up mesh.

Figure 7.29: a) The axially symmetric 2-dimensional domain for the Febex mock-up simulations along with the notations for the boundaries and the cross sections. b) The corresponding mesh with 407 nodes and 818 triangular elements.

  - Variation of relative permeability of gas in Figure 7.33.

- Comparison of simulated base case evolution of relative humidity to the observations at four material points of sections AB is illustrated in Figure 7.34.
- Simulated base case evolution of porosity at four material points of sections A3 or B3 is illustrated in Figure 7.35.
- Simulated evolution of gaseous pressure at a material point near the heater for sections A3 or B3 is illustrated in Figure 7.36 with variation of the relative permeability of gas.
- Comparison of simulated base case evolution of selected stress components to the observations at three material points of sections A2, B2, A3, and B3 is illustrated in Figure 7.37.

7.4.3 Discussion

Basic features and comparison to observations

The simulated temperature evolution (Figure 7.30) is dominated by the chosen boundary conditions. The shape of the simulated temperature curves

are not identical to the observed ones especially at the inner points of the buffer. However, the achieved steady state temperature gradients are reasonable which is important from the hydraulic point of view.

The simulated schematic relative humidity evolution in sections A3 and B3 is as expected and consistent with the observation (Figure 7.31). The outer buffer begins to slowly saturate by the liquid water applied from the tanks. In the meantime, quite rapid vaporization occurs near the hot heater, where gaseous pressure starts to increase rapidly (Figure 7.36). The excess vapor migrates relatively quickly away from the heater towards the colder region, where the vapor condensates again increasing the local relative humidity. The inner portion of the buffer dries further as the temperature gradually increases and a temperature gradient develops across the buffer. As a consequence, a cycle of wetting due to condensation and drying due to vaporization is encountered in our sample point of $r = 0.37$ m in the central buffer before the onset of slow wetting due to the entering of liquid water to the region.

However, a fundamental discrepancy is found between the simulation and the observation – the observed relative humidity has jumped to a higher level in the beginning and has stayed about ten percent units higher than the simulation during the first hundreds of days. The discrepancy is attributed here to the following differences between the real experimental set-up and the simulation assumptions.

1. The actual buffer is heterogeneous and anisotropic consisting of blocks of individual properties and construction gaps between the blocks.

2. A prewetting of the buffer with 634 l of water has been performed with an intention to seal the construction gaps of the buffer before the onset of the heat production.

3. The measurement probes are located in the construction gaps or in their close proximity.

Because of these differences the following is assumed to have occurred in the experiment.

1. The prewetting of the buffer has filled the construction gaps. The surfaces of the blocks in direct contact to the water have swollen and the gaps have begun to be sealed. The sealed or almost sealed and water filled gap and the swollen bentonite around the gap constitute a preferential pathway of relatively high permeability for fluid flow.

2. The thermohydraulic transient of vaporization, vapor flow, and condensation has occurred more intensively in and through this formed pathway than has occurred inside the intact block and that have been assumed in the model. Furthermore, more water vapor is directed to this pathway from the hot zone than is directed through the intact blocks. In addition, if there has been a large gap between the heater and the buffer filled with free water because of the prewetting, this kind of water is easily vaporized and directed to the preferential pathway where it contributes to the higher than predicted relative humidity.

3. As the measuring probes are located in direct contact to the gaps the observations are not done in the same conditions as expected in the simulation.

Symbolically – the prewetted Febex mock-up buffer has resembled '*a wall of bricks*' layed together with '*mortar*' of relatively high porosity and permeability. The given observations have been made in the region of this 'mortar' where transient thermo-hydraulic phenomena have occurred that are not predicted by the model in which a homogeneously and isotropically dense and intact buffer of low permeability has been assumed.

The disturbing influence of the prewetting is the most evident in the observation of relative humidity at the section AB in the middle of the two heaters (Figure 7.34). There has been complete initial saturation at the innermost point suggesting that the probe has been soaked with free water after the prewetting. At least for an individual measuring point the reality can be totally different from that expected in the idealized homogeneous and isotropic model.

The simplest way of assessing the effect of the differencies between the model and the reality is to discard the observed transient phase and to start the simulation after the observed rapid increase in the moisture content. The base case parameter values with the new initial conditions (7.4) yield a simulated relative humidity evolution (Figure 7.38), which is almost identical to the observation. This is actually unintentional, however, and the model does not explain the observation as completely as it seems.

If the assumptions made of the transient behavior are correct and if the model and its parameters are appropriate the following is indicated.

- The transient condensation has relatively rapidly completed the sealing of the gap. The properties, especially the permeability, of the closed gap are recovered and close to those of the intact blocks.

- Immediately after the transient the moisture content along the closed gap is higher than that along the radial direction in the adjacent intact blocks.

No directly observed evidence to support the latter conclusion is available. However, the result can be compared to similar experiments in which the conditions enabling the transient, especially the blocky geometry forming a direct route from the heater to the observation points, are not present. This is the case of CEA mock-up test that is analyzed later in this thesis. In fact, the observations of the CEA mock-up test do not exhibit the transient (Figure 8.3). Consequently, confidence to the assumptions made on the transient phenomenon involved in the Febex mock-up test and overall confidence to the present model to predict the moisture behavior are increased.

Porosity evolution in sections A3 and B3 (Figure 7.35) shows the moisture swelling behavior. The inner points near the heater have encountered shrinkage and the outer points near the rock swelling. For the points r = 0.55 m and 0.70 m a cycle of shrinking due to the swelling of the outer buffer followed by swelling due to the subsequent wetting of the point has occurred. The changes of the porosities are small and a steady state has not been reached in 1400 days.

The discrepancy between the simulated and observed stresses in sections A3 and B3 (Figure 7.37) is mainly due to the different achievable maximum swelling pressure. In the model the values obtained for the base case of the laboratory experiments are used while the material used in the Febex mock-up test has been considerably denser (Table 3.4) exhibiting considerably larger swelling pressures.

Sensitivity cases

Increasing of the intrinsic permeability increases the rate of long-term wetting but does not affect the initial drying phase. The approaching of a possible steady state can be seen both in the observation and the simulation. The value of permeability does not determine the steady state but the path of approaching it. Consequently, after the initially observed transient the observed and simulated results seem to approach each other.

Increasing of the exponent of the relative permeability of liquid decreases the unsaturated liquid permeability. This increases the magnitude and duration of initial drying but does not affect the consecutive rate of long-term wetting. The value of relative permeability of liquid does not determine the steady state but the path of approaching it. Consequently, after the initial

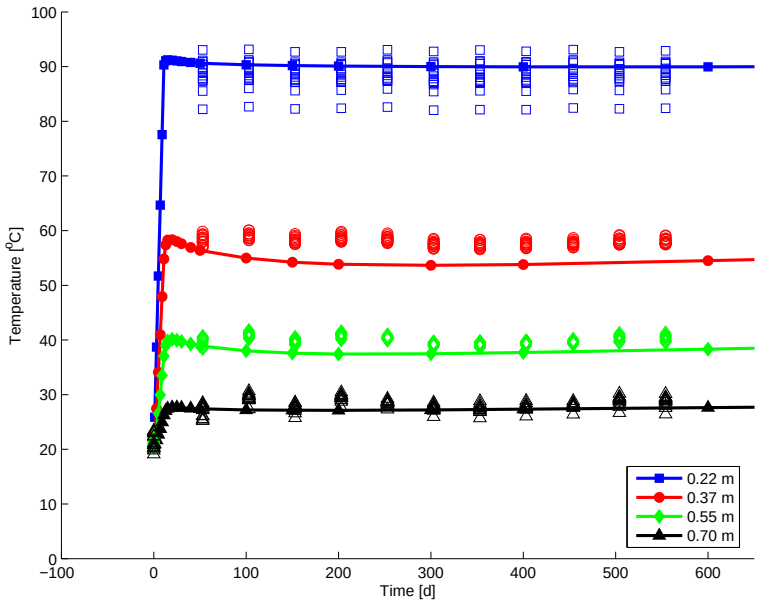

Figure 7.30: Febex mock-up experiment. Simulated (curves) and observed (symbols) evolution of temperature at four material points of the sections A5 and B5. Base case.

transient the observed and simulated results seem to approach each other.

Increasing of the relative permeability of gas increases the magnitude but not the duration of the initial drying and decreases the consecutive rate of long-term wetting. The value of relative permeability of gas affects both the steady state and the path of approaching it.

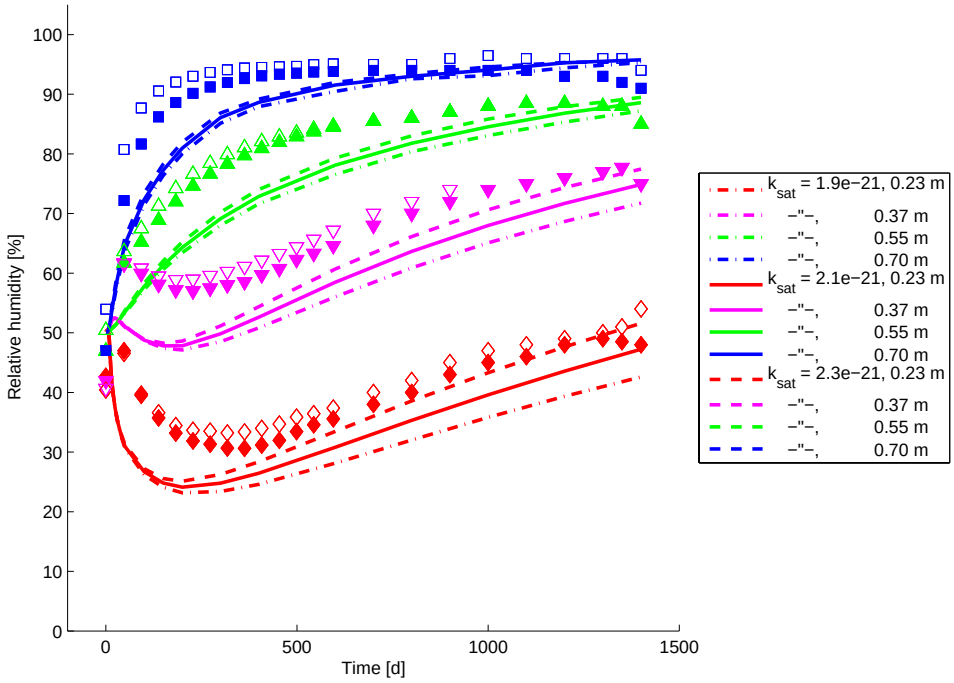

Figure 7.31: Febex mock-up experiment. Simulated (curves) and observed (symbols) relative humidity at four material points of the sections A3 and B3. Variation of the intrinsic permeability with $k_{\mathrm{sat}} = 2.1 \cdot 10^{-21}$ m^2 as the base case.

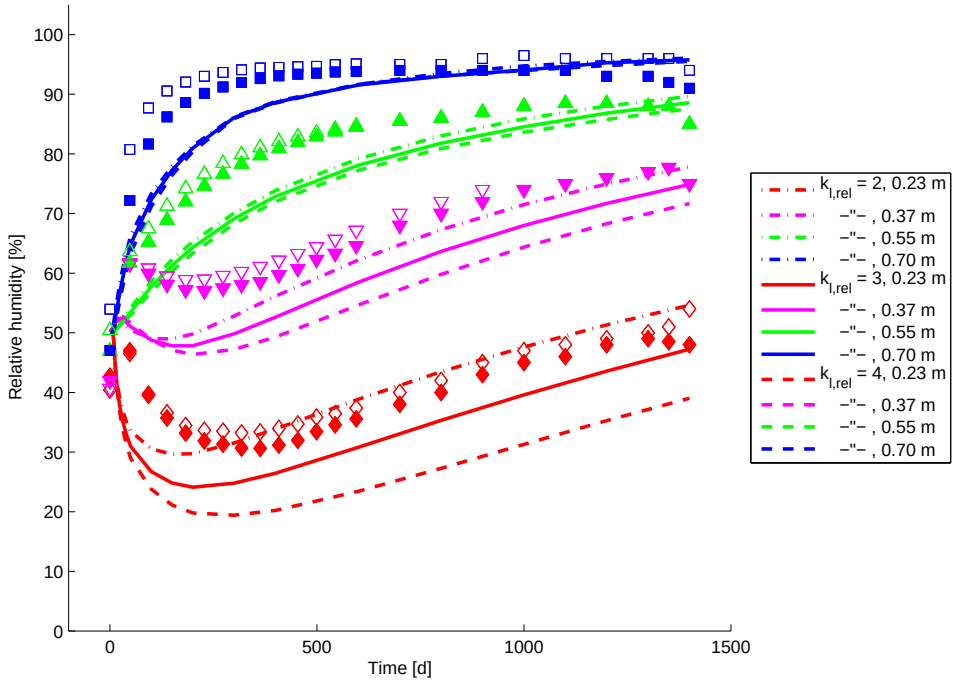

Figure 7.32: Febex mock-up experiment. Simulated (curves) and observed (symbols) relative humidity at four material points of the sections A3 and B3. Variation of the relative permeability of liquid with $k_{\mathrm{l,rel}} = \chi^3$ as the base case.

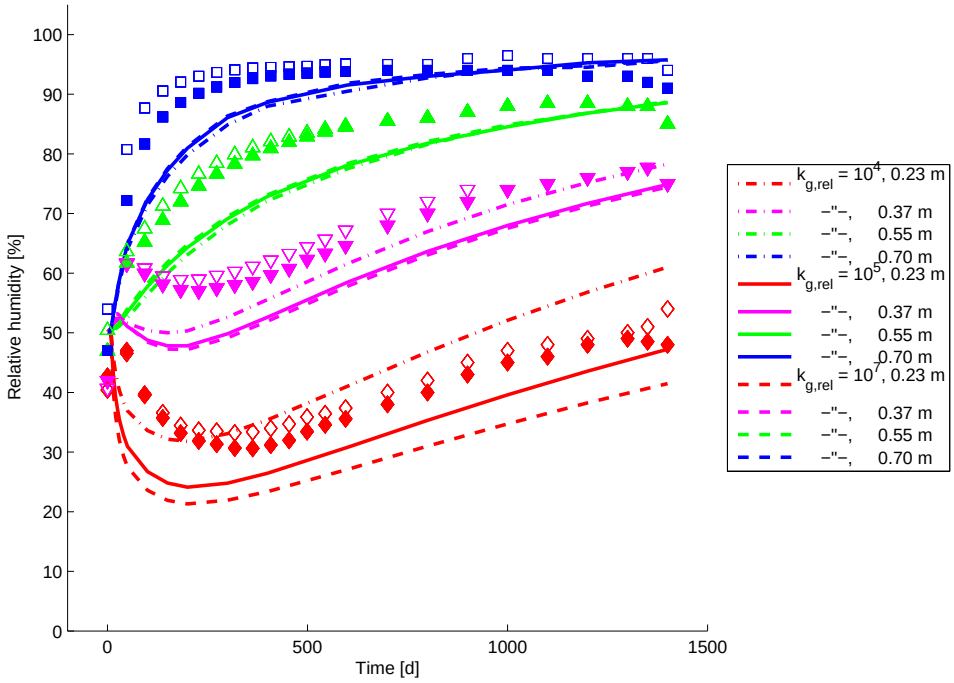

Figure 7.33: Febex mock-up experiment. Simulated (curves) and observed (symbols) relative humidity at four material points of the sections A3 and B3. Variation of the relative permeability of gas with $k_{\mathrm{g,rel}} = 10^5$ as the base case.

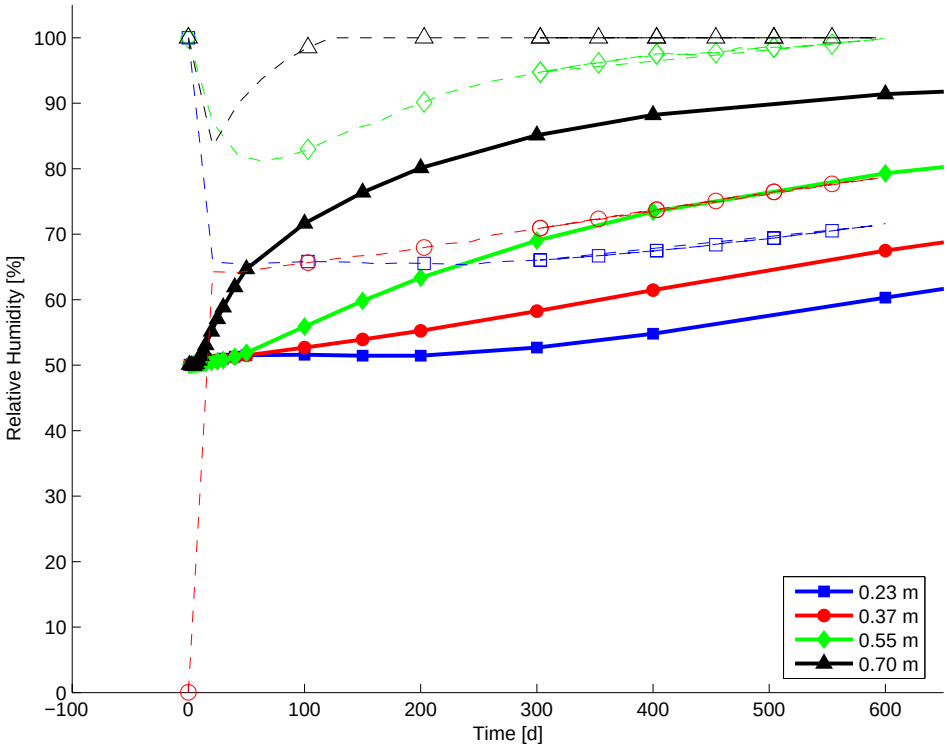

Figure 7.34: Febex mock-up experiment. Simulated (solid symbols) and observed (open symbols) relative humidity at four material points of the section AB in the middle of the heaters. Base case.

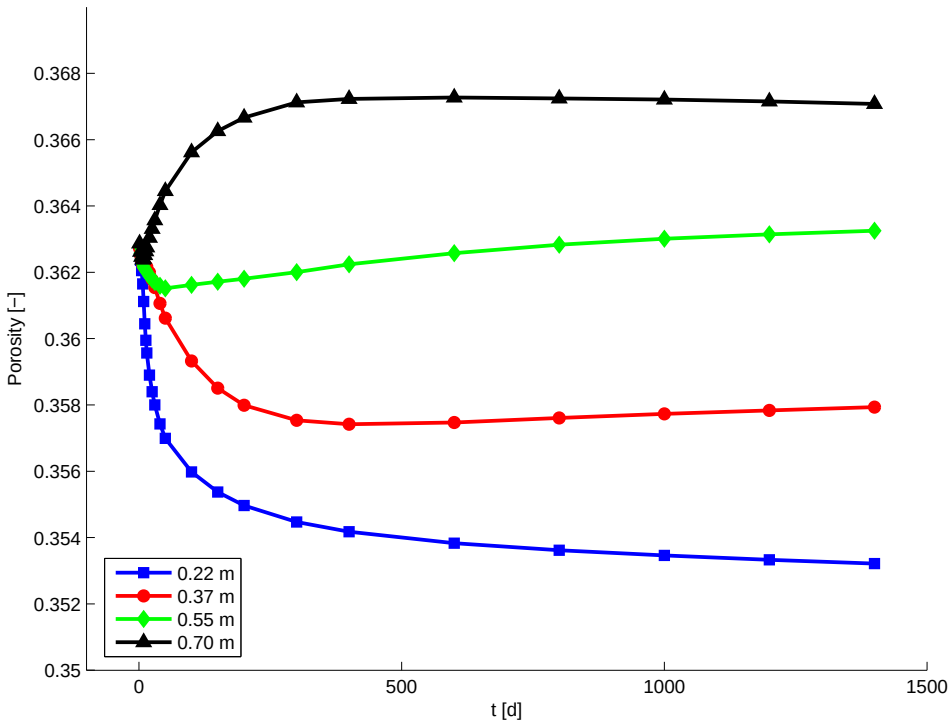

Figure 7.35: Febex mock-up experiment. Simulated evolution of porosity in four material points of the sections A3 and B3. Base case.

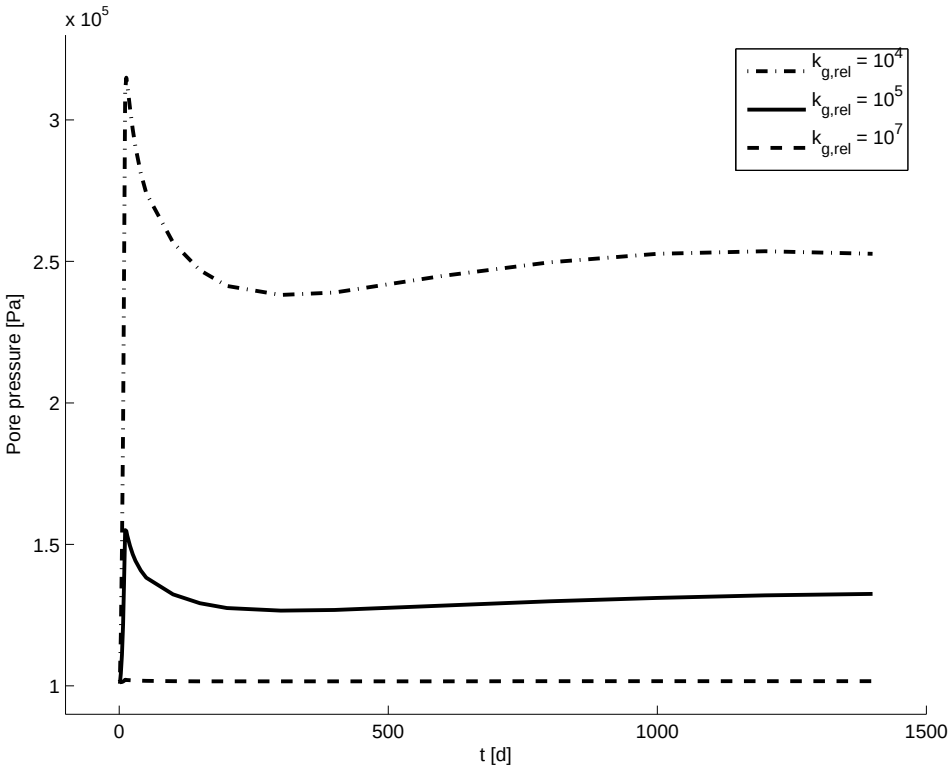

Figure 7.36: Febex mock-up experiment. Simulated evolution of gaseous pressure in a material point near the heater of the sections A3 and B3. Sensitivity analysis. Variation of the relative permeability of gas.

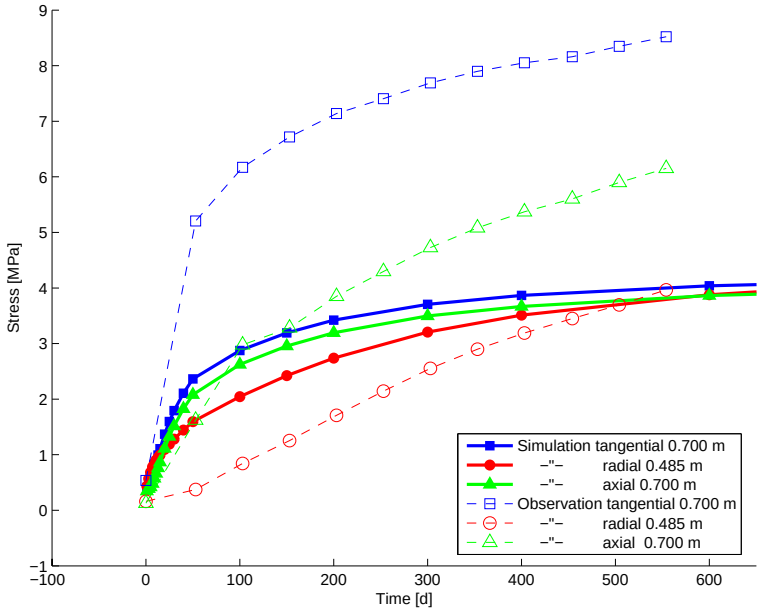

a) At the radii $r = 0.485$ and 0.70 m

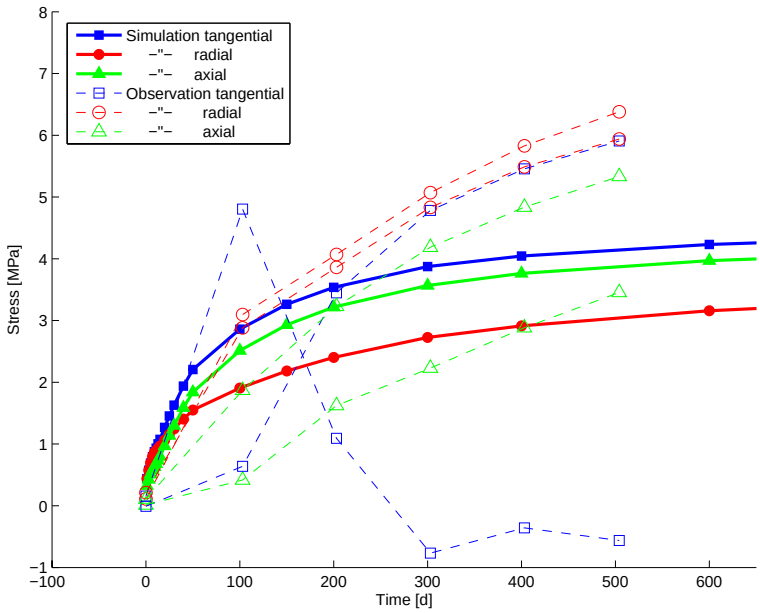

b) At the radius $r = 0.665$ m.

Figure 7.37: Febex mock-up experiment. Simulated (solid symbols) and observed (open symbols) base case evolution of selected stresses at four material points of the sections A3 and B3 with varying radii.

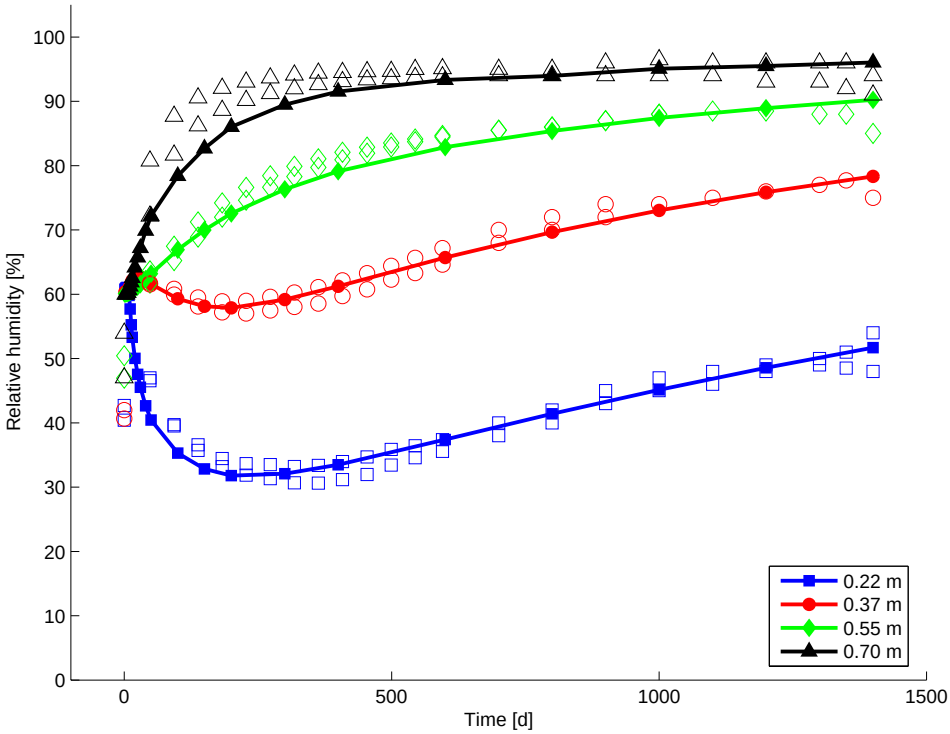

Figure 7.38: Febex mock-up experiment. Simulated (curves) and observed (symbols) evolution of relative humidity at four material points of the sections A3 and B3. A special simulation case with the base case material parameters but a larger initial saturation.

Table 7.4: The hydraulic parameters in the simulation of the Febex in-situ experiment.

CASE	k_{sat} [m^2]	$k_{\mathrm{l,rel}}$ [-]	$k_{\mathrm{g,rel}}$ [-]
lower variant	$1.9{\cdot}10^{-21}$	χ^2	10^4
base case	$2.1{\cdot}10^{-21}$	χ^3	10^5
upper variant	$2.3{\cdot}10^{-21}$	χ^4	10^6

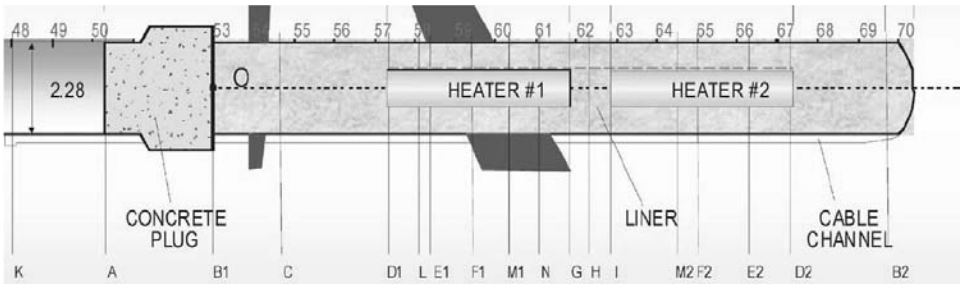

Figure 7.39: Notation for the cross sections involved in the Febex in-situ experiment [115].

7.5 Febex in-situ experiment

7.5.1 General

The simulation results are illustrated and compared to the observations in three cross-sections (H, E1, and E2) defined in Figure 7.39. The locations for temperature and relative humidity measurement points are illustrated in Figure 7.40. The base case mechanical parameters from the small scale laboratory experiments are used (Table 7.1). The considered sensitivity cases are given in Table 7.4. The cases are the same as for the small scale laboratory tests (Table 7.2) except that the lowest variant for the relative permeability of gas is higher and the highest variant is lower.

The same calculation geometry is used as for the Febex mock-up simulation with neglected gravity. The 2-dimensional axially symmetric domain (Figure 7.41a) was meshed (Figure 7.41b) with 644 nodes and 1292 triangular elements. Calculation reaching 100 years involved 38 time steps the sizes of which varied between 1 d to 20 years. The initial values were

$$\{\eta, \chi, \hat{B}, \mathbf{u}, T\}_{\mathrm{init}} = \{0.4245, 0.5439, \hat{B}_0, \mathbf{0}, (12 + 273.15)\ \mathrm{K}\}. \tag{7.5}$$

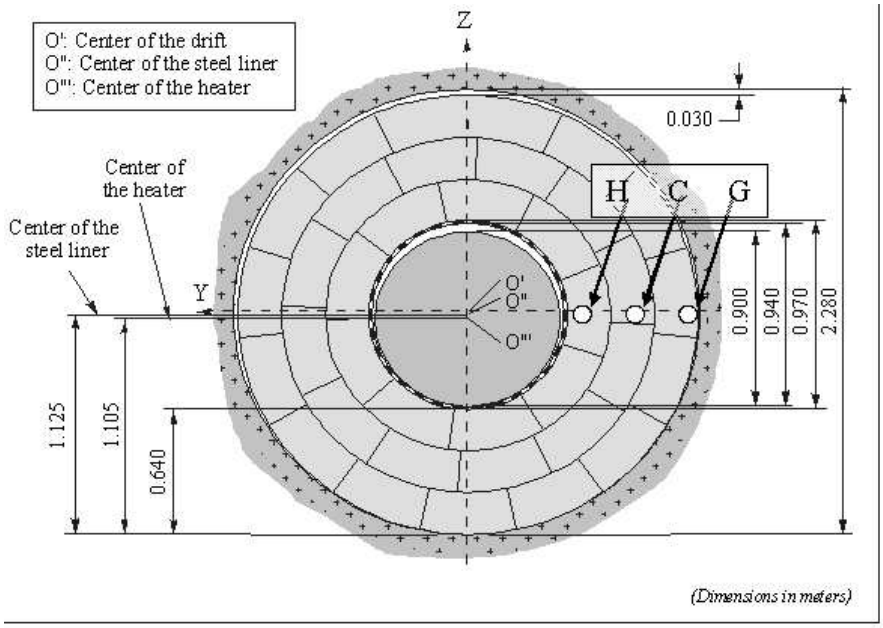

Figure 7.40: Typical cross section of the Febex in-situ experiment with the approximate location of the material points at which the time dependent simulation results are illustrated: Heater (H: 52 cm), Centre (C: 71 cm), and Granite (G:112 cm). Modified after [34]

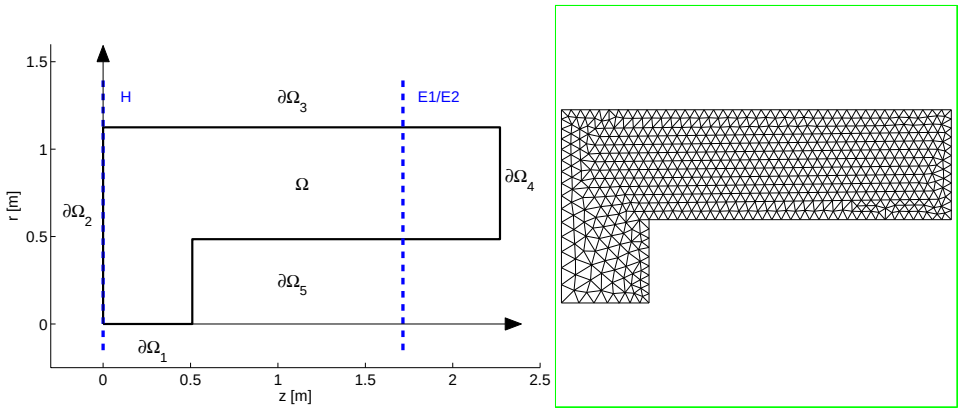

a) Febex in-situ geometry. b) Febex in-situ mesh.

Figure 7.41: a) The axially symmetric 2-dimensional domain for the Febex in-situ simulations along with the notations for boundaries and the cross sections. b) The corresponding mesh with 644 nodes and 1292 triangular elements.

The boundary conditions (Figure 7.41a) were the following.

$$\begin{aligned} \mathbf{u}\cdot\mathbf{n} = 0 \quad &\text{on} \quad \partial\Omega_{1,2,4}, \\ \chi = \chi_{\max},\ \hat{B} = \hat{B}_0,\ \mathbf{u}\cdot\mathbf{n} = 0,\ H = 2 \quad &\text{on} \quad \partial\Omega_3, \\ \mathbf{u}\cdot\mathbf{n} = 0,\ T = T(t) \quad &\text{on} \quad \partial\Omega_5, \end{aligned}$$

where the heater temperature is set to increase linearly from the initial value of $T_{\text{init}} = 12$ °C to the constant maximum value of $T_{\max} = 100$ °C in $t_{\text{crit}} = 53$ days, i.e., $T(t) = T_{\text{init}} + ((T_{\max} - T_{\text{init}})/t_{\text{crit}})t$ for $t < t_{\text{crit}}$ and $T = T_{\max}$ for $t > t_{\text{crit}}$.

7.5.2 Results

Base case results compared to observations

Evolutions at selected material points are illustrated in the following way.

- Comparison of simulated and observed evolution of temperature in three material points for sections E1 or E2 is illustrated in Figure 7.42.
- Comparison of simulated and observed evolution of relative humidity in three material points for sections E1 or E2 and for section H is illustrated in Figure 7.43.

- Simulated evolution of porosity in three material points for sections E1 and H is illustrated in Figure 7.44.
- Comparison of simulated and observed evolution of radial stress in three material points for section E2 is illustrated in Figure 7.45.

In addition, simulated relative humidity profiles at $t = \{300$ d, 5 a, 30 a, 100 a$\}$ for sections E1 and H are illustrated in Figure 7.46.

Sensitivity cases

Simulated evolution of relative humidity in three material points for sections E1 and H with variation of permeability parameters is illustrated in the following figures.

- variation of intrinsic permeability in Figure 7.47,
- variation of relative permeability of liquid in Figure 7.48, and
- variation of relative permeability of gas in Figure 7.49.

Simulated evolution of gaseous pressure at three material points for sections E1 and H is illustrated in Figure 7.50.

In addition, simulated relative humidity profiles at $t = 100$ a for sections E1 and H with variation of the permeability parameters are illustrated in the following figures.

- variation of intrinsic permeability in Figure 7.51,
- variation of relative permeability of liquid in Figure 7.52, and
- variation of relative permeability of gas in Figure 7.53.

7.5.3 Special cases: Simple involvement of rock

In the previous analyses the geometry consisted only of the buffer itself whereas the surrounding rock was only taken into account by means of boundary conditions, i.e., at the rock-buffer interface there prevails full saturation and heat transfer via a mixed Robin type condition. In the real disposal situation, however, the surrounding rock has a limited capacity of serving water. Even if the rock is assumed to be initially fully saturated the suction ability of the buffer is very much larger. Consequently, the water

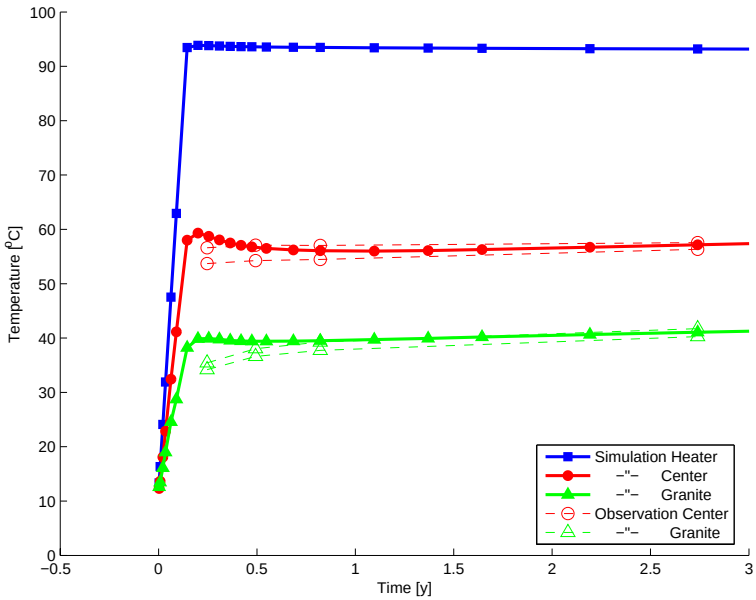

Figure 7.42: Febex in-situ experiment. Simulated and observed base case evolution of temperature in three material points for sections E1 and E2.

content of the rock can be, at least partially and in the beginning, reduced by the suction of the buffer.

Furthermore, the surrounding rock serves as a sink of heat. The temperature evolution in the buffer is faster than the moisture evolution and for a few years time an artificial temperature boundary condition can indeed yield satisfactory simulation results. However, in the real disposal situation, the temperature of the surrounding rock mass gradually increases and, consequently, also the temperature of the buffer-rock interface increases. More realistic boundary conditions for the heat equation in this case are now continuous heat flux and temperature at the buffer-rock interface and a constant temperature at a further distance from the buffer. In the following, we expect a constant temperature of 12 °C at 400 m from the axis of the container. Due to this assumption, the achieved temperature gradients across the buffer will be smaller. The computational mesh with the rock involved is illustrated in Figure 7.54.

In the real disposal situation the temperature rise is due to the heat production of the waste. Consequently, the real temperature does not rise as rapidly as in the current experiment and when the maximum has been

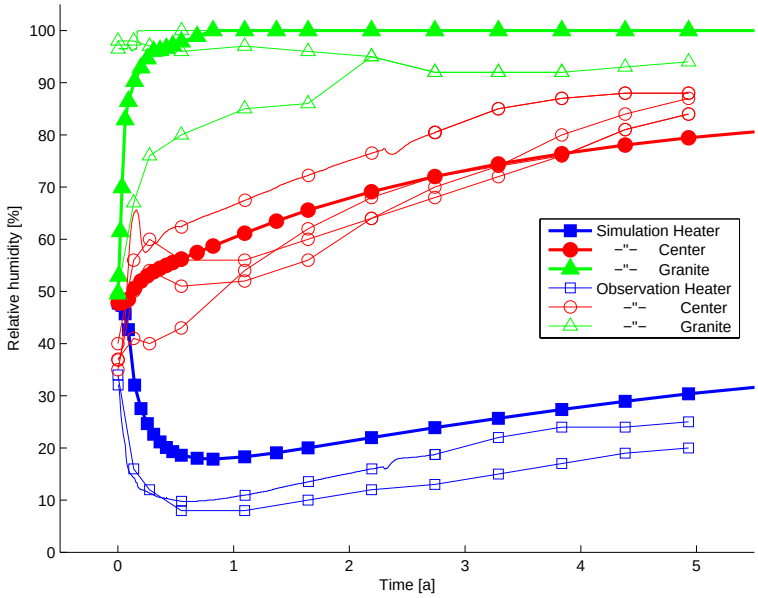

a) Section E1.

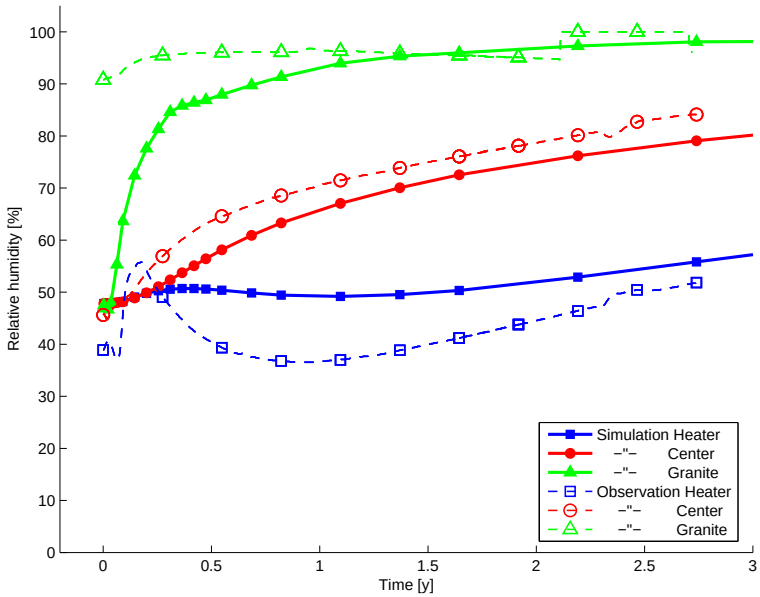

b) Section H.

Figure 7.43: Febex in-situ experiment. Simulated and observed base case evolution of relative humidity in three material points for sections E1 and H.

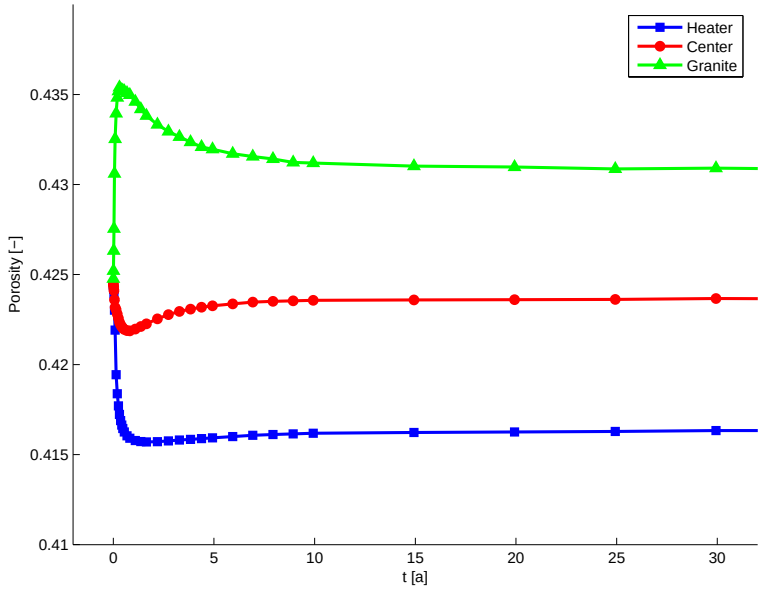

a) Section E1.

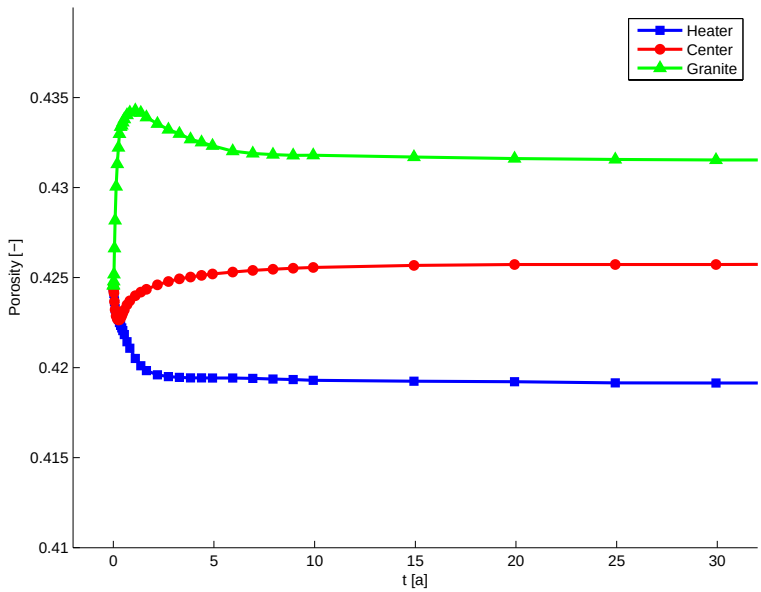

b) Section H.

Figure 7.44: Febex in-situ experiment. Simulated base case evolution of porosity in three material points for sections E1 and H.

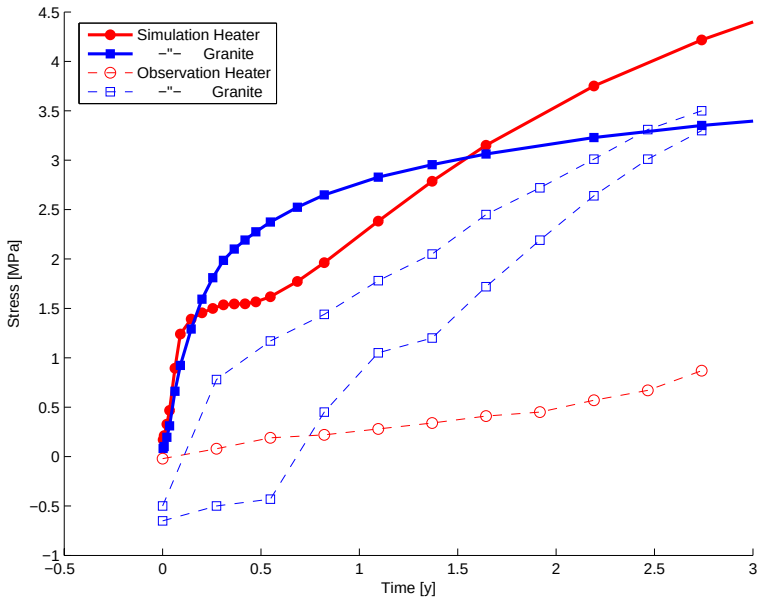

Figure 7.45: Febex in-situ experiment. Simulated and observed base case evolution of radial stress in three material points for section E2.

achieved the temperatures will gradually decrease. As a consequence, the achieved temperature gradients will be even smaller.

Two special cases of more realistic temperature boundary condition at the container-buffer interface are chosen to illustrate the possible evolution of the real disposal situation in which the adjacent disposal holes and tunnels are taken into account. The cases involve a duration of 100 years only to be comparable to the previous cases. Totally, three thermal boundary conditions are defined as follows. In all of these cases the rock is involved with the temperature of the outer rock surface at $r = 400$ m kept at 12 °C.

- Thermal Boundary Condition 1: The constant heater temperature is $T = 100$ °C. The case is compared to the previous case of ignoring the rock with the mixed thermal boundary condition at the rock-bentonite interface.

- Thermal Boundary Condition 2: Based on the temperature analysis by Raiko [97] the temperature of the container surface will rise to a maximum of 80 °C in 20 years and will gradually decrease to 65 °C in 100 years.

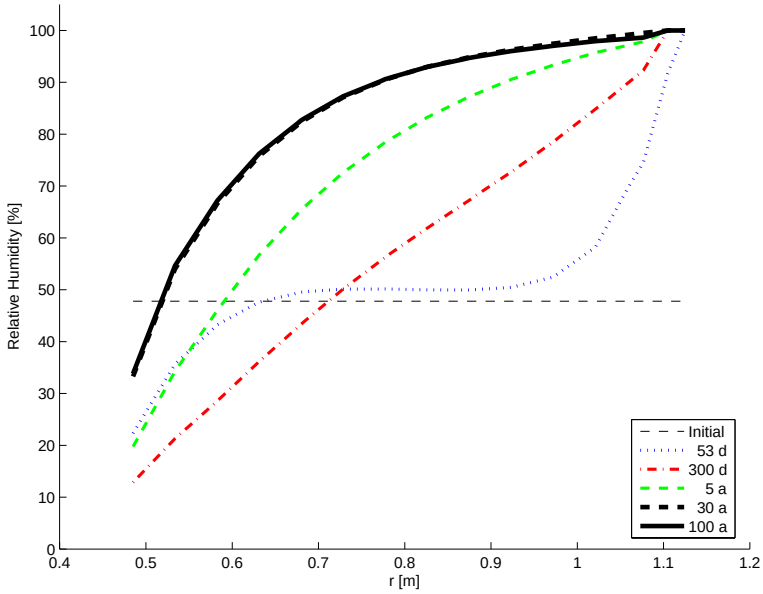

a) Section E1.

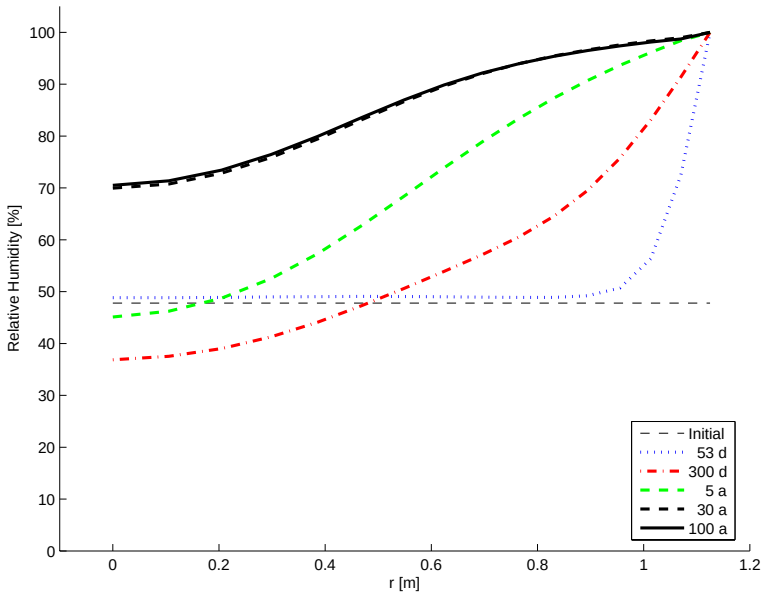

b) Section H.

Figure 7.46: Febex in-situ experiment. Simulated base case radial profiles of relative humidity for sections E1 and H. The dashed line shows the initial profile.

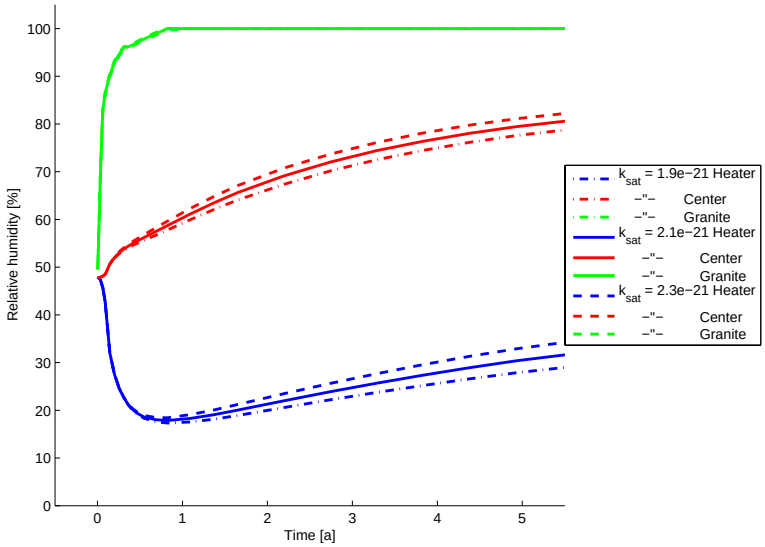

a) Section E1.

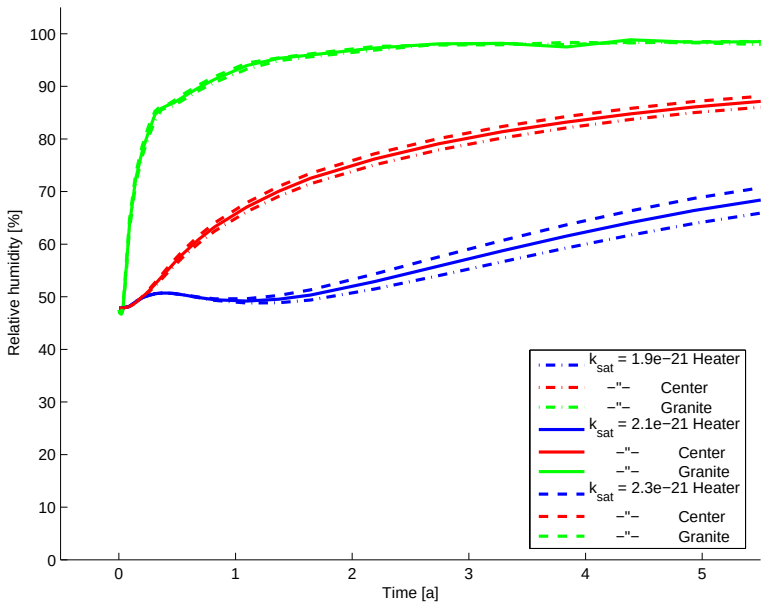

b) Section H.

Figure 7.47: Febex in-situ experiment. Simulated evolution of relative humidity in three material points for sections E1 and H. Sensitivity analysis. Variation of intrinsic permeability.

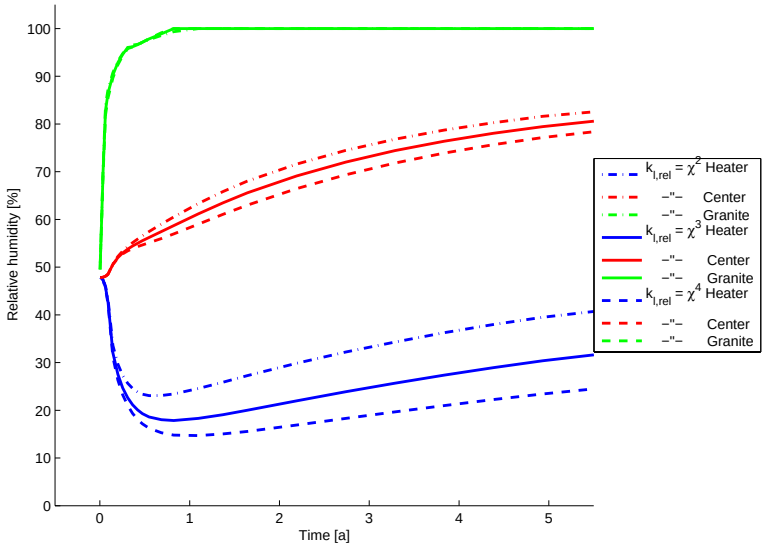

a) Section E1.

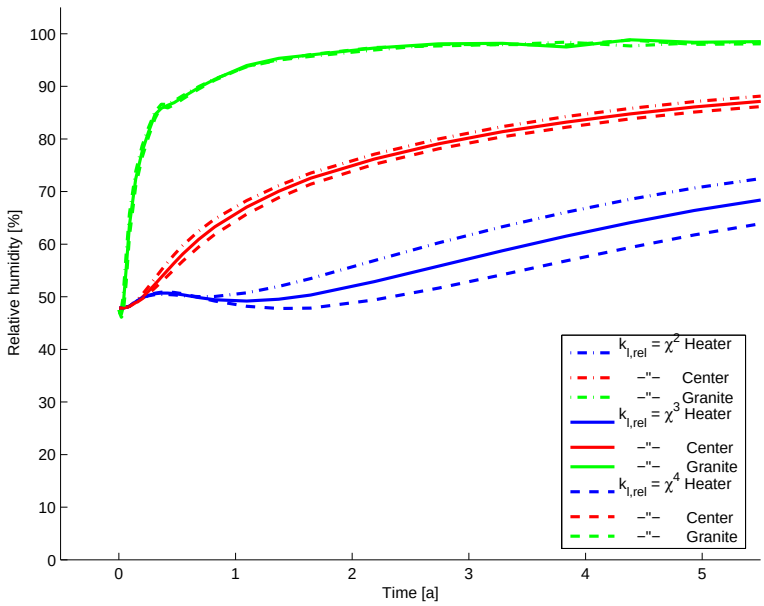

b) Section H.

Figure 7.48: Febex in-situ experiment. Simulated evolution of relative humidity in three material points for sections E1 and H. Sensitivity analysis. Variation of relative permeability of liquid.

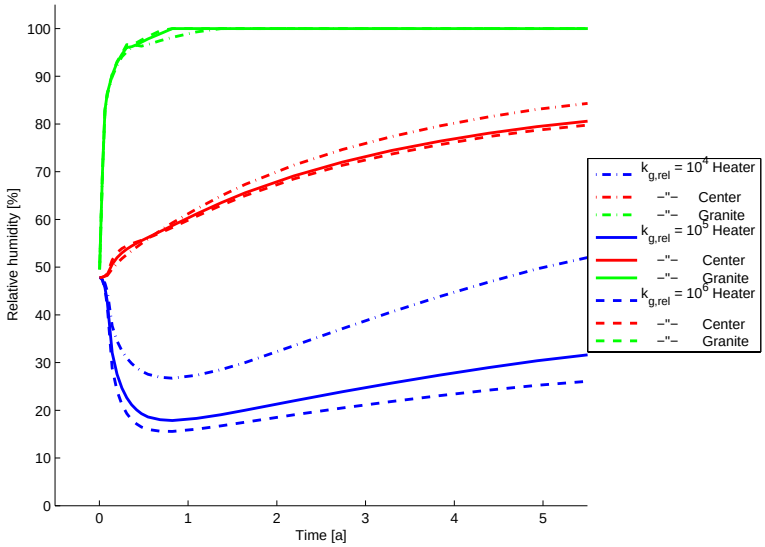

a) Section E1.

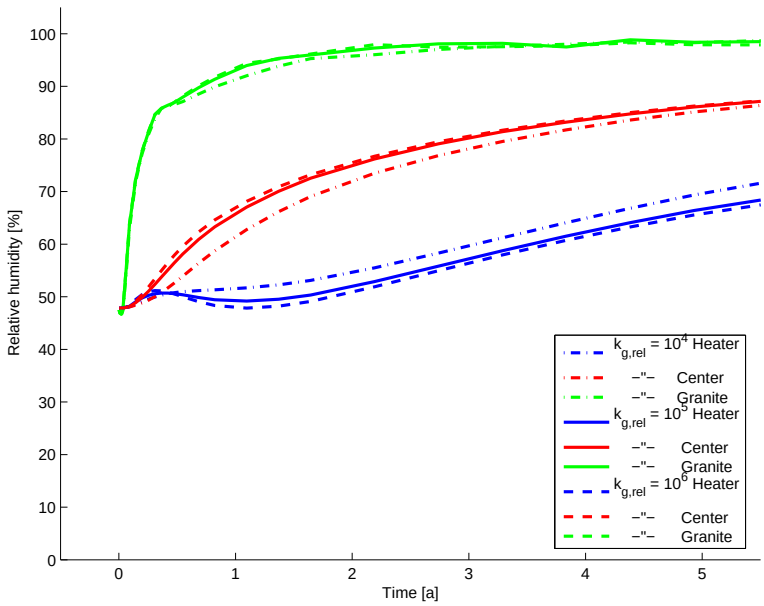

b) Section H.

Figure 7.49: Febex in-situ experiment. Simulated evolution of relative humidity in three material points for sections E1 and H. Sensitivity analysis. Variation of relative permeability of gas.

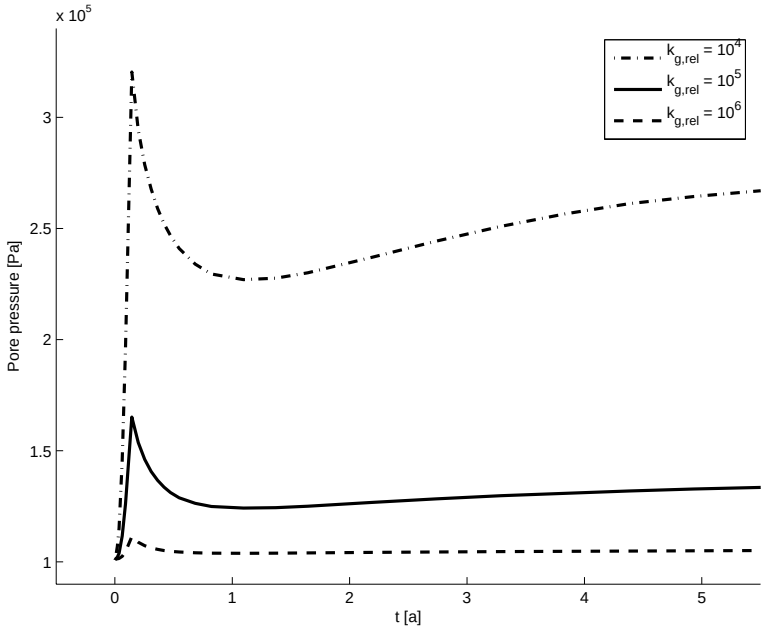

a) Section E1.

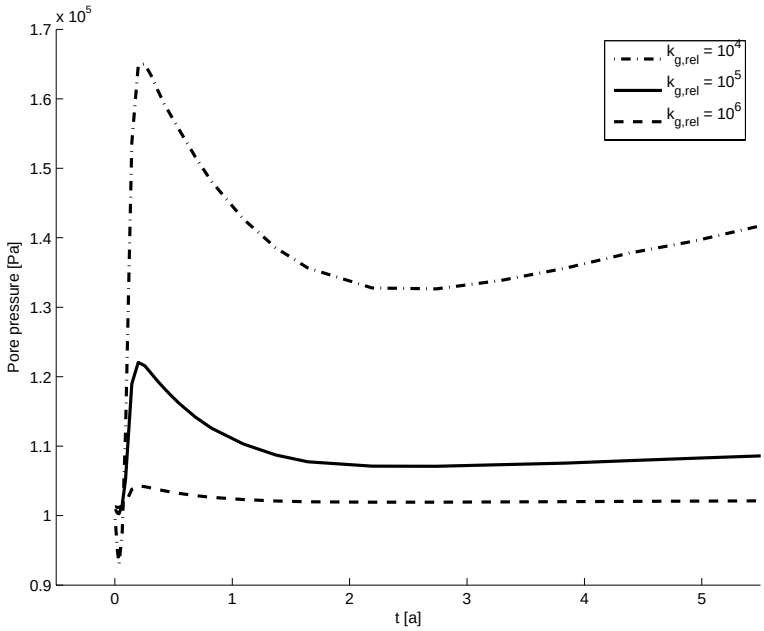

b) Section H.

Figure 7.50: Febex in-situ experiment. Simulated evolution of gaseous pressure at a material point near the heater for sections E1 and H. Sensitivity analysis. Variation of relative permeability of gas.

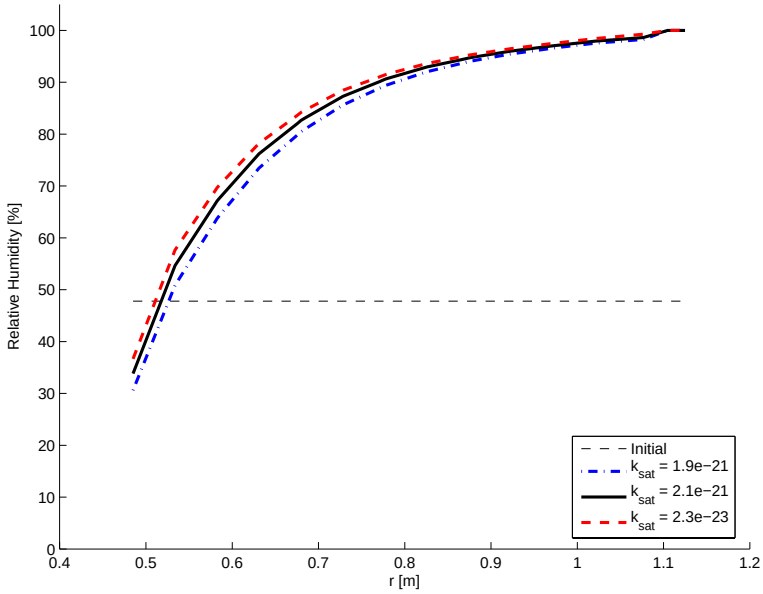

a) Section E1.

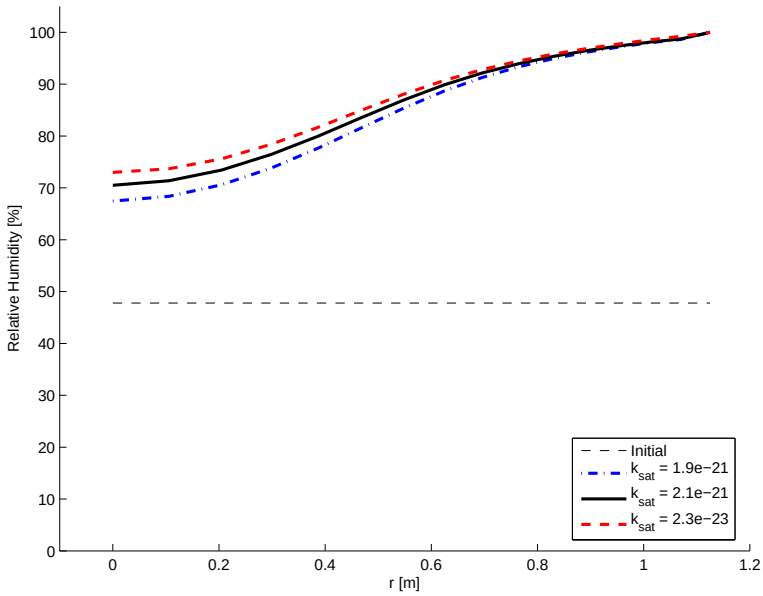

b) Section H.

Figure 7.51: Febex in-situ experiment. Simulated radial profiles of relative humidity for sections E1 and H, at 100 years corresponding to a steady state. Sensitivity analysis. Variation of intrinsic permeability. The dashed line shows the initial profile.

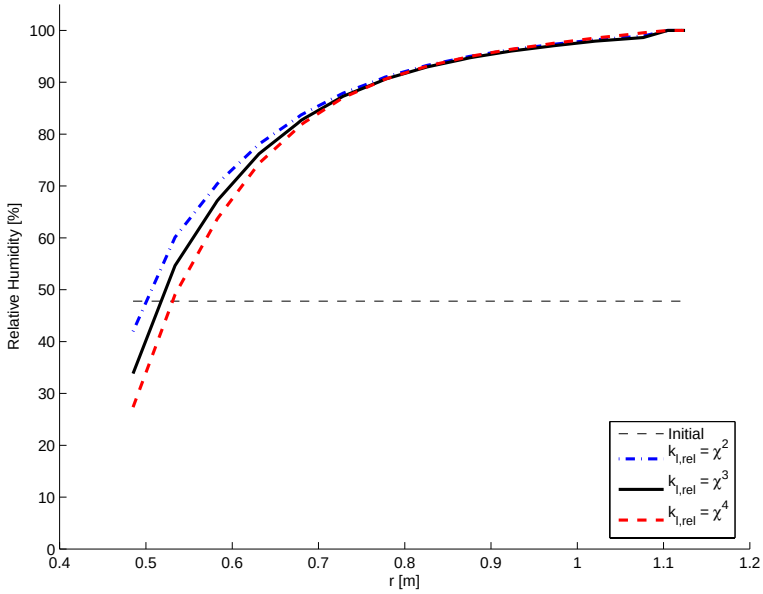

a) Section E1.

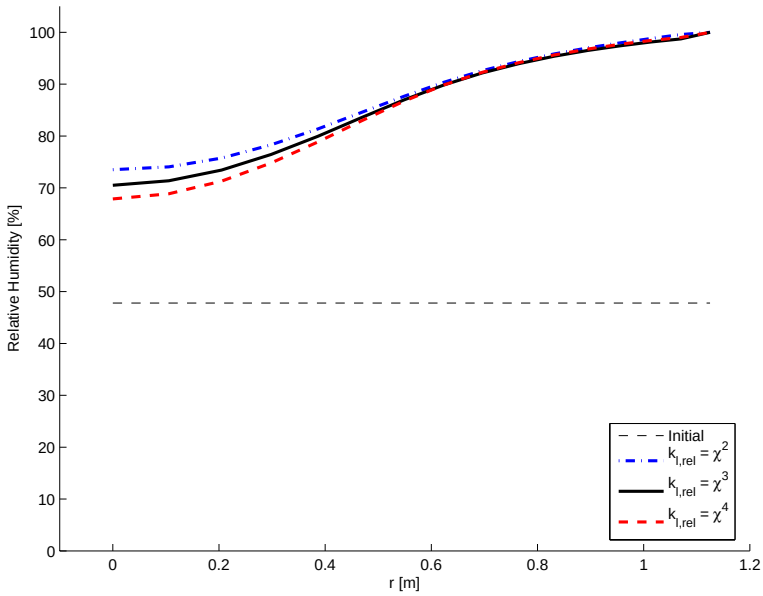

b) Section H.

Figure 7.52: Febex in-situ experiment. Simulated radial profiles of relative humidity for sections E1 and H, at 100 years corresponding to a steady state. Sensitivity analysis. Variation of relative permeability of liquid. The dashed line shows the initial profile.

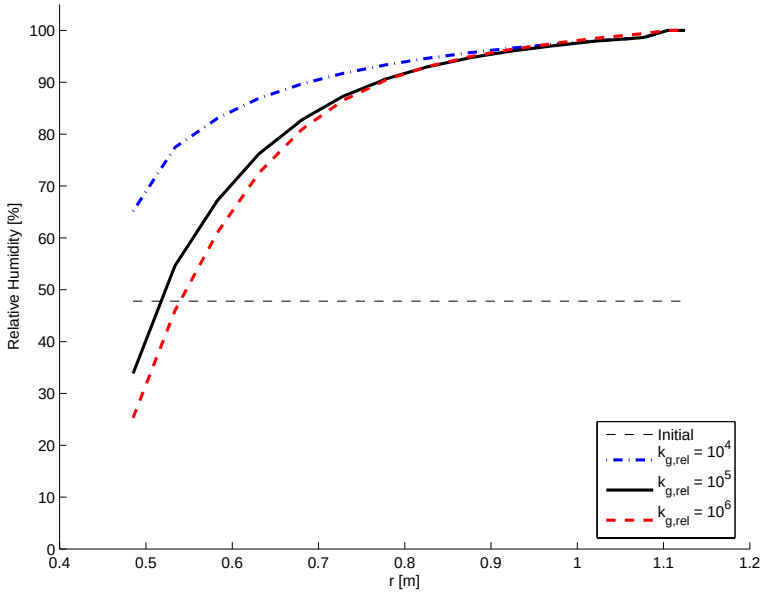

a) Section E1.

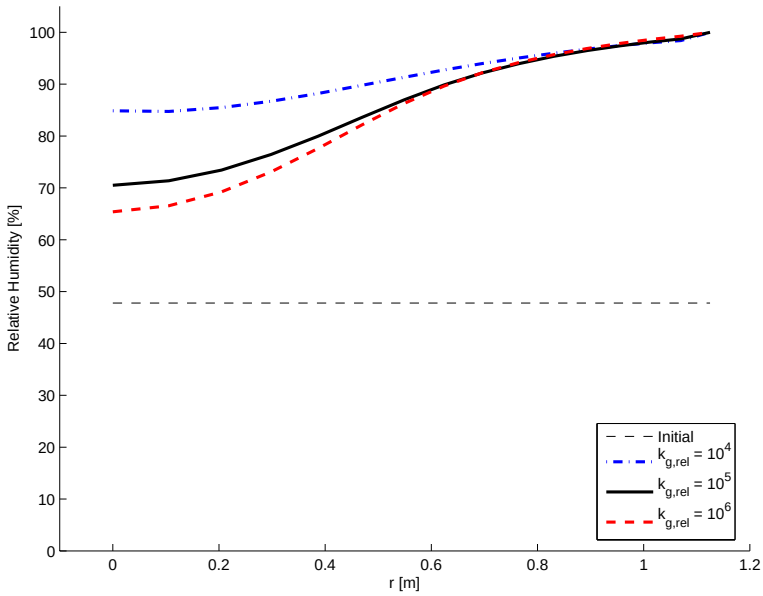

b) Section H.

Figure 7.53: Febex in-situ experiment. Simulated radial profiles of relative humidity for sections E1 and H, at 100 years corresponding to a steady state. Sensitivity analysis. Variation of relative permeability of gas. The dashed line shows the initial profile.

- Thermal Boundary Condition 3: Based on the analyses performed during Task A of the Decovalex-THMC project [89] the temperature of the container surface will rise to a maximum of 60 °C in about 8 years and will gradually decrease to 40 °C in 100 years.

These hypothetical and realistic temperature evolutions of the container surface are illustrated in Figure 7.55.

We now consider only the thermohydraulics and simplifying the current model by neglecting the mechanical behavior and the swelling by setting $G = K = f_{\Pi} = 0$.

Simulated radial profiles of temperature and relative humidity for thermal boundary condition 1 along with the corresponding result for the base case without the rock involved are illustrated in Figure 7.56 for section E1 and in Figure 7.57 for section H.

Simulated radial profiles of temperature and relative humidity for thermal boundary conditions 2 and 3 are illustrated in Figure 7.58 for section E1 and in Figure 7.59 for section H.

7.5.4 Discussion

Basic features and comparison to the observations

The simulation (Figure 7.42) seems apparently to overestimate the temperature near the beginning of the heating. Actually the model underestimates the temperature inside the buffer which phenomenon is overcome by adjusting the thermal boundary condition at the rock. Most importantly, the obtained temperature gradient across the buffer is consistent with the observation.

The observed relative humidity evolution near the heater and in the central portion of the buffer are rather regular and generally consistent with the simulations (Figure 7.43). The observed drying near the heater and the wetting in the center are both slightly faster than in the simulation. In both sections E1 and H there are individual observations in which a similar rapid hydraulic transient occurs as in the Febex mock-up test. Both the simulation and the observation seem to approach a possible unsaturated steady state. Certain individual points near the rock show the influence of the buffer being in contact with wet rock for months before the onset of the heating. However, there is at least one observation of considerably lower water content near the rock indicating the uneven natural conditions.

The simulated relative humidity profiles (Figure 7.46) suggest that an unsaturated steady state is reached at approximately 30 years and the inner

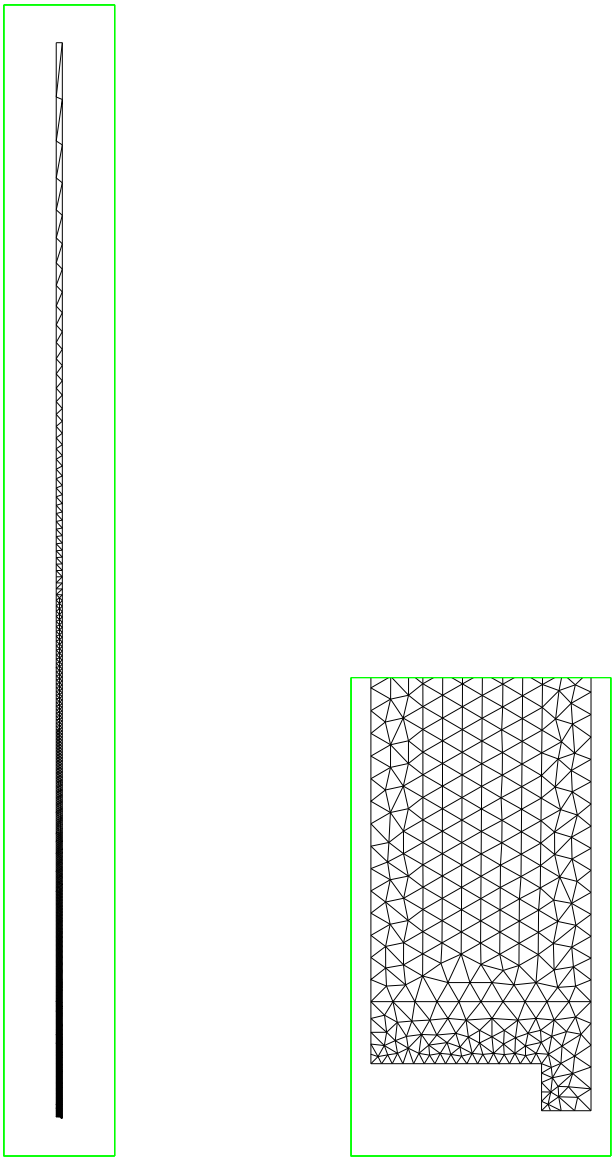

a) Febex in-situ mesh with rock. b) Close-up of the rock-buffer interface.

Figure 7.54: The mesh for the Febex in-situ simulations involving the buffer and the surrounding rock up to 400 m from the axis of the tunnel. The total mesh involves 2796 nodes and 5608 triangular elements.

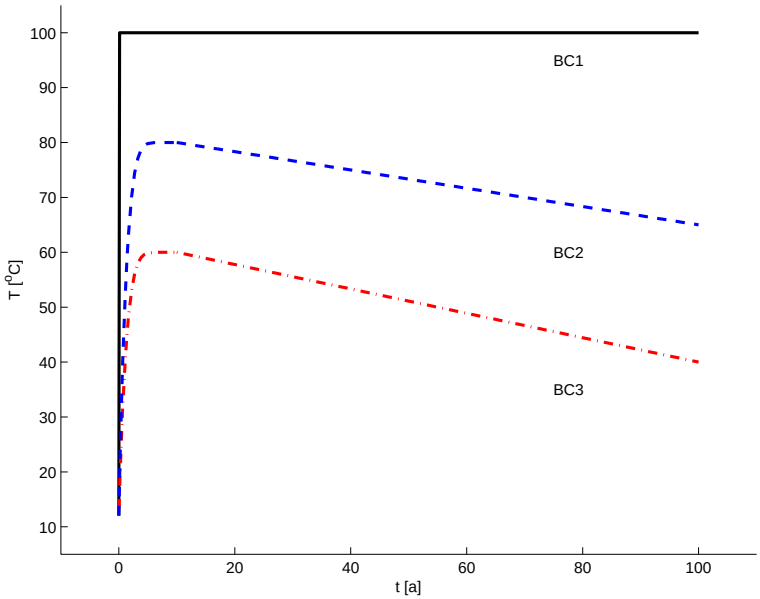

Figure 7.55: Febex in-situ experiment. Three variants for the thermal boundary condition at the heater surface. BC1 is compatible with the actual in-situ experiment in which the heater temperature is kept constantly at 100 °C. BC2 corresponds to a realistic disposal condition [97] with a maximum temperature of 80 °C. BC3 corresponds to a realistic disposal condition [89] with a maximum temperature of 60 °C.

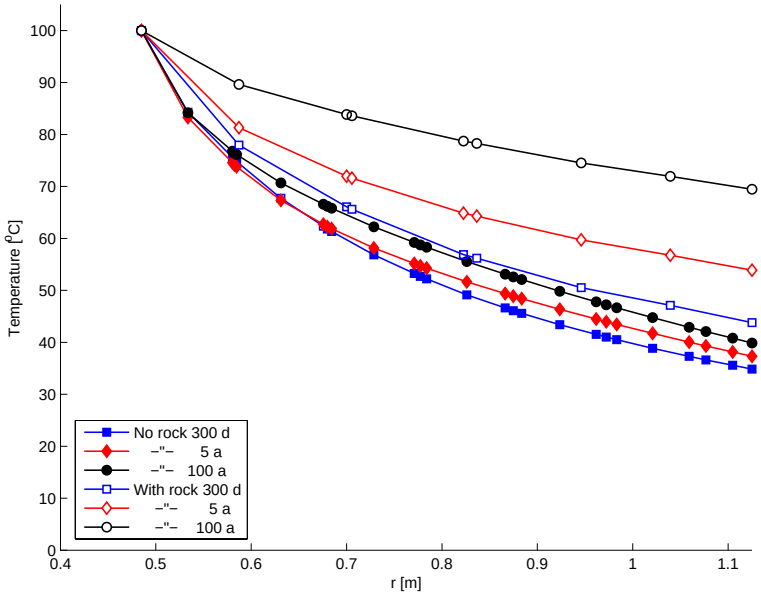

a) Temperature profiles.

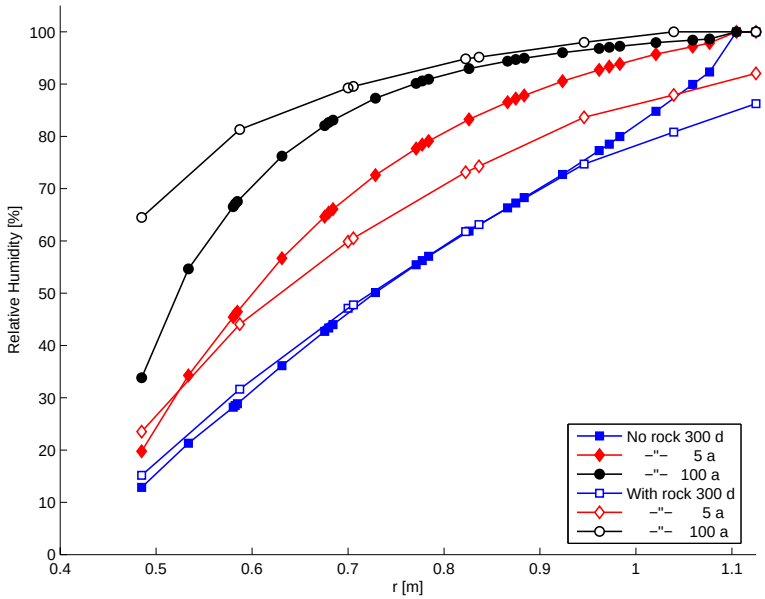

b) Relative humidity profiles.

Figure 7.56: Febex in-situ experiment. Simulated radial profiles of temperature and relative humidity, for section E1. Comparison of the results for the case without the rock involved (solid symbols) and with the rock involved (open symbols).

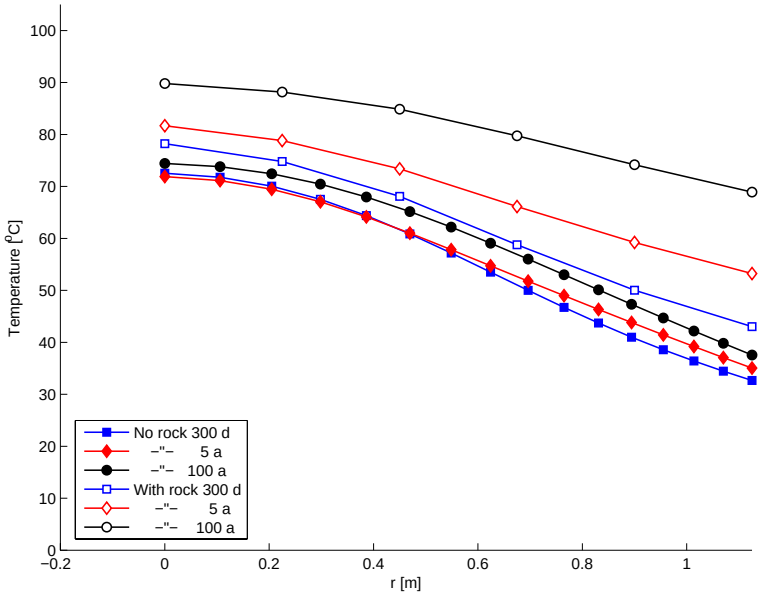

a) Temperature profiles.

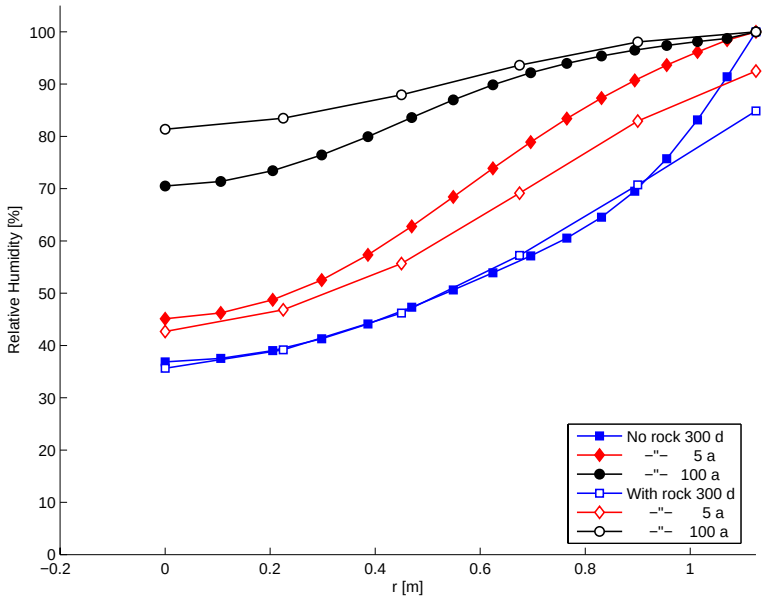

b) Relative humidity profiles.

Figure 7.57: Febex in-situ experiment. Simulated radial profiles of temperature and relative humidity, for section H. Comparison of the results for the case without the rock involved (solid symbols) and with the rock involved (open symbols).

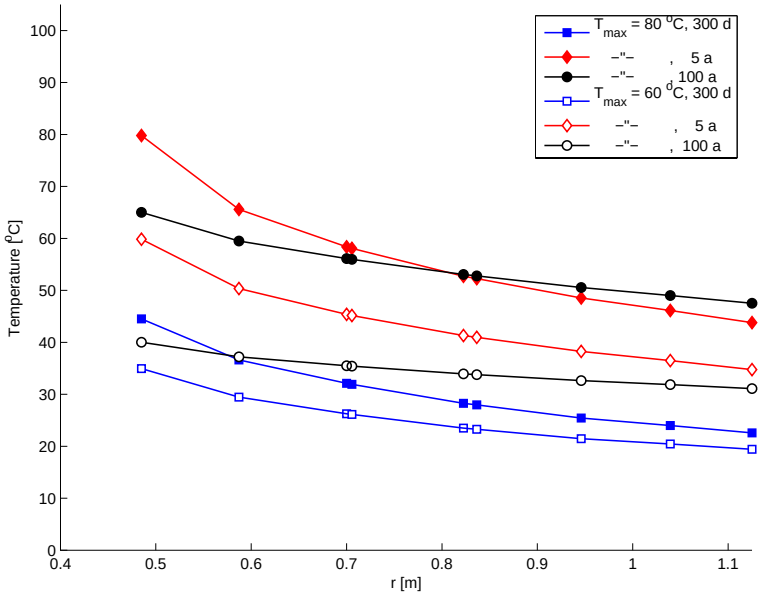

a) Temperature profiles.

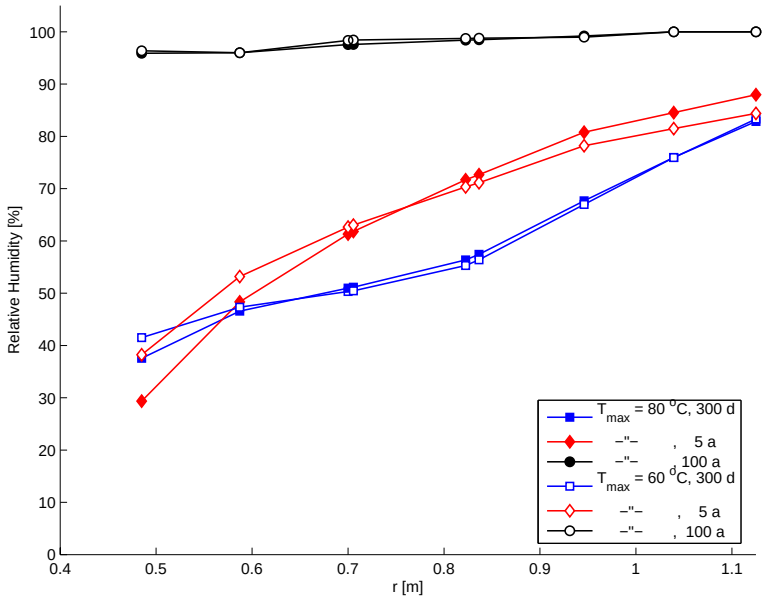

b) Relative humidity profiles.

Figure 7.58: Febex in-situ experiment. Simulated radial profiles of temperature and relative humidity, for section E1. The rock is involved. Comparison of the results for the two hypothetical and realistic cases for the heater temperature evolution

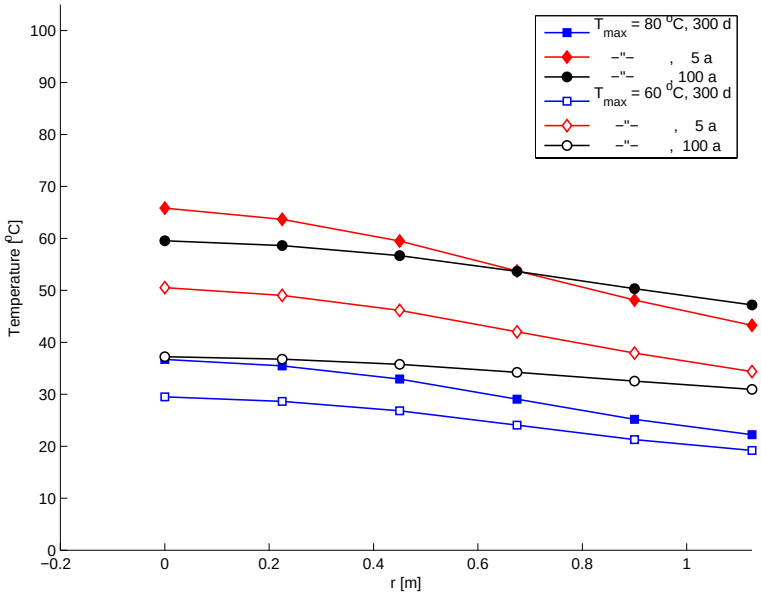

a) Temperature profiles.

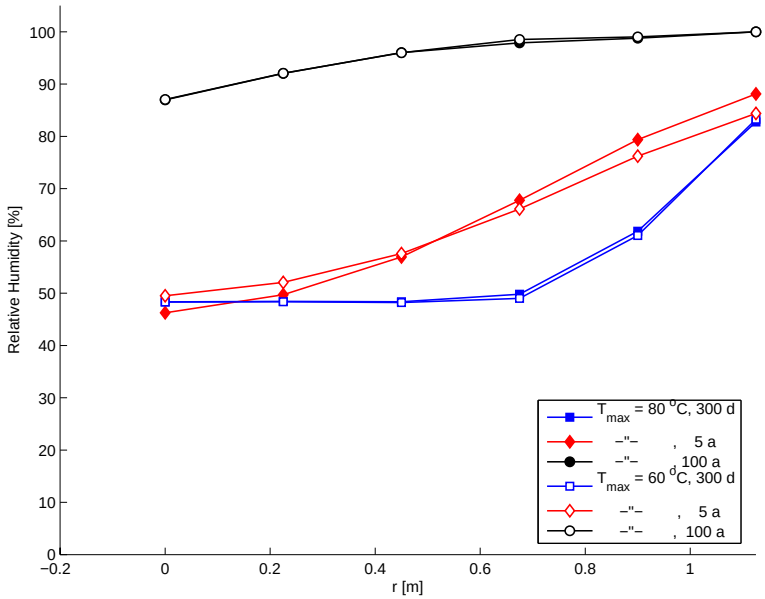

b) Relative humidity profiles.

Figure 7.59: Febex in-situ experiment. Simulated radial profiles of temperature and relative humidity, for section H. The rock is involved. Comparison of the results for the two hypothetical and realistic cases for the heater temperature evolution

buffer keeps relatively dry. For section H the small uniform increase of the relative humidity at 53 d is due to two reasons: mostly because of the swelling of the outer buffer which decreases the porosity of the inner buffer which apparently increases the relative water content in the pores, and secondly because of the condensation of the vapor coming from the hot areas near the heater. The latter reason is more dominant in the section E1 where the heater has more influence on the moisture field.

The simulated porosity evolution (Figure 7.44) shows the swelling behavior. The points near the heater have encountered shrinking. The points near the rock have first swollen when wetted and subsequently shrunken under the swelling pressure exerted by the swelling inner portion of the buffer. At the central points the shrinkage due to the swelling pressure exerted by the wetting outer buffer has in the beginning overcome the swelling due to the increase of the water content by condensation. At 30 years a non-uniform steady state seems to have been obtained.

There is an evident discrepancy between simulated and observed stress (Figure 7.45). The simulated stress near the heater obtains large values due to the contribution of the compression due to the swelling of the outer buffer. The simulated radial stress near the rock increases faster than the observation. The actual situation is very difficult to simulate because the wetting and measuring did not start at the same time and because of the blocky nature of the barrier. The actual stress at least in the beginning of the excercise is expected to be discontinuous because of the block joints. An interlocking phenomenon can have occured before sealing of the joints making the stress field inhomogeneous and discontinuous.

Sensitivity cases

The variation of the permeability parameters yields relative humidity and gaseous pressure evolution results (Figures 7.47–7.50) from which exactly the same conclusions can be drawn as for the corresponding analysis of the Febex mock-up test.

The intrinsic permeability (Figure 7.51) and the relative permeability of liquid (Figure 7.52) have minor influence on the steady state. Increasing of the permeability increases the saturation gradient driven liquid flow towards the heater. Relative permeability of gas (Figure 7.53) has a larger influence on the steady state. This is partly due to the larger uncertainties related to this parameter. Consequently, the used variation range for relative permeability of gas is huge when compared to that of the intrinsic permeability and of the relative permeability of liquid. The inner buffer keeps relatively

dry in all the simulated cases.

Special cases with the rock involved

The temperature of the rock will gradually increase in all of the considered cases, where the rock is taken into account. As a consequence, temperature of the outer buffer is higher and the temperature gradient across the buffer is smaller when the rock is involved. In the beginning the drying of the surrounding rock makes the relative humidity of the buffer smaller near the rock than when the rock is not involved. Towards the end of the simulation outer buffer will get fully saturated while the inner buffer gets wetter than when the rock is not involved.

In the case of thermal boundary condition 1, for the time less than five years, the obtained temperature gradient is not significantly higher than for the case in which the rock is not taken into account. Consequently, the major difference for the relative humidity profiles before five years is due to the slight drying of the rock in the case where the rock is taken into account. At the steady state at 100 years the obtained temperature gradient is small enough so that the steady state relative humidity is considerably closer to a full saturation. Nevertheless, with the taken modelling assumptions an unsaturated steady state is still predicted for the in-situ test.

For the case of thermal boundary conditions 2 and 3, it is interesting to note that the maximum temperature has only a minor influence on the result. With higher maximum temperature the region in the proximity of the container surface will be a little drier after few years. However, the rate of wetting will be approximately the same. A nearly fully saturated state is predicted to be achieved in 100 years.

Chapter 8

Analysis of MX-80 bentonite

8.1 General

The parameter values for MX-80 bentonite are chosen by the simulation of both the small scale laboratory experiments by SKB and the larger scale mock-up experiment by CEA. In practice, the most critical parameters values are chosen here by the simulation of the mock-up test. In the final presented simulations for the SKB laboratory experiments the only varied parameter is the relative permeability of liquid.

The choice for the analysis of these particular experiments originates from the participation to Task A of the international Decovalex-THMC project [17] in which MX-80 bentonite has been chosen as the reference material. The initial condition of dry density and moisture content for the simulations is chosen to be $\rho_{\mathrm{dry}} = 1570$ kg/m^3 and $w = 0.17$ as given in [13]. This choice yields the initial values of saturation degree and porosity as in Eq. (8.1). However, this condition is different from all of the experimental set-ups against which the simulations are to be calibrated. This leads to problems which are discussed in detail later.

Unfortunately, to the authors opinion, no valid experiments similar to those HM tests for Febex bentonite are available to determine the mechanical parameters for MX-80 bentonite. For this reason, the obtained mechanical parameter values for Febex bentonite are also applied for MX-80. As the emphasis here is in the resaturation under thermal load the choice has only a minor influence on the results of the following analysis.

8.2 CEA mock-up experiments

8.2.1 General

In the framework of co-operative research between the French Atomic Energy Commission (CEA), Electricité de France (EDF) and the French National Radioactive Waste Management Agency (Andra), an action has been initiated to characterise swelling clays at high temperature. To observe coupled phenomena especially in high temperature fields, CEA carried out 1D THM experiments on clay cylinders of approximately 20 cm in diameter and height contained in cells. Two identical cells or mock-ups were designed and built in order to test samples of MX-80 bentonite with different initial water contents according to a similar experimental set-up. For both cells the experimental protocol included two successive phases.

Phase 1 was performed with a constant total volume of the blocked bentonite sample without wetting. A high thermal gradient was obtained across the sample by raising the temperature on one face of the sample with the other face remaining at constant temperature. Phase 2 consisted of wetting the confined sample on its cold face while keeping the obtained high temperature difference between the faces.

The CEA mock-up test is a very interesting, useful, and adequately documented experiment. However, the application of the current swelling model to the experiment was not successful due to the following reason. The maximum applied temperature gradient of 130 °C/20 cm is very high. Consequently, there has occurred intensive water redistribution in the samples and corresponding intensive local swelling and shrinking. Although the samples have been confined with constant total volume the encountered large local deformations are beyond the scope of the current model. The calculations with the swelling model diverged after a few time steps.

Consequently, most of the results for CEA mock-up test presented here have been calculated without the swelling model, i.e., by neglecting the swelling interaction function. The limited amount of the presented results obtained for the swelling model illustrate the beginning of the swelling pressure build-up and the influence of the swelling model to the moisture evolution at the early stages of the experiments.

For the simulations the 2-dimensional axially symmetric domain (Figure 8.1a) was meshed (Figure 8.1b) with 341 nodes and 300 quadrilateral elements. The initial values were

$$\{\eta, \chi, \hat{B}, \mathbf{u}, T\}_{\text{init}} = \{0.4353, 0.6144, \hat{B}_0, \mathbf{0}, T_0\}. \tag{8.1}$$

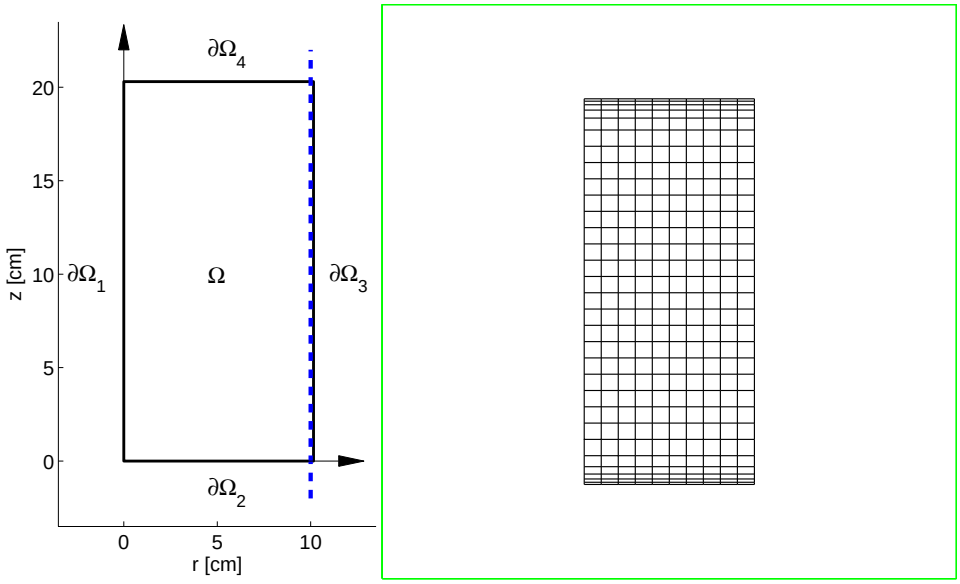

a) CEA geometry. b) CEA mesh.

Figure 8.1: a) The axially symmetric 2-dimensional domain for the CEA simulations along with the boundary notations and the position of the line for the pointwise results (dashed line). b) The corresponding mesh with 341 nodes and 300 quadrilateral elements.

Table 8.1: The hydraulic parameters in the simulation of the CEA mock-up and SKB small scale experiments for MX-80bentonite.

CASE	k_{sat} [m^2]	$k_{\text{l,rel}}$ [-]	$k_{\text{g,rel}}$ [-]
lower variant	$4.0{\cdot}10^{-21}$	χ^2	10^2
base case	$5.25{\cdot}10^{-21}$	χ^3	10^3
upper variant	$6.5{\cdot}10^{-21}$	χ^4	10^4

For the mechanical parameters, the base case values for the Febex bentonite were used (Table 7.1). The sensitivity cases are given in Table 8.1.

Phase 1

The calculation of the Phase 1 reaching 113 days involved 18 time steps the sizes of which varied between 1 to 10 days. The boundary conditions (Figure 8.1a) were the following.

$$\begin{aligned} \mathbf{u}\cdot\mathbf{n} = 0 \quad &\text{on} \quad \partial\Omega_{1,3}, \\ \mathbf{u}\cdot\mathbf{n} = 0,\ T = T(t) \quad &\text{on} \quad \partial\Omega_{2}, \\ \hat{B} = \hat{B}_0,\ \mathbf{u}\cdot\mathbf{n} = 0,\ T = (20+273.15)\ K \quad &\text{on} \quad \partial\Omega_{4}, \end{aligned}$$

where the heater temperature is set to increase piecewise linearly from the initial value of $T_{\text{init}} = T_0$ to the constant maximum value of $T_{\max} = 150$ °C in two steps in the following way

$$T(t) = \begin{cases} T_0 + \frac{T_1 - T_0}{t_1} t & \text{for} \quad 0 < t < t_1, \\ T_1 + \frac{T_2 - T_1}{t_2 - t_1}(t - t_1) & \text{for} \quad t_1 < t < t_2, \\ T_2 & \text{for} \quad t > t_2, \end{cases} \tag{8.2}$$

where $t_1 = 34$ d, $t_2 = 113$ d, $T_1 = 100$ °C, and $T_2 = 150$ °C.

Phase 2

The calculation of the Phase 2 with the time span of 113...368 days involved 21 time steps the sizes of which varied between 1 to 20 days. The boundary conditions (Figure 8.1a) were the following.

$$\begin{aligned} \mathbf{u}\cdot\mathbf{n} = 0 \quad &\text{on} \quad \partial\Omega_{1,3}, \\ \mathbf{u}\cdot\mathbf{n} = 0,\ T = (150+273.15)\ \text{K} \quad &\text{on} \quad \partial\Omega_{2}, \\ \chi = \chi_{\max},\ \hat{B} = \hat{B}_0,\ \mathbf{u}\cdot\mathbf{n} = 0,\ T = (20+273.15)\ \text{K} \quad &\text{on} \quad \partial\Omega_{4}. \end{aligned}$$

8.2.2 Results

Comparison to observations

The comparative simulations for relative humidity and temperature are performed without the swelling model.

- Comparison of simulated and measured evolution of temperature in four material points is shown in Figure 8.2a for $k_{\mathrm{l,rel}} = \chi^3$ and in Figure 8.2b for $k_{\mathrm{l,rel}} = \chi^2$. The observed temperature is shown for Sample 1 only, because the result for Sample 2 is almost identical.
- Comparison of observed evolution of relative humidity at three material points for the two samples and the corresponding simulation without the swelling model and with liquid relative permeability of $k_{\mathrm{l,rel}} = \chi^3$ is shown in Figure 8.3. The corresponding comparison with the simulated results with liquid relative permeability of $k_{\mathrm{l,rel}} = \chi^2$ is shown in Figure 8.4.

Sensitivity cases

The sensitivity cases are simulated without the swelling model.

- Simulated evolution of relative humidity at three material points for three different values of intrinsic permeability is shown in Figure 8.5.
- Simulated evolution of relative humidity at three material points for three different values of relative permeability of liquid is shown in Figure 8.6.
- Simulated evolution of relative humidity at three material points for three different values of relative permeability of gas is shown in Figure 8.7.
- Simulated evolution of pore pressure at two material points for three values of relative permeability of gas is shown in Figure 8.8.

Results with the swelling model

Results with the swelling model were achieved for the first few time-steps reaching the first 23 days of the experiment.

- Comparison of simulated and measured evolution of axial stress at the top of the Samples 1 and 2 is shown in Figure 8.9. The illustrated stress is an overburden pressure above the preapplied stress of approximately 0.5 MPa.
- Comparison of the simulated evolution of relative humidity at three material points with and without the swelling model in the base case is shown in Figure 8.10.

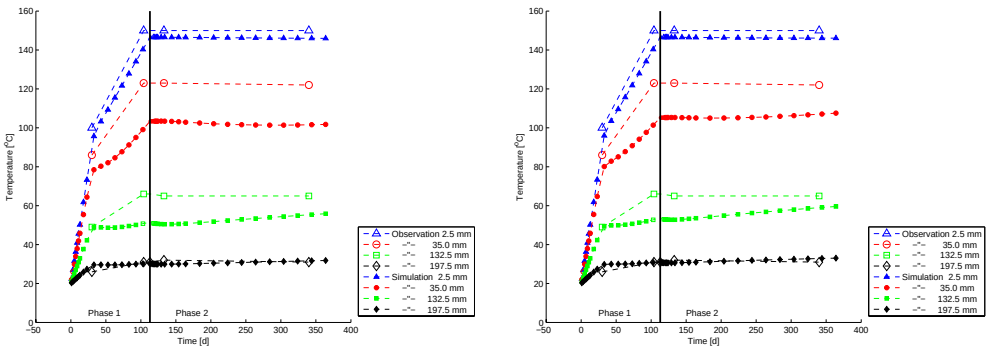

a) $k_{\mathrm{l,rel}} = \chi^3$. b) $k_{\mathrm{l,rel}} = \chi^2$.

Figure 8.2: CEA mock-up experiment. Simulated and measured evolution of temperature at four material points. Simulation without swelling and with relative liquid permeability of $k_{\mathrm{l,rel}} = \chi^3$ and χ^2.

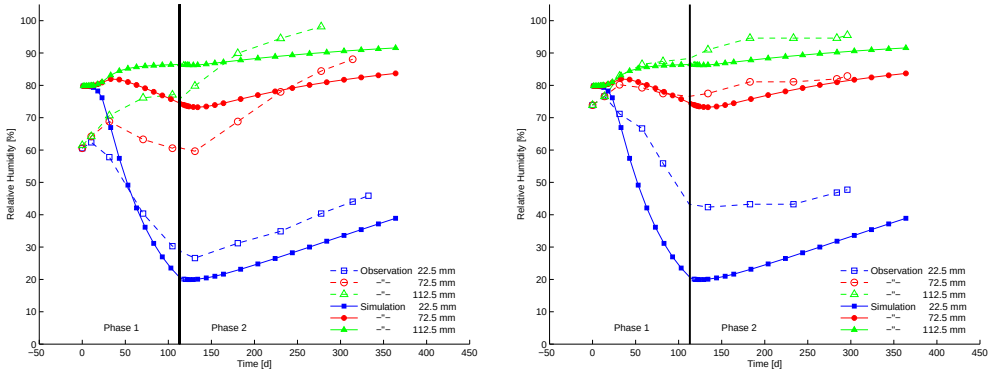

a) Sample 1. b) Sample 2.

Figure 8.3: CEA mock-up experiment. Simulated and measured evolution of relative humidity at three material points of two different samples with different initial moisture content. Simulation without swelling and with relative permeability of $k_{\mathrm{l,rel}} = \chi^3$.

8.2.3 Discussion

Comparison to observations

The simulation underestimates the temperature of the inner points of the sample (Figure 8.2) as the vaporization in the model cools the sample too much. This phenomenon was less observable for the Febex analyses (e.g., Figures 7.17, 7.30, 7.42) because of the cylindrical geometries and adjustable temperature boundary conditions.

The clear discrepancy between the observation and the simulation is attributed here to the use of heat conductivity which has been assessed with uncoupled thermal equation. In the current approach phase change affects the temperature and the thermal conductivity should be assessed accordingly.

Increasing the exponent of the relative permeability of liquid decreases the liquid permeability and, consequently, decreases the liquid flow towards the hot zone. As a consequence, the gaseous pressure and vaporization are decreased and temperature is slightly higher. A most important observation is that the observed moisture evolution in the CEA mock-up test (Figures 8.3 and 8.4) does not exhibit the transient phenomenon encountered in the Febex mock-up and in-situ experiments (e.g. Figures 7.31, 7.43). Instead, the simulated and the observed results are quite similar from the very beginning of the experiment. In this case, relative liquid permeability of $k_{\mathrm{l,rel}} = \chi^2$

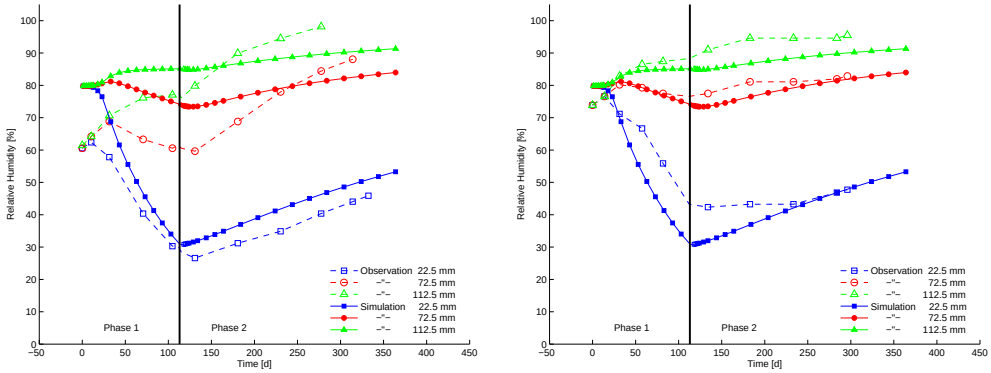

a) Sample 1. b) Sample 2.

Figure 8.4: CEA mock-up experiment. Simulated and measured evolution of relative humidity at three material points of two different samples with different initial moisture content. Simulation without swelling and with relative permeability of $k_{\mathrm{l,rel}} = \chi^2$.

leads to a better fit in Figure 8.4.

Sensitivity cases

The same phenomena related to variation of permeability parameters is observed in the simulated results for CEA mock-up experiment as was for the Febex experiments.

Intrinsic permeability does not affect the rate of change of water distribution in Phase 1 (see Figure 8.5). On the contrary, the effect on the rate of wetting in Phase 2 is obvious. Increasing of the intrinsic permeability increases the gradient driven liquid flow towards the heater. This phenomenon restricts the vaporization dominated moisture redistribution. The parameter also seems to affect the hypothetical steady state which has not yet been achieved in the time of experiment duration.

Increasing of the exponent of the relative permeability of liquid decreases the liquid permeability and restricts the rate of change of water distribution in Phase 1 (see Figure 8.6). In Phase 2, the rate of wetting is almost unaffected. In the beginning of Phase 2 the sample is the wettest for the case of $k_{\mathrm{l,rel}} = \chi^2$. Consequently, for this case the approaching steady state is the most obvious at the end of the experiment.

Increasing of the relative permeability of gas decreases the rate of change of water distribution in both Phases 1 and 2. The predicted hypothetical

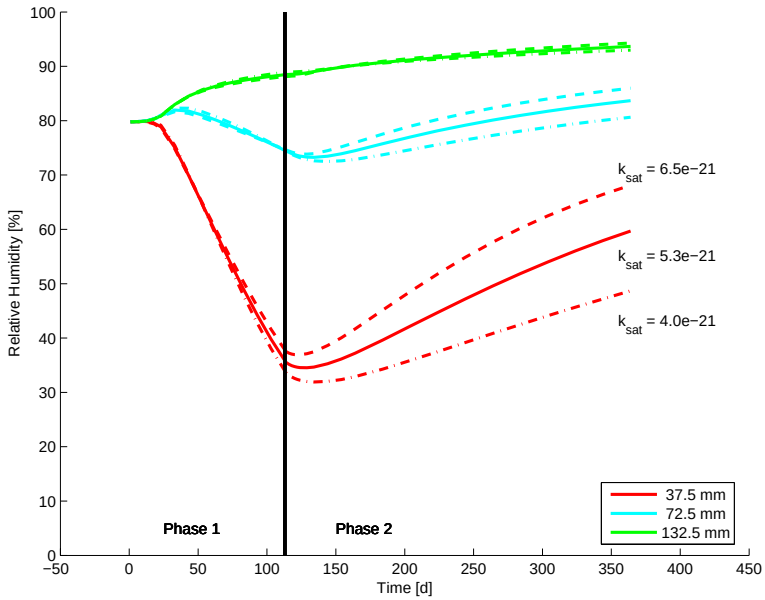

Figure 8.5: CEA mock-up experiment. Simulated evolution of relative humidity at three material points. Sensitivity analysis. Variation of intrinsic permeability. Base case is that of $k_{\text{sat}} = 5.25 \cdot 10^{-21}$ m^2.

steady state changes with gaseous permeability - increasing of the gaseous permeability makes the sample drier at the heater. Decreasing of the permeability increases the vaporization driven gaseous pressure build-up. As a consequence, quite large pore pressures are predicted by the simulation. The measurements, on the contrary, have shown virtually no change to the normal pore pressure. In the model this would correspond to high relative permeability of gas (at least $k_{\text{g,rel}} = 10^4$) and, consequently, intense water redistribution and quite dry hypothetical steady state. However, it can be questioned if the measured pore pressure results have any physical meaning, e.g. correspond to undisturbed state in the sample. Measuring always changes the target to be measured especially in the case of gaseous pressure. The measuring probe is larger than the pore scale and the permeability of the interface between the probe and the wire is likely to be much different from that of the intact porous sample. More precisely, the surroundings of the measuring device penetrating into the sample is a preferable route for the gas flow. Along this route gaseous pressure build-up does not occur, or, at least is drastically decreased when compared to the situation inside the

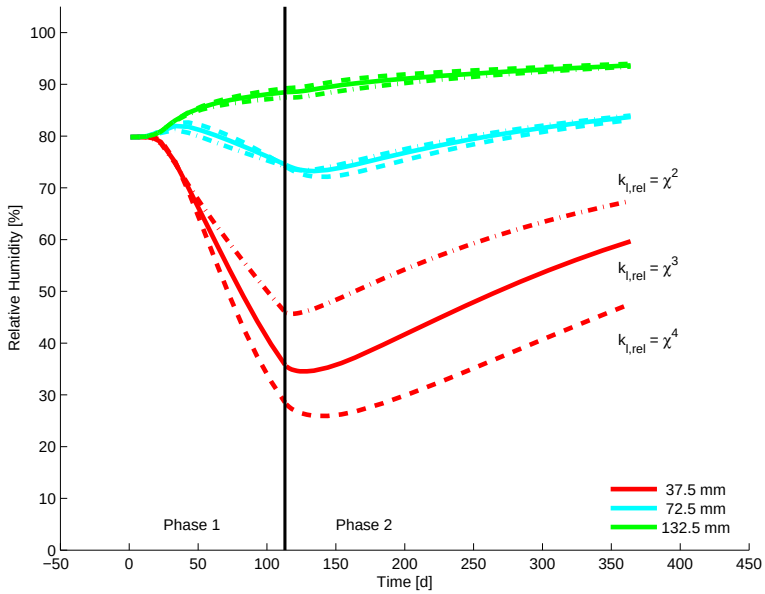

Figure 8.6: CEA mock-up experiment. Simulated (without the swelling model) evolution of relative humidity at three material points. Sensitivity analysis. Variation of relative permeability of liquid. Base case is that of $k_{\mathrm{l,rel}} = \chi^3$.

intact sample.

Results with the swelling model

The swelling model makes the numerical calculation unstable because the thermal load and the consequential water redistribution and swelling/shrinking are too intensive and the system is bound to take large local deformations. However, results are obtained up to 24 days after the start of the experiment.

The observed swelling stresses at the top of the samples (Figure 8.9) reveal the unsymmetry of the moisture swelling; high swelling pressure is observed even without extra wetting of the samples. Mere redistribution of the initial water content is enough to produce a significant swelling pressure. Relative shrinkage due to the loss of water content is smaller than the relative swelling with an equal change of water content. The simulated stress exhibits the same trend but is a clear underestimation. The illustrated stress is an overburden pressure above the preapplied 0.5 MPa stress.

Comparison of the results calculated with and without swelling reveals

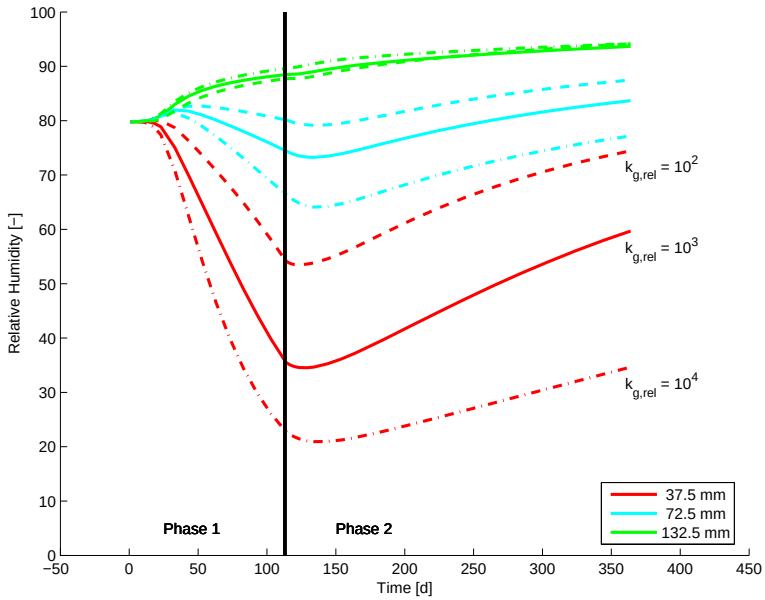

Figure 8.7: CEA mock-up experiment. Simulated (without the swelling model) evolution of relative humidity at three material points. Sensitivity analysis. Variation of relative permeability of gas. Base case is that of $k_{\mathrm{g,rel}} = 10^3$.

that taking swelling into account makes the water redistribution less intensive (Figure 8.10).

The swelling model restricts or smoothens the water redistribution in the following two ways.

1. **By definitions of saturation and relative humidity**: At the hot region the material shrinks and porosity decreases because of the drying. Because saturation is defined as the ratio of liquid volume fraction and porosity, the apparent saturation decreases less than without shrinking. At the cold region the opposite phenomenon occurs restricting the apparent increase of saturation.

   In a similar manner, relative humidity depends on the ratio of solid and liquid volume fractions. Shrinking at the hot region increases this ratio. As a consequence, decreasing of relative humidity is restricted when the swelling model is incorporated.

2. **By physical reason**: The adsorption function and the resulting suc-

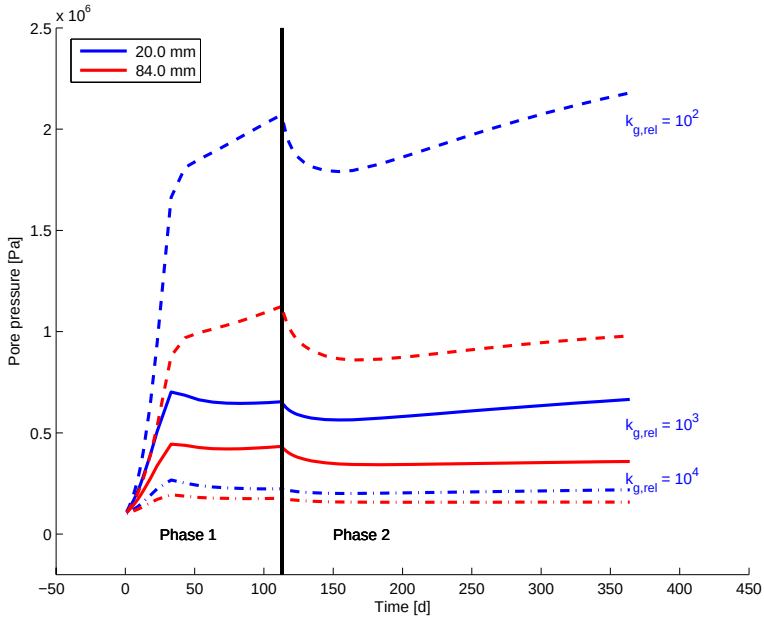

Figure 8.8: CEA mock-up experiment. Simulated evolution of pore pressure for two material points. Sensitivity analysis. Variation of relative permeability of gas.

tion depend on the solid-liquid ratio. Increasing of the ratio increases the suction and vice versa. In other words, shrinking of the material because of drying increases the suction more than drying without the shrinking. Consequently, shrinking increases the suction and restricts further drying. At the cold face the opposite occurs. Swelling of the material because of wetting decreases the solid-liquid-ratio. As a consequence, the suction ability of the material decreases more than without swelling and the rate of wetting is decreased.

In the actual case, however, swelling and shrinking affect the rate of wetting and drying in a more complicated way by changing the porous network and the permeability. This is not taken into account in the current model. The effect of swelling and shrinking would affect the water redistribution in different ways depending on the modelling assumptions for the porous structure.

- By a coarse approximation the porous network could be assumed to be homogeneous enough for the water flow to occur through the to-

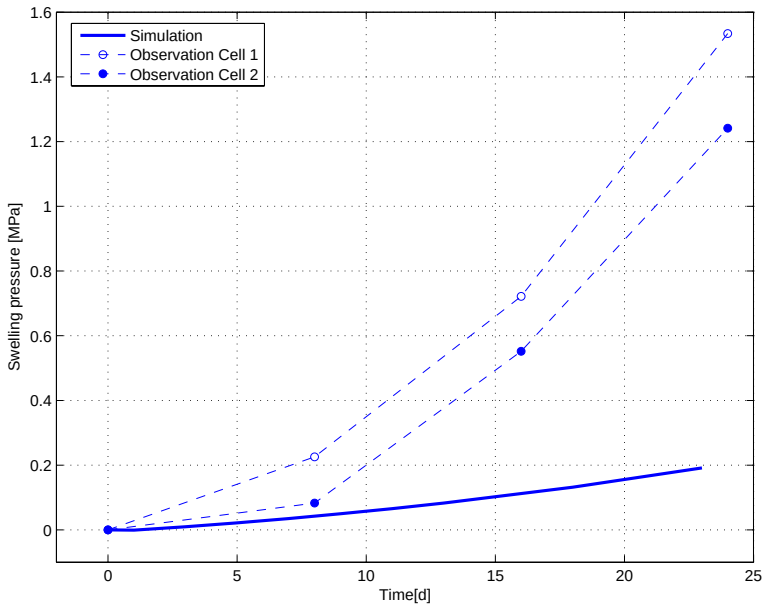

Figure 8.9: CEA mock-up experiment. Simulated and measured evolution of axial stress at the top of the samples 1 and 2. The illustrated stress is an overburden pressure above the preapplied 0.5 MPa stress.

tal porosity on which the intrinsic permeability depends. In this case swelling at the cold region increases the local porosity and the permeability while shrinking at the hot region decreases the local permeability. Depending on the dynamics of this coupled phemonenon, the swelling-shrinking effect can either enhance or restrict the water redistribution.

- A more realistic assumption would be to divide the total porosity in at least two categories: microporosity between the clay platelets and the macroporosity between the aggregates, i.e., $\eta_{\text{Total}} = \eta_{\text{Macro}} + \eta_{\text{micro}}$. ([41], [87]). With this assumption the fluid flow occurs mainly through the macroporous network and a change in the water content affects mostly the microporosity. If we further assume that the total volume and the total porosity are approximately unchanged, a change in one type of porosity causes a change of opposite direction in the other type of porosity. In this case, shrinking at the hot region decreases the microporosity and increases the macroporosity, consequently, increasing the permeability and the rate of fluid flow. At the cold region,

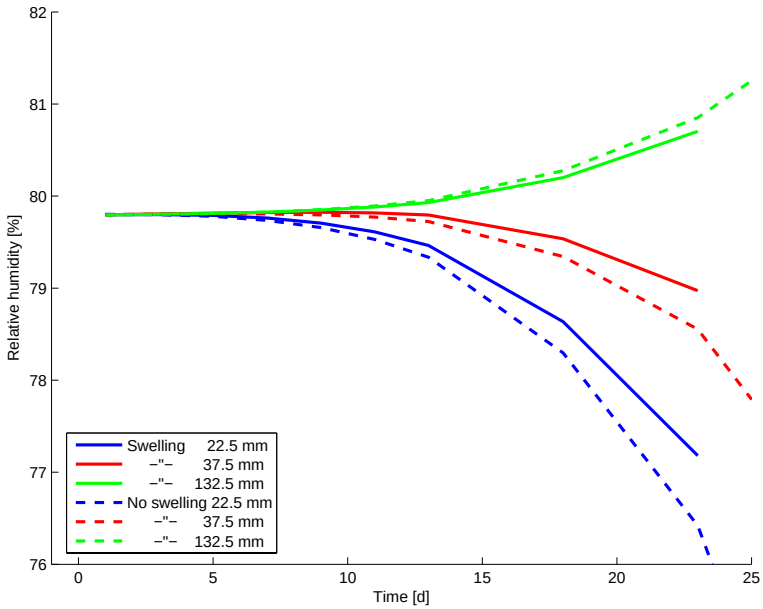

Figure 8.10: CEA mock-up experiment. Simulated evolution of relative humidity at three material points. Comparison of the results calculated with and without the swelling taken into account.

on the other hand, swelling increases the microporosity and decreases the macroporosity, consequently, decreasing the permeability and fluid flow. As a conclusion, the swelling-shrinking phenomenon can either enhance or restrict the water redistribution the net effect being exactly the opposite than in the previous assumption of one type of porosity.

To conclude, the neglected effect of swelling and shrinking on the porous network can influence the water redistribution in a way which is difficult to characterize. Definite conclusions on the actually occuring phenomena are very difficult to draw from experiments. On the other hand, the chosen simple approach for the swelling model with a single type of porosity restricts the water redistribution in an expected manner.

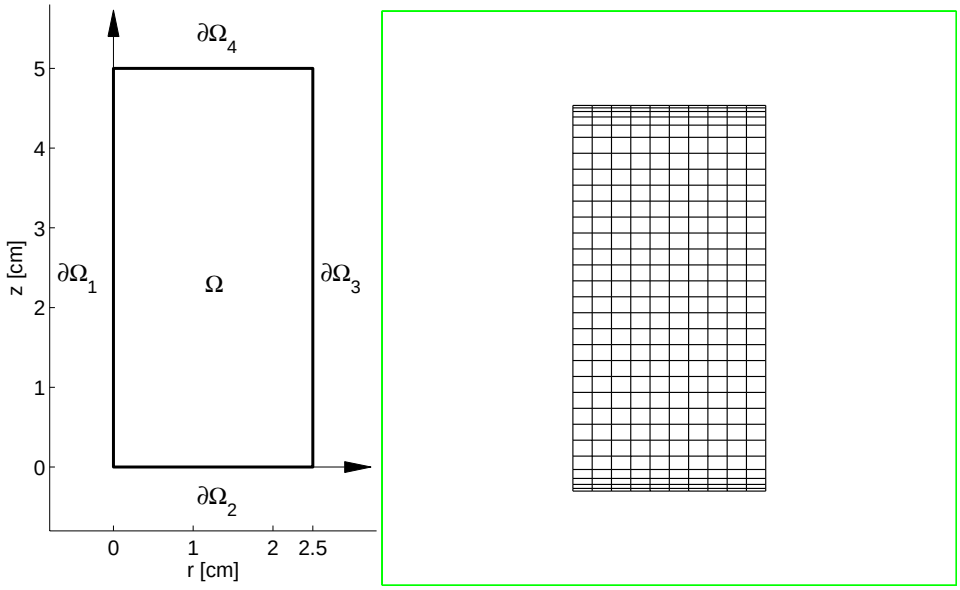

a) SKB geometry. b) SKB mesh.

Figure 8.11: a) The axially symmetric 2-dimensional domain for the SKB simulations along with the boundary notations. b) The corresponding mesh with 341 nodes and 300 quadrilateral elements.

8.3 SKB laboratory experiments

8.3.1 General

Swedish Nuclear Fuel and Waste Management Co (SKB) has presented a series of basic laboratory tests with small samples [13]. Two types of experiments utilized here, water uptake and temperature gradient test, can be used to determine the flow parameters as was done in the international Decovalex-THMC project [17].

Water uptake tests

These tests are performed by confining initially unsaturated samples in stiff cylinders and applying water through a filter stone at one end of the sample whereby the water is gradually sucked by the sample. The test is terminated at different times for different samples. The sample is then sliced into a number of pieces and the water ratio and, if possible, also the density of each piece is determined. The degree of saturation and void ratio are then

plotted as a function of the distance from the water inlet.

Temperature gradient tests

These tests are performed in a stiff oedometer with water tight boundaries by applying a constant temperature difference of 50 °C along the 5 cm long sample. The tests are terminated after different times and the samples sliced in the same way as in the water uptake tests. With these tests the degree of saturation and the void ratio can be plotted as a function of the distance to the hot end.

Several temperature gradient tests at different water ratios and temperature have been performed. Unfortunately, these tests were made at the initial void ratio of $\varepsilon = 1.0$ which differs considerably from our reference case of $\varepsilon = 0.77$. Consequently, a proper fitting of the model can not be done by means of these experiments.

A simple choice for the parameters is adopted. The mechanical parameters are the base case values from the Febex experiments (Table 7.1). Only the base case values of intrinsic permeability and relative permeability of gas are used (Table 8.1). For relative permeability of liquid the values $k_{\mathrm{l,rel}} \in \{\chi^2, \chi^3\}$ are used.

The same cylindrical calculation geometry is used as for the CEA mock-up experiment simulation. The 2-dimensional axially symmetric domain (Figure 8.11a) was meshed (Figure 8.11b) with 341 nodes and 300 quadrilateral elements. The illustrated results are calculated weighted averages of the corresponding quantities at the cylindrical cross-sections. The averaging procedure is presented in the appendix. The initial values were the same as for the CEA simulation, i.e.,

$$\{\eta, \chi, \hat{B}, \mathbf{u}, T\}_{\mathrm{init}} = \{0.4353, 0.6144, \hat{B}_0, \mathbf{0}, T_0\}. \tag{8.3}$$

The calculation of the water uptake experiment reaching 4 weeks involved 28 time steps of 1 day. The boundary conditions (Figure 8.11a) were the following.

$$\begin{aligned} \mathbf{u}\cdot\mathbf{n} = 0 \quad &\text{on} \quad \partial\Omega_{1,3}, \\ \hat{B} = \hat{B}_0,\ \chi = \chi_{\max},\ \mathbf{u}\cdot\mathbf{n} = 0, \quad &\text{on} \quad \partial\Omega_2, \\ \hat{B} = \hat{B}_0,\ \mathbf{u}\cdot\mathbf{n} = 0, \quad &\text{on} \quad \partial\Omega_4. \end{aligned}$$

The calculation of the temperature gradient experiment reaching 4 weeks involved 18 time steps the sizes of which varied between 1 to 10 days. The

boundary conditions (Figure 8.11a) were the following.

$$\begin{aligned} \mathbf{u}\cdot\mathbf{n} = 0 \quad &\text{on} \quad \partial\Omega_{1,3}, \\ \mathbf{u}\cdot\mathbf{n} = 0,\ T = (70+273.15)\ K \quad &\text{on} \quad \partial\Omega_{2}, \\ \hat{B} = \hat{B}_0,\ \mathbf{u}\cdot\mathbf{n} = 0,\ T = (20+273.15)\ K \quad &\text{on} \quad \partial\Omega_{4}. \end{aligned}$$

At the hot boundary $\partial\Omega_4$ the two variants for the gaseous pressure boundary condition for temperature gradient experiment were free gaseous pressure and constant gaseous pressure.

8.3.2 Results

Water uptake experiment

Comparison of simulated and observed profiles of water ratio, saturation, and void ratio for three different time points for the water uptake experiment is illustrated in Figure 8.12. The simulated results for relative liquid permeability of $k_{\mathrm{l,rel}} = \chi^3$ are on the left hand side in Figures 8.12a–c and the corresponding results for $k_{\mathrm{l,rel}} = \chi^2$ are on the right hand side in Figures 8.12d–f.

Temperature gradient experiment

The swelling model is incapable of reproducing the whole range of the temperature gradient test. Consequently, some of the simulations are performed without the swelling model. Results for three different cases are illustrated. For all the cases in Figures 8.13–8.16 the simulated results for relative permeability of liquid of $k_{\mathrm{l,rel}} = \chi^3$ are on the left hand side and the corresponding results for $k_{\mathrm{l,rel}} = \chi^2$ are on the right hand side.

- **Case 1**: The swelling is taken into account and the gaseous pressure is set free at the hot boundary. Comparison of simulated and observed profiles of water ratio and saturation for two different time points for the temperature gradient experiment is illustrated in Figure 8.13. The corresponding comparison for respective profiles of void ratio and pore pressure is illustrated in Figure 8.14.

- **Case 2**: The swelling is neglected and the gaseous pressure is set free at the hot boundary. Comparison of simulated and observed profiles of water ratio, saturation, and pore pressure for four different time points for the temperature gradient experiment is illustrated in Figure 8.15.

- **Case 3**: The swelling is neglected and the gaseous pressure is set to be constant normal pressure at every boundary. Comparison of simulated and observed profiles of water ratio, saturation, and pore pressure for four different points of time of the temperature gradient experiment is illustrated in Figure 8.16.

8.3.3 Discussion

Water uptake experiment

The general simulation result for the water uptake experiment in Figure 8.12 agrees with the experimental result and can be physically explained as follows. In the beginning, to conserve the total volume the drier region has to shrink as the wetter region swells gradually along with the wetting. After that, as the drier region gets gradually wet and starts to swell, the wetter region has to shrink again. Consequently, the porosity profile finally approaches the initial constant one. Full resaturation of the sample is not obtained in the considered four weeks duration of the experiment.

The influence of the relative permeability of liquid on the result is rather small and follows the physically reasonable line found in the simulations of the other experiments (see e.g. the simulation and discussion of the Febex experiments). Decreasing of the exponent from 3 to 2 increases the unsaturated relative permeability of liquid. Consequently, the corresponding wetting and swelling are faster and more uniform across the sample.

The simulated result exhibits faster resaturation than the observed one. This is reasonable because of the higher average void ratio in the simulation because of which the permeability is higher. Furthermore, the high local porosity changes encountered in the observations have a significant effect also on the local intrinsic permeability of the material. In other words, the permeability of the swollen region is increased and that of the shrunken region decreased. This is not taken into account in the model in which the permeability is constant.

The observed and simulated results differ from each other by two respects.

1. The initial condition for porosity and water content are different.

2. From the observed void ratio it can be seen that the average void ratio of the sample is different for different time points. In other words, the observed profile curves do not intersect. On the contrary, the simulated void ratio profile curves intersect each other indicating a

constant volume of the sample. Actually, the observed profiles are for three different samples. In this respect it is natural that the observed void ratio curves are not consistent.

In practice, the saturation fit can not be further improved because the initial conditions for porosity and saturation are different.

The void ratio fit can not be very accurate for three reasons:

1. The initial condition is different.
2. Large local deformations have occured in the experiment. These can not occur in the model which is based on small deformation theory.
3. The total average void ratio for the given three time points is different. This is because the given three time points correspond to observations for three different samples. It is obvious that a single simulation can not be accurately fitted to all of the three distinct samples with differing total void ratio.

The average void ratio of the sample corresponding to the last observation is considerably smaller than the average void ratios of the other samples. Consequently, the simulated water ratio at four weeks is relatively higher than the observed one when compared to the results for the other two time points. At one week and two weeks the simulated water ratio profiles are more accurate than needed considering the differences between the simulational and experimental set-ups.

Temperature gradient experiment

Heating of the sample causes vaporization of water near the heated end and condensation of the vapor at the cold end. As a consequence, the water is redistributed across the sample causing shrinking at the hot dry end and swelling at the cold wet end. The resulting moisture gradient restricts further moisture redistribution.

Vaporization tends to increase the local gaseous pressure. As the gaseous permeability is finite the gaseous pressure increases restricting further vaporization. The absolute value of the obtained gaseous pressure is up to six times the normal pressure. The experimental value is not measured and the actual value would be difficult to observe in practice.

The influence of the relative permeability of liquid on the result is rather small and as expected from the past experience with the model. Decreasing

of the exponent from 3 to 2 increases the unsaturated relative permeability of liquid. Consequently, the suction driven moisture flow towards the drier hot region restricts more the vaporization driven drying. Consequently, for $k_{\mathrm{l,rel}} = \chi^2$ the saturation and the void ratio are more uniform across the sample.

The influence of the gaseous pressure boundary condition is significant. First of all, forcing the gaseous pressure on the boundaries to be constant makes the gaseous pressure naturally more uniform across the sample. Consequently, the redistribution of the liquid due to the vaporization and condensation is more intense.

The influence of the swelling model to the simulated moisture distribution results is rather small. Theoretically, the moisture redistribution causes local swelling and shrinking i.e. local changes in the porosity. This affects both the porosity dependent local suction and the value of saturation that is defined with respect to the pore volume. However, no significant effect on the moisture distribution result can be seen if the swelling model is neglected.

The main difference between the simulation and the observation is that the actual initial void ratio of 1.0 is significantly larger than the value 0.77 expected in the simulation. The observed deformation is also very large. The simulated change of volume during the first illustrated time points is so large that convergence problems occur right after that. The drying and the temperature gradient driven redistribution of moisture are underestimated by the simulation.

Simulated void ratio change is small for the swelling model. Very large deformation occurs in the observation. Because of this the simulated water ratio can not be very accurate. Saturation is the most compatible quantity to be compared to the observation because its dependence on the porosity is the smallest. However, simulated saturation differs from the observation for at least three reasons.

1. The initial saturation of 0.61 for the simulation is different from that of the experiment of 0.5.

2. As the saturation is defined with respect to the porosity, the initial significantly different and strongly varying porosity of the experiment affects also the saturation.

3. The increasing gaseous pressure prevents further vaporization. Consequently, the simulation result depends significantly on the gaseous

pressure boundary condition. Definite conclusion can not be drawn as the actual gaseous pressure is not known.

The assumption of constant atmospheric gaseous pressure at every outer boundary yields better fit than the assumption of free gaseous pressure at the boundaries. Both assumptions are oversimplifications and the true actual pressure must be a combination of these two extremes. In practice, the experimental set-up is liquid-tight but not gas-tight. There has to be some preferable pathways for the gas flow through the natural boundaries of the sample and the container. Consequently, the build-up of gaseous pressure is not strictly determined by the applied thermal gradient and the porous matrix as the only pathway for the gas flow.

Comparison of the simulated and measured values of porosity and water ratio is not very meaningful. However, the main features and the evolution direction are the same. In other words, the qualitative fit is rather good, which is the only relevant way of comparing in this case. On the other hand, the obtained saturation degree profiles are accurate regarding all the discrepancies listed above.

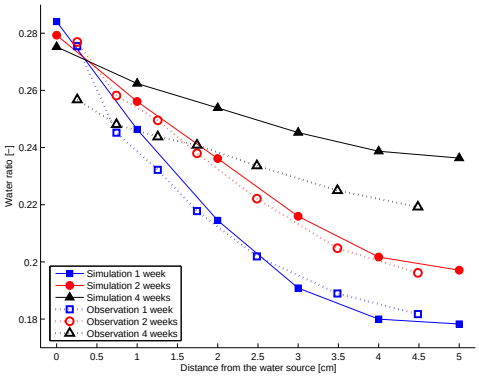

a) Water ratio with $k_{\mathrm{l,rel}} = \chi^3$.

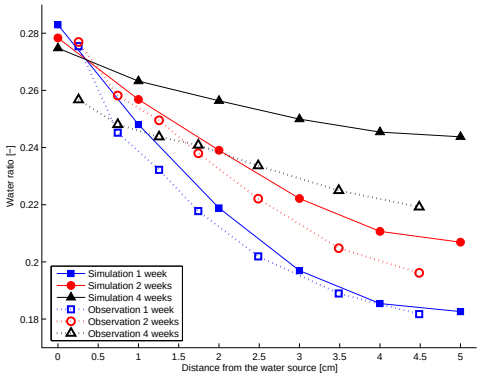

d) Water ratio with $k_{\mathrm{l,rel}} = \chi^2$.

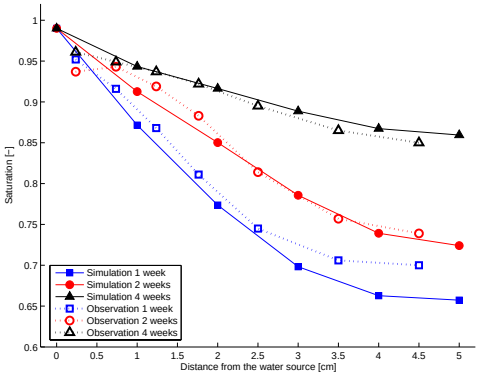

b) Saturation with $k_{\mathrm{l,rel}} = \chi^3$.

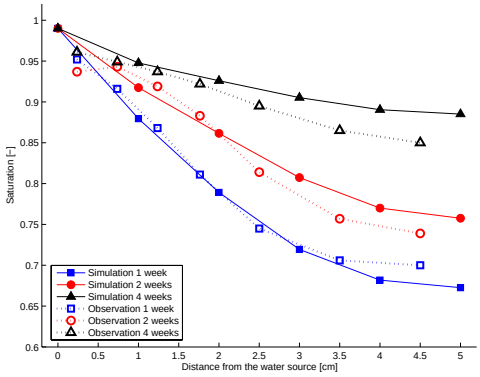

e) Saturation with $k_{\mathrm{l,rel}} = \chi^2$.

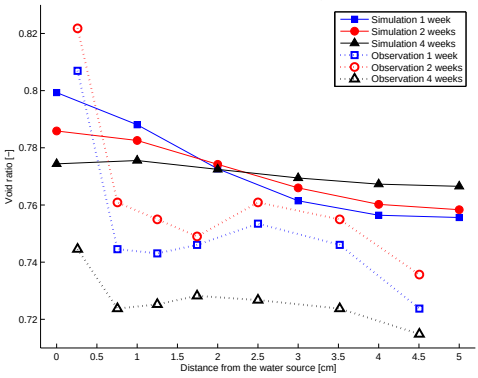

c) Void ratio with $k_{\mathrm{l,rel}} = \chi^3$.

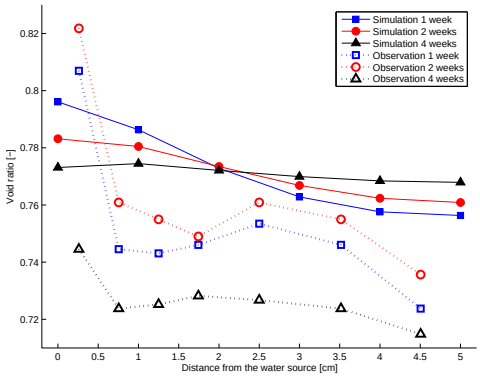

f) Void ratio with $k_{\mathrm{l,rel}} = \chi^2$.

Figure 8.12: SKB Water uptake experiment. Simulated and observed profiles of water ratio, saturation, and void ratio with two variants of relative permeability of liquid.

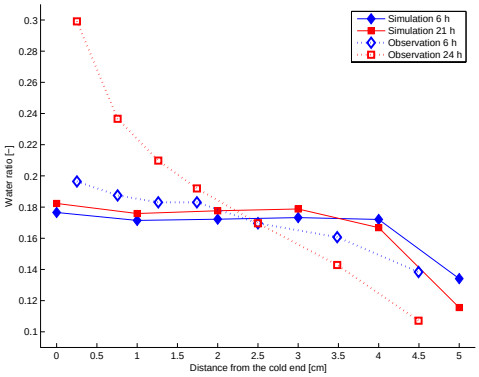

a) Water ratio with $k_{\mathrm{l,rel}} = \chi^3$.

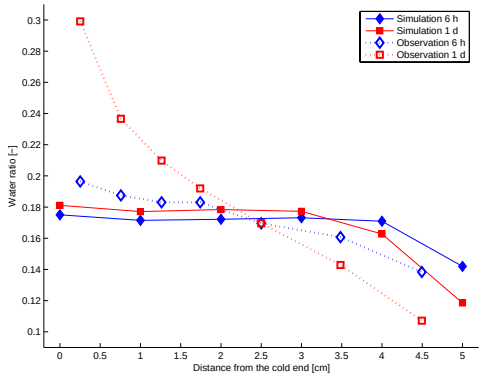

c) Water ratio with $k_{\mathrm{l,rel}} = \chi^2$.

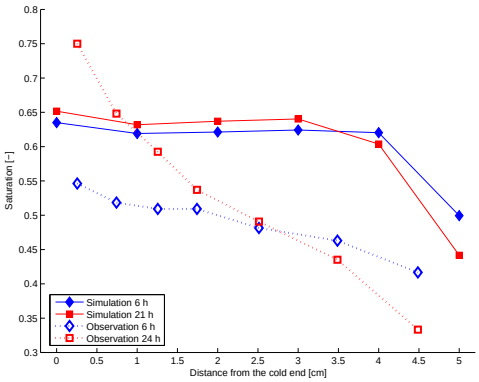

b) Saturation with $k_{\mathrm{l,rel}} = \chi^3$.

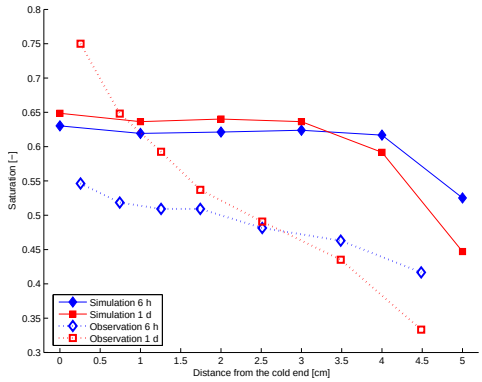

d) Saturation with $k_{\mathrm{l,rel}} = \chi^2$.

Figure 8.13: SKB temperature gradient experiment. Simulated and observed profiles of water ratio and saturation with two variants of relative permeability of liquid. The gaseous pressure is free at the hot boundary.

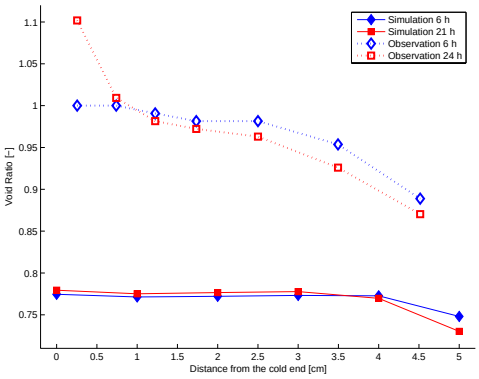

a) Void ratio with $k_{\mathrm{l,rel}} = \chi^3$.

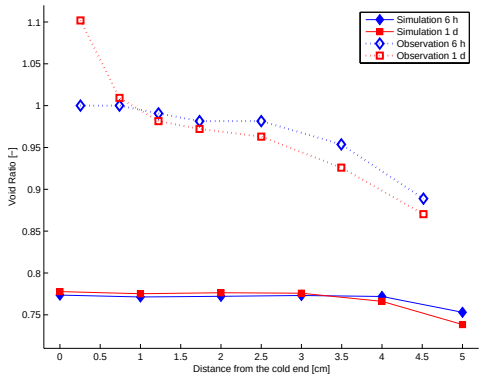

c) Void ratio with $k_{\mathrm{l,rel}} = \chi^2$.

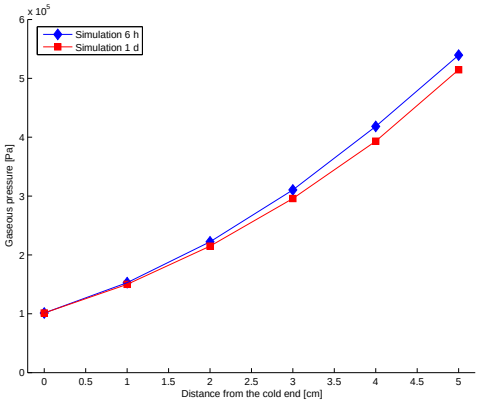

b) Pore pressure with $k_{\mathrm{l,rel}} = \chi^3$.

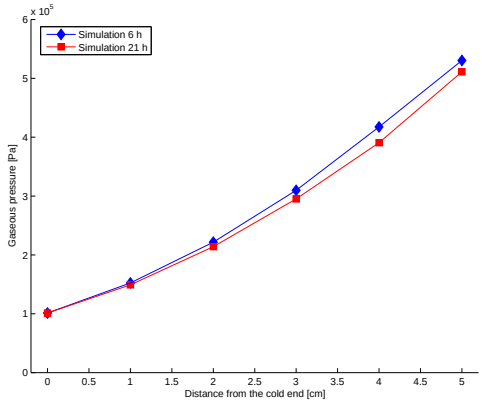

d) Pore pressure with $k_{\mathrm{l,rel}} = \chi^2$.

Figure 8.14: SKB temperature gradient experiment. Simulated and observed profiles of void ratio and gaseous (pore) pressure with two variants of relative permeability of liquid. The gaseous pressure is free at the hot boundary.

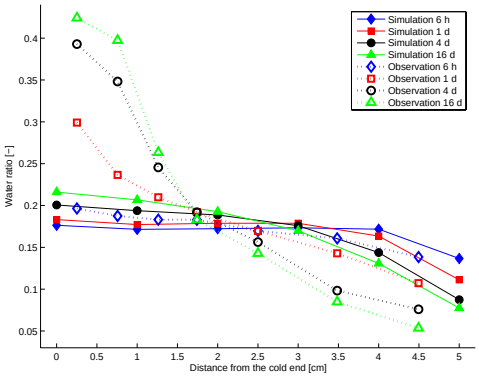

a) Water ratio with $k_{\mathrm{l,rel}} = \chi^3$.

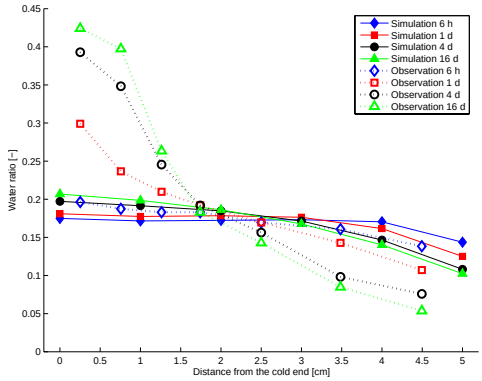

d) Water ratio with $k_{\mathrm{l,rel}} = \chi^2$.

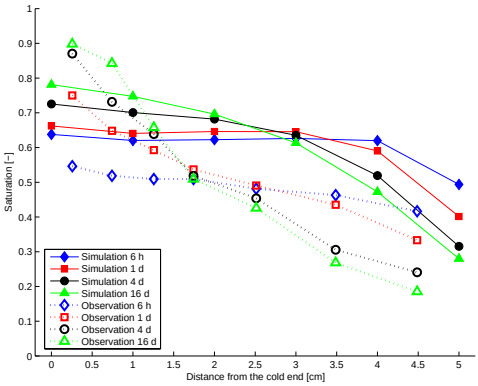

b) Saturation with $k_{\mathrm{l,rel}} = \chi^3$.

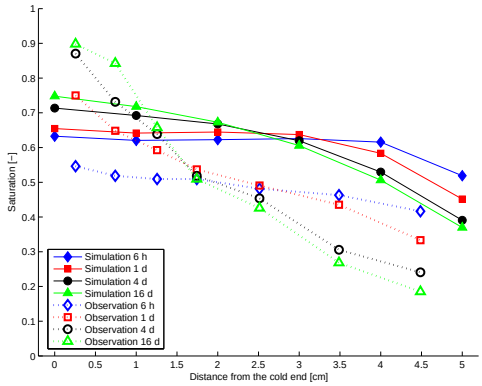

e) Saturation with $k_{\mathrm{l,rel}} = \chi^2$.

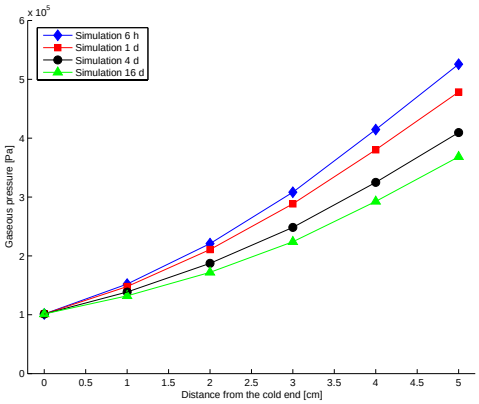

c) Pore pressure with $k_{\mathrm{l,rel}} = \chi^3$.

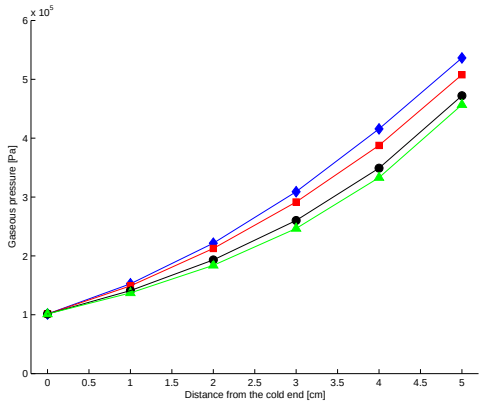

f) Pore pressure with $k_{\mathrm{l,rel}} = \chi^2$.

Figure 8.15: SKB temperature gradient experiment. Simulated and observed profiles of water ratio, saturation, void ratio, and gaseous (pore) pressure with two variants of relative permeability of liquid. The gaseous pressure is free at the hot boundary. Simulation without the swelling model.

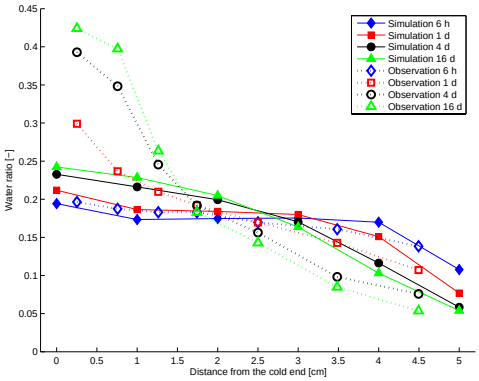

a) Water ratio with $k_{\mathrm{l,rel}} = \chi^3$.

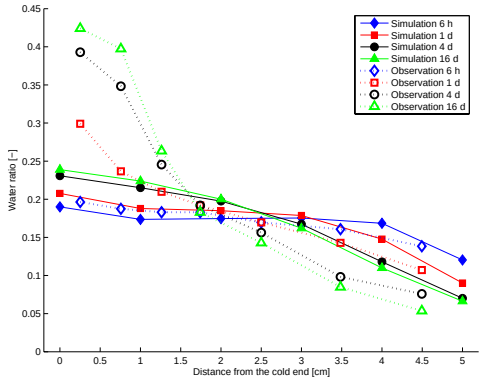

d) Water ratio with $k_{\mathrm{l,rel}} = \chi^2$.

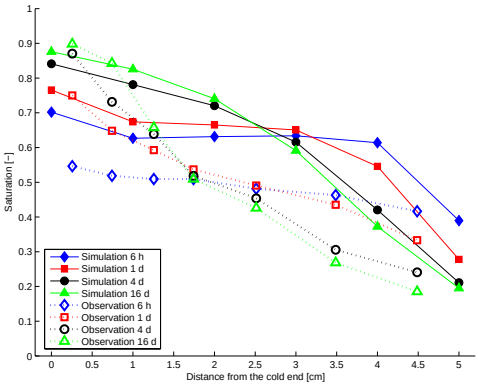

b) Saturation with $k_{\mathrm{l,rel}} = \chi^3$.

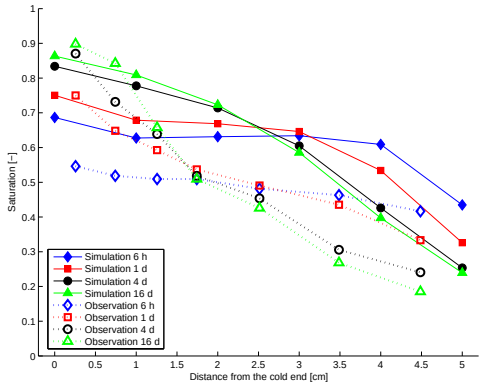

e) Saturation with $k_{\mathrm{l,rel}} = \chi^2$.

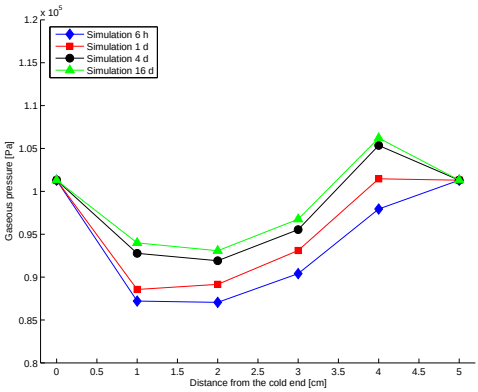

c) Pore pressure with $k_{\mathrm{l,rel}} = \chi^3$.

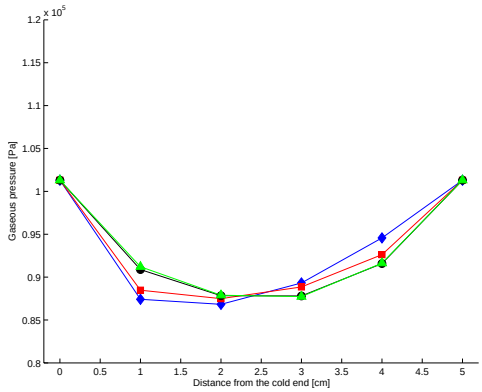

f) Pore pressure with $k_{\mathrm{l,rel}} = \chi^2$.

Figure 8.16: SKB temperature gradient experiment. Simulated and observed profiles of water ratio, saturation, void ratio, and gaseous (pore) pressure with two variants of relative permeability of liquid. The gaseous pressure is constant at every boundary. Simulation without the swelling model.

Chapter 9

Review of the analysis

9.1 The Febex analysis

The crude mechanical approach of the current model does not take into account the two structural levels of compacted bentonite and can not reproduce experiments in which the large deformations are involved. However, the hydro-mechanical simulation results are satisfactory near the initial state as was also the objective of the model. More experimental information, especially, multiple trajectories with identical initial state and loading history would increase the confidence on the results and improve the validity of the chosen HM parameters values.

The overall fit for the fully coupled THM behaviour is satisfactory. The chosen case specific thermal boundary conditions in the Febex THM experiment do not unambiguously validate the thermal part of the model. Because the actual sample was heterogeneous, a proper fit can not be achieved for the swelling and the porosity evolution. The relative permeability of gas has a significant influence on the moisture evolution. However, there are no pore pressure data available for an exact validation of this parameter.

A good fit for the moisture evolution of the Febex experiments can be achieved. The observed initial transient in the Febex mock-up test can be explained by the prewetting and, especially, by the anisotropy of the Febex buffer.

The simulated swelling pressure at the inner portion of the Febex in-situ buffer seems to be unrealistic. Together with the lack of capability to model large deformations this indicates a need for improvement of the swelling part of the model.

The model predicts an unsaturated steady state for the mock-up and

in-situ tests. More realistic disposal temperature evolutions yield nearly full saturation in up to 100 years. The exact timing depends at least on the chosen value for the relative permeability of gas.

An even more realistic temperature evolution could be achieved by taking the container as a third type of domain and applying a known time dependent heating power of the waste. However, the current approach was taken for convenience and for time saving purposes. It is interesting, that the rate of wetting is very similar for the two applied hypothetical and realistic temperature evolutions in which the maximum temperature is different but the rate of decrease of temperature is approximately the same. This indicates that the characteristics of the waste, i.e., the rate of radioactive decay determines the rate of resaturation while the total amount of waste in the container does not.

In addition, the applied special thermal boundary conditions correspond to the situations in which the adjacent disposal tunnels and holes are taken into account. The situation could be coped with by a 3D simulation with reflecting boundary conditions as was done in references [89] and [62]. However, the assumption made here is considered to give at least more realistic results than the boundary conditions of constant temperature at the heater and the Robin condition with the constant heat transfer coefficient at the rock. In this particular scenario, the evolution of the temperature gradient is the key factor to determine the time to achieve the complete saturation. The taken assumption of no adjacent tunnels yields higher temperature gradients across the buffer than in a case in which the adjacent tunnels are taken into account. Consequently, the simulated resaturation is slower than in reality.

Furthermore, the artificial high pore pressure of the mock-up test or the pore pressure gradient naturally occuring in the bedrock in the Febex in-situ experiment were not taken into account in the current analysis. In bedrock, the initially hydrostatic pore pressure is considerably high at the disposal depth. In the disposal tunnel, the initial pore pressure is close to the atmospheric one. Consequently, there is a large pore pressure gradient which also drives the groundwater towards the heater.

To conclude, the obtained time of 100 years to achieve the full saturation is considered as the upper estimate for the Febex type buffer in an ideal situation where there is enough water readily available from the rock.

However, there is experimental evidence [59], [28] that a practically full resaturation of a buffer can be achieved in a few years' time in realistic disposal conditions if enough water is available. This is the case of KBS3-type prototype repository buffer for which the initial water content is higher

and the buffer is thinner than in the considered Febex cases and for which the realistic heating power causes a small temperature gradient across the thin buffer.

9.2 The MX-80 analysis

The simulation of the Febex mock-up and in-situ tests predicted an unsaturated steady state when a large temperature gradient prevails across the buffer. The observed saturation evolution of the CEA mock-up tests do not contradict with this result. At the time of termination of the experiments, the hot regions of the samples have been quite dry and the rate of wetting has been quite small. The duration of the experiments has been too short to make final conclusions about the existence of an unsaturated steady state, however.

The most interesting and valuable piece of information given by the MX-80 experiments is the observed beginning of the moisture evolution of the CEA mock-up test: the transient phenomenon observed in the Febex mock-up experiment does not occur in the CEA mock-up test. This is an experimental evidence that the transient phenomenon is due to the anisotropic structure of the Febex buffer.

9.3 On the uncertainties

Parameters

The current modelling approach aimed at exhibiting relative minimalism. The derived rigorous thermomechanically consistent theory was reduced to reproduce the fundamental behaviour of swelling unsaturated porous material. The set of needed parameters is relatively small and all the parameters are physically reasonable.

From the resaturation point of view, the relative permeability of gas is the most uncertain parameter of the model and the most difficult to validate. Although it is evidently an intuitively clear physical parameter and its influence on the results is rational, a complete validation for its value is not achieved in the analysis.

The relative permeability of gas has been kept constant in every individual simulation. However, this is not true in reality. More precisely, the relative permeability of gas should depend at least on the amount of liquid which shares the same porous network. For thermo-hydro-mechanical

experiments this assumption could yield higher pore pressures and higher steady state saturation degrees.

The best fit of relative permeability of gas for different materials is different. Furthermore, the influence of the chosen value for different cases for the same material varies depending e.g. on the size of the sample and the applied temperature gradient. The chosen value is thus an effective value for the whole considered system. Apparently, the value should be variable depending on saturation degree, place, and time. However, as a relatively wide range of values for the relative permeability of gas (e.g. 10^3 - 10^7 for Febex mock-up experiment) yields rational results it is irrational to try to find any more detailed expression for the functional dependence of the relative permeability of gas on the primary variables.

On the other hand

1. A common assumption is [2], [42] that the gaseous pressure inside the buffer is constant which indicates infinite permeability of gas. In the current model this would yield the situation in which full saturation is not reached at the steady state.

2. To derive a better model for the relative permeability of gas would require even more information on the long-term evolution. In the current paper we have used virtually all the relevant currently available information on the Febex experiments (laboratory, mock-up, in-situ). With this information it seems that there is a realistic possibility that the Febex mock-up and in-situ experiments approach a steady state in which the respective buffers will not be fully saturated.

The experiments

Ideally, a large number of samples with identical initial conditions should be utilized in order to get a confident fit of the model. This was not the case in reality. However, the best possible available collection of experiments were used. The initial conditions vary considerably from each other despite the aim to have identical samples. Consequently, when choosing the parameter values one has to consider the qualitative behaviour and not the absolute values.

For MX-80 bentonite the experimental information is inadequate. Firstly, the initial state of the experiments is variable and in some cases significantly different from that of the planned disposal. Secondly, in both the CEA mock-up test and in the SKB temperature gradient test the applied thermal gradient, the consequential water redistribution, and the local volume

changes are much larger than in the planned disposal. It is impossible to reproduce these experiments with a model in which only small deformation is allowed. It has to be emphasized that it is the weakness of the model that it can not reproduce the large deformation response of the material to the intensive applied load.

It is very useful to have experimental data in extreme conditions. However, for modelling and predicting purposes majority of the experiments should be focused to small deviations from the initial state. In other words, as much experimental information as possible should be obtained from the close vicinity of this initial state.

The available large scale THM experiments have not reached a steady state. In the available small scale tests the applied temperature gradient has been unrealistically high and the tests have been terminated before an achievement of a steady state. This is unfortunate, because definite conclusions for the conditions for such a steady state can not be drawn.

Chapter 10

Overall Discussion

The objective of the thesis was to model THM behaviour of swelling compacted bentonite buffer used in a HLW repository. One of the fundamental questions is the full resaturation, i.e.,

1. How does the full resaturation occur?
2. How long will the full resaturation take?

A relatively quick achievement of a complete saturation is favorable to ensure the planned safety functions of the buffer, e.g., to seal the construction gaps and to isolate the waste, to achieve a sufficient swelling pressure to mechanically support the waste container and to decrease the microbial behavior in the buffer, to increase the heat conductivity of the buffer to dissipate the heat generated by the waste, and to achieve stable chemical conditions. However, the emphasis of the study has been on the verification and validation of the model performance. This can be done by comparative simulations only, i.e., by comparing to relevant measurements, if available. These measurements are restricted especially by means of duration. In other words, fully coupled THM measurements have usually been terminated before the full resaturation or before an achievement of a steady state.

In the available experiments a full resaturation of the sample or the experimental buffer in a reasonable time has been apparently expected. However, this has not occured during the measurements reviewed in the current thesis. Nevertheless, we still expect that this kind of full resaturation will occur in the real conditions of the high level waste respository. This is because of the fundamental differences between the current experiments and the real situation, namely,

- The experimental temperature gradient is applied by a controllable heater. Because of this, a very high temperature gradient has been applied in a relatively short time across the buffer or sample. In the real situation, the heating power of a container is much smaller and the achievement of maximum temperature takes years.
- The achieved high temperature gradient is artificially maintained in the experiments. In the real repository conditions the heating power will decay along with time.

The current model seems to take this into account. In particular, the model

1. reproduces the available measurements satisfactorily and
2. predicts a steady state, in which the experimental buffer will stay partially unsaturated.

Regarding the fully coupled THM phenomena the emphasis of the model is the TH behaviour which will essentially determine the resaturation. The crucial component is the vaporization-condensation behaviour.

A HM-coupling and moisture swelling has been incorporated in the model. The approach is rather crude and the model takes into account only small deformations. Consequently, the model can not reproduce certain coupled experiments in which large local or global deformations have been allowed to occur. These experiments include, e.g.,

- HM experiments in which the sample is relatively weakly confined allowing large moisture swelling of the sample, or if the applied confining load is too high causing irreversible collapse of the pore structure of the sample.
- THM experiments in which the temperature gradient is high causing intensive water redistribution in the sample by vaporization and condensation. This, in turn, will cause large local shrinking and swelling.

However, the current model gives relatively good results for the following reasons.

1. In the real disposal situation
    - the temperature gradient will not get very high because the rising time of the temperature is much larger than in the experiments

and the heating power will decay along with time. Because of these, the surrounding rock mass has time to warm up and the local temperature gradient will not be very high.

- The real buffer is large (thick) and confined. Because of this, only local deformations occur in the real repository conditions.

2. The influence of the HM coupling, i.e. moisture swelling, on the resaturation is restricted and the current model reproduces the behaviour in a rational way.

Chapter 11

Conclusions

In order to investigate the coupled THM behaviour of the bentonite buffer, a general thermomechanical and mixture theoretical model was derived and applied to the fully coupled THM description of swelling compacted bentonite. The particular form of the free energy of the system was chosen to take into account interactions of the mixture components, namely, mixing of the gaseous components and adsorption and swelling interactions between the liquid component and the solid skeleton. The mechanical part of the model is limited to reversible behavior within the limit of small strains. Numerical implementation was done with the multi-purpose finite element method software ELMER.

The model was applied to various coupled experiments: two kinds of laboratory scale tests for Febex bentonite, larger scale mock-up and in-situ tests for Febex bentonite, and to three kinds of laboratory scale experiments for MX-80 bentonite. In addition, a brief consideration of the difference of the large scale Febex experiments and the real HLW disposal situation was done by incorporating more realistic temperature evolution of the containers.

The inclusion of the mixing interaction yielded Clausius-Clapeyron equations which are valid both for the total pressure (i.e. the boiling pressure) and for the partial pressure of saturated vapor. Additionally, together with an appropriate dissipation function, the mixing interaction yielded a common form of the Fick law. The adsorption interaction together with the mixing interaction yields a modified Clausius-Clapeyron equation for the vapor-liquid equilibrium inside the porous medium with suction as the macroscopic result. The swelling interaction yielded the macroscopic swelling deformation and swelling pressure in confined condition. Together with the adsorption interaction function and the appropriate dissipation function, a modified

form the Darcy law was obtained.

The model was validated by the simulated experiments to reproduce the main coupled features of unsaturated swelling porous medium satisfactorily. The main results are related to the important questions of the evolution of resaturation and the final hydration stage.

- The observations for the Febex in-situ and, especially, for the Febex mock-up experiment exhibit an unexpected transient behaviour that the continuum model does not reproduce. This phenomenon is the fast initial wetting of the internal points of the buffer. This phenomenon was attributed here to the prewetting and, especially, to the anisotropic brick-wall like structure of the Febex buffer. Validation of this claim was based on the facts that the phenomenon is not encountered in the continuum mechanical simulations found in the literature, or in other experiments having a more isotropic structure. Furthermore, by neglecting the initial transient by assuming a higher initial water content the simulation results were consistent with the observations after the transient.

- The simulation of the experiments predicted a steady unsaturated state. Despite the artificial wetting, a Febex type bentonite buffer will not fully saturate if a high temperature gradient prevails as in the experimental set-ups considered.

- For the real disposal situation the simulations did predict a fully saturated state. However, the predicted time to achieve the full saturation is longer than commonly expected.

The difference between the results for the experiments and for the realistic disposal situation is due to the different heating powers and consequently different temperature profiles involved.

Bibliography

[1] Achanta, S., Cushman, J., Okos, M.: 1994, On multicomponent, multiphase thermomechanics with interfaces, *Int J Engng Sci* **32**, 1717–1738.

[2] Alonso, E.E., Alcoverro, J., Coste, F., Malinsky, L., Merrien Soukatchoff, V., Kadiri, I., Nowak, T., Shao, H., Nguyen, T.S., Selvadurai, A.P.S, Armand, G., Sobolik, S.R., Itamura, M., Stone, C.M., Webb, S.W., Rejab, A., Tijani, M., Maouche, Z., Kobayashi, A., Kurikami, H., Ito, A., Sugita, Y., Chijimatsu, M., Börgesson, L., Hernelind, J., Rutqvist, J., Tsang, C.-F, and Jussila, P.: 2005, The Febex benchmark test. Case definition and comparison of modelling approaches, *Int J Rock Mech Min Sci* **42**, 611–638.

[3] Baggio, P., Bonacina, C., and Schrefler, B.A.: 1997, Some Considerations on Modeling Heat and Mass Transfer in Porous Media, *Transport Porous Med* **28**, 233–251.

[4] Barrett, R., Berry, M., Chan, T.F., Demmel, J., Donato, J., Dongarra, J., Eijkhout, V., Pozo, R., Romine, C., and Van der Vors, H.: 1994, Templates for the Solution of Linear Systems: Building Blocks for Iterative Methods, SIAM, Philadelphia, PA.

[5] Bedford, A. and Drumheller, D.S.: 1983, Recent advances - Theories of immiscible and structured mixtures, *Int J Engng Sci* **21**, 863–960.

[6] Bennethum, L. and Cushman, J.: 1996a, Multiscale, hybrid mixture theory for swelling systems–I: Balance laws, *Int J Engng Sci* **34**, 125–145.

[7] Bennethum, L. and Cushman, J.: 1996b, Multiscale, hybrid mixture theory for swelling systems–II: Constitutive theory, *Int J Engng Sci* **34**, 147–169.

[8] Bennethum, L. and Cushman, J.: 1999, Coupled solvent and heat transport of a mixture of swelling porous particles and fluids: single time-scale problem, *Transport Porous Med* **36**, 211–244.

[9] Bennethum, L. and Cushman, J.: 2002a, Multicomponent, multiphase thermodynamics of swelling porous media with electroquasistatics: I. Macroscale field equations, *Transport Porous Med* **47**, 309–336.

[10] Bennethum, L. and Cushman, J.: 2002b, Multicomponent, multiphase thermodynamics of swelling porous media with electroquasistatics: II. Constitutive theory, *Transport Porous Med* **47**, 337–362.

[11] Bennethum, L. and Weinstein, T.: 2004, Three pressures in porous media, *Transport Porous Med* **54**, 1–34.

[12] Boek, E.S., Coveney, P.V., and Skipper, N.T.: 1995, Molecular modeling of clay hydration: a study of hysteresis loops in the swelling curves of sodium montmorillonites, *Langmuir* **11**, 4629–4631.

[13] Börgesson, L., Hernelind, J.: 1999, Coupled thermo-hydro-mechanical calculations of the water saturation phase of a KBS-3 deposition hole. Influence of hydraulic properties on the water saturation phase, *TR-99-41*, Swedish Nuclear Fuel and Waste Management Co.

[14] Bouddour, A., Auriault, J.-L., and Mhamdi-Alaoui, M.: 1998, Heat and mass transfer in wet porous media in presence of evaporation-condensation, *Int J Heat Mass Tran* **41**, 2263–2277.

[15] Callen, H.B.: 1985, *Thermodynamics and an introduction to thermostatistics*, Wiley, New York.

[16] Cases, J.M., Berend, I., Besson, G., Francois, M., Uriot, J.P., Thomas, F., and Poirier, J.E.: 1992, Mechanism of adsorption and desorption of water vapor by homoionic montmorillonite. 1. The sodium-exchanged form, *Langmuir* **8**, 2730–2739.

[17] Chijimatsu, M., Börgesson, L., Fujita, T., Hernelind, J., Jussila, P., Nguyen, T.S., Rutqvist J., and Jing, L.: 2006, Model calibration of small and large-scale laboratory THM experiments of the MX-80 bentonite, *GeoProc2006: 2nd International Conference on Coupled T-H-M-C Processes in Geosystems: Fundamentals, Modelling, Experiments and Applications*, Nanjing, China.

[18] Chou Chang, F-R., Skipper, N.T., and Sposito, G.: 1995, Computer simulation of interlayer molecular structure in sodium montmorillonite hydrates, *Langmuir* **11**, 2734–2741.

[19] Coleman, B. and Noll, W.: 1963, The thermodynamics of elastic materials with heat conduction and viscosity, *Arch Ration Mech Anal* **13**, 167–178.

[20] Collin, F., Li, X.L., Radu, J.P., and Charlier, R.: 2002, Thermo-hydro-mechanical coupling in clay barriers, *Engng Geol* **64**, 179–193.

[21] Coussy, O.: 1989, A General Theory of Thermoporoelastoplasticity for Saturated Porous Materials, *Transport Porous Med* **4**, 281–293.

[22] Coussy, O.: 1995, Mechanics of Porous Continua, Wiley, Chichester.

[23] CSC - The Finnish IT Center for Science: 2006, *ELMER*, [WWW document] http://www.csc.fi/Elmer/.

[24] Cui, Y.J., Yahia-Aissa, M., and Delage, P.: 2002, A model for the volume change behavior of heavily compacted swelling clays, *Engng Geol* **64**, 233–250.

[25] de Boer, R. and Didwania, A.K.: 2001, Saturated elastic porous solids: Incompressible, compressible and hybrid binary models, *Transport Porous Med* **45**, 425–445.

[26] de Boer, R. and Didwania, A.K.: 2004, Two-phase flow and the capillarity phenomenon in porous solids - a continuum thermomechanical approach, *Transport Porous Med* **56**, 137–170.

[27] de Boer, R. and Bluhm, J.: 1999, Phase transitions in gas- and liquid-saturated porous solids, *Transport Porous Med* **34**, 249–267.

[28] Cleall, P.J., Melhuish, T.A., and Thomas, H.R.: 2006, Modelling the three-dimensional behaviour of a prototype nuclear waste repository, *Engng Geol* **85**, 212–220.

[29] Decovalex-THMC - International co-operative project for the DEvelopment of COupled models and their VALidation against EXperiments in nuclear waste isolation: 2007, *Decovalex*, [WWW document] http://www.decovalex.com/.

[30] Delage, P., Howat, M.D., and Cui, Y.J.: 1998, The relationship between suction and swelling properties in a heavily compacted unsaturated clay, *Engng Geol* **50**, 31–48.

[31] Delville, A.: 1992, Structure of liquids at a solid interface: an application to the swelling of clay by water, *Langmuir* **8**, 1796–1805.

[32] de Vries, D.A.: 1958, Simultaneous transfer of heat and moisture in porous media, *Transac Am Geophys Union* **39**, 909–916.

[33] Dormieux, L., Lemarchand, E., and Coussy, O.: 2003, Macroscopic and Micromechanical Approaches to the Modelling of the Osmotic Swelling in Clays, *Transport Porous Med* **50**, 75–91.

[34] Enresa: 2000, *FEBEX project – full-scale engineered barriers experiment for a deep geological repository for high level radioactive waste in crystalline host rock. Final report*, Publicación técnica 1/2000. Enresa, Madrid.

[35] Franca, L.P. and Frey, S.L.: 1992, Stabilized finite element methods: II. The incompressible Navier-Stokes equations, *Comp Meth Appl Mech Engng* **99**, 209–233.

[36] Franca, L.P., Frey, S.L., and Hughes, T.J.R.: 1992, Stabilized finite element methods: I. Application to the advective-diffusive model, *Comp Meth Appl Mech Engng* **95**, 253–276.

[37] Frémond, M.: 2002, Non-smooth thermomechanics, Springer, Berlin.

[38] Frémond, M. and Nicolas, P.: 1990, Macroscopic thermodynamics of porous media, *Continuum Mech Therm* **2**, 119–139.

[39] Gawin, D., Baggio, P., and Schrefler, B.A.: 1995, Coupled heat, water and gas flow in deformable porous media, *Int J Num Meth Fluids* **20**, 969–987.

[40] Gawin, D., Majorana, C.E., and Schrefler, B.A.: 1999, Numerical analysis of hygro-thermal behaviour and damage of concrete at high temperature, *Mech Cohes-Fric Mat* **4**, 37–74.

[41] Gens, A. and Alonso, E.E.: 1992, A framework for the behaviour of unsaturated expansive clays, *Can Geotech J* **29**, 1013–1032.

[42] Gens, A., Garcia-Molina, A.J., Olivella, S., Alonso, E.E., and Huertas, F.: 1998, Analysis of a full scale in situ test simulating repository conditions, *Int J Numer Anal Meth Geomech* **22**, 515–548.

[43] Gens, A., Guimares, L. do N., Garcia-Molina, A., and Alonso, E.E.: 2002, Factors controlling rock-clay buffer interaction in a radioactive waste repository, *Engng Geol* **64**, 297–308.

[44] Gray, W.: 1983, General conservation equations for multi-phase systems: 4. Constitutive theory including phase change, *Adv Water Resour* **6**, 130–140.

[45] Gray, W. and Hassanizadeh, S.: 1991a, Paradoxes and Realities in Unsaturated Flow Theory, *Water Resour Res* **27**, 1847–1854.

[46] Gray, W. and Hassanizadeh, S.: 1991b, Unsaturated Flow Theory Including Interfacial Phenomena, *Water Resour Res* **27**, 1855–1863.

[47] Grimsel test site: 2006, *GTS*, [WWW document] http://www.grimsel.com/.

[48] Gu, W.Y., Lai, W.M., and Mow, V.C.: 1999, Transport of Multi-Electrolytes in Charged Hydrated Biological Soft Tissues, *Transport Porous Med* **34**, 143–157.

[49] Haase, R.: 1990, *Thermodynamics of irreversible processes*, Dover, New York.

[50] Hartikainen, J. and Mikkola, M.: 1997, Thermomechanical model of freezing soil by use of the theory of mixtures, in J. Aalto and T. Salmi (eds.), *Proceedings of the 6th Finnish Mechanics Days*, pp. 1 – 26.

[51] Hartikainen, J. and Mikkola, M.: 2005, Thermomechanical modelling for freezing of solute saturated soil, in Huyghe, J.M., Raats, P.A.C, and Cowin, S.C. (eds.), *Proceedings of the IUTAM Symposium on Physicochemical and Electromechanical Interactions in Porous Media*, Springer, pp. 335–342.

[52] Hassanizadeh, S.M., Gray, W.G.: 1979, General conservation equations for multiphase systems: 2. Mass, momenta, energy, and entropy equations, *Adv Water Resour* **2**, 191–208.

[53] Hassanizadeh, S.M., Gray, W.G.: 1980, General conservation equations for multiphase systems: 3. Constitutive theory for porous media flow, *Adv Water Resour* **3**, 30–45.

[54] Hensen, E.J.M. and Smit, B.: 2002, Why clays swell, *J Phys Chem B* **106**, 12664–12667.

[55] Huyghe, J.M. and Janssen J.D.: 1999, Thermo-Chemo-Electro-Mechanical Formulation of Saturated Charged Porous Solids, *Transport Porous Med* **34**, 129–141.

[56] Hökmark, H.: 2004, Hydration of the bentonite buffer in a KBS-3 repository, *Appl Clay Sci* **26**, 219–233.

[57] Ichikawa, Y., Kawamura, K., Nakano, M., Kitayama, K., Seiki, T, and Theramast, N.: 2001, Seepage and consolidation of bentonite saturated with pure- or salt-water by the method of unified molecular dynamics and homogenization analysis, *Engng Geol* **60**, 127–138.

[58] Ilic, M. and Turner, I.W.: 1989, Convective drying of a consolidated slab of wet porous material, *Int J Heat Mass Transfer* **32**, 2351–2362.

[59] Johannesson, L-E., Börgesson, L., Goudarzi, R., Sanden, T., Gunnarsson, D., and Svemar, C.: 2006, Prototype repository: A full scale experiment at Äspö HRL, *J Phys Chem Earth*, doi:10.1016/j.pce.2006.04.027.

[60] Jussila, P.: 2006, Thermomechanics of Porous Media - I: Thermo-hydraulic Model for Compacted Bentonite, *Transport Porous Med*, **62**, 81–107.

[61] Jussila, P. and Ruokolainen, J.: 2007, Thermomechanics of Porous Media - II: Thermo-hydro-mechanical Model for Compacted Bentonite, *Transport Porous Med*, **67**, 275–296.

[62] Jussila, P.: 2006, Thermo-hydro-mechanical model for unsaturated swelling porous media - application to Task A of the Decovalex-THMC project, *GeoProc2006: 2nd International Conference on Coupled T-H-M-C Processes in Geosystems: Fundamentals, Modelling, Experiments and Applications*, Nanjing, China.

[63] Kaasschieter, E.E., Frijns, A.J.H, and Huyghe, J.M.: 2003, Mixed finite element modelling of cartilaginous tissues, *Mathematics and Computers in Simulations* **61**, 549–560.

[64] Kanno, T., Kato, K., and Yamagata, J.: 1996, Moisture movement under a temperature gradient in highly compacted bentonite, *Engng Geol* **41**, 287–300.

[65] Karaborni, S., Smit, B., Heidug, W., Urai, J., and van Oort, E.: 1996, The swelling of clays: molecular simulations of the hydration of montmorillonite, *Science* **271**, 1102–1104.

[66] Komine, H.: 2004, Simplified evaluation for swelling characteristics of bentonites, *Appl Clay Sci* **71**, 265–279.

[67] Komine, H. and Ogata, N.: 1994, Experimental study on swelling characteristics of compacted bentonite, *Can Geotech J* **31**, 478–490.

[68] Komine, H. and Ogata, N.: 1996, Prediction for swelling characteristics of compacted bentonite, *Can Geotech J* **33**, 11–22.

[69] KYT - Finnish Research Programme on Nuclear Waste Management: 2002–2005, [WWW document] http://www.virtual.vtt.fi/kyt/.

[70] Lempinen, A.: 2006, *Thermo-hydro-mechanical analysis of a deposition hole for spent nuclear fuel*, Licentiate thesis, Helsinki University of Technology, Department of Technical Physics and Mathematics.

[71] Lloret, A., Villar, M.V.: 2006, Advances on the knowledge of the thermo-hydro-mechanical behaviour of heavily compacted "FEBEX" bentonite, *J Phys Chem Earth*, doi:10.1015/j.pce.2006.03.002.

[72] Lloret, A., Villar, M.V., Sanchez, M., Gens, A., Pintado, X., and Alonso, E.E.: 2003, Mechanical behaviour of heavily compacted bentonite under high suction changes, *Geotechnique* **53**, 27–40.

[73] Low, P.F.: 1980, The swelling of clay: II. Montmorillonites, *Soil Science Soc Am J* **44**, 667–676.

[74] Martin, P.L. and Barcala, J.M.: 2005, Large scale buffer material test: Mock-up experiment at CIEMAT, *Engng Geol* **81**, 298–316.

[75] Meerveld, J. van, Molenaar, M.M., Huyghe, J.M., and Baaijens, F.P.T.: 2003, Analytical Solution of Compression, Free Swelling and Electrical Loading of Saturated Charged Porous Media, *Transport Porous Med* **50**, 111–126.

[76] Mikkola, M. and Hartikainen, J.: 2001, Mathematical model of soil freezing and its numerical implementation, *Int J Num Meth Engng* **52**, 543–557.

[77] Montes-H, G., Duplay, J., Martinez, L., Mendoza, C.: 2003a, Swelling-shrinkage kinetics of MX-80 bentonite, *Appl Clay Sci* **22**, 279–293.

[78] Montes-H, G., Duplay, J., Martinez, L., Geraud, Y., and Rousset-Tournier, B.: 2003b, Influence of interlayer cations on the water sorption and swelling-shrinkage of MX-80 bentonite, *Appl Clay Sci* **22**, 309–321.

[79] Moyne, C. and Murad, M.: 2006, A Two-Scale Model for Coupled Electro-Chemo-Mechanical Phenomena and Onsager's Reciprocity Relations in Expansive Clays: I Homogenization Analysis, *Transport Porous Med* **62**, 333–380.

[80] Murad, M.: 1999a, Thermomechanical model of hydration swelling in smectitic clays: I Two-scale mixture theory approach, *Int J Num Anal Meth Geomech* **23**, 673–696.

[81] Murad, M.: 1999b, Thermomechanical model of hydration swelling in smectitic clays: II Three-scale inter-phase mass transfer: homogenization and computational validation, *Int J Num Anal Meth Geomech* **23**, 697–719.

[82] Murad, M., Bennethum, L., and Cushman, J.: 1995, A Multiscale theory of swelling porous media: I Application to one-dimensional consolidation, *Transport Porous Med* **19**, 93–122.

[83] Murad, M. and Cushman, J.: 1996, Multiscale flow and deformation in hydrophilic swelling porous media, *Int J Engng Sci* **34**, 313–336.

[84] Murad, M. and Cushman, J.: 1997, A Multiscale theory of swelling porous media: II Dual porosity models for consolidation of clays incorporating physico-chemical effects, *Transport Porous Med* **28**, 69–108.

[85] Murad, M. and Cushman, J.: 2000, Thermomechanical theories for swelling porous media with microstructure, *Int J Engng Sci* **38**, 517–564.

[86] Nassar, I.N. and Horton, R.: 1997, Heat, water, and solute transfer in unsaturated porous media: I - Theory development and transport coefficient evaluation, *Transport Porous Med* **27**, 17–38.

[87] Navarro, V. and Alonso, E.E.: 2000, Modeling swelling soils for disposal barriers, *Comp Geotech* **27**, 19–43.

[88] Nguyen, T.S., Selvadurai, A.P.S, and Armand, G.: 2005, Modelling the FEBEX THM experiment using a state surface approach, *Int J Rock Mech Min Sci* **42**, 639–651.

[89] Nguyen, T.S., Börgesson, L., Chijimatsu, M., Fujita, T., Hernelind, J., Jussila, P., Rutqvist, J., and Jing, L.: 2006, Influence of coupled THM phenomena on the performance of a spent fuel repository : a near-field study, *GeoProc2006: 2nd International Conference on Coupled T-H-M-C Processes in Geosystems: Fundamentals, Modelling, Experiments and Applications*, Nanjing, China.

[90] Olivella, S., Carrera, J., Gens, A., and Alonso, E.E.: 1994, Nonisothermal multiphase flow of brine and gas through saline media, *Transport Porous Med* **15**, 271–293.

[91] Olivella, S., and Gens, A.: 2000, Vapour transport in low permeability unsaturated soils with capillary effects, *Transport Porous Med* **40**, 219–241.

[92] Philip, J.R. and de Vries, D.A.: 1957, Moisture movement in porous materials under temperature gradients, *Transac Ame Geophys Union* **38**, 222–232.

[93] Pintado, X.: 2000, *Ensayos THM para el Proyecto FEBEX realizados por la UPC-DIT*, UPC, 70-UPC-M-0-03.

[94] Pintado, X.: 2002, *Caracterizacion del comportamiento termo-hidro-mecanico de arcillas expansivas*, PhD Thesis, Technical University of Catalonia.

[95] Pusch, R.: 2001, *The Buffer and Backfill Handbook Part 2: Materials and techniques*, SKB Technical Report TR-02-12.

[96] Pusch, R., Bluemling, P., and Johnson, L.: 2003, Performance of strongly compressed MX-80 pellets under repository-like conditions, *Appl Clay Sci* **23**, 239–244.

[97] Raiko, H.: 1996, *Käytetyn ydinpolttoaineen loppusijoituksen lämpötekninen optimointi*, POSIVA-96-03 (In Finnish).

[98] Romero, E., Gens, A., and Lloret, A.: 2003, Suction effects on a compacted clay under non-isothermal conditions, *Geotechnique* **53**, 65–81.

[99] Rutqvist, J., Börgesson, L., Chijimatsu, M., Kobayashi, A., Jing, L., Nguyen, T.S., Noorishad, J., and Tsang, C.-F.: 2001a, Thermohydromechanics of partially saturated geological media: governing equations and formulation of four finite element models, *Int J Rock Mech Mining Sci* **38**, 105–127.

[100] Rutqvist, J., Börgesson, L., Chijimatsu, M., Nguyen, T.S., Jing, L., Noorishad, J., and Tsang, C.-F.: 2001b, Coupled thermo-hydro-mechanical analysis of a heater test in fractured rock and bentonite at Kamaishi Mine – comparison of field results to predictions of four finite element codes, *Int J Rock Mech Mining Sci* **38**, 129–142.

[101] Schmidt, E.: 1989, *Properties of Water and Steam in SI-Units*, Springer, Berlin.

[102] Schrefler, B.A: 2002, Mechanics and thermodynamics of saturated/unsaturated porous materials and quantitative solutions, *Appl Mech Rev* **55**, 351–388.

[103] Schrefler, B.A: 2004, Multiphase flow in deforming porous material, *Int J Num Meth Engng* **60**, 27–50.

[104] Sposito, G., Prost, R.: 1982, Structure of water adsorbed on smectites, *Chem Rev* **82**, 553–573.

[105] Stepkowska, E.T.: 1990, Aspects of the Clay/Electrolyte/Water Systems with Special Reference to the Geotechnical Properties of Clays, *Engng Geol* **28**, 249–267.

[106] Stepkowska, E.T., Perez-Rodriquez, J.L., Maqueda, C., Starnawska, E.: 2004, Variability in water sorption and in particle thickness of standard smectites, *Appl Clay Sci* **24**, 185–199.

[107] Tambach, T.J., Hensen, E.J.M., and Smit, B.: 2004, Molecular simulations of swelling clay minerals, *J Phys Chem B* **108**, 7586–7596.

[108] Thomas, H.R., He, Y., Sansom, M.R., and Li, C.L.W.: 1996, On the development of a model of the thermo-mechanical-hydraulic behaviour of unsaturated soils, *Engng Geol* **41**, 197–218.

[109] Vargaftik, N.B.: 1975, *Tables on the thermophysical properties of liquids and gases*, 2nd edition, Wiley, New York.

[110] Villar, M.V., Cuevas, J., and Martin, P.L.: 1996, Effects of heat/water flow interaction on compacted bentonite: Preliminary results, *Engng Geol* **41**, 257–267.

[111] Villar, M.V. and Lloret, A.: 2004, Influence of temperature on the hydro-mechanical behaviour of a compacted bentonite, *Appl Clay Sci* **26**, 337–350.

[112] Villar, M.V.: 1999a, *Ensayos THM para el Proyecto FEBEX*, CIEMAT, 70-IMA-L-0-66.

[113] Villar, M.V.: 1999b, Investigation of the behaviour of bentonite by means of suction-controlled oedometer tests, *Engng Geol* **54**, 67–73.

[114] Villar, M.V.: 2002, *Thermo-hydro-mechanical characterisation of a bentonite from Cabo de Gata. A study applied to the use of bentonite as sealing material in high level radioactive waste repositories*, Publicationes tecnicas 04/2002, Enresa.

[115] Villar, M.V.: 2004, *Thermo-Hydro-Mechanical Characteristics and Processes in the Clay Barrier of a High Level Radioactive Waste Repository. State of the Art Report*, Informes Tecnicos Ciemat 1044.

[116] Villar, M.V., Garcia-Sineriz, J.L., Barcena, I., and Lloret, A.: 2005, State of the bentonite barrier after five years operation of an in situ test simulating a high level radioactive waste repository, *Engng Geol* **80**, 175–198.

[117] Xu, Y.F., Matsuoka, H., and Sun, D.A.: 2003, Swelling characteristics of fractal-textured bentonite and its mixtures, *Appl Clay Sci* **22**, 197–209.

[118] Yong, R.N. and Mohamed, A.-M.O.: 1996, Evaluation of coupled heat and moisture flow parameters in a bentonite-sand buffer material, *Engng Geol* **41**, 269–286.

[119] Ziegler, H.: 1977, *An introduction to thermomechanics*, North-Holland, Amsterdam.

[120] Ziegler, H. and Wehrli, C.: 1988, The derivation of constitutive relations from the free energy and dissipation function, *Adv Appl Mech* **25**, 183–238.

Appendix A

Mechanical top boundary condition for cylindrical symmetry

Experiments of cylindrical symmetry are simulated in the thesis. In an oedometric test a confining pressure is applied on top of the sample by a piston. If the piston is rigid the trivial boundary condition is zero vertical movement. For a swelling material the piston can also move depending on the applied force and the applied suction. An apparently natural choice for the mechanical boundary condition could be the applied constant force.

In the actual case, the vertical movement is the same for all of the points at the top boundary. On the contrary, the vertical stress is not the same at every point, i.e.,

$$\boldsymbol{\sigma}_{\mathrm{V}} = \boldsymbol{\sigma}_{\mathrm{V}}(r). \tag{A.1}$$

The vertical stress at a point of a horizontal cross section depends on the evolution of moisture and swelling in the whole sample. On the other hand, the applied external load is the total stress of the piston which is the weighted sum of the pointwise stresses.

As a solution for the boundary condition, we assume that the known applied stress is the same at every top boundary node. Because in the numerical model the boundary nodes are not stuck to each other they can move relative to each other in the vertical direction. We calculate the average vertical displacement of the top boundary by a weighted average of the individual vertical displacements of the top boundary nodes. The resulting error is considered acceptably small because the displacements are also small.

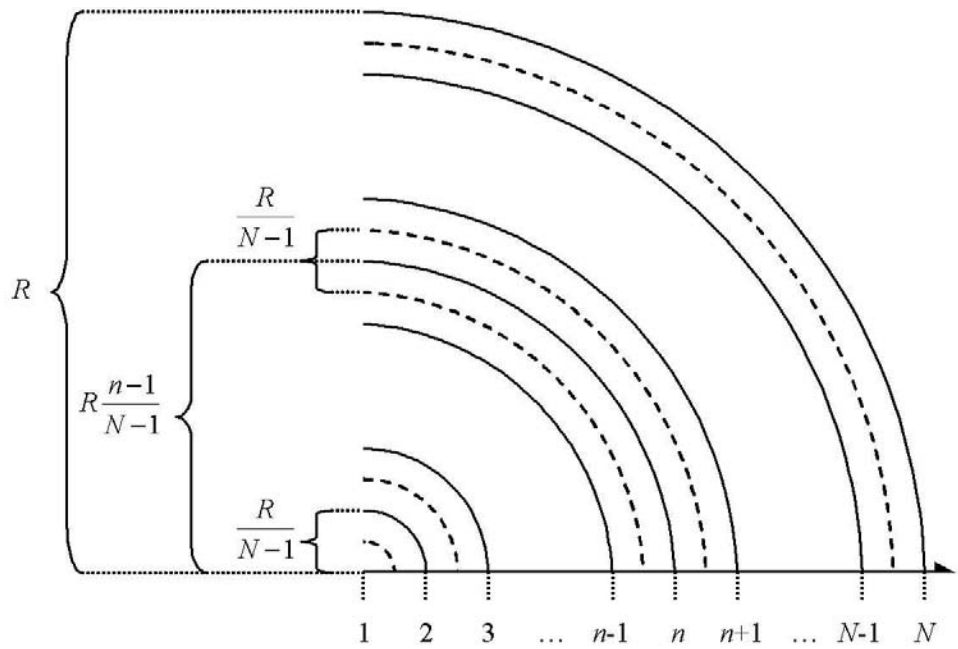

Figure A.1: A quarter of a cross-section of a cylindrical sample.

The same averaging procedure can be used for any quantity at any section perpedicular to the height axis.

The respective areas corresponding to the inner node ($n = 1$), outer node ($n = N$), and any node in between ($1 < n < N$) are (see Figure A.1)

$$A_1 = \pi\Big(\frac{1}{2}\frac{R}{N-1}\Big)^2 = 2\pi\frac{1}{8}\Big(\frac{R}{N-1}\Big)^2, \tag{A.2}$$

$$A_N = \pi\Big(N - \frac{5}{4}\Big)\Big(\frac{R}{N-1}\Big)^2, \tag{A.3}$$

$$A_n = 2\pi(n-1)\Big(\frac{R}{N-1}\Big)^2, \tag{A.4}$$

where R is the radius of the sample and N is the number of the boundary nodes. Obviously, the total area is

$$A = A_1 + \sum_{2}^{N-1} A_n + A_N = \pi R^2. \tag{A.5}$$

The weighted average F of any pointwise quantity f can now be approxi-

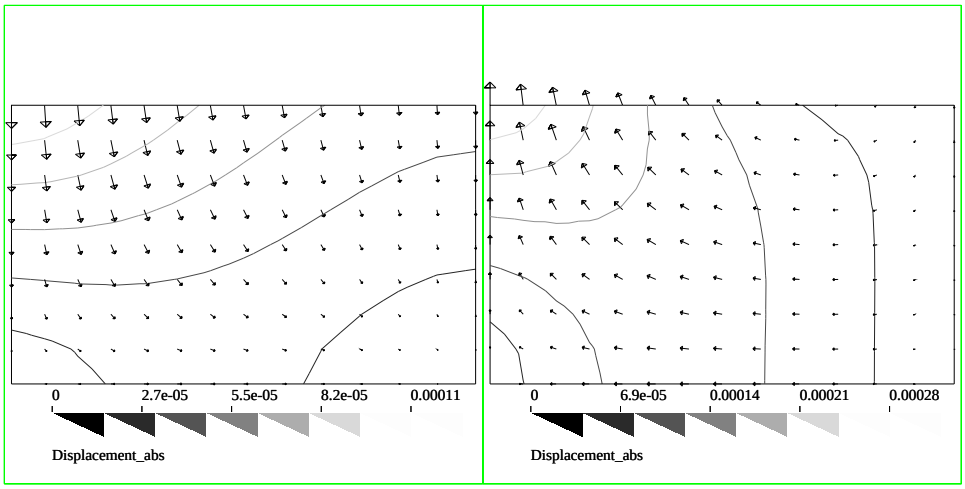

a) End of the initial phase. b) End of the phase 3.

Figure A.2: The simulated base case displacement field [m] of the trajectory 3 of the HM experiment at the end of the phases 1 and 3.

mated by

$$\begin{aligned} F &= \frac{f_1 A_1 + \sum_2^{N-1} f_n A_n + f_N A_N}{A} \\ &= \frac{f_1/4 + \sum_2^{N-1} (f_n 2(n-1)) + f_N \left(N - \frac{5}{4}\right)}{(N-1)^2}. \end{aligned} \tag{A.6}$$

For example, the simulated base case displacements of the trajectory 3 of the HM experiment for Febex bentonite at the end of the phases 1 and 3 are illustrated in Figure A.2. At phase 1 the applied vertical load is the same for all the top boundary nodes. Consequently, the top boundary displacements of the central nodes (left) are larger than those close to the outer boundary (right) (See Figure 7.10 for reference). The average deformation of the sample is calculated from the vertical displacements of the top boundary nodes with the method illustrated above. For example, the respective average deformations corresponding to Figures A.2a and A.2b are -0.39% and +0.23% (See Figure 7.10).